Structural Dynamics of Chlorinated Ruthenium Dioxide Model Catalysts under Reaction Conditions

im Fachbereich Biologie und Chemie
der Justus-Liebig-Universität Gießen
zur Erlangung des Grades
Doktor der Naturwissenschaften
-Dr. rer. nat.-
genehmigte Inaugural-Dissertation
von

Diplom-Chemiker Jan Philipp Hofmann
aus Solms

Gießen, 2009

Betreuer und 1. Gutachter: Prof. Dr. Herbert Over
2. Gutachter: Prof. Dr. Jürgen Janek
Tag der Disputation: 16.12.2009
Prüfer: Prof. Dr. Claus-Dieter Kohl
Prüfer: Prof. Dr. Siegfried Schindler

Preface

"Es gibt kaum etwas, was gegen die Regeln echter Naturforschung mehr streitet, als die Erfindung und der Gebrauch des Wortes Katalyse oder katalytische Kraft; wir alle wissen, dass in diesem Worte keine Wahrheit liegt..."
(Zitat Justus von Liebig, around 1865)

Meiner Familie

Contents

1 Motivation **11**

I Applied Experimental and Theoretical Methods **15**

2 Thermal Desorption Spectroscopy **17**

3 XPS and HRCLS **21**

4 Surface X-ray Diffraction **29**
  4.1 Introduction to SXRD 29
  4.2 Batch Reactor for Harsh Reaction Conditions at ESRF, ID03 . . . 31

5 Auger Electron Spectroscopy **37**

6 Reflection Absorption Infrared Spectroscopy RAIRS **43**
  6.1 Theoretical Survey of RAIR Spectroscopy 43
    6.1.1 IR Reflection Absorption 43
    6.1.2 Single Diatomic Adsorbate 44
    6.1.3 Coupling of the Vibrations in Adsorbed CO 47
  6.2 Measurement of a FT-RAIR Spectrum 47
  6.3 The RAIRS Apparatus 50

7 DFT Calculations on Adsorbate Systems **53**
  7.1 Structural Optimisation and Electronic Energy Calculation 54
  7.2 Adsorption Energies 56
  7.3 Frequency Calculations 56
  7.4 Calculation of Surface Core Level Shifts 57
  7.5 Modelling Chemical Reactions 60

7.5.1 Manual Shift of Atoms or Atom Groups along a Predefined Reaction Coordinate . . . 61
7.5.2 Nudged Elastic Band Calculations . . . 61

8 Atmospheric Pressure Reaction Measurements 65
8.1 Reactor System . . . 66
8.1.1 Gas Supply and Gas Mixture . . . 66
8.1.2 Fixed Bed Reactor . . . 68
8.1.3 Analytics - Quadrupole Mass Spectrometer . . . 68

9 Sample Cleaning and Preparation Procedures 71
9.1 Ru(0001) . . . 71
9.2 $RuO_2(110)$ . . . 72
9.3 $RuO_{2-x}Cl_x(110)$ . . . 77
9.4 Preparation of Chlorinated RuO_2 Catalysts at High Pressures . . 79

II Ruthenium Dioxide(110) as Model Catalyst - Literature Survey 81

10 The $RuO_2(110)$ Surface 83
10.1 Oxidation of Ru(0001) . . . 83
10.2 $RuO_2(110)$ films on Ru(0001) . . . 86

11 Chemical Activity of $RuO_2(110)$ 91
11.1 Adsorption of CO on Reduced $RuO_2(110)$ . . . 91
11.2 Adsorption of O_2 on $RuO_2(110)$ . . . 94
11.3 CO Oxidation on $RuO_2(110)$ - from UHV to 1 atm . . . 95
11.4 HCl Oxidation over RuO_2 . . . 97

III Chlorination of $RuO_2(110)$ 101

12 Chlorination Mechanism of $RuO_2(110)$ 103
12.1 Introduction . . . 103
12.2 DFT Study: Proposal of a Reaction Mechanism . . . 104

12.3 Chlorination of Hydrogen Pretreated $RuO_2(110)$ by HCl . . . 110
12.4 Chlorination of $RuO_2(110)$ by HCl Exposure . . . 113
12.5 Chlorination of CO Pre-reduced $RuO_2(110)$ by Cl_2 . . . 118

13 Determination of the Degree of Chlorination 121
13.1 The $(\sqrt{3} \times \sqrt{3})R30°$-Cl-Ru(0001) Phase . . . 121
13.2 Chlorine Content on $RuO_{2-x}Cl_x(110)$ . . . 124
13.2.1 Determination of the Sum Formula of Chlorinated RuO_2 . 126
13.3 Summary: Chlorination of $RuO_2(110)$ . . . 126

IV Structural Dynamics of Chlorinated RuO_2 129

14 Interaction of CO with $RuO_{2-x}Cl_x(110)$ 131
14.1 CO Adsorption on $RuO_{2-x}Cl_x(110)$ . . . 131
14.1.1 HRCLS Study: CO Adsorption on $RuO_{2-x}Cl_x(110)$ . . . 132
14.1.2 Adsorption of CO on $RuO_{2-x}Cl_x(110)$ under UHV . . . 134
14.1.3 Influence of Cl_{ot} on the Vibrational Properties of CO_{ot} . . 138
14.1.4 CO_{ot} + O_{ot} Coadsorbates . . . 140
14.2 Mild Reduction of $RuO_{2-x}Cl_x(110)$ . . . 144
14.2.1 Reduction of $RuO_{2-x}Cl_x(110)$ by CO in a *One-Step* Procedure . . . 146
14.2.2 Thermal Desorption of CO_{ot} from $(Cl_{br}+CO_{br})/CO_{ot}$ on $RuO_{2-x}Cl_x(110)$ . . . 147
14.3 Chapter Summary . . . 150

15 Influence of Oxygen on $RuO_{2-x}Cl_x(110)$ 153
15.1 Thermal Stability of $RuO_{2-x}Cl_x(110)$ . . . 153
15.2 The $Cl_{br} \leftrightarrow Cl_{ot}$ Shift Reaction . . . 159
15.2.1 HRCLS Study: O_2 Treatment of $RuO_{2-x}Cl_x(110)$ . . . 159
15.2.2 RAIRS Study: O_2 Treatment of $RuO_{2-x}Cl_x(110)$ at $\boldsymbol{T}$ = 700 K . . . 162
15.2.3 The $Cl_{br} \leftrightarrow Cl_{ot}$ Shift Reaction . . . 164
15.2.4 CO RAIRS Double Feature after Restoration of $RuO_{2-x}Cl_x(110)$ in O_2 . . . 173

15.3 Discussion 178

16 CO Oxidation on $RuO_{2-x}Cl_x(110)$ - Reactivity 181

16.1 O_{ot} Titration by CO - RAIRS Study 181

16.1.1 O_{ot} Titration on s-$RuO_2(110)$ 182

16.1.2 O_{ot} Titration on $RuO_{2-x}Cl_x(110)$ 184

16.2 *In situ* CO Oxidation - RAIRS Study 192

16.2.1 CO Oxidation on $RuO_{2-x}Cl_x(110)$ under HV conditions (10^{-6} mbar) 193

16.3 Reactivity and Stability of $RuO_{2-x}Cl_x(110)$ 198

16.3.1 Combined Reactivity and Stability Measurements under Reducing Feed Gas Composition 198

16.3.2 Stability against CO in Different Pressure Regimes 204

16.4 Summary of the Results - CO Oxidation over $RuO_{2-x}Cl_x(110)$ . . 207

17 CO Oxidation under Atmospheric Pressure Conditions 209

17.1 CO Oxidation over Fully Oxidised RuO_2 209

17.2 CO Oxidation over H_2-Reduced RuO_2 212

17.3 CO Oxidation over Chlorinated RuO_2 214

17.4 CO Oxidation over Chlorinated RuO_2 after O_2 Treatment 214

17.5 CO Oxidation over Chlorinated RuO_2 after Reduction by H_2 . . . 217

17.6 Discussion 219

V Conclusions 221

18 Summary and Outlook 223

VI Appendices 229

A Graphical Representations of the $RuO_2(110)$ Surface 231

B Lebenslauf 233

C Danksagung 235

D Eidesstattliche Erklärung 237

E Zusammenfassung in deutscher Sprache 239

Chapter 1

Motivation

Vast quantities of chlorine (Cl_2) are needed for the manufacture of many different plastics and drugs, for example of polyurethane polymers, which constitute a large share (approximately 30 % in Europe in 2008 [1]) of the Cl_2-consuming processes. During polyurethane synthesis, isocyanates are an essential intermediate, whose syntheses involve the reaction of amines with phosgene ($COCl_2$), and the elimination of two hydrogen chloride (HCl) molecules (cf. figure 1.1).

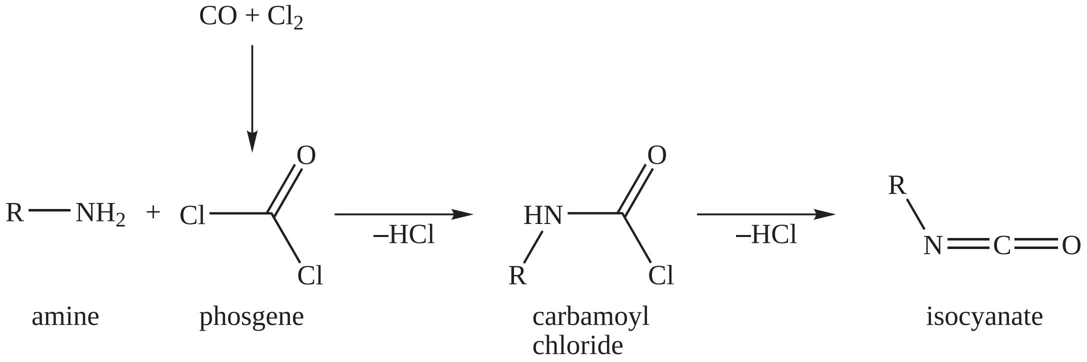

Figure 1.1: Isocyanate synthesis from amines and phosgene involving the elimination of two HCl molecules per molecule isocyanate. Isocyanates, especially toluene diisocyanate (TDI) and methylene diphenyl diisocyanate (MDI), are precursors in the synthesis of polyurethane polymers.

The byproduct HCl is environmentally undesirable and has only a very restricted market. Consequently, there has been growing interest in finding efficient methods for converting HCl back into Cl_2. The production and recycling of chlorine by electrochemical methods is widely applied and is one of the most energy-consuming processes in the chemical industry [2].

With the newly developed Sumitomo process on titania (TiO_2) supported ruthenium dioxide (RuO_2) catalysts based on the Deacon reaction, i.e. the heterogeneously catalysed oxidation of hydrogen chloride (HCl) to molecular chlorine (Cl_2) by air (cf. figure 1.2 [3]), a very energy efficient process for the HCl waste recovery to the more valuable Cl_2 has been introduced [4].

$$4\,\mathrm{HCl} + \mathrm{O_2} \rightleftharpoons 2\,\mathrm{H_2O} + 2\,\mathrm{Cl_2};\ \Delta H = -59\ \mathrm{kJ/mol}$$

Figure 1.2: The Deacon reaction - heterogeneously catalysed oxidation of HCl by oxygen.

The Sumitomo process is considered a real breakthrough in industrial catalysis, since chlorine can be recycled from waste HCl with low energy cost and conversion yields as high as 95 %. The energy consumption of the Sumitomo process is only 15 % of that required by the Bayer&UhdeNora electrolysis method, developed at the same time [5]. This radical improvement in the energy efficiency constitutes an important step towards a ‘greener’ chemistry in chlorine industry.

However, a large scale application of economically efficient ruthenium based catalysts, such as demonstrated in the Sumitomo process, is severely restricted by the limited availability of ruthenium, whose worldwide production amounts to only eight tons annually.

Detailed studies performed by Sumitomo Chemical [4] indicated that the catalytically active phase in the Sumitomo process is an ultra thin RuO_2 film (about 1-2 monolayers) supported on rutile-TiO_2. The introduction of a stable, supported catalyst, which only needs microscopic quantities of the active compound (here RuO_2), is a further necessary step towards a more efficient resource management. In the future, resource efficiency can not be further increased by trial-and-error methods alone, such as customarily applied in industrial catalysis research. Knowledge-based research has to be conducted instead in order to develop a molecular-level understanding of the catalytically relevant processes like structure-activity correlations, structural stability, and reactivity of the industrially applied catalysts. The present work is intended as a contribution in this direction.

In the present thesis, the complex interactions of Cl, O and CO with the $RuO_2(110)$ surface will be investigated within a mixed approach combining theoretical and several experimental methods. The results will be obtained by density functional theory (DFT) calculations as well as by means of high resolution core level shift spectroscopy (HRCLS), thermal desorption spectroscopy (TDS), Auger electron spectroscopy (AES) and reflection absorption IR spectroscopy (RAIRS). The validated approach of combining theoretical and experimental methods in catalysis research [6] benefits from the synergism: Interpretative models proposed by theoretical methods [7] are verified by clear-cut experiments and conversely, DFT calculations give helpful advice in the assignment and interpretation of experimental data.

One of the main topics of the present work was the elucidation of the chlorination mechanism of stoichiometric $RuO_2(110)$ by HCl exposure. During the Sumitomo process, the RuO_2 catalyst has been shown to incorporate chlorine atoms - by our group for the model catalyst $RuO_2(110)$ [8, 9, 10, 11] and by López et al. for a RuO_2 powder catalyst [12]. However, the incorporation of chlorine was shown to be limited to the surface of the catalyst. This surface selective chlorination accounts for the extraordinary stability of the catalyst during the HCl oxidation [9]. Experimental and theoretical studies will be conducted in order to develop a deeper understanding of how the chlorine uptake of the RuO_2 catalyst takes place under conditions which are also present in the Sumitomo process.

The knowledge gained about the chlorination process will provide a solid foundation for a further treatment of the properties of the chlorinated $RuO_2(110)$ model surface including the interaction with oxygen (important for the HCl oxidation process) and carbon monoxide (CO).

In this context, CO will be used as a chemically sensitive IR probe molecule, which allows for a detailed RAIRS analysis of the surface under both ultra high vacuum (UHV) and higher pressure conditions, in the manner as recently published by Farkas et al. [13, 14]. For that purpose, IR fingerprints of several representative coadsorbate phases of CO with O and Cl on the chlorinated $RuO_2(110)$ surface have been obtained under UHV at low temperature. This data was then used in the interpretation of RAIRS spectra obtained under different conditions such as reactions at higher pressure. A very detailed picture of the distribution of chemisorbed CO, O and especially of Cl species under different experimental conditions can be gained by exploiting this sensitive technique.

Another key issue of the present thesis has been the high degree of mobility of Cl atoms in the complex Cl/O/CO coadsorbate system on the chlorinated RuO_2 model catalyst, shown here to dynamically adjust itself in response to the presence of O and CO on the surface under the given experimental conditions. Especially the interplay of chlorine and oxygen atoms (accommodated on the surface) was found of decisive importance for an understanding of the stability and dynamic response of the RuO_2 catalyst under the conditions of the Sumitomo process. Further emphasis will be put on the complex pattern of mobility of the Cl atoms, observed to be strongly influenced by the chemical nature of the coadsorbed species (O and CO).

The introduction of chlorine atoms as a further component of the RuO_2 catalyst presumably induces a change not only in the stability of the oxide but also in its reactivity. The promoting effect of surface chlorine atoms has already been described e.g. for the epoxidation of ethylene on silver catalysts, being found to enhance the selectivity towards ethylene oxide at the expense of unwanted byproducts like acetaldehyde [15]. However, the reactivity was reported to decrease by 75 % upon cofeeding of 1 ppm Cl_2 to the reactant mixture [16].

In this thesis, special attention will be devoted to the impact of surface chlorination on the activity of the catalyst in a model reaction (in this case CO oxidation) in different pressure regimes. The determination of the influence of Cl substitution with respect to reactivity and stability of the RuO_2 catalyst in the CO oxidation constitutes a first necessary step towards a prospective, knowledge-based adjustment of catalytical activity and selectivity of the RuO_2 catalyst for more complex oxidation reactions.

In conclusion, the present work is aimed to give a detailed, molecularly resolved picture of the dynamic surface processes taking place on chlorinated RuO_2 model catalysts induced by the complex interplay of Cl with CO and O.

Part I

Applied Experimental and Theoretical Methods

Chapter 2

Thermal Desorption Spectroscopy

The main goal of thermal desorption spectroscopy (TDS) is the determination of the desorption parameters, such as activation energy of desorption ΔE^*_{des} and its coverage dependence, the frequency factor ν, and the reaction-order coefficient x.

At temperature T_{ad} a surface of area A is exposed to a certain amount of the species i which will adsorb and cover the surface by σ_i particles/cm^2 (or coverage Θ_σ). A thermodynamically transient state under UHV conditions (relative to the total system: clean surface + gas phase species) is formed. The desorption of the adsorbate is kinetically activated. The system is linearly and uniformly heated with a heating rate $\beta = \frac{dT}{dt}$, while the vacuum chamber is effectively pumped in order to minimise readsorption.

The desorption process of the species i can be described in terms of chemical reaction kinetics. The rate of desorption is given by

$$-\frac{d\sigma_i}{dt} = k_r \sigma_i^x \tag{2.1}$$

where σ_i is the surface concentration of species i and x is the order of the reaction. The rate constant k_r is temperature dependent according to the Arrhenius equation

$$k_r = k_{r,0} \cdot exp\left(-\frac{\Delta E^*_{des}}{RT}\right). \tag{2.2}$$

Replacing k_0 by the frequency factor ν and the surface concentration σ_i by coverages Θ_σ gives the Wigner-Polanyi equation for non-interacting adsorbates. It is the basis for all further considerations and data evaluation of TD spectra

$$-\frac{d\sigma_i}{dt} = -\sigma_{i,max} \cdot \frac{d\Theta_\sigma}{dt} = \nu_x \cdot exp\left(-\frac{\Delta E^*_{des}}{RT}\right) \cdot \Theta^x_\sigma. \tag{2.3}$$

ΔE^*_{des} is the activation energy for desorption, which can frequently be identified with the binding energy of a molecular adsorbate on the surface for the case, that no additional kinetic barriers have to be overcome in the desorption process.

In a simple picture, the desorption maximum occurs at the temperature T_{max}, where the most adsorbate-substrate bonds per time interval are thermally dissociated.

Concerning the rate constant of the desorption kinetics, there are mainly four different desorption orders [17]:

- $x = 1$: A first order desorption kinetic occurs, when the breaking of the adsorbate-substrate bond is the rate determining step. This type is characteristic of molecular desorption. The peak form is asymmetric and T_{max} depends on the heating rate β. As a rough approximation ν_i may be assumed as $\approx 10^{13}$ s^{-1}. For first order kinetics ΔE^*_{des} can be derived from the Redhead equation [18]

  $$\Delta E^*_{des} = RT_{max}\left(ln\frac{\nu_1 T_{max}}{\beta} - 3.64\right) \tag{2.4}$$

- $x = 2$: If the recombination of two adsorbate fragments is the rate determining step, one observes a second order desorption with a symmetric peak form. T_{max} shifts to lower temperatures with increasing coverages σ_i [17].

- $x = 0$: Zero order desorption occurs less frequently. In this case, the desorption of the adsorbate is not the rate determining step. An example is the desorption of condensed multilayer adsorbates. The peak form is strongly asymmetric with an exponential attack on the low-temperature side and an abrupt (almost vertical) decay beyond T$_{max}$. ΔE^*_{des} can be evaluated from a plot of $ln(d\sigma_i/dT)$ versus $1/T$ via the equation

  $$ln\left(\left|\frac{d\sigma_i}{dT}\right|\right) = -\frac{\Delta E^*_{des}}{RT} + ln\left(\frac{\nu_0}{\beta}\right) \tag{2.5}$$

  whereby a single TDS trace contains all the information.

A desorption kinetics with fractional order occasionally emerges if the adsorbate forms two-dimensional islands on the substrate. The rate determining step is the detachment of particles from the perimeter of the islands. A characteristic shift of T_{max} to higher temperatures for higher initial coverages is observed. The determination of the desorption order can be complicated by multiple-peak structures caused by adsorbates in different adsorption (binding) states or coverage dependent desorption energies $\Delta E^*_{des}(\sigma_i)$ and frequency factors $\nu(\sigma_i)$. Both complications can be related to lateral interactions between adsorbed particles.

The TDS experiments have been carried out in an ultrahigh vacuum (UHV) chamber equipped with LEED optics (low energy electron diffraction), a quadrupole mass spectrometer (QMS, Pfeiffer Prisma), and facilities for surface preparation and cleaning (design by H. Bludau [19]). The QMS was connected to the main chamber via a closed cone with a small aperture ($d = 2$ mm) facing the sample at a distance of approximately 1 mm. This ensures that only molecules released from the sample surface can reach the QMS. The heating rate for the temperature programmed desorption experiments was $\beta = 5$ K/s.

Chapter 3

XPS and HRCLS

X-ray photoelectron spectroscopy (XPS) is a surface sensitive spectroscopic technique that is able to measure the elemental composition, chemical and electronic state of adsorbates [20, 21, 22]. XP spectra are obtained by irradiating a material with a beam of monochromatic X-rays while simultaneously measuring the kinetic energy and number of the photoelectrons that are ejected from the topmost 1 to 10 nm (depending on the kinetic energy of the photoelectrons) of the material in question. XPS as a method, where electrons are the carriers of information, requires usually ultra high vacuum (UHV) conditions. However, ambient pressure XP spectrometers have been developed over the past years [23].

Interaction of X-rays with matter Applying X-rays, core shell electrons of the material will also be excited to energies above the vacuum level and consequently ejected. The valence electrons have a spatial probability in the core region and thus, are able to shield the nuclear charge. Therefore, different binding states of the atom in question have an impact on the core shell electron binding energies, which makes XPS not only element specific but also sensitive for the chemical environment of an atom. High energy resolution is required for distinguishing signals of the first monolayers from the bulk (surface core level shift).

XPS is based on the photoelectric effect, as shown schematically in figure 3.1. The sample is connected to the spectrometer so that the Fermi levels are equal.

To a first approximation, the kinetic energy of the ejected electrons E_{kin} is given by equation 3.1,

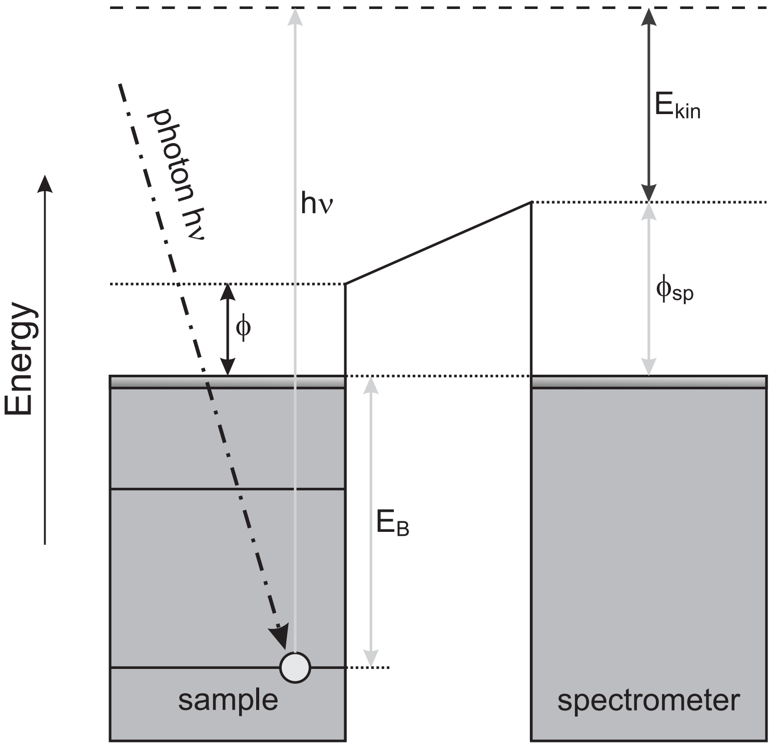
Energy
photon hν
hν
E_{kin}
ϕ
ϕ_{sp}
E_B
sample
spectrometer

Figure 3.1: Energy level diagram in photoelectron spectroscopy including sample and spectrometer.

$$E_{kin} = h\nu - E_B - \phi_{sp} \tag{3.1}$$

where $h\nu$ is the energy of the X-ray photons, E_B the binding energy of the ejected electron and ϕ_{sp} the work function of the spectrometer. The electron binding energies with respect to the vacuum level can only be obtained when the work function of the spectrometer is known. In the case of metallic conducting materials, this obstacle can be met by taking the Fermi level (zero-point of the E_B scale) as reference.

Quantum mechanical survey A system of N electrons, which is described by the wave function $\Psi^i(N)$ with the energy $E^i(N)$, is excited upon absorption of a photon of energy hν and thereby converted into an ion ($\Psi^f(N-1,k)$, $E^f(N-1,k)$) and a photoelectron with kinetic energy E_{kin}. The energy balance is then given by

$$E^i(N) + h\nu = E^f(N-1,k) + E_{kin} \tag{3.2}$$

whereby k denotes the energy level of the photoelectron in the initial state from which it was ejected.

If the wave function of the final state $\Psi^f(N-1,k)$ represents an atom with a hole in the niveau k, and if one assumes, that the spatial distribution and the energies of the $N-1$ remaining electrons of the atom stay unchanged with respect to the initial state, the binding energy E$_B$(k) of the photoemitted electron can be given as the negative orbital energy $-\varepsilon$ of the niveau k.

$$E_B(k) = -\varepsilon_k \tag{3.3}$$

This approach is also called the Koopmans' Theorem [24] which is based on the following assumptions:

1. Relativistic as well as electron-electron correlation effects are explicitly excluded in accordance to the Hartree-Fock model. By these effects, the binding energies of the core electrons are increased by $\delta\varepsilon_{rel}$ and $\delta\varepsilon_{corr}$, respectively.

2. Final state effects: The electronic environment of the remaining $N-1$ electrons is changed by the core hole. Their total energy is reduced by

relaxation, and thus, the binding energy is reduced by the amount of the relaxation energy $\delta\varepsilon_{relax} > 0$. $\delta\varepsilon_{relax}$ can be splitted in two terms: an intraatomic term, which describes the relaxation energy in the free atom and an interatomic term, which accounts for shielding of the core hole by electrons of the surrounding atoms in the crystal. For metals, these energies can be as high as 5-10 eV. Furthermore, either excited states (electron shake up) can emerge or electrons can be emitted (electron shake off) due to the spontaneous ionisation.

Taking the above mentioned assumptions into account, equation 3.3 can be expressed more precisely by

$$E_B(k) = -\varepsilon_k - \delta\varepsilon_{relax} + \delta\varepsilon_{rel} + \delta\varepsilon_{corr} \tag{3.4}$$

However, the chemical shifts observed in XPS are mainly discussed in terms of a change of the initial state orbital energies, whereby the energy levels of the remaining electrons in the final state stay constant (frozen orbital approximation):

$$\Delta E_B(k) = -\Delta\varepsilon_k \tag{3.5}$$

Analysis of High Resolution Core Level Shift Spectra (HRCLS) The main goal of high resolution core level shift spectroscopy experiments is the identification of atoms in different chemical surroundings as well as the determination of their concentrations. The analysis of the spectra is done by means of line shape analysis.

The intensity of the XP signal is as a first approximation proportional to the number of atoms, which induce the signal, i.e. a measure for the concentration of the species in question. However, the number of emitted photoelectrons can be influenced by diffraction processes which occur while the electrons leave the bulk. These effects dominate at low photon energies, whereas the mean free path of the photoelectron increases with increasing kinetic energy of the photoelectrons (cf. figure 3.2).

Choosing a higher photon energy minimises this problem, but leads to a decrease in surface sensitivity. The spectra analysed in the present thesis were recorded at low photon energies (580 eV for O 1s and 250 eV for Cl 2p), thus being as highly as possible surface sensitive, but with the drawback of a rela-

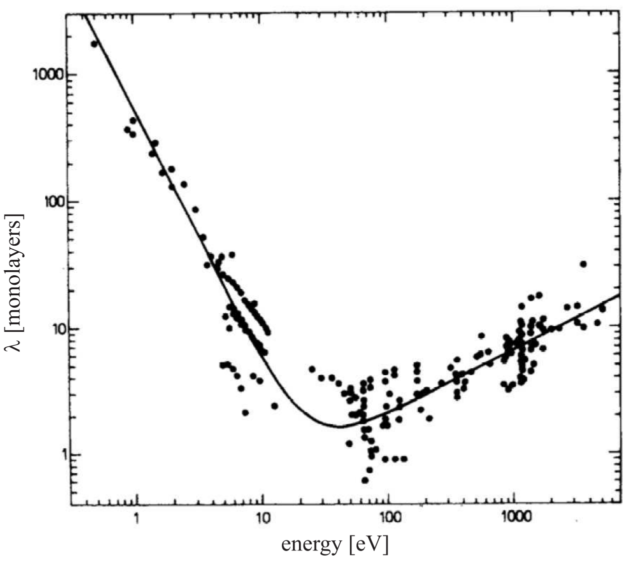

Figure 3.2: Mean free path of electrons in the solid given as monolayers as a function of energy. Figure taken from [25].

tively large secondary electron background, which complicates the quantification and calls for background correction. The resulting signal line shape is composed of three parts: a Lorentzian (finite core hole lifetime), a Gaussian (instrument) and an asymmetric term (excitation of valence band electrons by leaving photoelectrons). The overall line shape function used in the PC based analysis software FitXPS [26] was adapted from Doniach et al. [27]. The line shape of each peak is a (numerical) convolution of an analytical Doniach-Šunjić line shape with a Gaussian. The asymmetric Doniach-Šunjić line shape reduces to a (symmetric) Lorentzian line shape if the Doniach-Šunjić parameter α is zero. The parameters chosen for the line shape fits were the binding energy, intensity, FWHM(Gaussian), FWHM(Lorentzian) and the Doniach-Šunjić parameter α. The assignment of the XP signals in the recorded spectra was guided by high level DFT calculations described in section 7.4 and by plausibility considerations.

HRCLS measurements at beamline I311, MAX-lab (Lund) The high-resolution core level shift spectroscopy measurements reported and analysed in this thesis were obtained at beamline I311 at MAX-lab at the Department of Synchrotron Radiation Research at Lund University in Sweden. Beam line I311 is placed at the third-generation storage ring MAX II in which electrons are stored with a kinetic energy of 1.5 GeV. The beam line and end station were designed to achieve high energy resolution and high intensity in photoemission experiments from solids. The monochromator operates in the energy range between 30 to 1500 eV [28]. Typical working conditions at high photon flux allow 100 meV resolution at 400 eV photon energy. The spectroscopy end station is composed of two chambers, one for sample treatment as cleaning, preparation and low energy electron diffraction (LEED) analysis and one dedicated to the photoemission analysis. An array of leak valves, each with its own gas reservoir, enables the introduction of various gases. The samples are held with tungsten wire and can be cooled to liquid nitrogen temperature and heated to 1500 K. The temperature is measured by a Ni-NiCr thermocouple spot-welded on the back of the sample. The SCIENTA-SES200 hemispherical electron energy analyser, shown in figure 3.3 is composed of two main parts, the electrostatic lens and the hemisphere for the energy analysis. The lens collects the electrons from the sample, focusing them at the entrance slit of the hemispheres. The lens is also responsible for retarding (accelerating) the electrons to the desired pass energy. The pass energy is the energy that will keep the electrons in the ideal path midway between the two charged hemispheres (see figure 3.3).

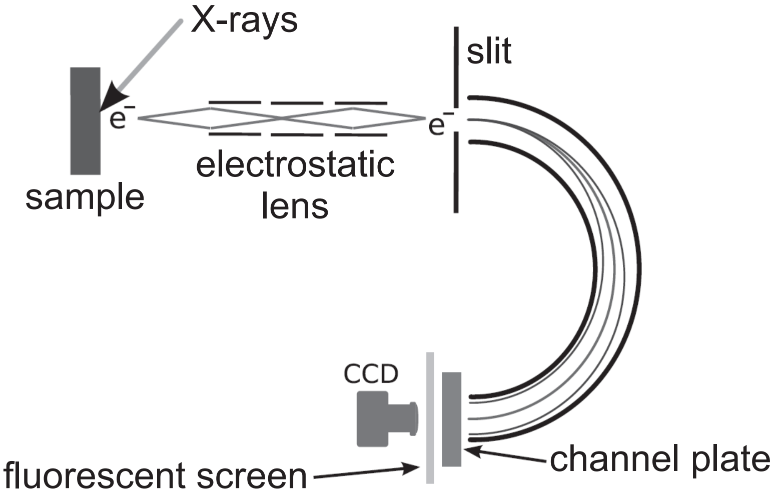

Figure 3.3: Schematic representation of a hemispherical electron analyser using a CCD based multichannel detector. Figure taken from [29].

The field present between the two hemispheres provides energy analysis of the electrons. The electrons with kinetic energy lower than the pass energy move towards the inner hemisphere while instead electrons with higher energy will move towards the outer hemisphere. If the energy of the electrons is too different from the pass energy they will hit one of the hemispheres. The electrons that reach the end of the hemispheres are now separated in energy and ready to be collected. Their deviation from the central path is proportional to their energy difference from the pass energy. The electrons that pass through the hemispheres will impinge on the channel plate where the electrons are multiplied and then accelerated towards a phosphorous screen preserving the spatial distribution. The light emitted from the phosphorous screen is collected by a CCD sensor. The energy range collected by the channel plate corresponds to approximately 10 % of the pass energy. This energy window is divided into the number of channels present on the CCD chip. Each channel collects an electron intensity and is associated to a specific energy in the window.

Chapter 4

Surface X-ray Diffraction

4.1 Introduction to SXRD

X-ray diffraction (XRD) is a relatively old technique, pioneered by von Laue and Bragg in the 1910's and 1920's [30, 31]. It is a structure sensitive technique: a crystal is illuminated by monochromatic X-ray photons, which are then scattered by the electrons in the crystal lattice. Because the photons are scattered by a regular array of electrons which reflects the crystal structure, the photons leaving the crystal will create an interference pattern according to Bragg's law. From this pattern one can analyse the crystallographic structure of the crystal.

With *surface X-ray diffraction* (SXRD) the incoming photons have a glancing incidence angle α_i with respect to the crystal surface, typically smaller than 1°. Because of their limited penetration depth, the incoming beam of X-rays will only illuminate a thin slice of typically 1 to 2 μm for a typical metal, measured in the direction perpendicular to the surface of the crystal. The index of refraction of a solid at X-ray wavelength is only very slightly less than unity and so, from Snell's Law, at very grazing angles of incidence the incoming X-ray beam undergoes total external reflection (figure 4.1).

For example, for a typical X-ray wavelength of 1.5 Å the critical angle from the surface, below which total external reflection occurs, is around 0.2°-0.6°, depending on the material. Under these conditions there is a finite penetration depth of the X-ray beam into the solid, caused by absorption of X-rays by the sample. For angles of incidence below the critical angle, the penetration depth is of the order of 10-50 Å.

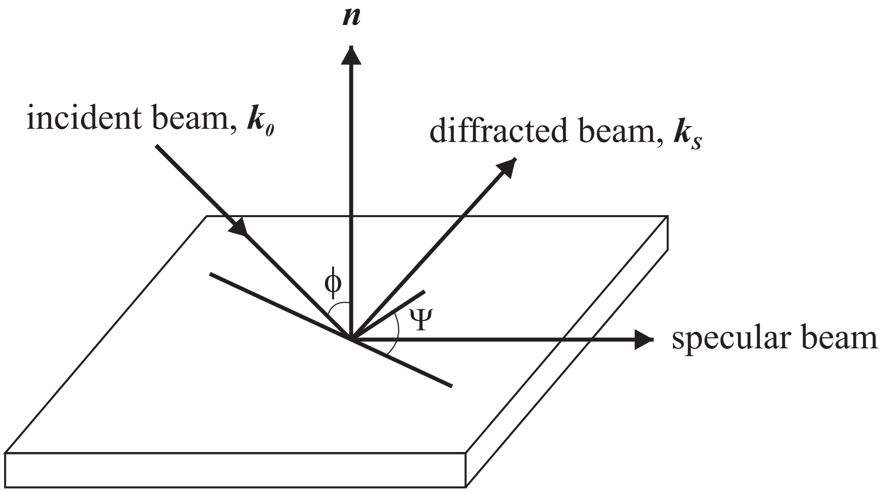

Figure 4.1: The grazing angle geometry used in surface X-ray diffraction. An incident beam of wave vector $\boldsymbol{k}_0$ is incident at a gracing angle to the surface, such that the polar angle ϕ with the surface normal $\boldsymbol{n}$ is typically $\approx 89.5°$. After diffraction through an azimuthal angle Ψ the beam leaves the surface at a grazing angle similar to the angle of incidence. Figure adapted from [32].

A two-dimensional treatment is appropriate, so that diffracted beams emerge wherever the Ewald sphere intersects the surface reciprocal lattice *rods*. An advantage, however, is that multiple scattering effects are negligible, so that the diffraction process may be treated by kinematic rather than dynamical theory. The two-dimensional X-ray diffraction experiment will, of course, still be subject to the phase problem but, using refinement techniques developed from conventional X-ray diffraction, atom positions can be estimated to within ±0.01-0.03 Å [32] and references therein.

The summation, which gives rise to the Laue equations (for an arbitrary 3D crystal N_1, N_2, N_3 unit cells, lattice vectors $\mathbf{a}_1$, $\mathbf{a}_2$, $\mathbf{a}_3$) for the scattered intensity in the reciprocal lattice, can be written as:

$$I(\mathbf{q}) \propto |F(\mathbf{q})|^2 \frac{\sin^2(\frac{1}{2}N_1\mathbf{q}\cdot\mathbf{a}_1)}{\sin^2(\frac{1}{2}\mathbf{q}\cdot\mathbf{a}_1)} \frac{\sin^2(\frac{1}{2}N_2\mathbf{q}\cdot\mathbf{a}_2)}{\sin^2(\frac{1}{2}\mathbf{q}\cdot\mathbf{a}_2)} \frac{\sin^2(\frac{1}{2}N_3\mathbf{q}\cdot\mathbf{a}_3)}{\sin^2(\frac{1}{2}\mathbf{q}\cdot\mathbf{a}_3)} \tag{4.1}$$

where $F(\mathbf{q})$ is the structure factor that determines the intensity of the observed diffraction peaks. For scattering from an isolated 2D monolayer, this is equivalent to setting $N_3 = 1$ in equation 4.1, when the $\mathbf{a}_3$ vector is along the surface normal and $\mathbf{a}_1$ and $\mathbf{a}_2$ lie in the 2D plane. In this case the diffracted intensity is independent of the component of the wave vector transfer $\mathbf{q}\cdot\mathbf{a}_3$ in the surface normal direction of the reciprocal lattice and intensity is observed for all values of the Miller index **l**, when the Laue conditions are met in the plane of the surface (integer values of **h** and **k**).

If the 2D monolayer has the same periodicity as the underlying bulk crystal, then the diffuse scattering is superimposed upon the bulk scattering and spots now indicate the bulk Bragg reflections. In the case of a real surface there is actually interference between the scattering from the surface atoms and the bulk and the intensity becomes modulated along the **L** direction as indicated in figure 4.2 for the Ru(0001) surface[1]. The diffracted intensity in between the Bragg reflections forms the so-called crystal truncation rods (CTRs) as they are rods of scattering that arise from the truncation of the crystal lattice at the surface [33, 34].

For a surface structure that has a different symmetry than the underlying bulk crystal, the rods are separated in reciprocal space and can be measured independently. Surface structures that are commensurate with the underlying bulk crystal can also be probed by detailed measurement and modeling of the CTRs.

Figure 4.3 summarises the unit cell of RuO_2(110) epitaxially grown on a Ru(0001) and the corresponding diffraction pattern.

For time-resolved stability measurements of RuO_2(110) on Ru(0001) under various feed gas conditions, the intensity of the ($\mathbf{H}$, $\mathbf{K}$, $\mathbf{L}$) = (0.884, 0.884, 1.3) reflex has been monitored (cf. figure 4.4).

All SXRD measurements presented and discussed in the present thesis were recorded at beamline ID03 at ESRF (European Synchrotron Radiation Facility, Grenoble, France) in cooperation with O. Balmes and E. Lundgren. Further details concerning the beamline can be found in references [37, 38].

4.2 Batch Reactor for Harsh Reaction Conditions at ESRF, ID03

Especially for the purpose of handling HCl and Cl_2 a new batch reaction chamber (figure 4.5) has been developed by Balmes et al. at beamline ID03 for measuring

---

[1] Miller indices of Ru (hexagonal crystal system) are written in capital letters: $\mathbf{H} = \mathbf{h}$, $\mathbf{K} = \mathbf{k}$, $\mathbf{I} = -(\mathbf{H}+\mathbf{K})$, $\mathbf{L} = \mathbf{l}$

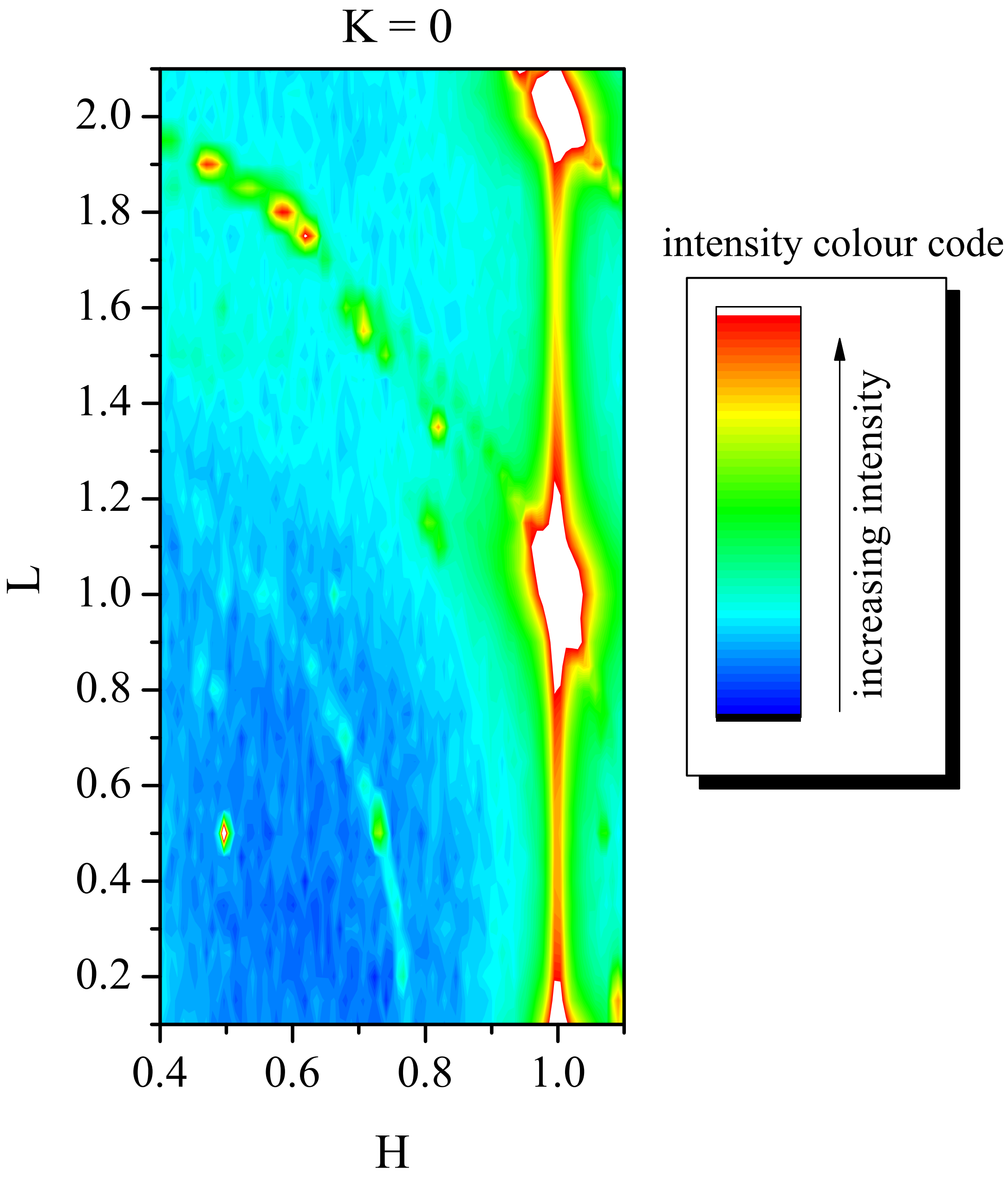

Figure 4.2: Crystal truncation rod recorded for Ru(0001) [35]. The plot is composed of a series of **H**-scans with stepwise increasing **L** values. The intensity is mapped by the colour code described in the legend. The CTR of Ru(0001) can be seen at $\mathbf{H} = 1.0$. The corresponding reflections of Ru are located at integer **L** values of $\mathbf{L} = 0$, $\mathbf{L} = 1$, and $\mathbf{L} = 2$.

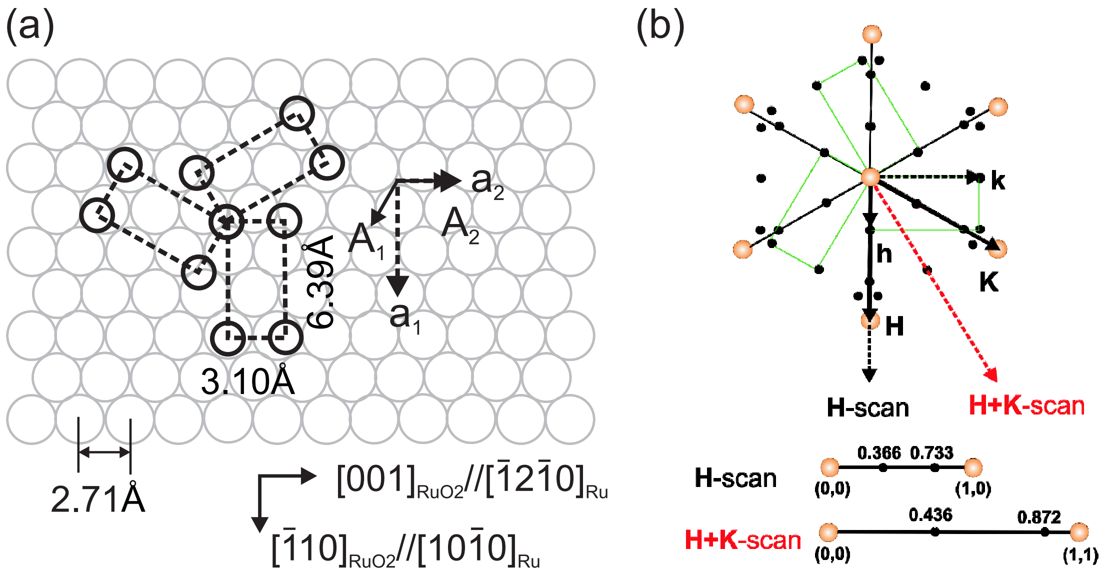

Figure 4.3: *a)* Top view of $RuO_2(110)$ grown on Ru(0001). The in-plane lattice vectors $\mathbf{A}_1$ and $\mathbf{A}_2$ and the out-of-plane lattice vector $\mathbf{A}_3$ define the crystal lattices of Ru(0001): $A_1 = A_2 = 2.71$Å; angle $= 120°$; $A_3 = 4.28$Å. The $RuO_2(110)$ surface is oriented along the A_3 axis of Ru(0001). The in-plane lattice vectors of $RuO_2(110)$ are depicted in *a)*, forming a rectangular surface unit cell (three rotational domains), defined by the lattice vectors $\mathbf{a}_1$ and $\mathbf{a}_2$. The in-plane epitaxial growth relationship between the $RuO_2(110)$ film and the Ru(0001) substrate is indicated, i.e., RuO_2- $[001]//Ru[\bar{1}2\bar{1}0]$ and $RuO_2[\bar{1}10]//Ru[10\bar{1}0]$. *b)*: In reciprocal space, $\mathbf{H}$ and $\mathbf{K}$ are the in-plane lattice vectors and $\mathbf{L}$ is parallel to $\mathbf{A}_3$. The reciprocal lattice vectors of $RuO_2(110)$ are $\mathbf{h}$, $\mathbf{k}$, $\mathbf{l}$, where $\mathbf{h}$ is parallel to $\mathbf{H}$ and $\mathbf{k}$ is aligned along an equivalent direction of $\mathbf{H} + \mathbf{K}$, while $\mathbf{l}$ and $\mathbf{L}$ are parallel. *b), lower part:* Illustration of the $\mathbf{H}$ and $\mathbf{H} + \mathbf{K}$ scans, indicating the positions of expected diffraction maxima of $RuO_2(110)$ with respect to Ru(0001). Figure modified from [36].

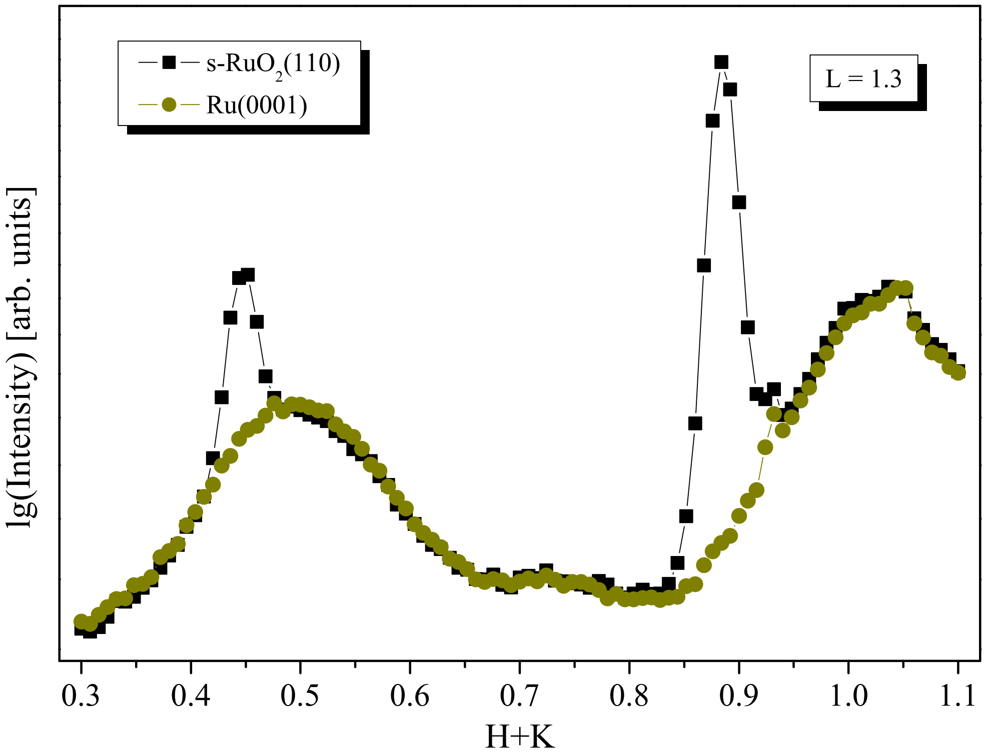

Figure 4.4: SXRD **H+K** scans for **L** = 1.3 of metallic Ru(0001) (brown dots) and s-RuO_2(110) on a Ru(0001) substrate (black squares). The reflex at (**H**, **K**, **L**) = (0.884, 0.884, 1.3) is indicative of the presence of the RuO_2(110) film. Figure by courtesy of S. Zweidinger.

in operando SXRD combined with on-line mass spectroscopical analysis of the reaction products [38]. The 360° X-ray window is made of a 1 mm thick aluminum cylinder. This imposes the restriction of working at high X-ray energies around 20 keV or above. The UHV components together with the gas line and the quadrupole mass spectrometer are located at the lower part of the apparatus. In the top part e-beam evaporators together with an ion gun for sample sputtering can be installed. The sample can be annealed up to 1100 °C under UHV conditions (minimum pressure 10^{-9} mbar) and heated up to 500–600 °C under operating conditions. The chamber can be used with corrosive gases such as HCl and Cl_2. For pressure measurement, the reaction chamber is equipped with two capacitive pressure gauges for elevated pressures and a cold cathode gauge for UHV. The reaction mixture in the separable batch reactor can be analysed by leaking a certain amount of the reactor filling through a leak valve into the MS chamber. There, the gas composition can be monitored via a residual gas analyser (RGA, Satellite, Spectra International) enabling combined reactivity and stability measurements like CO oxidation on chlorinated $RuO_2(110)$ as treated in the present work. A HCl trap based on sodium hydroxide impregnated active charcoal [39] was mounted on the gas outlet of the pump to adsorb HCl residues from the exhaust gas.

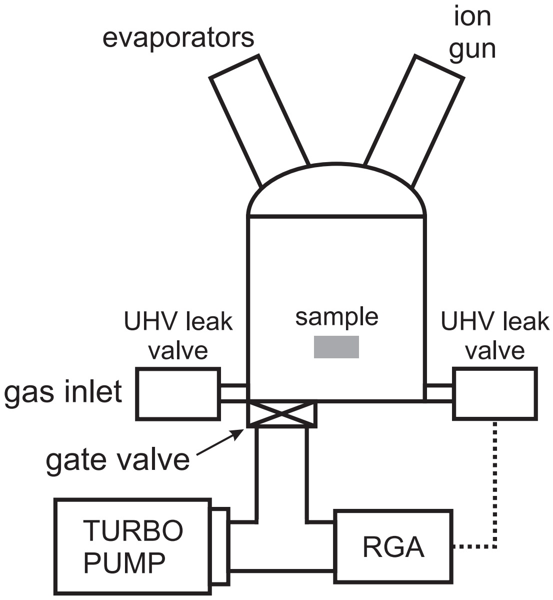

Figure 4.5: Schematic drawing of the batch reactor for harsh reaction conditions. The sample position is indicated by the grey rectangle. [38].

Chapter 5

Auger Electron Spectroscopy

The Auger process is a radiationless transition in an ionised atom in which the atom relaxes to a state of lower energy and ejects an electron to carry off the energy difference, leaving the atom doubly ionised. The effect is illustrated in figure 5.1.

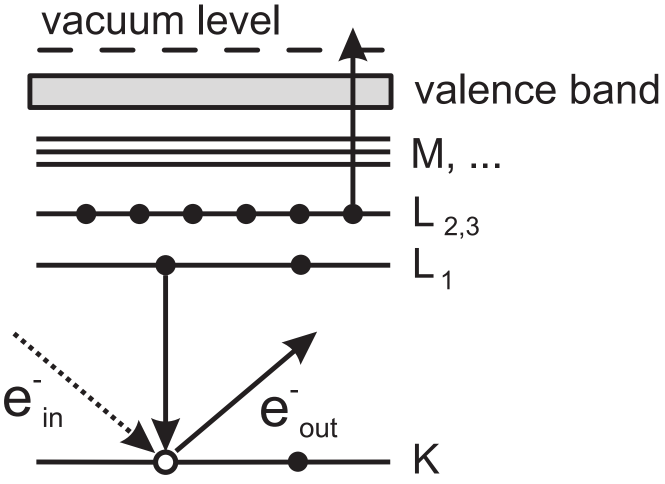

Figure 5.1: Illustration of the Auger process for an arbitrary KLL transition. An incident electron creates a core hole in the K shell. An electron from the L_1 level fills the K hole and the transition energy is imparted to a $L_{2,3}$ electron, which is emitted. The energy is characteristic of the energy levels of the ejecting atom. The final atomic state thus has two holes, one in the 1s orbital and the other in the 2p orbital.

The energy is characteristic of the energy levels of the ejecting atom, thus enabling a chemical element sensitive surface analysis. The production of Auger electrons by bombardment of surfaces with electrons is also accompanied by emission of secondary and backscattered electrons. These electrons range in energy from a first maximum (near 10 eV for secondary electrons), through the Auger spectrum, to a second maximum for backscattered electrons at the energy of the incident electron beam. An additional source is associated with Auger electrons which are inelastically scattered while leaving the specimen. Signal differentiation is among the earliest methods employed to remove the background from an Auger spectrum and to enhance the Auger features [40]. It may be employed in real time or in post acquisition. In real time which is the mode applied in our Auger spectrometer system, differentiation is accomplished by means of a sinusoidal potential modulation on the cylindrical mirror analyser (CMA). The output signal is then processed by a lock-in amplifier and the Auger spectrum is displayed as the derivative of the original energy distribution N(E).

Systematical errors in differential mode cover misalignment of the CMA, changes of line shape and position due to chemical state effects and variations of the matrix of the emitting atom [41]. Electron stimulated desorption is an issue in quantitative Auger spectroscopy as well [42]. The beam damage effect was estimated for chlorinated RuO_2 by longer irradiation of the sample with 3 keV electrons and thus found to be negligible for the time periods, which were needed to record the spectra. The analysis of the spectra can be complicated by overlapping features of different elements [43]. In principle, electron stimulated Auger spectroscopy is a surface sensitive analysis method. However, Auger electrons are emitted from a surface depth of approximately down to 20 Å depending on the mean free path of the Auger electrons in the material [44], which is shown in figure 3.2 for XP spectroscopy.

In Auger electron spectroscopy, intensities have traditionally been measured as peak-to-peak values in the differential spectrum [45]. This is relatively straightforward and a background correction is only required at low energies or low intensitites [46]. It is assumed, that the peak height is linearly proportional to the intensity of the line in the direct spectrum and thus to the surface coverage [47]. The analyses presented in the following study are based on this assumptions.

Temperature Programmed Auger Electron Spectroscopy In order to follow the surface coverage of a certain species (here oxygen or chlorine) during heating, a combined temperature programmed desorption - Auger electron spectroscopy experiment has been carried out in the analysis chamber of the RAIRS apparatus. Especially the detection of chlorine by means of standard TD spectroscopy applying quadrupole mass spectrometry causes problems due to the low sensitivity of the mass spectrometer to chlorine. Bowker et al. reported from temperature programmed Auger spectrocopy as a suitable method to assess the surface concentration of Cl on silver single crystal surfaces [48, 49]. The intensity of the Auger peak in the differential spectrum of the species in question has been monitored while ramping the sample temperature. Both temperature and Auger intensity (lock-in amplifier output) have been recorded by means of an analogue digital converter modul. A typical TP-AES graph resembles an integrated thermal desorption spectrum as obtained by mass spectrometry. The inflexion point of the curve corresponds to the maximum of the desorption peak in the TD spectrum.

To test the influence of the electron impact heating (filament heating current and acceleration voltage as well) on the stability of the Auger signal, the most intense Ru_{MNN} peak has been monitored during annealing the Ru(0001) crystal to temperatures as high as $T = 1200$ K. The corresponding plot of the Auger intensity versus sample temperature is displayed in figure 5.2. During cooling down both the filament current I_{fil} and the acceleration voltage U_{acc} have been switched off, so that the observed drift in the Ru_{MNN} intensity should only be due to thermal expansion effects of the sample and the sample holder, respectively or instabilities of the spectrometer system (cylindrical mirror analyser and channeltron). Thus, the variation of the Auger signal upon heating the crystal during a combined temperature programmed desorption - Auger experiment can be assumed to be less than 10 %, giving the reproducibility of the TP-Auger spectra.

By means of temperature programmed Auger spectroscopy, the detection of chlorine desorption from either Ru(0001) or $\mathrm{RuO_2}(110)$ is facilitated. Thereby, the detection problems due to the low sensitivity of our quadrupole mass spectrometers to chlorine were overcome and the chlorine content could be easily monitored during annealing of the sample.

Figure 5.3 shows the thermal desorption spectrum of chlorinated $\mathrm{RuO_2}$ and overlayed the TP-Auger signal, monitoring the temperature dependent evolution of the Cl_{LMM} signal in the Auger spectrum. At $T = 400$ K desorption of O_{ot} occured as can be seen from the very small $\mathrm{O_2}$ desorption in the mass spectrum. Chlorine atoms, adsorbed on-top of 1f-cus Ru sites desorb via recombination of

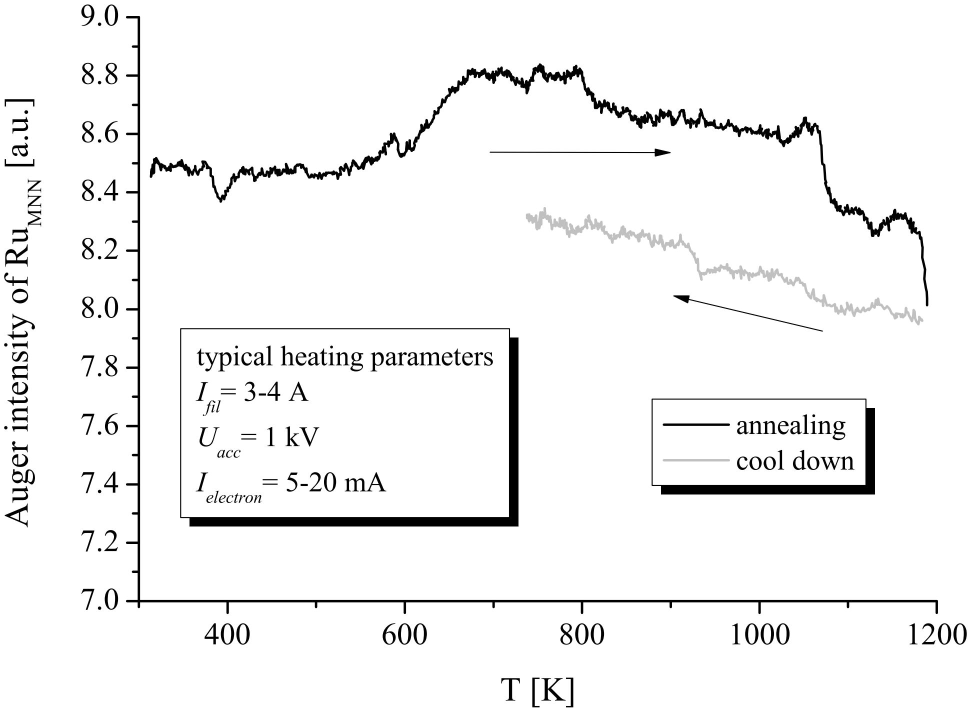

Figure 5.2: Stability of the Auger signal of Ru$_{MNN}$ at $E = 270$ eV upon heating the Ru(0001) single crystal from room temperature to $T = 1200$ K by means of electron impact heating. The deviation of the signal during the annealing process can be specified to be as low as 10% of the initial signal.

two Cl_{ot} forming Cl_2. This led to the Cl_2 peak centred at $T = 690$ K, which is in accordance to the findings reported by Crihan et al. [9]. At this temperature, the first drop in Auger intensity could be seen. Upon further heating, the bridging chlorine atoms (Cl_{br}) left the surface with a desorption maximum of HCl centred at $T = 890$ K. Here, the inflection point of the Cl_{LMM} Auger signal is shifted by approximately 20 K to lower temperatures, which could be caused by a lower heating rate $\beta \approx 3$ K/s in the case of the TP-Auger experiment.

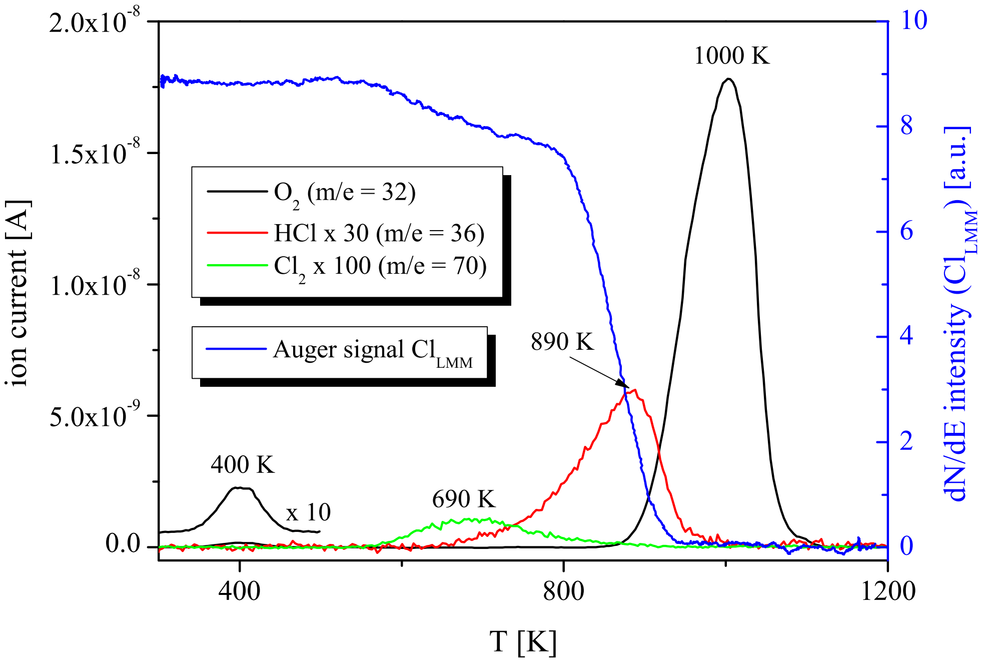

Figure 5.3: Combined plot of both a thermal desorption spectrum and a TP-Auger spectrum of chlorinated $RuO_2(110)$.

In conclusion, TP-Auger spectroscopy is a suitable method for the detection of the surface concentration of Cl and its temperature dependent evolution.

Chapter 6

Reflection Absorption Infrared Spectroscopy RAIRS

Reflection absorption infrared spectroscopy (RAIRS) is a versatile technique for the study of adsorbate and adsorbate-substrate vibrations on surfaces. Since the probe particles are photons, the method is applicable both under ultra high vacuum (UHV) conditions and higher pressures in the mbar regime. For measurements in the atmospheric pressure regime, polarisation modulation reflection absorption infrared spectroscopy (PM-RAIRS) has to be applied (cf. [50]). Farkas et al. demonstrated the suitability of this method to gain deep insight into the CO adsorbate properties / CO oxidation on $RuO_2(110)$ model catalysts [13, 14].

6.1 Theoretical Survey of RAIR Spectroscopy

6.1.1 IR Reflection Absorption

The mechanism of vibrational excitation of molecules with RAIRS is based on the interaction of the electromagnetic field of the incident and reflected light with the dipole moment of an adsorbed molecule (here CO). Theoretical considerations on RAIRS are based on classical electrodynamics, as first introduced by Greenler [51, 52]. This early treatment has indicated that the incident light should be reflected at the surface under grazing incidence for a maximum reflection signal. Moreover, the validity of a strict dipole selection rule for metallic surfaces requires that the incident light should have a perpendicular polarised component (so-called 'p' polarisation) and only vibrational modes with a component of the dipole moment perpendicular to the surface will be excited. However, group theory gives a more precise formulation for the surface selection rule for allowed RAIRS transitions being that only modes with the character 'A' (i.e. of highest symmetry) may yield features in the RAIR spectrum. In the determination of the symmetry and thus, the character of the modes of an adsorbed molecule, the whole system, i.e. surface and adsorbed molecule, is being considered [32].

6.1.2 Single Diatomic Adsorbate

Shift of the C-O stretch frequency upon chemisorption

When a CO molecule adsorbs on a metal surface, the force constant of the C-O bond is diminished relatively to its gas phase value. Thus, the CO stretch frequency is 2143 cm^{-1} in the gas phase but it shifts to 1984 cm^{-1} upon chemisorption on the Ru(0001) surface [53]. Several factors determine the frequency shift of a single adsorbed CO molecule from its gas phase value: i) mechanical renormalisation due to the formation of the Ru-CO bond, ii) interaction of the vibrating molecular dipole with its image in the metal, iii) chemical effects, such as back-donation, which change the C-O bond strength upon chemisorption [54, 55].

Mechanical renormalisation Within a purely mechanistic picture, the bond of the CO molecule to the rigid Ru substrate can be treated as an elastic spring with the force constant k_{RuC}. If one suppose that the internal force constant of the C-O bond is not influenced by the adsorption of the CO molecule, one will get two vibration eigenfrequencies for this Ru-C-O 'molecule' [55]. One of the eigenfrequencies corresponds to the Ru-CO vibration, where the CO molecule is regarded as a rigid body, the other frequency corresponds to the internal C-O vibration, when the center of mass of the CO molecule is considered fixed. This second frequency, denoted as ω_s, is blue shifted relatively to the gas phase frequency ω_g

$$\left(\frac{\omega_s}{\omega_g}\right) \approx 1 + \frac{k_{\mathrm{RuC}}}{k_{\mathrm{CO}}} \frac{\mu^2}{M_{\mathrm{C}}^2} \quad , \tag{6.1}$$

where μ is the reduced mass of the CO molecule and M_{C} is the mass of the carbon atom. By taking physically plausible values for the force constants k_{RuC} and k_{CO}, Bradshaw and Schweizer [55] have obtained typical shifts of about +50 cm^{-1} to higher frequencies for CO adsorbed on transition metals.

Self-image effect Due to the screening of electric fields in a metal by the conducting electrons, the dipole moment of the adsorbed molecule will induce an electrostatic image dipole in the metal. The interaction of the adsorbate dipole with its electrostatic image leads, in case of a perfectly conductive substrate, to a red shift of the C-O internal stretch frequency

$$\left(\frac{\omega_s}{\omega_g}\right) = 1 - \frac{\alpha_V(0)}{4z^3 - \alpha_e} \quad , \tag{6.2}$$

where z denotes the distance from the CO molecular dipole to its electrostatic image, $\alpha_V(\omega)$ is the vibrational polarisability and α_e is the electronic polarisability of the CO molecule. Bradshaw and Schweizer [55] have shown that, for CO adsorbed on transition metals, the self-image effect leads to a shift of about -50 cm^{-1} to lower frequencies. Thus, the blue shift induced by mechanical renormalisation is more or less compensated by the red shift due to the self-image effect.

Chemical shift: The Blyholder model The weakening of the C-O internal bond in the chemisorbed CO molecule has been traditionally explained within the backbonding model proposed by Blyholder [56]. This model assumes that the chemical bond between CO and the metal (Ru) is formed by charge transfer from the 5σ molecular orbital (MO) of CO into the metal and by 'backdonation' of electrons from the metal d-bands into the unoccupied $2\pi^*$ MO of CO, as shown in figure 6.1. Since the 5σ MO is only weakly bonding, but the $2\pi^*$ strongly anti bonding, the C-O internal bond is weakened by the formation of the C-Ru chemisorption bond. The amount of backdonation into the $2\pi^*$ MO is reflected by a lowering of the C-O stretching frequency [54].

Further support for the strong influence of backdonation on the CO stretch frequency is provided experimentally by coadsorption experiments. If CO is coadsorbed with strong 'electron donors' such as hydrocarbons, shifts to lower frequencies of up to -100 cm^{-1} are observed [58], a fact which is consistent with an increased backdonation to the CO molecule as charge from the coadsorbate is transferred to the metal. On the other hand, coadsorption of 'electron acceptors', such as oxygen or chlorine, reduces backdonation to the CO molecule and hence

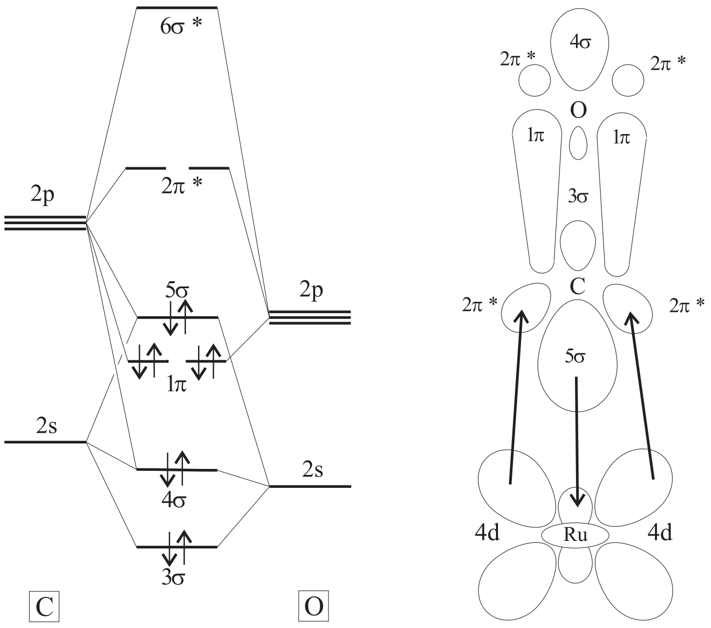
6σ *
2p
2π *
5σ
2p
1π
2s
2s
4σ
3σ
C
O
4σ
2π *
2π *
O
1π
1π
3σ
C
2π *
2π *
5σ
4d
Ru
4d

a) b)

Figure 6.1: Chemisorption of CO on Ru. a) Schematic molecular orbital diagram for CO [57], b) Schematic representation of the Blyholder model (after reference [54]).

cause a shift to higher frequencies. Later in this work these important observations will be applied in the interpretation of the IR spectra of CO adsorbed on the ruthenium dioxide surface.

6.1.3 Coupling of the Vibrations in Adsorbed CO

The observed shift in the wavenumber of the stretching vibrations $\Delta\tilde{\nu}(\mathrm{CO})$ of the CO molecules which are adsorbed on a surface, as a function of coverage is the sum of both static and dynamic coupling contributions. The static coupling arises from a through metal interaction between molecules adsorbed on different metal atoms and may cause an upward or downward shift [59]. Static shifts can be determined experimentally by deliberate coadsorption experiments. The dynamic coupling is due to through vacuum dipole-dipole interactions of the vibrating CO molecules and induces an continuous upshift with increasing coverage. Hence, the blue shift induced by dynamic coupling may also be used for the determination of coverages. A detailed theoretical treatment was provided by Hollins and Pritchard [60].

6.2 Measurement of a FT-RAIR Spectrum

Reflection absorption spectroscopy of adsorbed species is a so-called two channel method, as shown in figure 6.2. This means that in order to obtain a RAIR spectrum it is necessary to measure two separate (single channel) spectra, one for the reflecting substrate (denoted $S_0(\tilde{\nu})$) and one for the substrate with the adsorbed molecules (denoted $S(\tilde{\nu})$), where $\tilde{\nu}$ denotes the wavenumber of the incident light.

The acquisition of a single channel spectrum begins with the recording of an interferogram. For this purpose, the movable mirror of the interferometer is translated at constant speed, which results in a series of maxima and minima of different intensity at the detector. The exact positioning of the mirror is achieved by means of a HeNe-laser beam passing through the interferometer. The equally spaced interference maxima of the laser beam along the path of the mirror serve as a precise reference, enabling for a localisation of the mirror within half the wavelength of the laser ($\lambda = 633$ nm). The position of the mirror and the corresponding detector signal are recorded in the so-called interferogram, which is subsequently stored on the computer. To obtain the single channel spectrum, the single channel interferogram is Fourier-transformed. The result is the single channel spectrum $S(\tilde{\nu})$ of the sample.

The single channel spectrum $S(\tilde{\nu})$ is a so-called reflection absorption spectrum of the sample. By means of the reflectivity $R(\tilde{\nu})$ of the sample, the measured spectrum can be written as

$$S(\tilde{\nu}) = I(\tilde{\nu})\, R(\tilde{\nu}) \tag{6.3}$$

where $I(\tilde{\nu})$ is the intensity of the incident light beam.

The reflectivity of the substrate $R_0(\tilde{\nu})$ changes to $R(\tilde{\nu})$ after the adsorption of molecules. Since the molecules absorb energy from the incident light beam, the change of reflectivity

$$\Delta R = R_0 - R \tag{6.4}$$

is positive, i.e. the reflectivity must diminish upon adsorption. The quantity ΔR is called the *reflectivity change* of the surface due the adsorption of molecules. In order to obtain this quantity from the measured single channel spectra $S(\tilde{\nu})$ and $S_0(\tilde{\nu})$, the following quotient can be formed

$$\frac{S(\tilde{\nu})}{S_0(\tilde{\nu})} = \frac{R(\tilde{\nu})}{R_0(\tilde{\nu})} \tag{6.5}$$

whereby the factor $I(\tilde{\nu})$ has the same value for both single channel spectra and cancels out. By writing equation 6.5 as

$$\frac{S(\tilde{\nu})}{S_0(\tilde{\nu})} = 1 - \frac{\Delta R(\tilde{\nu})}{R_0(\tilde{\nu})} \tag{6.6}$$

one can see that the spectroscopic measurement provides actually the *relative reflectivity change* spectrum of the substrate due to the adsorbed molecules

$$[\text{Relative Reflectivity Change}](\tilde{\nu}) = \frac{\Delta R(\tilde{\nu})}{R_0(\tilde{\nu})} \quad . \tag{6.7}$$

For the rest of the present thesis, the following convention to represent the RAIR spectra in the shorthand notation will be used

$$\frac{S}{S_0} = 1 - \frac{\Delta R}{R} \quad . \tag{6.8}$$

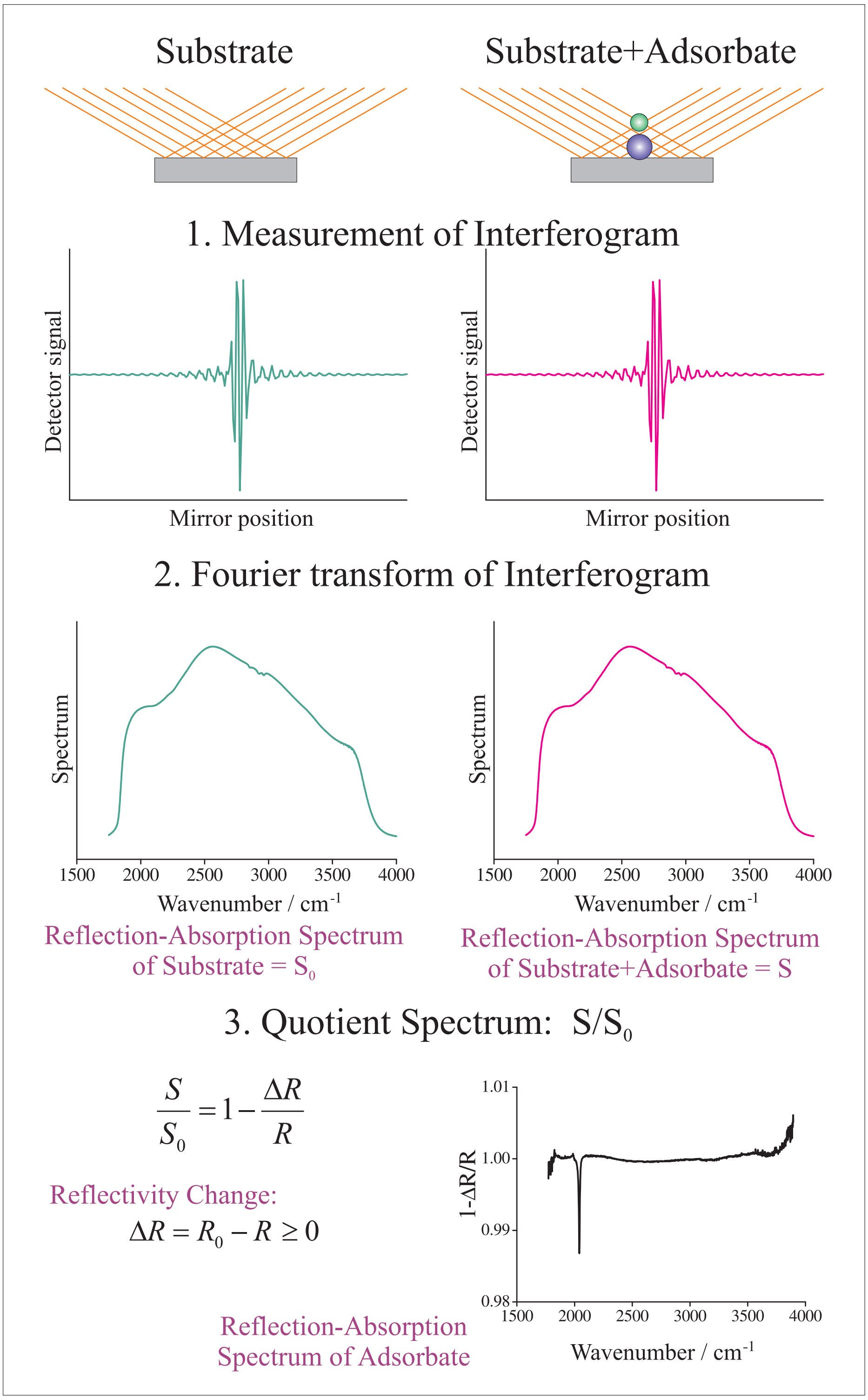
Substrate
Substrate+Adsorbate
1. Measurement of Interferogram
Detector signal
Mirror position
Detector signal
Mirror position
2. Fourier transform of Interferogram
Spectrum
1500 2000 2500 3000 3500 4000
Wavenumber / cm-1
Spectrum
1500 2000 2500 3000 3500 4000
Wavenumber / cm-1
Reflection-Absorption Spectrum of Substrate = S0
Reflection-Absorption Spectrum of Substrate+Adsorbate = S
3. Quotient Spectrum: S/S0
S/S0 = 1 − ΔR/R
Reflectivity Change:
ΔR = R0 − R ≥ 0
1-ΔR/R
1.01
1.00
0.99
0.98
1500 2000 2500 3000 3500 4000
Wavenumber / cm-1
Reflection-Absorption Spectrum of Adsorbate

Figure 6.2: Acquisition of the reflection absorption IR spectrum of an adsorbate (scheme taken from [13]).

6.3 The RAIRS Apparatus

The RAIRS measurements presented and discussed during this thesis were all recorded using the RAIRS setup coupled to a Bruker IFS120 HR FTIR spectrometer as planned and commissioned by A. Farkas during his PhD work [13]. A very detailed description of this apparatus and its specifications can be found in [13]. Figure 6.3 depicts the essential parts of the two chamber UHV system suitable for high vacuum as well as higher pressure (up to several mbars) experiments.

During the present experiments, the analysis chamber was additionally equipped with an Auger electron spectrometer system in order to provide a surface selective, chemical analysis method.

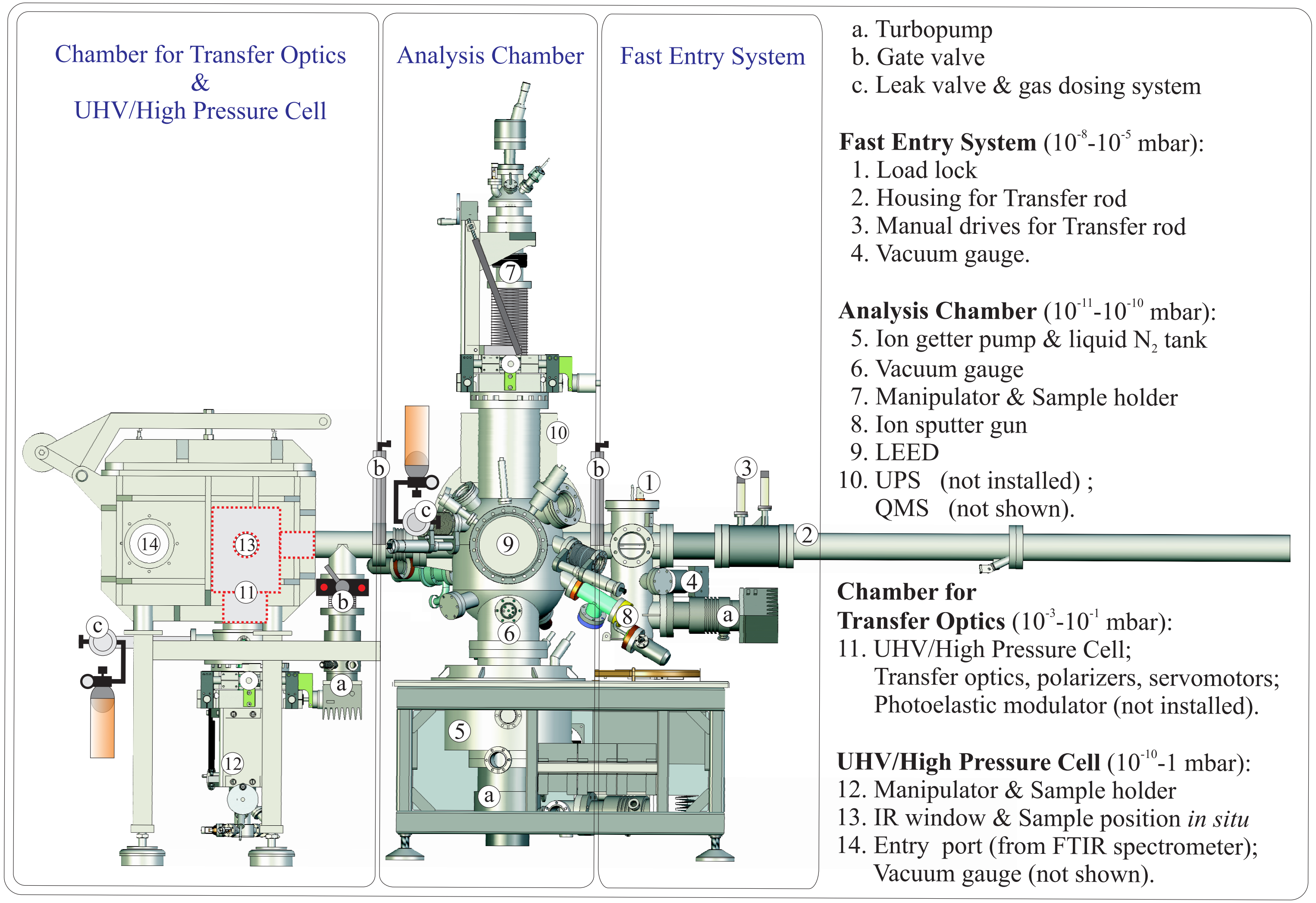
Chamber for Transfer Optics
&
UHV/High Pressure Cell
Analysis Chamber
Fast Entry System
a. Turbopump
b. Gate valve
c. Leak valve & gas dosing system
Fast Entry System (10^{-8}-10^{-5} mbar):
1. Load lock
2. Housing for Transfer rod
3. Manual drives for Transfer rod
4. Vacuum gauge.
Analysis Chamber (10^{-11}-10^{-10} mbar):
5. Ion getter pump & liquid N_2 tank
6. Vacuum gauge
7. Manipulator & Sample holder
8. Ion sputter gun
9. LEED
10. UPS (not installed) ;
QMS (not shown).
Chamber for
Transfer Optics (10^{-3}-10^{-1} mbar):
11. UHV/High Pressure Cell;
Transfer optics, polarizers, servomotors;
Photoelastic modulator (not installed).
UHV/High Pressure Cell (10^{-10}-1 mbar):
12. Manipulator & Sample holder
13. IR window & Sample position *in situ*
14. Entry port (from FTIR spectrometer);
Vacuum gauge (not shown).
14
13
11
12
c
c
b
b
b
a
a
a
7
10
9
6
5
8
1
2
3
4

Figure 6.3: Overview of the UHV system. Only the instruments used in the present work are shown. Figure taken from [13].

Chapter 7

DFT Calculations on Adsorbate Systems

In addition to the experimental methods applied in the present work like TDS, HRCLS, SXRD, AES and RAIRS, density functional theory (DFT) calculations were used as a theoretical tool in the interpretation of the experimental results and vice versa to support the interpretation of the data by providing plausible models.

In a DFT calculation the electronic structure of an atomic system is solved explicitly, in contrast to methods where the interactions between the atoms are parametrised. This approach causes a vast increase in the computing time required, but leads to a *first-principles* approach with no adjustable parameters, thus lending credibility to the results. In practice the Kohn-Sham method [61] is customarily employed. The solution of the quantum-mechanical many-body Schrödinger equation is replaced by the solution of the single-particle equations for the Kohn-Sham orbitals ψ_i with an adjoint effective, local Kohn-Sham potential V_{KS}, that intrinsically carries the many-body character of the complicated interactions

$$\begin{aligned} \left\{-\frac{1}{2}\nabla^2 + V_{\mathrm{KS}}\left(\vec{r}\right)\right\}\psi_i\left(\vec{r}\right) &= \varepsilon_i\psi_i\left(\vec{r}\right) && (7.1)\\ n\left(\vec{r}\right) &= \sum_i \left|\psi_i\left(\vec{r}\right)\right|^2 && (7.2)\\ V_{\mathrm{KS}}\left(\vec{r}\right) &= V_{\mathrm{ext}}\left(\vec{r}\right) + V_{\mathrm{H}}\left(\vec{r}\right) + V_{\mathrm{xc}}\left(\vec{r}\right) && (7.3) \end{aligned}$$

where $V_{\mathrm{ext}}\left(\vec{r}\right)$ denotes an external potential and $V_{\mathrm{H}}\left(\vec{r}\right)$ the Hartree potential

[62]. These equations have to be solved self-consistently, since the Kohn-Sham potential depends explicitly on the electron density n. All the terms in V_{KS} are exactly known – except the exchange-correlation potential V_{xc} that has to be approximated in practice. A reasonable compromise between accuracy and computational effort are the Generalised Gradient Approximations (GGA). In all calculations present in this work, the PBE-GGA (Perdew, Burke, Ernzerhof) are used [63].

For the solution of the Kohn-Sham equations the wave functions are expanded in a basis set. A popular choice for the basis are plane waves since they obey the translational symmetry of the periodic system. They combine a straightforward implementation with no positional bias, thus avoiding the Pulay forces in the expression for the gradients on the atomic positions [64]. The quality of the basis set and thus the accuracy of the results can be adjusted with a single parameter. The large number of plane waves and the constraint of using either pseudo potentials or the projected-augmented wave (PAW) method [65] complicate the plane wave codes, but they still remain widely used and are being further developed.

Throughout this thesis, the computer code `VASP` [66, 67], Vienna Ab Initio Simulation Package - version 4.6.31 has been used for the calculations. The parallelised code was run on Hessischer Hochleistungsrechner (HHLR, TU Darmstadt), and on an ALTIX system (HLRB, Leibniz-Rechenzentrum Garching, TU Munich). Structure optimisations, energy, frequency and core level shift calculations have been usually run on 8 CPUs parallel at HHLR. Nudged Elastic Band calculations for the simulation of reaction paths, the determination of transition states and reaction barriers with 4 to 12 images have been carried out on ALTIX with 8 CPUs per image.

7.1 Structural Optimisation and Electronic Energy Calculation

When calculating the electronic structure of atoms, molecules or clusters the object is isolated and does not interact with other particles. However, when studying crystals in one (wires, chains), two (surfaces, planes), or three dimensions (bulk crystals) the number of atoms would be macroscopic along the continuous direction, leading to atom densities in the order of 10^{23} $1/\mathrm{cm}^3$. Simulating this amount of particles is a formidable task and a simplification needs to be applied. If the system is fully periodic, an obvious choice is to use the periodic boundary conditions, i.e. the atomic and electronic structure is repeated along the three basis vectors $\mathbf{a}_{1,2,3}$ so that if there is an atom at position $\mathbf{R}$ there are atoms also at $\mathbf{R} + i\mathbf{a}_1 + j\mathbf{a}_2 + k\mathbf{a}_3$, where i, j, k are integers. The calculational saving comes if only the atoms and electrons inside the unit cell of the calculation, the so-called *super-cell*, needs to be explicitly considered and the replicas of these objects are incorporated implicitly.

If heterogeneities are introduced to the system the periodicity is often lost. This is the case for surfaces. One way of modelling such a system is to use still the periodic boundary conditions but the super-cell is chosen to be so large that the surfaces do not interact. An example of this approach is the *slab geometry*, which is used in most of the calculations of surfaces nowadays: the system is treated periodically in all the three directions but perpendicular to the surface the replicas of the slab are isolated by a large region of vacuum between them. The thickness of the slab has to be carefully chosen to prevent artificial interactions between the two surfaces of the slab.

The structure and the energy of the surface has been optimised by means of a conjugate gradient (CG) algorithm [68, 69]. A CG algorithm relaxes the ions into their instantaneous ground state. In the first step the coordinates of the ions are changed along the direction of the steepest descent (i.e. the direction of the calculated forces and stress tensor). The conjugate gradient method requires a line minimisation, which is performed in several steps: i) First a trial step into the search direction (scaled gradients) is done. Then the energy and the forces are recalculated. ii) The approximate minimum of the total energy is calculated form a cubic (or quadratic) interpolation taking into account the change of the total energy and the change of the forces (3 pieces of information), then a corrector step to the approximate minimum is performed. iii) After the corrector step the forces and energy are recalculated and it is checked whether the forces contain a significant component parallel to the previous search direction. If this is the case, the line minimisation is improved by further corrector steps. To summarise: In the first ionic step the forces are calculated for the initial configuration read from input file, the second step is a trial (or predictor step), the third step is a corrector step.

Applying this scheme, the total energy of the system is minimised until the convergence criterion for the ionic relaxation is met, usually 10^{-5} eV for estimative calculations and 10^{-7} eV for precision calculations. Based on the optimised structure of the slab, further properties of the adsorbate can be calculated as will be described in the next sections.

7.2 Adsorption Energies

To investigate the binding of adsorbates on surfaces, adsorbate-substrate binding energies have been evaluated from the relaxed structures. The binding energy with respect to an atom A, a dimer A_2 or a molecule AB in the gas phase, respectively is:

$$E_b^{A/S} = E(A/S) - [E(S) + E(A_{atom,gas})] \tag{7.4}$$

$$E_b^{A_2/S} = E(A_2/S) - [E(S) + E(A_{2,gas})] \tag{7.5}$$

$$E_b^{AB/S} = E(AB/S) - [E(S) + E(AB_{gas})] \tag{7.6}$$

where A, A_2 and AB stand for the adsorbed species and S for the substrate, E is the total energy of the system [70]. Negative values indicate an energy gain upon adsorption and positive values repulsion. Furthermore, if the adsorbate-adsorbate interaction is repulsive, then a lowering of the coverage reduces the repulsion and increase the binding of the remaining adsorbed species.

7.3 Frequency Calculations

DFT calculations of the electronic structure of a surface system provide also the ability of calculating the vibrational characteristic of a system. In order to do a frequency calculation of a surface adsorbate system, the structure in question has to be energetically relaxed in a preceding calculation until the difference between two ionic relaxation steps is less than 10^{-7} eV. Afterwards, the Hessian matrix (matrix of the second derivatives of the energy with respect to the atomic displacement around the equilibrium positions) can be calculated from which the harmonic vibrational frequencies of the system can be determined in a separate calculation. To calculate the Hessian matrix each ion is displaced in the direction of the Cartesian coordinates by certain step widths, and from the forces the Hessian matrix is determined.

Before the frequency calculations have been carried out on $RuO_2(110)$, tests were necessary in order to check for the convergence of the frequency calculations with respect to *a)* the electronic structure convergence of the system and *b)* how many atoms have to be displaced (number of degrees of freedom):

The example has been the determination of the vibrational frequency of CO adsorbed on r-$RuO_2(110)$-1x1-Cl_{br}-CO_{ot}. For the determination of the frequency convergence versus the accuracy with which the structure was optimised, the x, y, and z coordinates of CO and the underlying 1f-cus Ru atom were set to be displaced. Figure 7.1 shows the convergence of the CO stretching vibration wavenumber as determined by DFT calculations depending on the accuracy of the electronic structure relaxation. As can be inferred from figure 7.1, the electronic convergence criterion can be set to 10^{-7} eV, which seems to be the best compromise between computation time and precision.

The next test was done to estimate the influence of the number of degrees of freedom taken into account in a frequency calculation on the CO stretching vibration on r-$RuO_2(110)$-1x1-Cl_{br}. The convergence criterion for the electronic self consistent calculation has been set to 10^{-7} eV. In the case of CO, which exhibits a stiff intramolecular spring constant, i.e. high frequency of the stretching frequency, the coupling to the bulk phonons and the other surface species, respectively is negligible. Thus, the number of degrees of freedom does not have a mentionable influence of the shift of the CO_{ad} stretching frequency, at least for the case tested here (see figure 7.2).

7.4 Calculation of Surface Core Level Shifts

Another very valuable property that has been simulated by means of DFT calculations was the shift of core level binding energies of adsorbate species. HRCLS spectroscopy was widely applied throughout this thesis and the DFT calculated core level shifts actually enabled the assignment of the spectral features. The core level energies were calculated by removing half of an electron from the core orbital and performing a self-consistent calculation of the electronic structure [71].

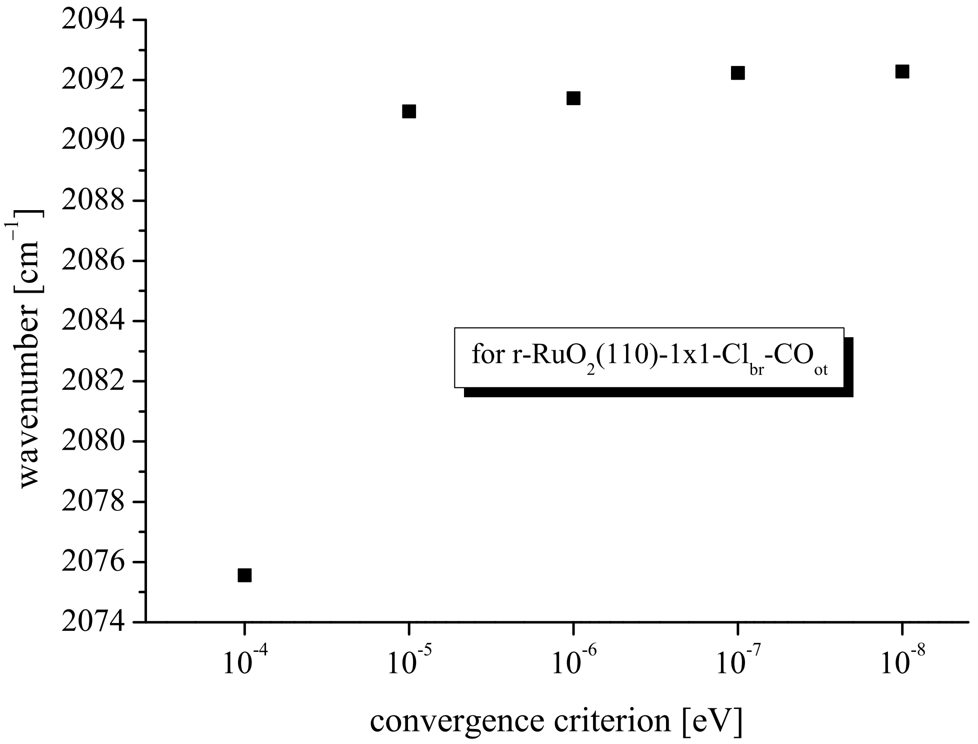

Figure 7.1: Convergence test of the CO stretching vibration wavenumber in dependence of the accuracy of the preceding electronic structure optimisation carried out on the system r-RuO$_2$(110)-1x1-Cl$_{br}$-CO$_{ot}$.

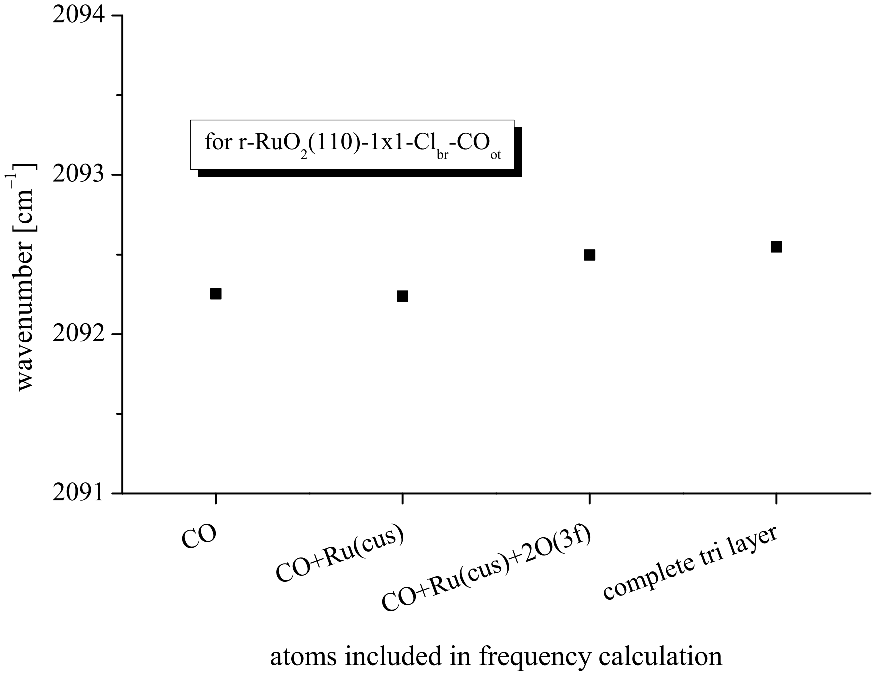

Figure 7.2: Convergence test of the CO stretching vibrational frequency with respect to the number of atoms displaced in the frequency calculation, i.e. the number of degrees of freedom for the determination of the Hessian matrix carried out on the system r-RuO$_2$(110)-1x1-Cl$_{br}$-CO$_{ot}$.

Thus, screening effects (final state) of the core hole were included. The surface core level shift Δ_{SCLS} is defined as the difference in energy that is needed to remove a core electron either from a surface atom or from a bulk atom,

$$\Delta_{SCLS} = [E^{surface}(n_c - 1) - E^{surface}(n_c)] - [E^{bulk}(n_c - 1) - E^{bulk}(n_c)], \quad (7.7)$$

where $E^{surface/bulk}(n_c)$ is the total energy of the system considered as a function of the number of electrons n_c in a particular core level c of a surface or a bulk atom, respectively [72]. Within the initial state approximation, $\Delta_{SCLS}^{initial}$ is given by

$$\Delta_{SCLS}^{initial} \approx [\epsilon_c^{surface}(n_c) - \epsilon_c^{bulk}(n_c)]. \quad (7.8)$$

Here, $\epsilon_c^{surface}$ and ϵ_c^{bulk} are the Kohn-Sham eigenvalues of the particular core state c, so that in this approximation the SCLS is simply due to the variation of the orbital eigenenergies before the excitation of the core electron. The binding energies of the O 1s and Cl 2p core levels were obtained as the energy difference of the Kohn-Sham eigenvalue of the core state of the atom in question and the Fermi energy applying a script by Seitsonen [73]. The evaluated core level shifts correspond very well to the experimental values, as can be seen in the course of this thesis (cf. table 12.1)

7.5 Modelling Chemical Reactions

Electronic structure optimisation of adsorbate structures enables for a discussion of the thermodynamics of the structures. But however, chemical reactions obey not only thermodynamics but also kinetics. The activation energies of various processes taking place on the chlorinated $RuO_2(110)$ surface were determined by DFT calculations. Two different methods have been applied, which will be described in the following.

7.5.1 Manual Shift of Atoms or Atom Groups along a Predefined Reaction Coordinate

For simple reactions like the diffusion of single atoms on the $RuO_2(110)$ surface a manual shift with increments of 0.25 to 1.0 Å have been applied in order to estimate the reaction barrier as well as the transition structure. This method is also referred to as the drag method [74]. The species in question was shifted in one dimension along a predefined reaction coordinate, e.g. the x coordinate of the reacting / moving adsorbate atom, while all remaining coordinates were set to be optimised. Starting from the relaxed initial structure of the reacting system, the adsorbate is shifted by the increment along the reaction coordinate and a relaxation is done. The next step will use the coordinate set of the preceding structure, the adsorbate is shifted again by the increment and another relaxation is done. This scheme is repeated until the final structure of the reaction is reached. In this manner, the potential energy curve is sampled along the predefined reaction coordinate. Thus, a first estimation of the reaction barrier can be obtained by taking the energy difference between the initial structure and the shift step with the maximum energy. For a more accurate determination, the increment between the shift steps around the maximum of the potential energy was chosen to be smaller. The transition state is defined to be the structure with the maximum energy along the reaction coordinate, the remaining $3N - 1$ (N = number of atoms) coordinates being relaxed.

Figure 7.3 displays a typical reaction energy profile obtained by shifting a bridging water molecule O_{br}-H_2, stabilised by Cl_{ot} via hydrogen bonding, to a position on top of a 1f-cus Ru site. This is a crucial reaction step of the chlorination mechanism of stoichiometric $RuO_2(110)$ by HCl (cf. chapter 12). The x coordinate of the oxygen atom of the shifting water molecule was defined as the reaction coordinate. The coordinates given in figure 7.3 are relative coordinates, i.e. the fractional position of the atom in question with respect to the unit cell.

7.5.2 Nudged Elastic Band Calculations

For the study of concerted reactions, Nudged Elastic Band calculations have been applied. In the Nudged Elastic Band (NEB) method [74, 75] a string of replicas (or

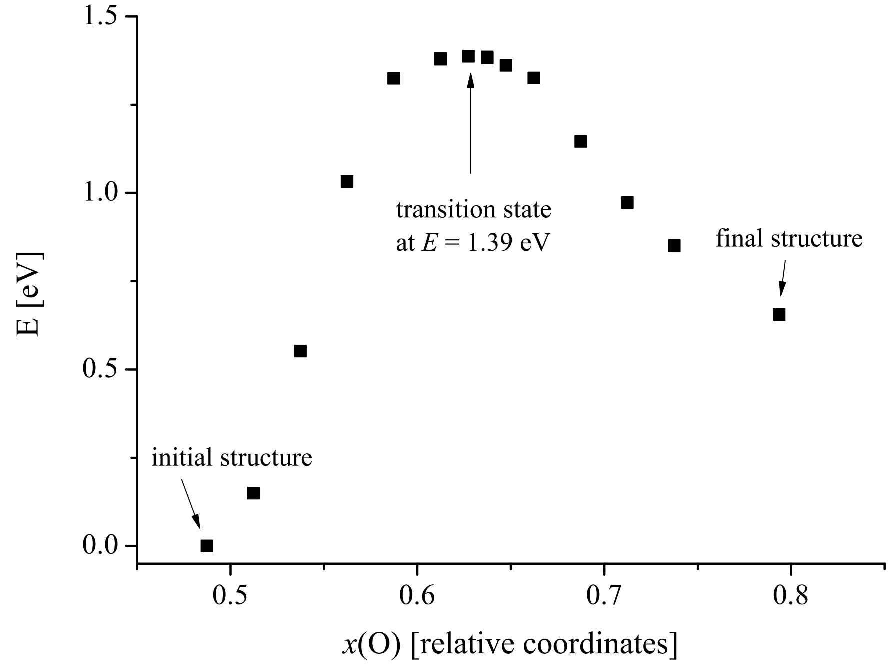

Figure 7.3: Reaction energy profile for the shift reaction of O_{br}-H_2 (neighbouring Cl_{ot}) to O_{ot}-H_2. The x coordinate of the oxygen atom in the water molecule served as reaction coordinate and was incrementally increased. The coordinates of the H atoms were not restricted during movement of the oxygen atom along the reaction coordinate. The maximum of the energy profile at $E = 1.39$ eV corresponds to the transition state energy along that particular reaction coordinate.

'images') of the system are created and connected together with springs in such a way as to form a discrete representation of a path from the reactant configuration **R**, to the product configuration **P**. Initially, the images may be generated along the straight line interpolation between **R** and **P**. An optimisation algorithm is then applied to relax the images down towards the minimum energy path (MEP). The NEB method is able to give a more comprehensive picture of the energy landscape compared to the drag method (chapter 7.5.1) because the NEB reaction coordinate is not restricted to only one dimension. The string of images can be denoted by $[\mathbf{R}_0, \mathbf{R}_1, \mathbf{R}_2, \mathbf{R}_3, ..., \mathbf{R}_N]$ where the endpoints are fixed and given by the initial and final states, $\mathbf{R}_0 = \mathbf{R}$ and $\mathbf{R}_N = \mathbf{P}$, but $N-1$ intermediate images are adjusted by the optimisation algorithm. The most straightforward approach would be to construct an object function

$$\mathrm{S}(\mathbf{R}_1, ..., \mathbf{R}_N) = \sum_{i=1}^{N-1} E(\mathbf{R}_i) + \sum_{i=1}^{N} \frac{k_S}{2}(\mathbf{R}_i - \mathbf{R}_{i-1})^2 \tag{7.9}$$

and minimise it with respect to the intermediate images, $\mathbf{R}_1$,...,$\mathbf{R}_N$. This mimics an elastic band made up of $N-1$ beads and N springs with spring constant k_S. The band is strung between the two fixed endpoints. The problem with this formulation is that the elastic band tends to cut corners and gets pulled off the MEP by the spring forces in regions where the MEP is curved. Also, the images tend to slide down towards the endpoints, giving lowest resolution in the region of the saddle point, where it is most needed [75]. Both the corner-cutting and the sliding-down problems can be solved easily with a force projection. This is referred to as 'nudging'. The reason for corner-cutting is the component of the spring force perpendicular to the path, while the reason for down-sliding is the parallel component of the true force coming from the interaction between atoms in the system. Given an estimate of the unit tangent to the path at each image, $\hat{\tau}_i$, the force on each image should only contain the parallel component of the spring force, and perpendicular component of the true force

$$\mathbf{F}_i = -\nabla E(\mathbf{R}_i)_\perp + \mathbf{F}_i^S \cdot \hat{\tau}_i \hat{\tau}_i \tag{7.10}$$

where $\nabla E(\mathbf{R}_i)$ is the gradient of the energy with respect to the atomic coordinates in the system at image i, and $\mathbf{F}_i^S$ is the spring force acting on image i. The perpendicular component of the gradient is obtained by subtracting the parallel component

$$\nabla E(\mathbf{R}_i)_\perp = \nabla E(\mathbf{R}_i) - \nabla E(\mathbf{R}_i) \cdot \hat{\tau}_{||}\hat{\tau}_{||} \tag{7.11}$$

where $\hat{\tau}_{||}$ represents the parallel part of the unit tangent of the image i.

In order to ensure equal spacing of the images (when the same spring constant, k_S, is used for all the springs), even in regions of high curvature where the angle between $\mathbf{R}_i - \mathbf{R}_{i-1}$ and $\mathbf{R}_{i+1} - \mathbf{R}_i$ deviates significantly from 0°, the spring force should be

$$\mathbf{F}^S_{i||} = k_S(|\mathbf{R}_{i+1} - \mathbf{R}_i| - |\mathbf{R}_i - \mathbf{R}_{i-1}|)\hat{\tau}_i. \tag{7.12}$$

NEB calculations were carried out in the context of the chlorination of s-$RuO_2(110)$ on HLRB (LRZ Garching). 12 images have been applied along the reaction paths, obtained by linear interpolation of the coordinates of the reactant configuration **R** and the product configuration **P**. Every image was optimised to 10^{-7} eV using 8 CPUs in parallel summing up to a total number of 96 CPUs per NEB calculation. The choice of the optimisation algorithm was a special issue, since the conjugate gradient algorithm [69] used for standard geometry optimisation failed to converge in the image optimisations during the NEB calculations. According to Kresse et al. [68], the quick-min algorithm has been chosen.

Chapter 8

Atmospheric Pressure Reaction Measurements

Bridging the pressure and materials gaps between surface science and industrial heterogeneous catalysis has often been and is still a hot topic in catalysis research (for example see [76]). A major problem of the surface science approach applying UHV methods is the transferability of the results obtained for model systems to real world heterogeneous catalysis. Therefore, experiments have been carried out in order to estimate the influence of chlorine atoms on the reactivity towards a model reaction, i.e. the CO oxidation over RuO_2 and chlorinated RuO_2 powder catalysts (bridging the materials gap) at elevated, atmospheric pressure (bridging the pressure gap).

To study the reactivity and stability of heterogeneous RuO_2 powder catalysts under atmospheric pressure conditions and in a continuous reactant gas feed, an experimental setup has been designed, which allows for quantitative on-line analysis of the product gas composition by means of mass spectrometry. This approach has been successfully applied by Aßmann et al. with respect to the CO and methanol oxidation reactions over RuO_2 [76, 77].

8.1 Design of a Reactor System for Atmospheric Pressure Experiments on Heterogeneous Powder Catalysts with on-line Analytics of Reaction Products

In the following section, the configuration of the fixed-bed reactor apparatus with on-line mass spectrometrical product analysis will be described. The assembly and the configuration of the experimental setup as well as the reaction measurements were the scope of the diploma thesis of C. H. Kanzler [78] under supervision of Prof. Dr. H. Over and J. P. Hofmann.

The system is composed of four sections: supply of reactant gases, gas mixture, reaction chamber with oven, and analytics. Figure 8.1 displays the experimental setup of the reactor system as commissioned for CO oxidation measurements.

8.1.1 Gas Supply and Gas Mixture

In its configuration for the study of CO oxidation, the reaction system was equipped with the following gases necessary for preparation of the catalyst samples and the CO oxidation reaction itself:

- argon 5.0, AirLiquide
- argon 5.0 / oxygen 4.5, 90/10 v/v, Messer Industriegase
- argon 5.0 / carbon monoxide 4.7, 90/10 v/v, Messer Industriegase
- argon 5.0 / hydrogen 5.0, 90/10 v/v, Messer Industriegase
- hydrogen chloride 2.8, AirLiquide

All reactant gases except hydrogen chloride were dried using molecular sieve Baylith T143 (4 Å, activated by annealing 5 h at 350 °C).

The reactant gases were mixed by using three mass flow controllers (type 1179B, MKS Instruments) and introduced to the reactor with constant flow rate, variable in the range of f = 1-100 sccm (cm^3 at standard temperature and pressure). The mass flow controller possibly exposed to hydrogen chloride or molecular chlorine was equipped with Kalrez® gaskets to prevent corrosion.

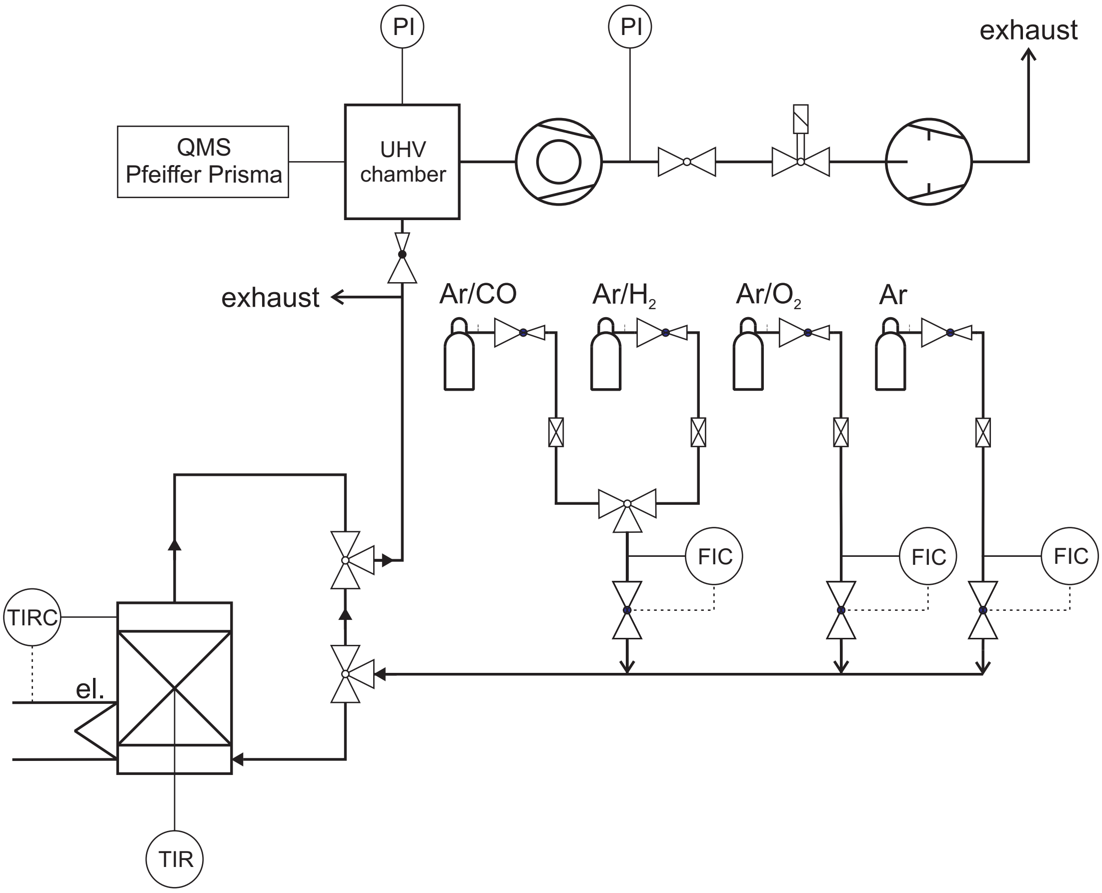
PI
PI
exhaust
QMS
Pfeiffer Prisma
UHV
chamber
exhaust
Ar/CO
Ar/H_2
Ar/O_2
Ar
FIC
FIC
FIC
TIRC
el.
TIR

Figure 8.1: Flowchart of the atmospheric pressure fixed-bed reaction system, configured for measurement of the CO oxidation reaction over RuO_2 powder catalysts [78]. PI = pressure indicator, TIR = temperature indicator and recorder, TIRC = temperature indicator, recorder and controller, FIC = flow indicator and controller.

8.1.2 Fixed Bed Reactor

The fixed bed plug flow reactor applied in the atmospheric pressure, continuous flow setup was manufactured by the institute's glassblower after a concept of Narkhede [79]. Its volume is $V_R = 88$ cm^3. Figure 8.2 shows the schematic drawing of the quartz glas reactor.

The catalyst powder (1-10 mg of RuO_2, diluted by quartz powder of the same grain size fraction) was placed on coarse quartz meal directly at the neck above the tube for the thermocouple at the bottom of the reactor.

The flow reactor was heated by an electrical tube furnace (inner diameter 40 mm, tube length 350 mm), controlled by an Eurotherm temperature controller type 103. The temperature was measured both at the inner wall of the furnace tube and in the reactor, applying K type thermo elements with a tolerance of ±2 K. Temperatures were recorded as analogue voltages (10 mV/K) via the I/O interface of the Pfeiffer QMS 200 Prisma mass spectrometer. The overall temperature tolerance was specified to amount to $\Delta T = \pm 3$ K by cross-checking with a mercury thermometer.

8.1.3 Analytics - Quadrupole Mass Spectrometer

The product gas, that exits the reactor is passing a variable UHV leak valve (Varian 951-5106), where it is introduced into the UHV chamber (CF40 cross) carrying the quadrupole mass spectrometer (Pfeiffer QMS 200 Prisma). The UHV chamber is pumped by a turbopump (Varian Turbo-V70 LP MacroTorr) and a rotary vane pump (Pfeiffer Duo5MC) as fore pump (Pfeiffer F4 oil, perfluoro polyether). The pressure in the UHV chamber was measured by a Penning cold cathode high vacuum transmitter (Leybold PTR 237) and a Pirani gauge in the fore pump line (Edwards PRE 10K). Without bake out, the base pressure in the UHV chamber was below 1×10^{-9} mbar, which is sufficient for the purpose of monitoring the product gas composition by mass spectrometry. During the reaction measurements, a constant pressure of 1×10^{-7} mbar was introduced by the leak valve into the UHV chamber. The pressure in the fore pump line amounts to 4×10^{-2} mbar and did not rise upon pressure increase in the UHV chamber to up to 1×10^{-5} mbar.

To determine conversions in the CO oxidation, the ion currents of the mass signals of CO (m/e = 28), CO_2 (m/e = 44) and O_2 (m/e = 32) have been recorded

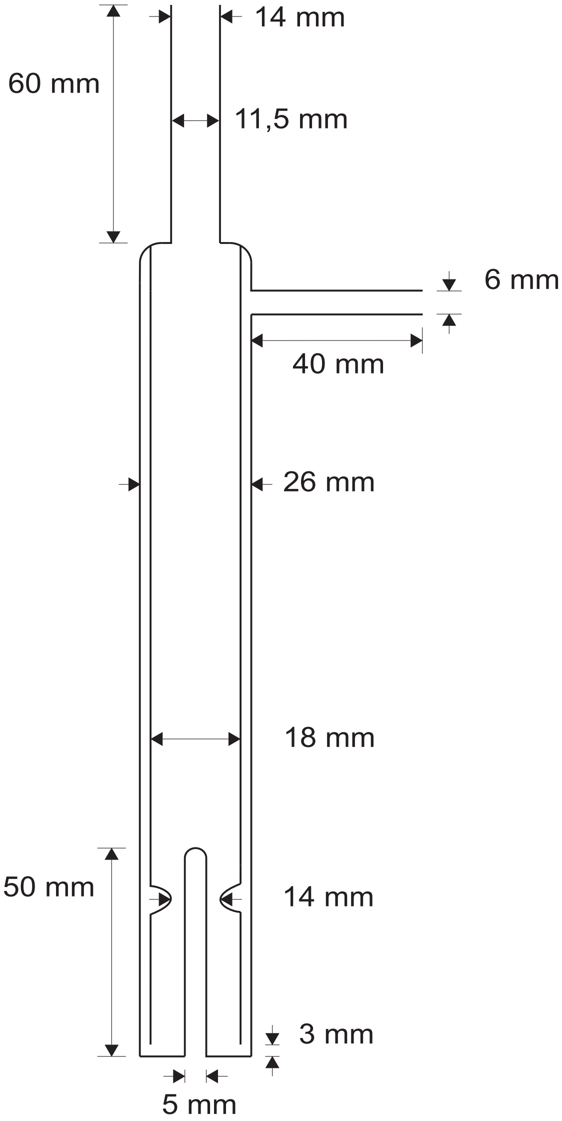
14 mm
60 mm
11,5 mm
6 mm
40 mm
26 mm
18 mm
50 mm
14 mm
3 mm
5 mm

Figure 8.2: Fixed bed plug flow quartz reactor. The small tube at the bottom of the reactor enables the introduction of a thermocouple and thereby the temperature measurement in the direct proximity of the catalyst bed placed at the neck. Figure taken from [78].

versus time.

The conversion regarding the species X (CO, O_2 or CO_2) was calculated from the corrected ion currents by

$$\text{Conversion of component } X[\%] = \frac{(I(X)_{inlet} - I(X)_{outlet})}{I(X)_{outlet}} \tag{8.1}$$

where $I(X)$ are the ion currents of the species X measured both at the inlet (bypass) and the outlet (after reaction) of the reactor. Instabilities in the pressure of the MS-UHV chamber were corrected by normalising all ion currents by the ion current of Ar (m/e = 40), which was introduced into the reactor system as a diluent. The conversion rates of O_2 and CO were later used to determine the activity towards CO oxidation of the catalyst after different pretreatment in the reactor.

Chapter 9

Sample Cleaning and Preparation Procedures

In the following chapter, the preparation methods for the single crystal and powder catalyst samples is summarised. Slight variations to the standard protocol were applied if necessary depending on the UHV chamber.

9.1 Ru(0001)

The single crystal sample used in the RAIRS setup was a commercial (Mateck) Ru(0001) crystal 8 mm in diameter and 2 mm thick, cut perpendicularly to the c axis to a precision of 0.1°, the surface roughness after polishing being better than 0.3 μm. Its cleaning and preparation procedures are being showcased for all other Ru(0001) single crystals used within this thesis.

The purity of the crystal was 99.99%, the main contaminants are Os, Ir, Ca and Fe (in the ppm range) and most importantly carbon. The sample was initially cleaned by heating to T = 700 K in vacuum for a cumulated period of 48 hours, interrupted by repeated cycles of sputtering with Ar^{+} ions ($p(\mathrm{Ar}) = 1 \times 10^{-5}$ mbar, E_{ion} = 1.5 keV, sample at T = 800 K) and flash-annealing to 1100 K in $p(\mathrm{O_2}) = 1 \times 10^{-7}$ mbar. Roasting in oxygen was necessary in order to eliminate carbon, which segregated during prolonged annealing from the bulk to the surface. The crystalinity of the clean Ru(0001) surface was qualitatively checked by LEED. During the experiments the sample had to be occasionally cleaned, whereby two sputtering-annealing cycles have been found to be sufficient to recover a clear LEED background with sharp diffraction spots. Furthermore, Auger spectra were taken of the cleaned metallic Ru(0001) sample or the 2x2 O-covered Ru(0001) after annealing in oxygen.

A further method to check the quality of the Ru(0001) surface was RAIRS of a saturated CO layer formed by low temperature adsorption of CO on Ru(0001) as described by Pfnür et al. [53]. The stretch frequency of adsorbed CO shifts continuously from 1984 cm^{-1} to 2061 cm^{-1} as a function of increasing CO coverage, which is attributed mainly to dipole-dipole coupling. The shape and half-width of the absorption band critically depend on the ordering of the CO layer. A linear relationship between coverage and integrated IR absorption intensity exists only below 0.33 ML. At larger CO coverages the absorption intensity falls, with the result that at saturation coverage the absorption per adsorbed molecule is only 35-40% of that of the absorption at 0.33 ML. This effect is also ascribed to strong lateral interactions in the CO layer. Figure 9.1 shows the adsorption of a saturated CO layer on Ru(0001), which is in good agreement with the finding of Pfnür et al. [53].

9.2 $\mathrm{RuO_2}$(110)

For the growth of the ultra thin $\mathrm{RuO_2}$(110) epitaxial film on the Ru(0001) surface, the clean sample was moved in front of a gas doser, where it was exposed to 2×10^6 L of O_2 (1 L = 1 Langmuir = 1.33×10^{-6} mbar·s)[1] at a sample temperature of T= 650 K. The pressure in the analysis chamber of the RAIRS setup was $p(O_2) = 1 \times 10^5$ mbar during the oxidation step, whereas the local pressure in front of the sample was two orders of magnitude higher [80].

The ordering of the produced $\mathrm{RuO_2}$(110) film was qualitatively checked by LEED. The LEED image of the oxide film displayed a rather intense background indicative of a somewhat rough oxide film. At the same time the characteristic diffraction spots of $\mathrm{RuO_2}$(110) (figure 9.2.*b*) were sharply defined. The characteristic reflexes of the $O(1 \times 1)$ phase were absent, indicating that the sample surface is completely covered by the $\mathrm{RuO_2}$(110) patches.

In addition to the LEED check, a protocol based on the RAIR spectrum of CO adsorbed on the pristine $\mathrm{RuO_2}$(110) film was adopted, and routinely applied

---

[1] In the present thesis, 1 L was defined as 1 L = 1×10^{-6} mbar·s, due to the limited accuracy of the UHV pressure gauges of ±30%.

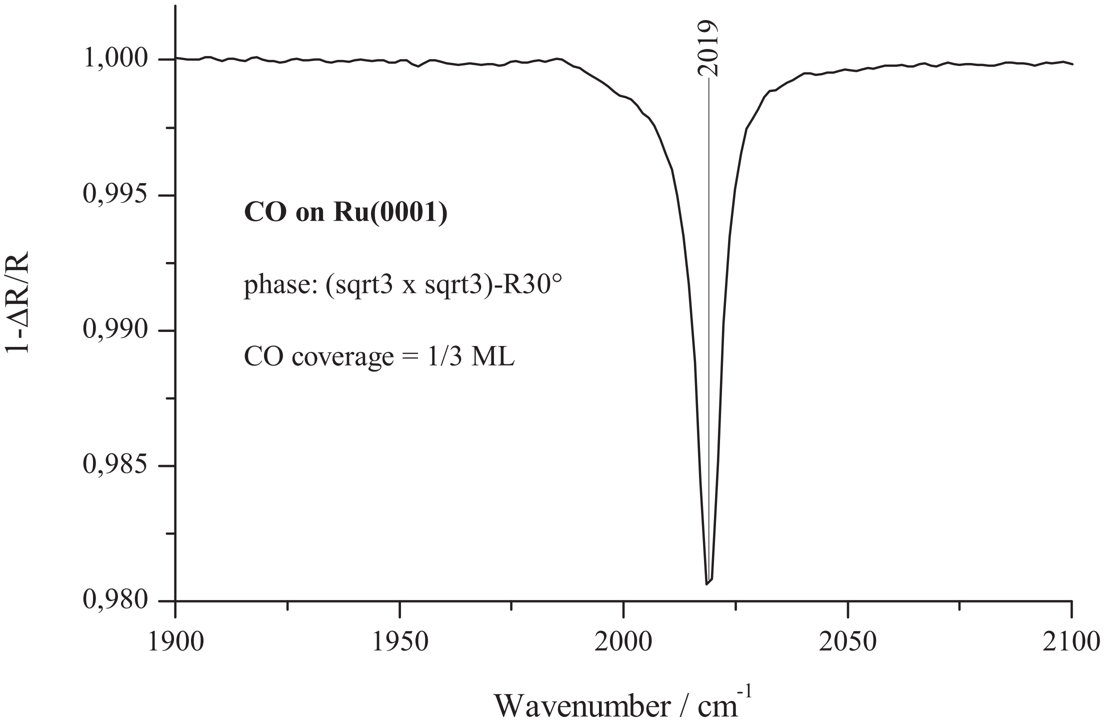

Figure 9.1: RAIR spectrum of the $(\sqrt{3} \times \sqrt{3})$R30°-CO-Ru(0001) phase, with CO coverage of 0.33 ML. The integrated IR absorption of the band can be used for calibration of the coverage up to 0.3 ML. Figure taken from [13].

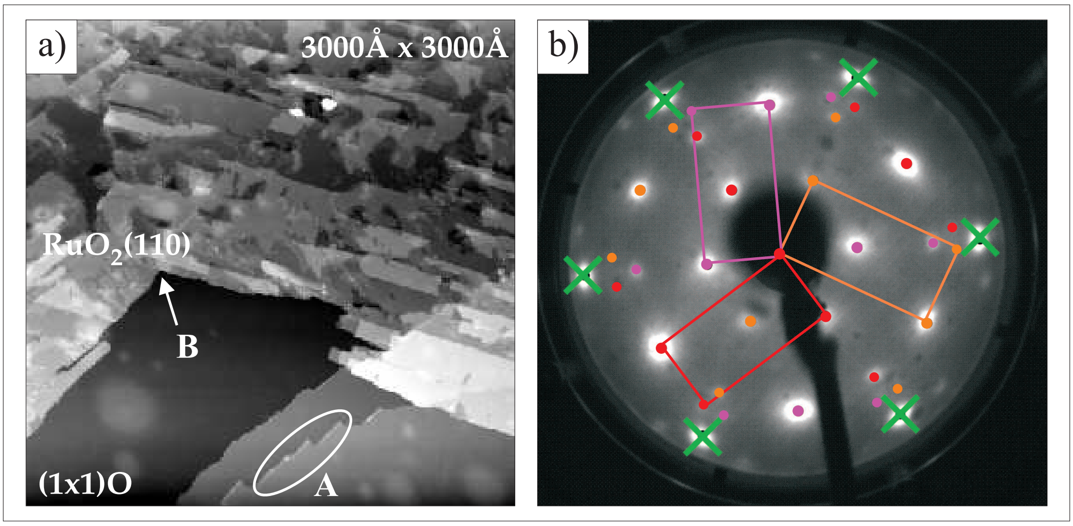

Figure 9.2: $RuO_2(110)$ epitaxial film grown on the Ru(0001) surface. a) Large scale STM images [81] show the coexistence of the $RuO_2(110)$ film with the (1×1)-O phase of chemisorbed oxygen. The $RuO_2(110)$ film is broken up into multiple patches, each few hundreds of Å wide. The oxide film grown at the step edges of the (1×1)-O area is indicated by A. The intersection of two $RuO_2(110)$ rotational domains, rotated 120° relatively to each other, is marked by B. b) The LEED pattern consists of a superposition of a hexagonal pattern (indicated by crosses) due to the (1×1)-O areas and of three rectangular patterns rotated by 120° (each indicated by dots of a different colour) stemming from $RuO_2(110)$ patches of the three orientations. Image adapted after references [82, 83].

during the present work [13]. After cooling the $RuO_2(110)$ surface to T = 110 K and subsequent exposure to 6 L CO, a narrow and intense vibrational line emerged in the RAIR spectrum at 2120-2123 cm^{-1}, with FWHM of 8-10 cm^{-1} and intensity in the range 0.8-2.2% (cf. figure 9.3). However, in this thesis no absorption line stronger than 1.5% has been observed.

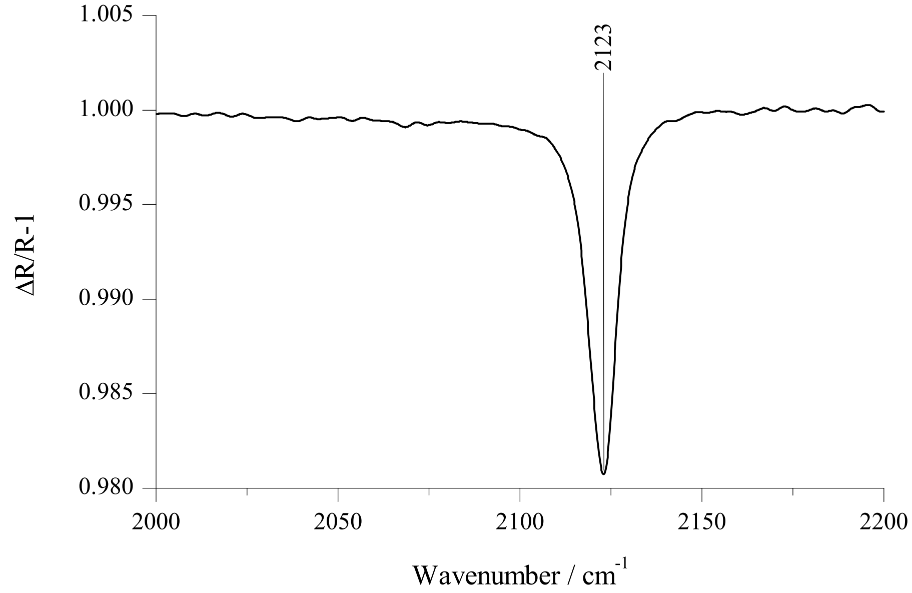

Figure 9.3: RAIR spectrum of the pristine $RuO_2(110)$ surface, after exposure to 6 L CO at T = 110 K. The CO molecules occupy the on top sites, while the bridge sites are occupied by O_{br}. Figure taken from [13].

A fully developed absorption line at 2123 cm^{-1} was considered to be indicative of a clean, well ordered stoichiometric $RuO_2(110)$ surface, with full rows of O_{br} and with all 1f-cus Ru sites occupied by on top CO_{ot}. If the RAIRS line was found to be broader and less intense than of this standard oxide, a substantial improvement could be achieved by repeatedly carrying out the so-called *restoration* procedure: quick annealing (β = 5 to 10 K/s) of the sample to T = 700 K in 2×10^{-7} mbar oxygen, followed by evacuation of oxygen and annealing to T = 500 K in vacuum [84]. This procedure restores the stoichiometric $RuO_2(110)$ patches and eliminates eventual contaminants (H, H_2O, CO) stemming from the residual gas adsorption, leading to a visibly more intense CO ‘signature’ line (figure 9.4).

The recipe for a standard restoration procedure allowed for an exact reproduction of the characteristic IR line (2123 cm^{-1}) of CO_{ot} adsorbed on the stoi-

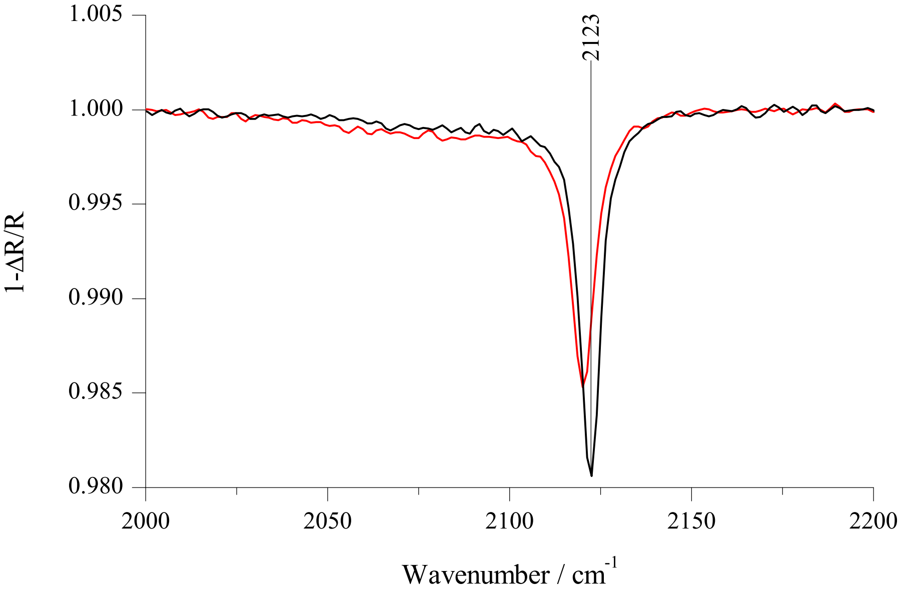

Figure 9.4: Effect of the restoration procedure. CO adsorbed on the stoichiometric $RuO_2(110)$ film: after holding the film for 12 hours in UHV residual gas at 1×10^{-9} mbar (red curve) and after one restoration procedure (black curve). Figure taken from [13].

chiometric $RuO_2(110)$ oxide film, prior to each RAIRS experiment. Bringing the oxide film back into this reference state provided a well defined starting situation, a necessary condition to obtain reproducible results. Repeating the restoration procedure between the experiments enabled us to carry out more experiments on the same oxide film, hence, avoiding the time consuming preparation of a new oxide film starting from the clean Ru(0001) surface.

9.3 $RuO_{2-x}Cl_x(110)$

The chlorinated ruthenium dioxide (further denoted as $RuO_{2-x}Cl_x(110)$) was prepared starting from the clean, restored, stoichiometric oxide. The common preparation procedure reads as follows: The stoichiometric oxide was treated with 20 L (2×10^{-7} mbar×100 s) H_2 at room temperature (T = 298 K) to transform all bridging oxygen atoms (O_{br}) into bridging hydroxyl groups (O_{br}-H) [85]. Subsequently, the surface was flashed to 700 K in dry hydrogen chloride (p(HCl) = 5×10^{-8} mbar) and afterwards cooled to room temperature in the background pressure of HCl. After this procedure, most of the bridging oxygen atoms (O_{br}) were replaced by chlorine atoms (Cl_{br}) [9]. Furthermore, the 1f-cus positions were filled with HCl_{ot} and Cl_{ot}. To recover the 'clean' chlorinated oxide, i.e. chlorine occupies only bridging and the 1f-cus Ru sites are empty, the sample had to be flashed to T = 700 K. The degree of chlorination was controlled by Auger electron spectroscopy. In figure 9.5 Auger spectra of the stoichiometric oxide and the chlorinated oxide $RuO_{2-x}Cl_x(110)$ are compared.

The determination of the actual chlorine content will be within the scope of chapter 13. The initial chlorination of a stoichiometric $RuO_2(110)$ surface does not lead to maximum chlorination. Therefore, a second chlorination step, can be necessary to obtain a maximum chlorinated surface. After prolonged experiments, a rechlorination can be necessary as well, to bring back the oxide to the maximum chlorinated state. For this purpose, the incompletely chlorinated surface is restored by flashing in oxygen atmosphere in order to reset the oxygen bridges followed by a hydrogen treatment (20 L H_2 at T = 298 K) and a flash to T = 700 K in HCl. After cooling to room temperature a flash to T = 700 K in vacuum recovers the on top adsorbate free, bridging chlorinated ruthenium dioxide.

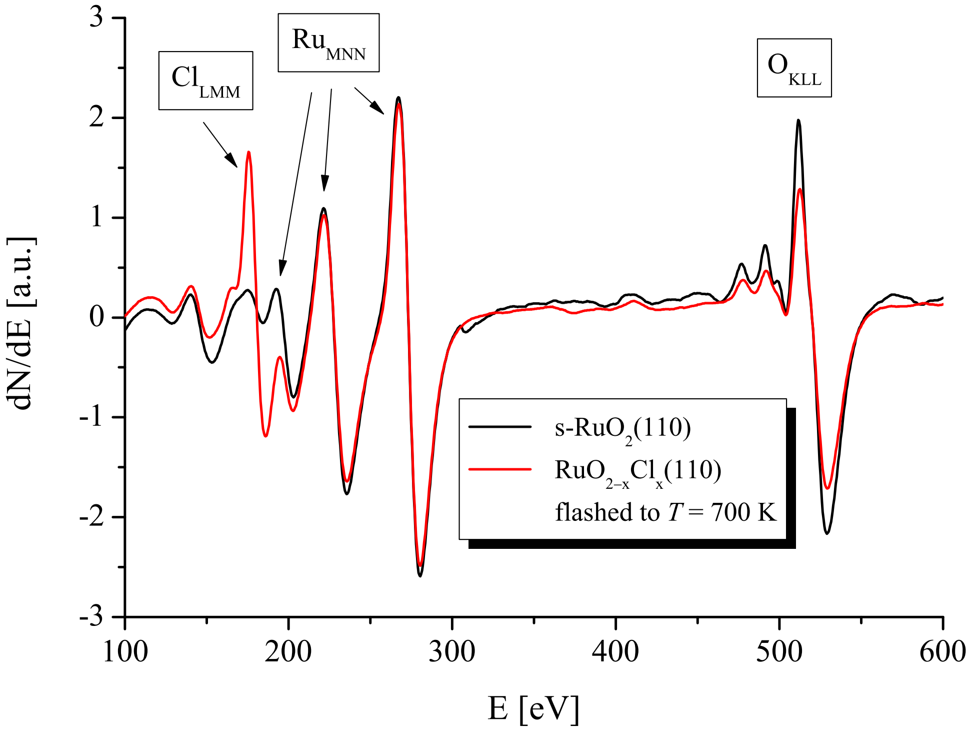

Figure 9.5: Auger spectra of stoichiometric $RuO_2(110)$ and chlorinated $RuO_{2-x}Cl_x(110)$ after a flash to T = 700 K (E = 3 keV). The Cl_{LMM} Auger peak interferes with the lowest energy Ru_{MNN} peak.

9.4 Preparation of Chlorinated RuO_2 Catalysts at High Pressures

RuO_2 powder was used as catalyst in the fixed bed atmospheric pressure reactor system. The sieve fraction diameter should be in the range of 250-350 μm, to prevent a loss of the catalyst filling by the gas flow and to exclude the influence of pore diffusion on the reaction rate [86]. The preparation of the initial reactor filling reads as follows: 500 mg of nano crystalline RuO_2 powder (Alfa Aesar) were immersed by poly vinyl alcohol and pelletised in a hydraulic press (20 min, 10 mm diameter, 150 kN/cm^2). The pellet was annealed in a muffle furnace under normal atmosphere (2 h, T = 773 K), grinded carefully in an agate mortar and sieved to yield 207 mg (40%) of sintered RuO_2 (250-355 μm).

Then, 10 mg of the so prepared catalyst were put into the reactor and flushed by argon (15 min, $f(\mathrm{Ar}) = 50$ sccm). Organic residues were removed by annealing 60 min in oxygen at T = 573 K (f(10% v/v O_2 in Ar) = 50 sccm). In order to fully reduce the RuO_2 particles to yield metallic Ru, the sample was annealed in a hydrogen flow f(5.2% v/v H_2 in Ar) = 50 sccm) for 60 min at temperatures in the range of T = 693-773 K.

The chlorination of the catalyst was achieved by exposing the active (reoxidised) catalyst after CO oxidation, i.e. the reduced sample which oxidised under CO oxidation conditions, in the reactor to HCl at room temperature followed by an annealing step to T = 573 K (30 min). Afterwards, the system was flushed by Ar (30 min, $f(\mathrm{Ar}) = 50$ sccm) at T = 693 K to remove residual HCl and Cl_{ot} after the chlorination step.

Unfortunately, in the present stage of development of the atmospheric reactor setup there was no possibility to determine the degree of chlorination of the RuO_2 powder catalyst samples by any analytical method at all. Thus, the chlorinated catalyst has been prepared blindly be transferring the chlorination recipe from UHV to atmospheric pressure conditions.

Part II

Ruthenium Dioxide(110) as Model Catalyst - Literature Survey

Chapter 10

The $RuO_2(110)$ Surface: Properties and Preparation

The present chapter is intended as a brief review of the principal results in the literature concerning the $RuO_2(110)$ surface and can be seen as a sequel to the literature review given in [13]. The first section presents the oxidation of the Ru(0001) surface, leading to the formation of the so-called 'oxygen-rich' Ru surfaces, much more active in the CO oxidation than the original metallic Ru(0001) surface. The structure of the catalytically active phase of these 'oxygen-rich' Ru surfaces, the ultra thin epitaxial $RuO_2(110)$ film, is described in chapter 10.2. The chemical activity of the $RuO_2(110)$ surface towards CO, O_2 and the oxidation of CO is summarised in chapter 11.

10.1 Oxidation of Ru(0001)

Ruthenium forms only one stable solid oxide phase, namely ruthenium dioxide. The growth of a ruthenium dioxide layer on the surface of a ruthenium single crystal is a complex process which was clarified mainly during the past decade [76, 87, 88]. Ruthenium dioxide (RuO_2) crystallises in a rutile-type structure (figure 10.2.*a*), the crystalline structure of the mineral rutile (titanium dioxide). In the bulk structure of RuO_2 the Ru atoms bind to six O atoms, forming a slightly distorted RuO_6 octahedron, while the O atoms are coordinated to three Ru atoms in a planar way, consistent with an sp^2 hybridisation of the oxygen atoms. The ruthenium dioxide surfaces studied in the present work are ultra thin epitaxial

RuO_2 *films* grown under intensive oxygen exposure on the facets of Ru single crystals, rather than facets of a bulk RuO_2 single crystal. The *epitaxial* growth of the ruthenium dioxide films yields a well defined orientation of the films relatively to the lattice of the Ru substrate. The orientation of an epitaxially grown RuO_2 film is conditioned by the orientation of the single crystalline Ru substrate. For instance, the epitaxial RuO_2 layer exposes preferentially the (110) facet when grown on Ru(0001) and the (100) facet when grown on Ru($10\bar{1}0$). The structures of these two ruthenium dioxide layers are denoted RuO_2(110) and RuO_2(100), respectively.

Exposing the Ru(0001) surface at room temperature to molecular oxygen under UHV conditions, a (2×2)-O [89] and a (2×1)-O overlayer are formed [90], containing 0.25 and 0.50 monolayers of chemisorbed oxygen, respectively. The dissociative sticking coefficient of O_2 drops, from about 1 on the clean Ru(0001) surface, to less than 10^{-3} on the chemisorbed O overlayers, such that under UHV conditions the (2×1)-O phase was considered to be the saturation phase. Recently, it has been shown that by dosing much more oxygen (10^3-10^6 L), the Ru(0001) surface can accommodate two additional phases with even higher contents of chemisorbed oxygen, namely (2×2)-3O with 0.75 monolayers of O [91] and (1×1)-O with one monolayer of O [92]. The dissociative sticking coefficient of O_2 over the Ru(0001)-(1×1)-O surface is estimated to be less than 10^{-6} [93]. Consequently, oxygen uptake beyond the coverage of one monolayer becomes the rate determining step in the initial oxidation of Ru(0001). However, as soon as an oxide nucleus is formed on the Ru(0001)-(1×1)-O surface, oxide formation proceeds in an autocatalytic way [94], since the dissociative sticking coefficient of O_2 on the oxide nucleus is as high as 0.7 [93]. Autocatalytic oxidation implies that the surface produces the ‘catalyst’ for its own oxidation in the form of small oxide nuclei which, by efficiently dissociating the O_2 molecules, lead to a self-acceleration of the oxidation process. The threshold temperature for the oxidation of Ru(0001) by molecular oxygen turns out to be T = 540 K. Below this temperature, RuO_2(110) cannot be formed on Ru(0001), as shown by *in situ* SXRD measurements performed at oxygen pressures up to 0.1 mbar [36] and by recent high-pressure X-ray photoelectron spectroscopy experiments as well [88]. Below T = 400 K only chemisorbed oxygen can be stabilised on Ru(0001).

Exposure of the Ru(0001) surface to O_2 at T = 580-630 K in a wide pressure range (10^{-5}-10^{-1} mbar) results in the growth of a 1.6 nm thick $RuO_2(110)$ epitaxial film on Ru(0001), as shown by *in situ* SXRD measurements [36] and corroborated by a recent STM study by Wintterlin et al. [95]. The thickness of the $RuO_2(110)$ film was practically independent of the preparation conditions in the indicated range, being limited to five $RuO_2(110)$ crystal planes. The growth of the $RuO_2(110)$ film on Ru(0001) may be briefly characterised as *autocatalytic* and *self-limited*. SXRD data have indicated the dimensions 3.10 Å × 6.39 Å [36] for the unit cell of the $RuO_2(110)$ epitaxial film, which are incommensurate to the lattice constant of 2.71 Å of the Ru(0001) substrate.

Large-scale STM images [81] show that the $RuO_2(110)$ epitaxial film breaks up into separate patches several hundreds of Å^2 in size, rotated 120° to each other (figure 9.2.*a*). The coexistence of distinct rotational $RuO_2(110)$ domains of different orientations is induced by the three-fold symmetry of the substrate and is most directly observed by low-energy electron diffraction (LEED). Instead of the rectangular LEED pattern characteristic of the $RuO_2(110)$ structure, the LEED pattern of the epitaxially grown $RuO_2(110)$ film on Ru(0001) presents hexagonal symmetry, consisting of the superposition of three separate rectangular patterns rotated 120° relatively to each other (figure 9.2.*b*). Furthermore, STM images [81, 87] have shown the coexistence of $RuO_2(110)$ patches with areas occupied by the (1×1)-O phase, both several hundreds of Å wide (figure 9.2.*a*). The presence of the (1×1)-O phase on the oxidised Ru(0001) surface is easily recognised in the LEED pattern, since its characteristic diffraction spots (marked by crosses in figure 9.2.*b*) are distinct from those of the $RuO_2(110)$ patches [82]. The (1×1)-O phase is chemically inert, neither CO nor O_2 adsorption being observed at temperatures higher than 50 K [96].

The observation of a self-limited growth mechanism of the $RuO_2(110)$ layers does not exclude the growth of thicker ruthenium dioxide films on Ru(0001). Oxidation of the Ru(0001) surface at higher temperatures (T = 670-720 K) leads to the growth of thicker RuO_2 films consisting of 7-11 $RuO_2(110)$ crystal planes [36]. This finding is further corroborated by HP-XPS measurements of Blume et al., which indicated a film thickness of >15 Å for oxidation at $T = 620$ K ($p(O_2)=10^{-2}$ mbar) [88]. The thicker RuO_2 films present roughened surfaces, exposing other facets in addition to the favoured (110) plane. In STM images taken during the initial stages of the roughening of a $RuO_2(110)$ film, the catalytically inactive c(2×2)-reconstructed $RuO_2(100)$ facet has been identified [97]. This observation has proved to be of key importance in understanding the puzzling deactivation of Ru-based catalysts under oxidizing conditions [98, 99], first reported by Cant et al. [100].

10.2 Surface structure of epitaxially grown RuO_2(110) films on Ru(0001)

The literature data presented in the previous section have shown that exposure of the Ru(0001) surface to large doses (10^6 L) of molecular oxygen, at sample temperatures exceeding $T = 540$ K, results in the formation of an epitaxially, ultra thin RuO_2(110) film which may coexist with an (1×1)-O phase.

Two structure models for the ultra thin RuO_2(110) epitaxial film have been investigated [87, 102], in order to establish the atomic geometry at the surface of a RuO_2(110) film in pristine condition [82]. The models, represented in figure 10.1.*a* and figure 10.1.*b*, are truncations of the bulk RuO_2 structure along the (110) crystal plane. In the model of figure 10.1.*a*, during the present work termed the *stoichiometric* RuO_2(110) surface, oxygen atoms (O_{br}) are bridging over pairs of Ru atoms, forming ordered rows oriented in the [001] direction. The model in figure 10.1.*b*, in the following termed the *mildly reduced* RuO_2(110) surface, is obtained from model *a* after removal of the O_{br} atoms. In the rest of this work, the RuO_2(110) surfaces in figure 10.1.*a* (stoichiometric) and in figure 10.1.*b* (reduced) will be denoted as s-RuO_2(110) and r-RuO_2(110), respectively. However, it has to be mentioned that the clean r-RuO_2(110) surface can not be prepared and is only stable when covered by e.g. CO (figure 10.1.*c*).

In reference [82], a combined LEED-DFT analysis was applied to an oxidised Ru(0001) surface in order to discriminate between the models of s-RuO_2(110) and r-RuO_2(110) (figure 10.1.*a*, *b*) of the pristine RuO_2(110) epitaxial film. The Ru(0001) sample was exposed to 6×10^6 L O_2 at $T = 600$ K, which led to the accumulation of 6 monolayers of oxygen at the sample surface. The LEED data recorded on the freshly prepared sample have unambiguously indicated that s-RuO_2(110) (figure 10.1.*a*) rather than r-RuO_2(110) (figure 10.1.*b*) is the structure of the pristine RuO_2(110) epitaxial film. Moreover, DFT optimisation of the s-RuO_2(110) structure has reproduced the LEED-determined geometry to within 0.04 Å accuracy. In contrast, the disagreement between the DFT-optimised r-

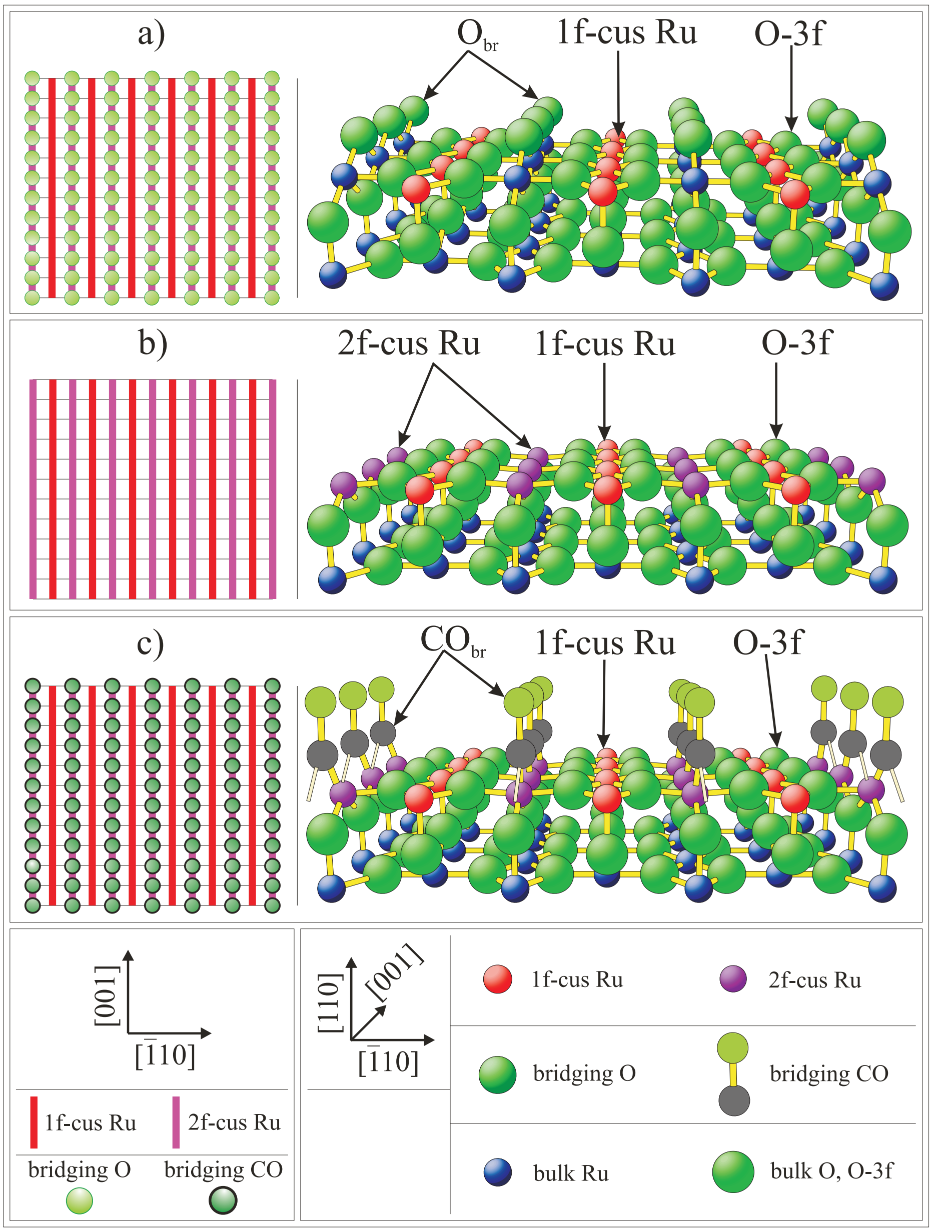
a)
O_{br}
1f-cus Ru
O-3f
b)
2f-cus Ru
1f-cus Ru
O-3f
c)
CO_{br}
1f-cus Ru
O-3f
[001]
[$\bar{1}$10]
1f-cus Ru
2f-cus Ru
bridging O
bridging CO
[110]
[001]
[$\bar{1}$10]
1f-cus Ru
2f-cus Ru
bridging O
bridging CO
bulk Ru
bulk O, O-3f

Figure 10.1: Schematic representation (left column) and ball-and-stick model [87] (right column) of the $RuO_2(110)$ surface. *a*) On the *stoichiometric* (pristine) surface, pairs of Ru atoms are bridged by oxygen atoms (O_{br}). *b*) The *mildly reduced* surface is obtained after removal of the O_{br} atoms from the stoichiometric surface. *c*) The vacant bridge sites on the mildly reduced surface can be occupied by other adsorbates, for example CO_{br}. The O-3f oxygen atoms keep their bulk like coordination to three Ru atoms and are not chemically active. The active sites are the O_{br} atoms and the one- and twofold coordinatively unsaturated (cus) Ru atoms, denoted 1f-cus Ru and 2f-cus Ru respectively. Figure by courtesy of A. Farkas [13].

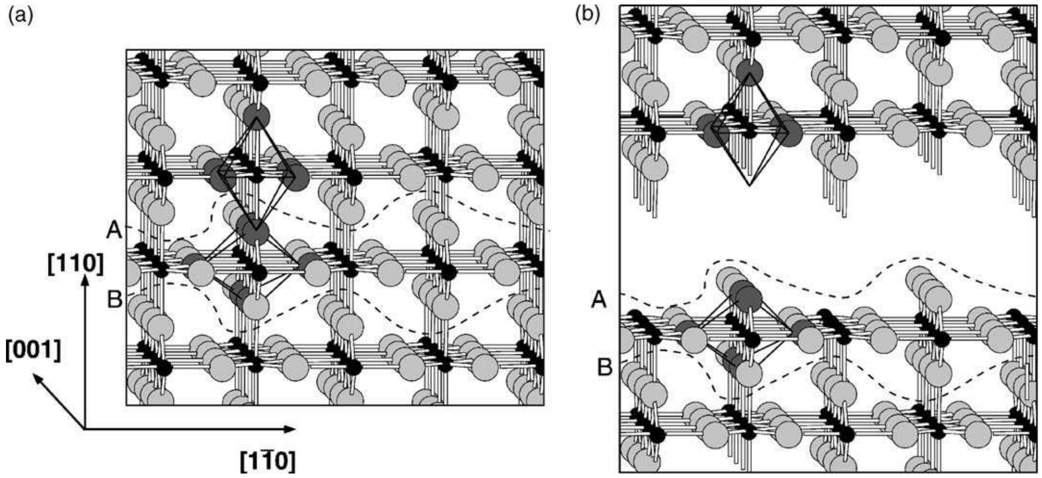

Figure 10.2: a) Ball-and-stick model of the rutile crystal structure. It is composed of slightly distorted octahedra, two of which are indicated. Along the [110] direction these octahedra are stacked with their long axes alternating by 90°. Open channels are visible along the [001] direction. The dashed lines *A* and *B* enclose a charge-neutral repeat unit. b) The crystal is cut along line *A*. The same number of Ru-O and O-Ru bonds are broken. The resulting $RuO_2(110)$ surface is autocompensated (see text) and stable. Figures taken from reference [101].

$RuO_2(110)$ structure and the LEED data was found too large [82] and consequently, this model was rejected.

The bridging oxygen atoms (O_{br}) contribute essentially to the stability of the s-$RuO_2(110)$ surface, as may be shown with reference to the concept of charge autocompensation on ionic surfaces [101, 103]. While truncating the bulk RuO_2 structure such as to expose the s-$RuO_2(110)$ surface, the same number of coordinatively unsaturated (cus) O atoms and Ru atoms are formed, by breaking the respective O-Ru and Ru-O bonds (figure 10.2.*b*). Each of these cus atoms has an unsaturated valence, also referred to as a dangling bond [87]. Transferring electrons from the dangling bonds on the Ru cations will exactly compensate the missing charge in the dangling bonds on the O_{br} anions. Thus, due to the presence of the bridging O_{br} atoms, the s-$RuO_2(110)$ surface is stabilised via the autocompensation mechanism [82].

The $RuO_2(110)$ surface (figure 10.1.*a*) presents two different kinds of Ru atoms. Along the [001] direction, rows of six-fold coordinated (bulk like) Ru atoms alternate with rows of five-fold coordinated (or one-fold coordinatively unsaturated) Ru atoms. The two kinds of Ru atoms are denoted as 2f-cus Ru and

1f-cus Ru, respectively. Two kinds of O atoms are present as well. Similarly to the oxygen atoms in the bulk, the oxygen atoms denoted as O-3f (figure 10.1.*a*) maintain a planar coordination to three Ru atoms, consistent with an sp^2 hybridisation of the oxygen atom [87]. The bridging O_{br} atoms are coordinated to two instead of three Ru atoms, their unsaturated valence being oriented perpendicularly to the surface. Together with the 1f-cus Ru atoms, which also expose dangling bonds oriented perpendicularly to the surface, the O_{br} atoms are the chemically active centers on the stoichiometric s-RuO_2(110) surface. The O-3f atoms are not chemically active during the CO oxidation reaction [104].

The *mildly reduced* r-RuO_2(110) surface (figure 10.1.*b*) is obtained after removal of all O_{br} atoms from the stoichiometric s-RuO_2(110) surface (figure 10.1.*a*), for example by exposure to CO at room temperature. It has to be noted, that the reduced r-RuO_2(110) surface, as represented in figure 10.1.*b*, is not stable and has not been prepared experimentally. DFT calculations have shown that its surface energy would be in the range 90-120 meV/Å^2, far less favourable than that of the stoichiometric s-RuO_2(110) surface (71 meV/Å^2) [76, 82]. The mildly reduced RuO_2(110) surface can be stabilised by populating the vacant bridging sites with CO molecules. Figure 10.1.*c* shows the r-RuO_2(110) surface with the bridge positions occupied by so-called *asymmetric* bridging CO molecules (see next section).

Chapter 11

Chemical Activity of $RuO_2(110)$

On the atomic scale, the extraordinarily high activity of stoichiometric $RuO_2(110)$ toward CO oxidation was demonstrated to be controlled by the presence of 1f-cus Ru sites [87, 102]. It must be emphasised that, unlike to other oxide surfaces, not the defects but rather the regularly under-coordinated surface atoms determine the activity of $RuO_2(110)$ [105].

11.1 Adsorption of CO on Reduced $RuO_2(110)$

On the stoichiometric $RuO_2(110)$ surface the CO molecules adsorb strongly (-1.2 eV [102]) on top of the 1f-cus Ru atoms, from where the actual oxidation reaction takes place by recombination with the bridging O_{br} atoms to form CO_2.

HREELS measurements [106] have shown that exposure of the stoichiometric $RuO_2(110)$ surface to CO at room temperature leads to the gradual depletion of the bridging O_{br} population, until for a cumulative exposure of about 1 L CO all bridging O atoms are consumed. The stoichiometric $RuO_2(110)$ turns into a reduced $RuO_2(110)$ surface where the 2f-cus Ru atoms are, at least partially, capped by bridging CO molecules. Seitsonen et al. [104] have obtained the mildly reduced, CO capped $RuO_2(110)$ surface by exposing several times (typically, five to ten times) 0.25 L CO at T = 170 K and annealing to T = 550 K while monitoring the CO_2 signal with a quadrupole mass spectrometer. They have considered the vanishing of the CO_2 signal as indicative of the complete removal of the O_{br} species, i.e. of the mild reduction of the $RuO_2(110)$ surface.

The adsorption geometry of CO on the reduced $RuO_2(110)$ surface depends

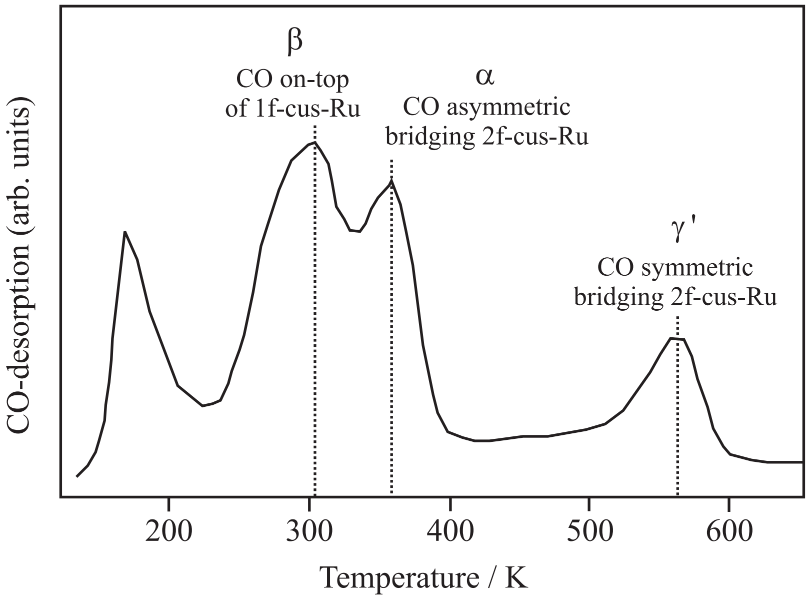

Figure 11.1: Thermal desorption spectrum of CO from a mildly reduced $RuO_2(110)$ surface (all O_{br} have been previously removed) [104].

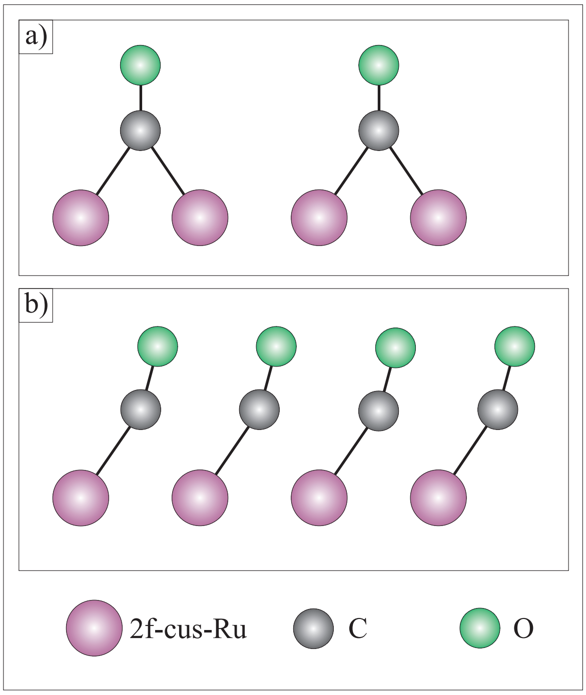

Figure 11.2: Two adsorption geometries for bridging CO_{br} molecules on the mildly reduced $RuO_2(110)$ surface. a) *Symmetric bridging* CO_{br} molecules occupy the bridge positions above every second pair of 2f-cus Ru atoms. b) *Asymmetric bridging* CO_{br} molecules bind in a tilted geometry to a single 2f-cus Ru atom [13].

critically on the CO coverage. This point is well illustrated by the thermal desorption spectrum (TDS) of CO from the reduced $RuO_2(110)$, shown in figure 11.1. The low-temperature desorption states β and α, and a high-temperature desorption state γ' can be clearly discriminated. Based on DFT calculations, Seitsonen et al. have proposed well defined adsorption sites and binding geometries for these thermal desorption (TD) states [104].

The TDS measurement can be described as follows. The reduced surface has been saturated with CO by exposure at $T = 170$ K, i.e. the bridge and on top sites are in the beginning occupied by CO. By increasing the sample temperature with a constant rate, the different species of adsorbed CO molecules start to desorb, provided that the sample temperature is high enough for the CO molecule to overcome the energy barrier for desorption. The TD spectrum represents in principle the number of desorbed CO molecules as a function of the sample temperature.

At $T = 300$ K the on top CO_{ot} leaves the surface, as reflected by the desorption state β. Now the on top sites are vacant but the bridge sites are still saturated with CO. For this state, Seitsonen et al. have proposed the model depicted in figure 11.2.*b*, characterised by a complete row of CO_{br} molecules coordinated in a tilted geometry to each 2f-cus Ru atom. In the rest of the present thesis this kind of bridging CO molecules are denoted as *asymmetric* CO_{br}.

At $T = 360$ K half of the asymmetric bridging CO_{br} molecules of the β state leave the surface. The remaining CO_{br} molecules change their coordination to the 2f-cus Ru atoms, from single and tilted to double and upright, as shown in figure 11.2.*a*. In the rest of the present thesis this kind of bridging CO_{br} molecules are denoted as *symmetric* CO_{br} or CO_{br}^{II}. Desorption of the symmetric CO_{br} molecules at $T = 560$ K is manifested in the high-temperature desorption state γ'. These findings were also corroborated by a HREELS study by Fan et al. [106].

It is interesting to note that, according to LEED experiments and DFT calculations [104], the 2f-cus Ru atoms attached to the symmetric CO_{br} molecules are drawn towards the CO molecule by as much as 0.2 Å. This lateral relaxation of the 2f-cus Ru atoms allows for a much better overlap of the CO molecular frontier orbitals with those of the substrate.

The binding energies of CO on reduced $RuO_2(110)$ have been calculated by DFT. For low coverages, when on the average only every second 2f-cus Ru atom is occupied, the symmetric bridge position above 2f-cus Ru atoms is the preferred adsorption site with −1.85 eV, followed by the on top position above 1f-cus Ru atoms with −1.61 eV. With CO capping all dangling bonds of the 2f-cus Ru atoms, the preference changes from the symmetric bridge position to the asymmetric bridge position above the 2f-cus Ru atoms, with −1.59 eV [104].

11.2 Adsorption of O_2 on RuO_2(110)

Like reduction, an equally important process is the facile reoxidation of the partially reduced RuO_2(110) surface by oxygen supplied from the gas phase.

At temperatures below $T = 140$ K, molecular oxygen lays down on the s-RuO_2(110) surface as an intact entity, bridging two adjacent 1f-cus Ru atoms. On increasing the sample temperature, the molecular oxygen dissociates and forms terminal Ru-O bonds to the 1f-cus Ru atoms. At room temperature, oxygen molecules from the gas phase can efficiently adsorb (sticking probability ~ 0.7) and dissociate.

Exposure of the stoichiometric RuO_2(110) surface to oxygen at room temperature stabilises a weakly held oxygen species, which desorbs at about 450 K in molecular form [102]. This species consists of O atoms on top of the 1f-cus Ru atoms, in the following denoted as O_{ot}. According to DFT calculations, the binding energy (with respect to atomic oxygen) of the on top O_{ot} atoms is, with only −3.2 eV, much lower than that of the bridging O_{br} species (−4.6 eV), which makes O_{ot} a potentially active species [102]. O_2 dissociation on the 1f-cus Ru sites of RuO_2(110) becomes limited by the configurational constraints of the oxide surface: as O_2 dissociation proceeds on an unsaturated surface, stranded vacant 1f-cus Ru sites are generated that become adsorption sites for molecular O_2 [107].

The diffusion barrier for O_{ot} along the [001] direction has been calculated by DFT as 1.2 eV [105]. For that reason, even at room temperature the on top O_{ot} atoms are primarily grouped in pairs, as shown by STM [105]. However, if there is an adjacent vacancy in the rows of O_{br}, the diffusion barrier of oxygen to move from the on top site to the bridge site is only 0.6 eV. This diffusion process is very likely at room temperature and accordingly important for the restoration of the mildly reduced RuO_2(110) surface.

11.3 CO Oxidation on RuO_2(110) - from UHV to 1 atm

The CO oxidation over Ru-based model catalysts has been a subject of controversial debates and scientific discussion over the last years, concerning the active phase of the catalyst.

Metallic, defect free Ru(0001) was reported to be a very poor CO oxidation catalyst [108] under UHV conditions with significantly lower reactivity compared to other group VIII metals (Pt, Pd, Rh, and Ir). Only stepped Ru(0001) surfaces have a mentionable activity towards CO oxidation [109]. However, under higher pressure oxidising atmospheres, Ru was found to turn into a very efficient oxidation catalyst [100, 110]. CO oxidation over ruthenium is therefore a prime example of a catalytic system with an apparent pressure gap, which has been shown to be closely associated with an active surface phase capable to adapt in response to the composition of the reactant feed gas.

At least two catalytically active phases have been identified up to now: a nonoxidic phase and the RuO_2(110) phase [111]. While the surface structure and composition of the RuO_2 phase are well characterised, thus serving as a model catalyst [87, 105] the chemical nature of the active nonoxidic phase is still elusive and a matter of ongoing discussion [88, 112, 113, 114, 115]. It is important to note that over the past years several other surface oxides on transition metal (TM) surfaces such as Rh, Pt, and Pd have been shown to develop under reaction conditions concomitant with a dramatic increase in the reactivity [116, 117, 118, 119, 120]. Whether these oxide phases are catalytically active in the CO oxidation is currently debated [118, 121, 122] since these findings challenge the generally accepted chemical view whereupon oxide formation is considered to deteriorate the activity of transition metals in the CO oxidation reaction [96].

Recent *in situ* studies on the CO oxidation over the Ru(0001) model catalysts have focused on the actual surface structure under high pressure reaction conditions, applying the techniques of in situ surface X-ray diffraction (SXRD) and online mass spectrometry. This unique combination of techniques allowed the elucidation of the complex structure-activity correlation of the RuO_2(110) model catalyst under reaction conditions [111, 123].

Farkas et al. have very recently given new insight into the CO oxidation on

RuO_2(110) by means of in situ RAIR spectroscopy [13, 14]. The study was based on a detailed vibrational characterisation of CO and CO+O coadsorbate phases under UHV conditions. Thereby, CO was introduced as a versatile probe molecule to analyse the surface composition of RuO_2(110) during CO oxidation even *in situ* under higher pressure conditions up to 10^{-3} mbar. The experiments allowed for a stepwise bridging of the pressure gap. The actual stretching vibration frequency of CO depends not only on the adsorption site but also sensitively on the local adsorption environment on the catalyst's surface (cf. chapter 6). Thus, this technique offered unprecedented information about the distribution and the local configuration of adsorbed CO and O species on the surface of the working catalyst in the CO oxidation. The surface was shown to alter from a bridging O_{br} coverage to a CO_{br} coverage under working conditions at highest activity. As indicated recently by *ex situ* HREELS [124] the stoichiometric oxide was completely covered by symmetric CO_{br} molecules after CO oxidation, suggesting that CO_{ot} reacts efficiently with both O_{ot} and/or O_{br} and replaces readily O_{br} by symmetric bridging CO_{br} molecules ($\tilde{\nu}(CO) = 1867\ \mathrm{cm}^{-1}$). The areas with a low coverage of symmetric CO_{br} molecules were referred to as being the active phase, since they provide enough free 1f-cus Ru sites for O_2 dissociative adsorption.

However, the surface may contain inactive, i.e. poisoned, areas which are densely packed by asymmetric CO_{br} and CO_{ot} molecules. The spontaneous emergence of such high coverage CO domains is facilitated by the rather stringent condition for the adsorption of O_2 requiring two neighbouring 1f-cus Ru sites [125]. Furthermore, Ziff et al. showed by means of kinetic Monte Carlo simulations of the CO oxidation, that, depending on the composition of the feed gas, the catalyst's surface can either be fully poisoned by one of the reactants (CO or O) or, in a wide range of feed ratios around a stoichiometric CO/O_2 mixture, it can accommodate an active phase consisting mostly of large O-covered areas.

Aßmann et al. have shown in 2008, that both the pressure and material gaps could be bridged in the case of the CO oxidation over RuO_2 [76]. The microscopic reaction steps on RuO_2 were identified by a combined experimental and theoretical approach applying density functional theory. Steady-state CO oxidation and transient kinetic experiments such as temperature-programmed desorption were performed with polycrystalline catalysts and single-crystal surfaces and analysed on the basis of a microkinetic model. During their work, the most active and stable state of the powder catalyst was identified being an ultra thin RuO_2 shell coating a metallic Ru core.

This section concludes with a summary of the microscopic steps governing the CO oxidation over RuO_2 on the atomic scale [105]. Gas phase CO and O_2 encounter strongly binding adsorption sites on the $RuO_2(110)$ surface, in the form of the 1f-cus Ru atoms. For instance, CO adsorbs on stoichiometric $RuO_2(110)$ by -1.2 eV (over the 1f-cus Ru sites), while on the mildly reduced $RuO_2(110)$ surface the CO binding energy is -1.85 eV for the adsorption over 2f-cus Ru atoms. The RuO_2 surface provides active oxygen species to react with CO, i.e. O_{ot} and O_{br} atoms, respectively. The recombination of adsorbed CO with O_{br} creates vacancies [126], which are immediately filled with CO_{br} leading to a predominantly CO_{br} covered $RuO_2(110)$ surface [14]. At room temperature, oxygen molecules from the gas phase can efficiently dissociate on $RuO_2(110)$ via a molecular precursor state. This leads to weakly bound O atoms, which adsorb on top of the 1f-cus Ru atoms (O_{ot}). The CO oxidation reaction mainly takes place between CO_{ot} and O_{ot} species in terms of a Langmuir-Hinshelwood mechanism [14]. The $RuO_2(110)$ surface was shown to be active towards the CO oxidation and to be responsive to the feed gas stoichiometry. This dynamic behaviour was induced by the CO oxidation reaction itself taking place on the surface.

11.4 HCl Oxidation over RuO_2

Besides the oxidation of CO, the oxidation of HCl to Cl_2 is another, industrially relevant and applied reaction catalysed by RuO_2 and thus, will be reviewed in the context of chemical activity of RuO_2 based on the results of Seitsonen et al. [11]. Furthermore, the HCl oxidation put the focus on chlorinated $RuO_2(110)$ as a possible model system, which constitutes the main issue of this thesis.

In 2004, Sumitomo Chemical introduced a stable Deacon-like process for the oxidation of HCl by air over a RuO_2 based catalyst producing Cl_2 and water (Sumitomo process) [4]. For $RuO_2(110)$, which can be regarded as a proper model catalyst for the Sumitomo process, the stability of the RuO_2 catalyst was shown to be related to the selective replacement of O_{br} atoms by chlorine atoms. The chlorination process of $RuO_2(110)$ is self limiting in that chlorine incorporation terminates when all bridging O_{br} atoms are replaced [9]. In a recent publication

Zweidinger et al. showed that the kinetics of the HCl oxidation reaction over chlorinated RuO_2(110) is purely determined by surface thermodynamics, i.e. the adsorption energies of the reaction intermediates rather than by true kinetic barriers [10]. A very similar conclusion has been drawn by Lopez et al. in the case of RuO_2(110) powder catalyst under atmospheric reaction conditions [12]. The reaction mechanism of the HCl oxidation is summarised in figure 11.3. Dissociative adsorption of O_2 is non-activated, forming on top O (O_{ot}) on the 1f-cus Ru sites. HCl adsorbs on the 1f-cus Ru sites while transferring the H atom to the O_{ot} species. Without the presence of O_{ot}, HCl may not adsorb on the chlorinated RuO_2(110) surface. According to DFT calculations the dehydrogenation of HCl_{ot} via O_{ot} proceeds without any noticeable activation barrier [10]. The final production of adsorbed water (H_2O_{ot}) via H transfer [85, 127] between two neighbouring $O_{\mathrm{ot}}H$ groups is activated by 0.3 eV, an energy barrier that is easily surmounted at typical reaction temperatures. The recombination of two Cl_{ot} atoms to form the desired product Cl_2 constitutes the rate determining step with an activation barrier of 1.2 eV.

Since hydrogen cannot be accepted by the bridging Cl_{br} atoms (activation barrier is as high as 2.6 eV), an efficient communication between neighbouring 1f-cus Ru rows is suppressed. Therefore the chlorinated $RuO_{2-x}Cl_x$(110) catalyst was envisioned as a one-dimensional catalyst offering isolated rows of 1f-cus Ru sites where a Langmuir-Hinshelwood-type dehydrogenation reaction between HCl and O_2 takes place. As shown in figure 11.3 only the hydrogen transfer from adsorbed HCl to adsorbed OH is kinetically activated by 0.3 eV.

All the other activation barriers are determined by the adsorption/desorption energies of reaction intermediates such as water (on top) ($\Delta E_{\mathrm{act}} = 1.1$ eV) and Cl_{ot} ($\Delta E_{\mathrm{act}} = 1.2$ eV). Under typical reaction conditions in excess of oxygen and temperatures between 500 and 600 K, the chlorinated RuO_2(110) surface is mainly covered with Cl_{ot} and O_{ot} atoms. The released hydrogen is removed from the catalyst surface via water formation and subsequent desorption above 400 K (cf. figure 11.3). The remaining Cl_{ot} atoms on the surface have to diffuse along the 1f-cus Ru rows to meet a second Cl_{ot} to react with it. This diffusion process is activated by 0.65 eV (DFT) and is therefore not rate determining at reaction temperatures between 500 and 600 K.

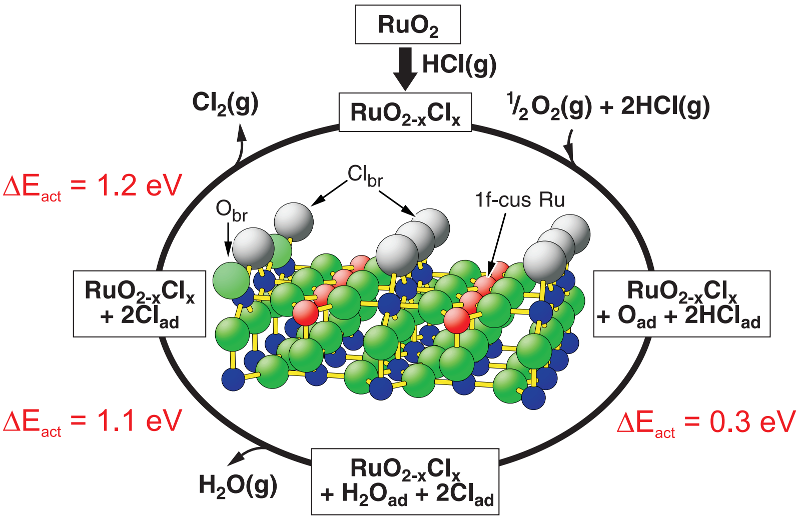
RuO2
HCl(g)
RuO2-xClx
Cl2(g)
½O2(g) + 2HCl(g)
ΔEact = 1.2 eV
Clbr
Obr
1f-cus Ru
RuO2-xClx + 2Clad
RuO2-xClx + Oad + 2HClad
ΔEact = 1.1 eV
ΔEact = 0.3 eV
H2O(g)
RuO2-xClx + H2Oad + 2Clad

Figure 11.3: The catalytic cycle of the HCl oxidation over $RuO_2(110)$, starting with a selective and self-limiting replacement of the bridging O atoms by bridging chlorine forming $RuO_{2-x}Cl_x(110)$. The reactant molecules O_2 and HCl both adsorb first on the 1f-cus Ru sites. O_2 dissociates to form adsorbed O and HCl dehydrogenates via a hydrogen transfer to form Cl and OH species in on top positions. H-transfer among the OH species leads to water formation which is released from the surface around 420 K. Neighbouring on top adsorbed Cl atoms recombine to form Cl_2 which is immediately liberated into the gas phase. The activation energies ΔE_{act} are determined by DFT calculations and are given in eV. The rate determining step is constituted of the association of two neighbouring Cl_{ot} atoms to form Cl_2. Figure modified from reference [11].

Part III

Chlorination of $RuO_2(110)$

Chapter 12

Chlorination Mechanism of RuO_2(110)

12.1 Introduction

The heterogeneous oxidation of HCl to Cl_2 and H_2O over RuO_2 (Sumitomo process, cf. chapter 11.4) leads to a, at least partial, surface selective chlorination and thereby stabilisation of the RuO_2 catalyst [9, 10, 12]. However, the actual chlorination mechanism of RuO_2 was up to now not well understood. In the following chapter density functional theory (DFT) calculations as well as high resolution core level shift spectroscopy (HRCLS) and temperature programmed desorption (TPD) experiments will be discussed, targeted to identify the microscopic details of the elementary reaction steps during the chlorination process of RuO_2(110) by HCl exposure. It will be shown that chlorine can only replace undercoordinated O atoms (O_{br}) when these oxygen atoms have been transformed into a better leaving group being either water or carbon dioxide. In the case of water formation this process is strongly facilitated by preadsorbed hydrogen for stoichiometry reasons. The chlorination of RuO_2 is surface selective. No formation of a bulk ruthenium chloride has been observed, neither by means of HRCLS nor by SXRD.

12.2 DFT Study: Proposal of a Reaction Mechanism

The discussion of the reaction mechanism of the hydrogen promoted chlorination of a $RuO_2(110)$ model surface will be initiated by proposing a mechanism based on density functional theory (DFT) calculations.

The crucial role of water formation in the chlorination mechanism is connected to the property of water being a good leaving group. During the chlorination of $RuO_2(110)$ or hydrogenated $RuO_2(110)$ by HCl, respectively water plays the role as a leaving group, as will be shown by DFT calculations in the following section.

Hydrogen chloride adsorbs dissociatively on stoichiometric $RuO_2(110)$ or hydrogenated $RuO_2(110)$ to form Cl_{ot} and O_{br}-H or O_{br}-H_2, respectively (cf. figure 12.1). Molecular HCl could not be stabilised while neighbouring either an O_{br} or O_{br}-H group. The acidic hydrogen of HCl is immediately transferred to the O_{br}-species, which is commonly referred to as dissociative adsorption. Adsorption energies with respect to HCl_{gas} are -1.83 eV for Cl_{ot} adjacent to O_{br}-H and -0.94 eV for Cl_{ot} adjacent to O_{br}-H_2. Furthermore, it is interesting to note that the adsorption of HCl_{ot} adjacent to a Cl_{br} atom is only slightly exothermic. The binding of HCl adsorbed on 1f-cus Ru adjacent to a Cl_{br} with a Ru-Cl_{ot}-H angle of 180° is by $+0.04$ eV endothermic whereas the bent HCl molecule binds with -0.56 eV, which should be only due to hydrogen bonding between H and Cl_{br}. This finding will be important in the discussion of the stability of chlorinated $RuO_2(110)$ against HCl exposure at elevated temperatures. But this is not in the scope of the present thesis and will be treated elsewhere [128].

The chlorination of the s-$RuO_2(110)$ surface proceeds via a ***two step process*** (see figure 12.1). The ***first step*** is the formation of a bridging water species O_{br}-H_2 as a good leaving group, which in turn may be formed via two different reaction mechanisms:

Mechanism A (figure 12.1 *ii*): If the stoichiometric oxide is exposed to H_2 at room temperature, the bridging oxygen atoms are selectively converted into O_{br}-H groups [85]. This O_{br}-H precovered surface is exposed to HCl, which adsorbs dissociatively to form immediately Cl_{ot} and O_{br}-H_2 without an activation barrier.

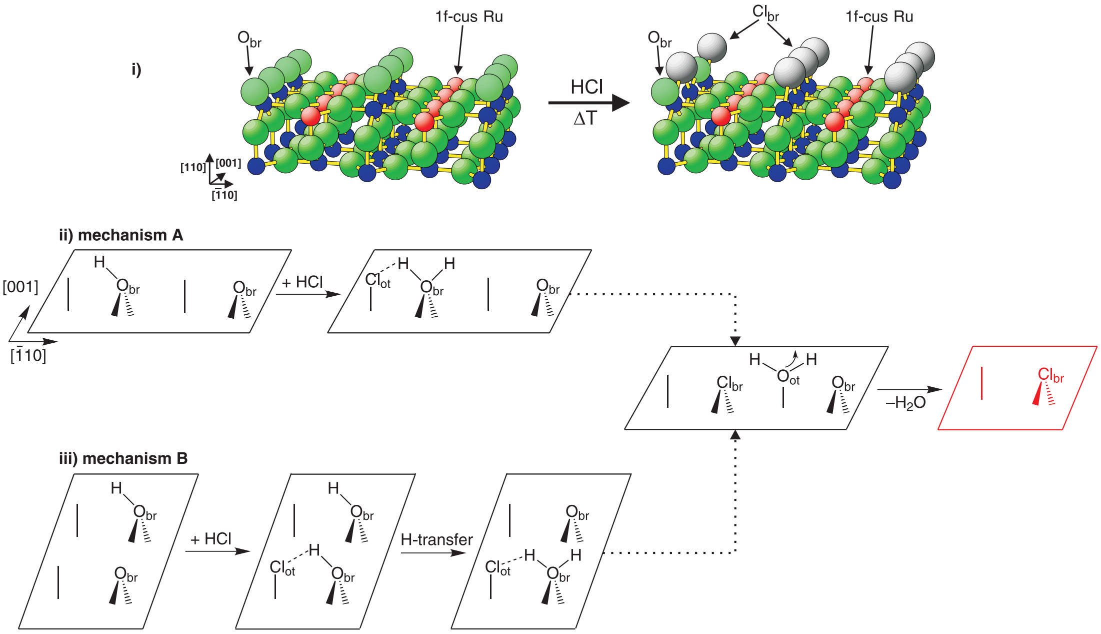
i)
O_br
1f-cus Ru
[110]
[001]
[1̄10]
HCl
ΔT
O_br
Cl_br
1f-cus Ru
ii) mechanism A
[001]
[1̄10]
H
O_br
O_br
+ HCl
Cl_ot
H
H
O_br
O_br
H
H
O_ot
Cl_br
O_br
–H2O
Cl_br
iii) mechanism B
H
O_br
O_br
+ HCl
H
O_br
Cl_ot
H
O_br
H-transfer
O_br
Cl_ot
H
H
O_br

Figure 12.1: Schematic representation of the chlorination mechanism of $RuO_2(110)$. *i)* Ball-and-stick model of bulk truncated $RuO_2(110)$ revealing undercoordinated surface atoms: bridging O atoms (O_{br}) and one fold coordinatively unsaturated Ru-sites (Ru 1f-cus), which are called on top sites. Upon HCl exposure at higher temperatures the stoichiometric surface transforms into a chlorinated surface where the bridging O atoms are replaced by bridging chlorine atoms (Cl_{br}) (shown in grey colour). *ii)* Simplified representation of $RuO_2(110)$: Solid upright lines refer to cus-sites and double wedges indicate bridge positions. **Mechanism A**: Bridging water O_{br}-H_2 is formed by hydrogen transfer from adsorbed HCl to an adjacent O_{br}-H group. *iii)* **Mechanism B** proceeds via the recombination of two neighbouring O_{br}-H groups to form water O_{br}-H_2. In the case of a deficit of available neighbouring O_{br}-H groups, a H-diffusion step along the O_{br} rows is necessary. The H-diffusion mediated O_{br}-H recombination, which is assisted by Cl_{ot}, is operating at higher temperatures. As soon as bridging water is formed, it shifts to a 1f-cus Ru site from which it desorbs immediately and leaves a vacancy V_{br}. The vacancies are in turn filled by diffusion of Cl_{ot} to form Cl_{br} (red structure).

Mechanism B (figure 12.1 *iii*): A second way to produce water is the recombination of two neighbouring O_{br}-H groups to form O_{br}-H_2 and a remaining O_{br} atom. This process is activated by only 1.1 eV irrespective of the presence of Cl_{ot} atoms adjacent to one of the O_{br}-H groups [73] and thus, may also occur at temperatures as low as $T = 400$ K.

However, if no neighbouring O_{br}-H groups are available, a H-diffusion step along the O_{br}-rows is required for the water formation by O_{br}-H + O_{br}-H recombination. The diffusion is highly activated in the case of s-RuO_2(110) by 2.5 eV as determined by means of DFT calculations [85] and thus, should only take place at temperatures in the region of the decomposition of the RuO_2(110) substrate. Since water formation by O_{br}-H recombination was observed at $T > 550$ K by means of TDS in this publication (cf. reference [83] as well), the calculated diffusion barrier for this process may be too high. The diffusion of H along the bridging rows is facilitated by Cl_{ot} atoms as suggested by means of TDS experiments. Thus, the recombination of O_{br}-H groups with an intermediate H-diffusion step along the bridging oxygen rows could account for the part of the chlorination taking place at temperatures of $T \approx 520$ K and under hydrogen deficient situations like the chlorination of s-RuO_2(110) by HCl alone without hydrogen pretreatment. Since the binding of HCl on the 1f-cus Ru sites of s-RuO_2(110) for $\theta(\mathrm{HCl}) = 1$ is thermodynamically less favourable by 0.43 eV compared to a smaller coverage of $\theta(\mathrm{HCl}) = 0.25$, the presence of two neighbouring O_{br}-H groups is unlikely. In this case Cl_{ot} promoted H-diffusion is the only path to the recombination of O_{br}-H groups to form water.

Once water is formed in a bridging position by either mechanism A or B, the ***second reaction step*** consists of the desorption of O_{br}-H_2 and the chlorination of the bridging position by Cl_{ot}:

The hydrogen-bound complex $Cl_{ot} \cdots$ H-O_{br}-H can release water via a shift of water from a bridging to an on top site, a process which is activated by 1.4 eV followed by a subsequent desorption of H_2O from the 1f-cus site ($E_{des} = +0.84$ eV). The direct desorption of water from the Cl_{ot} stabilised bridging position is thermodynamically unfavourable, the desorption energy with respect to water vapour being +2.1 eV. The relatively high activation energy of the water shift reaction of 1.4 eV is due to hydrogen bonding to the associated Cl_{ot} atom and can significantly be lowered to $E_{act} = 0.8$ eV by shifting the Cl_{ot} to the next 1f-cus

Ru site ($E_{act} = 0.9$ eV), thereby removing the hydrogen bond stabilisation of the bridging water. The reaction pathways tested for the water shift reaction, either with or without hydrogen bond mediated stabilisation of O_{br}-H_2, are compiled in figure 12.2. The pathway with the overall lowest activation barriers is highlighted in green. The removal of the hydrogen bond of Cl_{ot} to O_{br}-H_2 leads to a decrease of the activation barrier for the water shift. However, this effect should be also possible by tilting the Cl_{ot} away from the bridging water in order to reduce the hydrogen bond, either in cus-direction or towards the neighbouring O_{br}.

As soon as the bridging water has shifted to an on top position, the formation and thus the desorption of HCl as a competing reaction is hindered and the chlorination process proceeds.

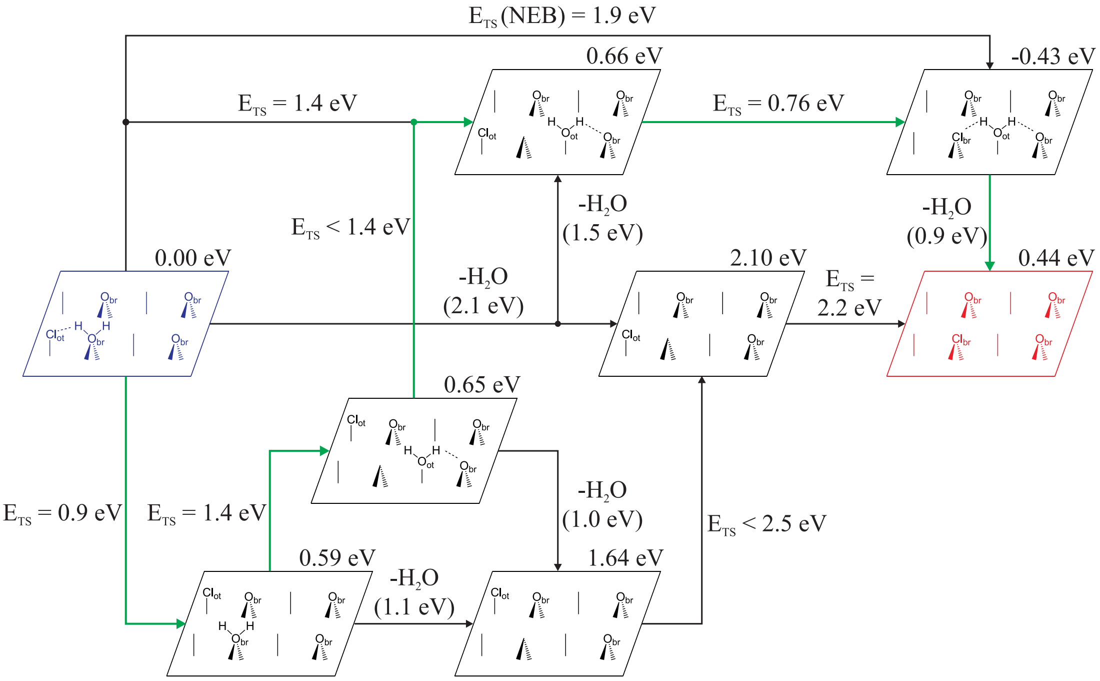

E$_{TS}$ (NEB) = 1.9 eV
0.66 eV
-0.43 eV
E$_{TS}$ = 1.4 eV
E$_{TS}$ = 0.76 eV
-H$_2$O (1.5 eV)
-H$_2$O (0.9 eV)
E$_{TS}$ < 1.4 eV
0.00 eV
-H$_2$O (2.1 eV)
2.10 eV
E$_{TS}$ = 2.2 eV
0.44 eV
0.65 eV
E$_{TS}$ = 0.9 eV
E$_{TS}$ = 1.4 eV
-H$_2$O (1.0 eV)
E$_{TS}$ < 2.5 eV
0.59 eV
-H$_2$O (1.1 eV)
1.64 eV
Cl$_{ot}$
O$_{br}$
O$_{ot}$
Cl$_{br}$
H

Figure 12.2: Different reaction pathways for the reaction Cl_{ot}+O_{br}-H_2 $\rightarrow$ Cl_{br}+O-H_2(gas). Energies are given in eV. All DFT calculations have been carried out on a $RuO_2(110)$-2x2 surface unit cell. The initial structure is drawn in blue, the final structure in red. The pathway with the lowest activation barriers is marked in green. The relative energies of the structures containing no adsorbed H_2O are corrected by $E(H_2O_{gas})$.

After desorption of water from the surface, the resulting bridging vacancy is filled by the diffusion of an adjacent Cl_{ot}, which is activated by only $E_a < 0.1$ eV. This step is the actual chlorination step and occurs instantaneously after the vacancy was formed. The intermediate structure (Cl_{ot} + V_{br} + O_{ot}-H_2) is not spectroscopically observable by means of XPS, due to the low activation barrier of the Cl diffusion.

A competing reaction to the chlorination of the bridging position is the so-called healing of the oxide [97]: the bridging vacancies can be filled by O(bulk) as well. The activation energy for O(bulk) + V_{br} → V(bulk) + O_{br} was determined to $E_a = 0.88$ eV [73]. However, the formation of a bulk oxygen vacancy (V(bulk)) is thermodynamically less favourable in comparison to a bridging vacancy by 0.4 eV (at least for s-RuO_2). Thus, the bridging vacancy V_{br} is preferably filled by a Cl_{ot} atom via diffusion.

In comparison to the above-mentioned processes, the activation energies for the concerted reactions, where Cl and O, OH, or H_2O shift simultaneously, have been estimated by nudged elastic band (NEB) calculations on a 2×2 surface unit cell of RuO_2(110):

- Cl_{ot} + O_{br} → Cl_{br} + O_{ot}, $E_a = 2.6$ eV
- Cl_{ot} + O_{br}-H → Cl_{br} + O_{ot}-H, $E_a = 3.1$ eV
- Cl_{ot} + O_{br}-H_2 → Cl_{br} + O_{ot}-H_2, $E_a = 1.9$ eV

These comparatively high activation energies suggest that the previously described two-step mechanism of the chlorination is more favourable than the concerted reactions.

The reaction energies as well as the activation energies of the processes taking place during chlorination of s-RuO_2 by HCl exposure are summarised in figure 12.3. Activation energy E_{act2} can be significantly lowered by removing the hydrogen bond stabilisation of the bridging water by shifting/tilting of the neighbouring Cl_{ot} atom, thereby disfavouring the desorption of HCl into the gas phase.

By means of DFT calculations, a mechanism for the hydrogen promoted chlorination of the stoichiometric RuO_2(110) surface by HCl exposure has been proposed, although the high activation energy for the H-diffusion step remains debatable. As will be shown in the following sections, HRCLS and TDS experiments confirm the chlorination mechanism suggested by the present DFT calculations.

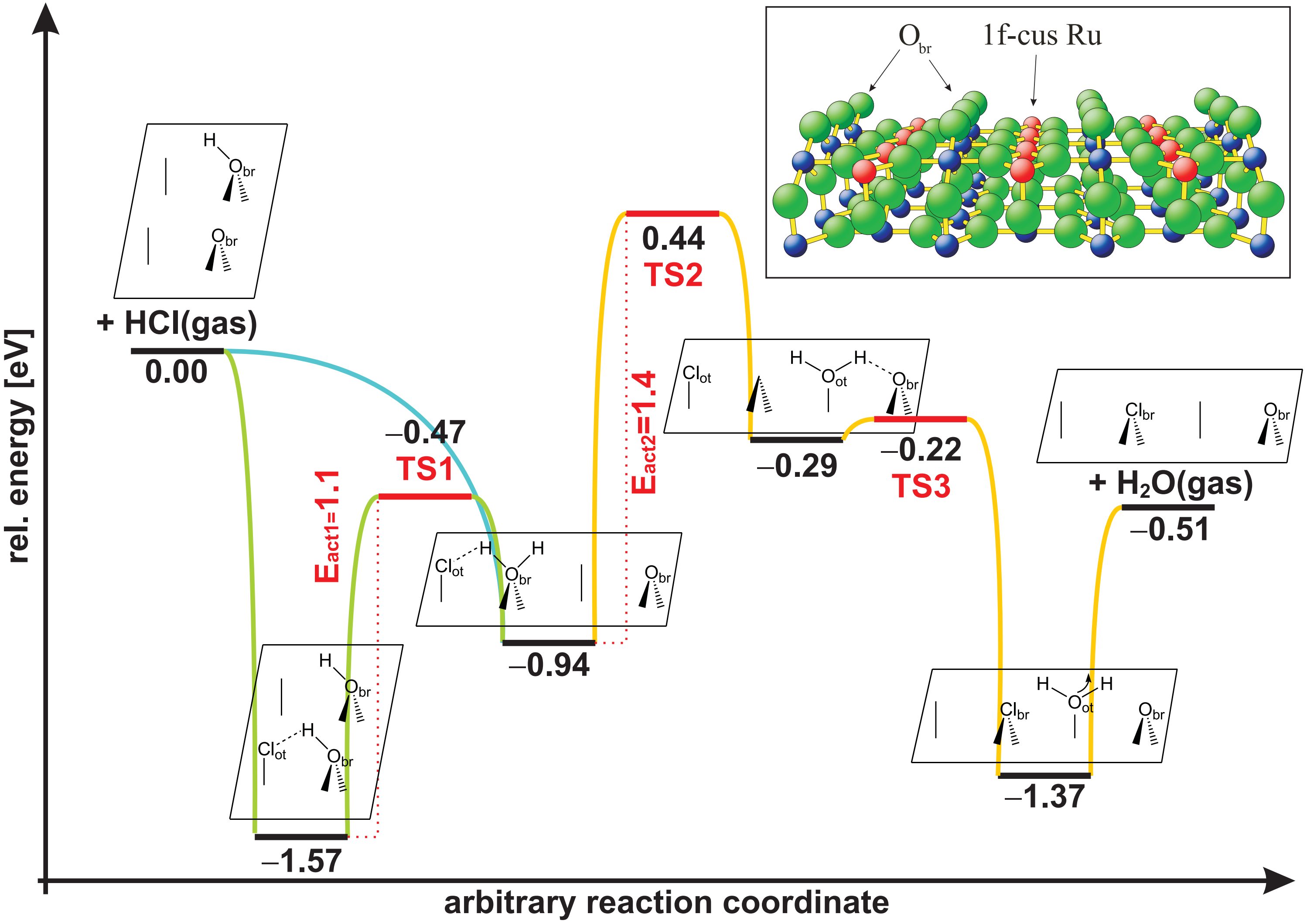
rel. energy [eV]
arbitrary reaction coordinate
O_{br}
1f-cus Ru
H
O_{br}
O_{br}
+ HCl(gas)
0.00
–0.47
TS1
E_{act1}=1.1
H
O_{br}
Cl_{ot}
H
O_{br}
–1.57
Cl_{ot}
H
H
O_{br}
O_{br}
–0.94
0.44
TS2
E_{act2}=1.4
Cl_{ot}
H
O_{ot}
H
O_{br}
–0.29
–0.22
TS3
Cl_{br}
O_{br}
+ H_2O(gas)
–0.51
H
O_{ot}
H
Cl_{br}
O_{br}
–1.37

Figure 12.3: Energy scheme of chlorination of RuO_2 by HCl exposure. Relative energies are given in eV. The blue lines correspond to mechanism A and the green lines to mechanism B, respectively. Structures connected by yellow lines denote the further reaction path which is identical for both mechanisms. The chlorine promoted H-diffusion step, that is necessary for the O_{br}-H recombination at lower O_{br}-H coverages taking place at higher temperatures, is not shown.

12.3 Chlorination of Hydrogen Pretreated RuO_2(110) by HCl

In the following, the stepwise chlorination of a hydrogen pre-exposed s-RuO_2(110) surface is investigated by high resolution core level shift spectroscopy (beamline I311, MAX-lab, Lund).

Stoichiometric RuO_2 was prepared following the standard procedure described in chapter 9.2. The quality of the oxide was checked by both LEED and HRCLS. An exposure of 15 L H_2 to s-RuO_2(110) at room temperature led to the selective formation of bridging hydroxyl (O_{br}-H) groups [85]. Subsequently, 5 L of HCl were dosed at T = 300 K followed by a stepwise thermal treatment: flash to T = 420 K, flash to T = 520 K and a 15 min annealing at T = 520 K. After each step, the surface was characterised by the Cl 2p and O 1s core level shift spectra indicated in figure 12.4. The assignment of the observed spectral features is based on the DFT calculated surface core level shifts summarised in table 12.1.

After dosing 5 L of HCl at T = 300 K a broad signal appeared in the O 1s spectrum in the water region at 532.5 eV (FWHM = 1.38 eV). In comparison with adsorbed on top water on s-RuO_2(110) [85] this water feature was shifted by +0.6 eV to higher binding energy. Together with DFT calculations (cf. table 12.1) this water signal was assigned to a bridging water species O_{br}-H_2.

The broad emissions at 197.5/199.1 eV in the Cl 2p spectrum at T = 300 K were ascribed to a Cl species adsorbed on a 1f-cus site (Cl_{ot}) and hydrogen bonded to ab adjacent water molecule sitting either in a bridging or in an on top position. Spin-orbit splitting causes the doublet structure with an energy separation of 1.60 eV. The peak at higher core level energy is assigned to Cl $2p_{1/2}$ and the one at lower energy to Cl $2p_{3/2}$. The intensity ratio amounts to Cl $2p_{1/2}$ vs. Cl $2p_{3/2}$ = 1:2. The large FWHM (0.79 eV) of these Cl_{ot} features is related to hydrogen bonding to the adsorbed water species. Upon flashing the surface to T = 420 K, the water signal vanishes and the Cl_{ot} features shifts to lower binding energies by 0.6 eV (196.9/198.5 eV) concomitant with a narrowing of the profiles. Simultaneously, an additional Cl doublet appears at 197.8/199.4 eV which DFT calculations assign to chlorine atoms in bridging positions (Cl_{br}). Chlorination of the bridging positions at temperatures as low as T = 420 K together with the identification of bridging water indicate that mechanism A can be operative

assignment	expt. BE [eV]	expt. shift [eV]	calc. shift [eV]	surface structure
O_{bulk}	529.2	reference	reference	
O_{br}	528.4	–0.8	–0.87[a]	(1x1) O_{br}
O_{br}-H	530.4	1.2	1.46[a]	(1x2) O_{br}-H + O_{br}
(1x1)-O, chemisorbed	529.8	0.6	0.5[a]	Ru(0001)-(1x1)-O
O_{ot}-H_2	531.9	2.7	2.96[a]	(1x2) 2O_{br} + O_{ot} + O_{ot}-H_2
O_{br}-H_2	532.5	3.3	4.06	(2x2) 3O_{br} + 1Cl_{ot}+ O_{br}-H_2
O_{br}-H, hydrogen-bound	529.8	0.6	0.72[a]	(1x2) O_{ot}-H + O_{br}-H
Cl_{ot}	196.9/198.5	–0.9	–1.46	(2x2) 4Cl_{br} + 1Cl_{ot}
Cl_{ot}, hydrogen-bound	197.5/199.1	–0.3	–0.31	(2x2) 3O_{br} + 1O_{br}-H_2 + 1Cl_{ot}
Cl_{br}	197.8/199.4	reference	reference	(1x1) Cl_{br}
Cl_{br} neighbouring Cl_{ot}	197.6/199.2	–0.2	–0.2	(2x2) 4Cl_{br} + 1Cl_{ot}
HCl_{ot}	n/a	n/a	1.7	(1x2) 2Cl_{br} + 1Cl_{ot}-H

Table 12.1: Experimentally observed core level energies of O 1s and Cl 2p and their shifts in comparison with DFT calculated shifts. Except from Ru(0001)-(1x1)-O, all other species reside on $RuO_2(110)$. For Cl 2p, the binding energies of both spin-orbit split doublets are given. [a] Data taken from [85].

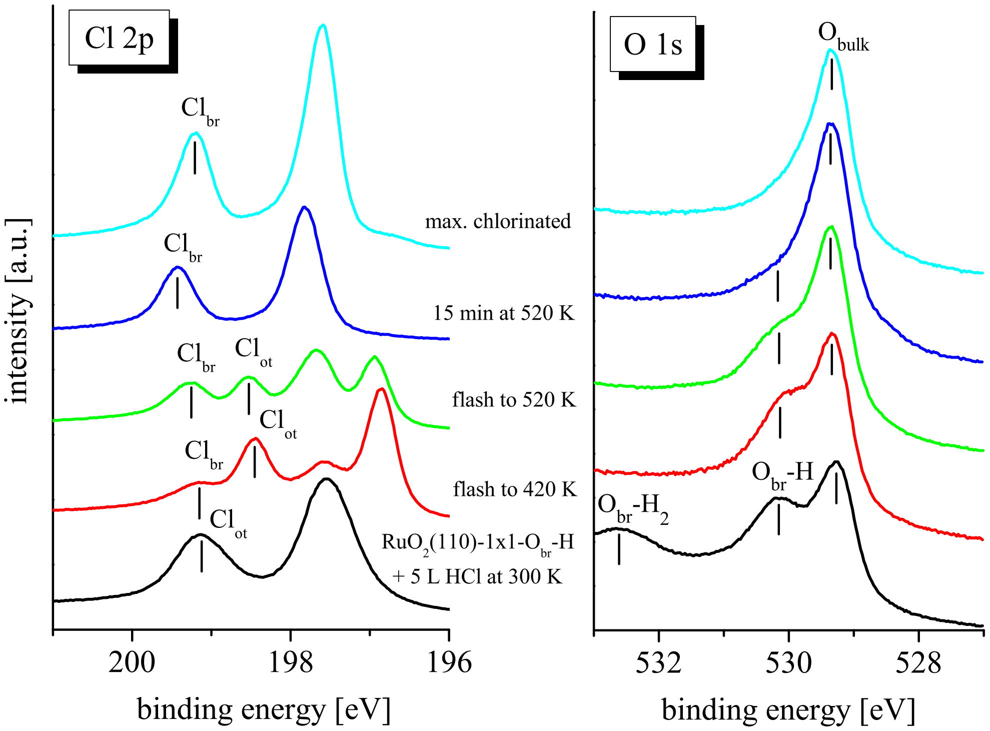

Figure 12.4: Cl 2p and O 1s HRCL spectra of hydrogen pre-treated RuO_2(110) exposed to 5 L HCl at T = 300 K, followed by stepwise annealing to specific temperatures as indicated. The observed doublets in the Cl 2p spectra, separated by 1.60 eV, are due to spin-orbit splitting. The uppermost spectra show the maximum chlorination after a further exposure to H_2 followed by annealing in HCl.

(figure 12.1 *ii*).

Flashing the surface to $T = 520$ K leads to a further increase of the Cl_{br} emissions and a decrease in the Cl_{ot} intensities. After 15 min of annealing at $T = 520$ K, a complete transformation of the signals assigned to Cl_{ot} into the signals corresponding to Cl_{br} is observed. The decrease of the Cl_{ot} signals can result either from transfer of Cl_{ot} into Cl_{br} or from the desorption of HCl, as will be shown later by means of TDS experiments. Chlorination at elevated temperatures ($T = 520$ K) is proposed to proceed via mechanism B together with H-diffusion along the O_{br} rows (cf. figure 12.1) accounting for bridging water formation. The level of chlorination after the described heating treatment was determined to be 60% of the maximum chlorination achieved after applying 4 L of HCl during slow heating from $T = 300$ K to $T = 700$ K. Notice that he maximum chlorinated surface contains a small amount of Cl_{ot} which led to a shift of the Cl_{br} emissions by −0.3 eV (cf. 12.4).

12.4 Chlorination of RuO_2(110) by HCl Exposure

To demonstrate the important role of hydrogen and thereby the formation of water as a leaving group in the chlorination mechanism, a further set of experiments was carried out where stepwise chlorination started from stoichiometric RuO_2(110) without previous hydrogen exposure. This situation will be compared with the chlorination of the O_{br}-H pre-covered surface by HCl exposure. The stoichiometric surface s-RuO_2(110) was exposed to 5 L HCl at $T = 300$ K followed by a stepwise thermal treatment: flash to $T = 420$ K, flash to $T = 520$ K and 15 min annealing at $T = 520$ K. The corresponding Cl 2p and O 1s spectra are depicted in figure 12.5.

After dosing 5 L of HCl, two broad features in the Cl 2p spectrum appear at 197.1/198.7 eV, which are attributed to hydrogen bound Cl_{ot} atoms (cf. table 12.1). The emission in the O 1s spectrum at 531.9 eV is attributed to on top water (O_{ot}-H_2) which has been introduced with HCl as an inevitable contaminant, very likely by an exchange reaction with the chamber walls. No O 1s emission related to O_{br}-H_2 is observed in the spectra consistent with the fact that O_{br}-H_2 formation is unlikely under the hydrogen deficient situation on the surface. Upon flashing the sample to $T = 420$ K, the broad O 1s water signal disappears due to

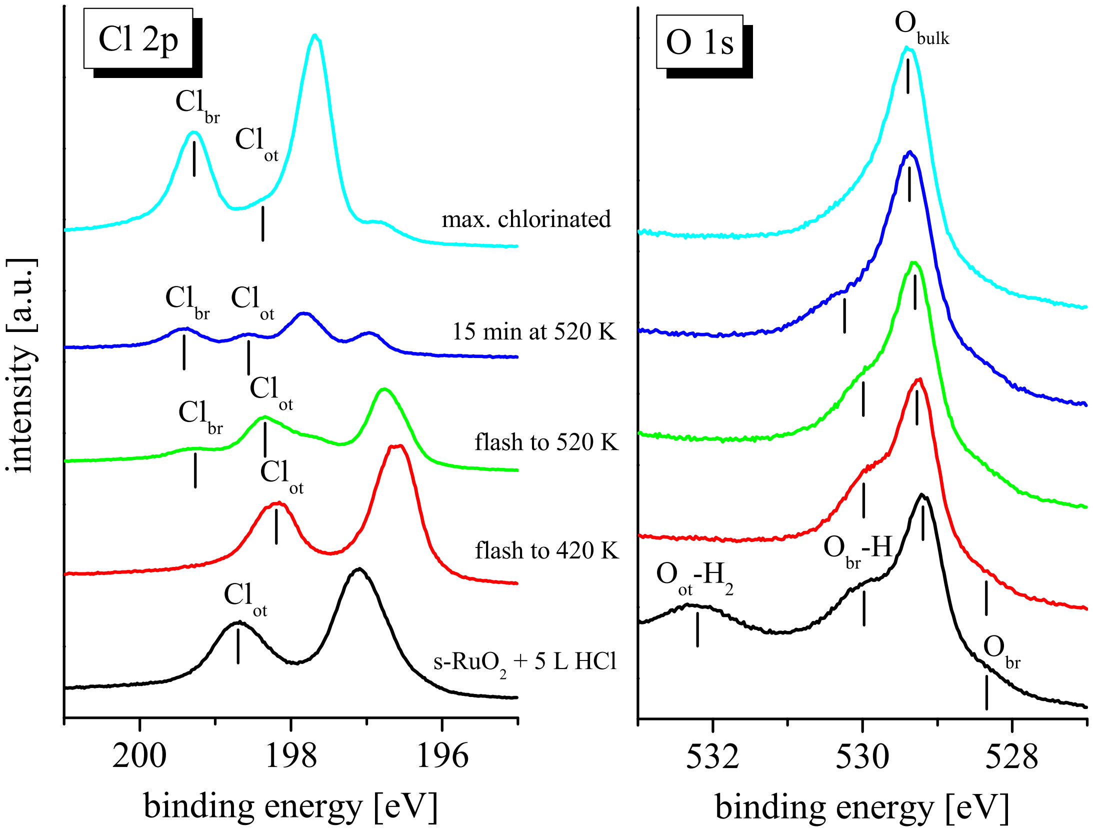

Figure 12.5: HRCL spectra of Cl 2p and O 1s of s-RuO_2(110) exposed to 5 L HCl at room temperature, followed by thermal annealing to T = 420 K, T = 520 K and 15 min annealing at T = 520 K. The uppermost spectra show the maximum chlorination after a further exposure to H_2 followed by annealing in HCl.

water desorption followed by a shift of the Cl_{ot} feature to lower binding energies (196.6/198.2 eV) and by a narrowing of the peak profile. Notice that no Cl_{br} related features in the Cl 2p spectrum are discernible, quite in contrast to the case of the hydrogen pre-covered RuO_2(110) surface, where an initial chlorination occured already at 420 K. This effect is caused by a lack of hydrogen atoms on the surface, which are a prerequisite for the transformation of the bridging O_{br} atoms into water as a leaving group.

Finally, further increase of the temperature (flash to $T = 520$ K, annealing 15 min at $T = 520$ K) led to the appearance of Cl_{br} emissions in the Cl 2p spectra at 197.7/199.3 eV. The formation of bridging water by the recombination of neighbouring O_{br}-H groups mediated by H-diffusion along the O_{br} rows is suggested by the continuous decline of the O_{br}-H signal (530.4 eV) in the O 1s spectra. However, a separate O_{br}-H_2 emission does not occur in the O 1s spectrum of figure 12.5, since the surface temperature of $T = 520$ K causes instantaneous desorption of water.

Direct evidence for water formation at $T = 520$ K is provided by the temperature programmed desorption spectrum (figure 12.6) which reveals a second chlorine modified water desorption feature, centered at $T = 530$ K. The set of HRCL spectra in figure 12.5 indicate that without H_2 pre-treatment, the chlorination process proceeds preferentially via H-diffusion mediated recombination of O_{br}-H groups (cf. figure 12.1) and the chlorination efficiency is substantially reduced in comparison with the hydrogen pre-covered RuO_2(110) surface. The level of chlorination after 15 min of annealing at $T = 520$ K was only 23% of the maximum achievable chlorination, i.e. 37% less than in the chlorination experiment with H_2 pre-treatment.

Preceding hydrogenation of s-RuO_2(110) results in a higher chlorination yield for stepwise chlorination for simple stoichiometry reasons:

$$O_{br}\text{-H} + \text{HCl} \rightarrow H_2O_{gas} + Cl_{br} \tag{12.1}$$

The chlorination of s-RuO_2(110) by dosing only HCl faces two problems: First, the deficiency of hydrogen and therewith a lack of neighbouring O_{br}-H groups on the surface and second, a blockade of the 1f-cus Ru sites by the excess Cl_{ot} atoms:

$$2O_{br} + 2HCl \rightarrow O_{br} + H_2O_{gas} + Cl_{br} + Cl_{ot} \qquad (12.2)$$

The high degree of chlorination in the case of the hydrogenated surface after 15 min of annealing at $T = 520$ K is manifested in the complete disappearance of the Cl_{ot} signal in the Cl 2p HRCL spectra accompanied by no noticeable loss of Cl_{ot} by HCl desorption (cf. figure 12.4). Contrarily, in the case of s-RuO_2(110) a significant amount of HCl desorbs and furthermore, a residual amount of Cl_{ot} remains on the surface even after 15 min heating at $T = 520$ K as indicated by HRCLS. Therefore, the measurements demonstrate clearly that a more efficient chlorination of RuO_2(110) can be accomplished by pretreating the stoichiometric oxide with molecular hydrogen to produce a O_{br}-H covered surface first and then dosing HCl at elevated temperatures to accomplish maximum chlorination.

In figure 12.6 the thermal desorption spectra of water and hydrogen chloride from the hydrogenated RuO_2(110) surface are compared with those of the hydrogenated RuO_2(110) surface which was exposed to molecular chlorine. With this TDS experiment, the influence of on top chlorine on the water formation by recombination of neighbouring O_{br}-H species was studied. Without chlorine on the surface, two desorption features were discernible. The water desorption at $T = 420$ K is assigned to water from the recombination of two neighbouring O_{br}-H groups[1], while the feature at $T = 625$ K is assigned to water formation due to the H-diffusion mediated recombination of O_{br}-H species.

In the case where the hydrogenated RuO_2(110) surface was exposed to 5 L of Cl_2 at room temperature, the high temperature water peak disappears and a shoulder at $T = 530$ K appears instead, concomitant with desorption of HCl (figure 12.6, right). Since still most of the produced water is originating from the recombination of neighbouring O_{br}-H species, this experiment indicated nicely the promoting action of Cl_{ot} on the H-diffusion process and thereby on the water formation.

---

[1] Moreover, O_{ot}-H_2 might be present as well, as a contaminant from the residual gas and contributed to the desorption at $T = 420$ K.

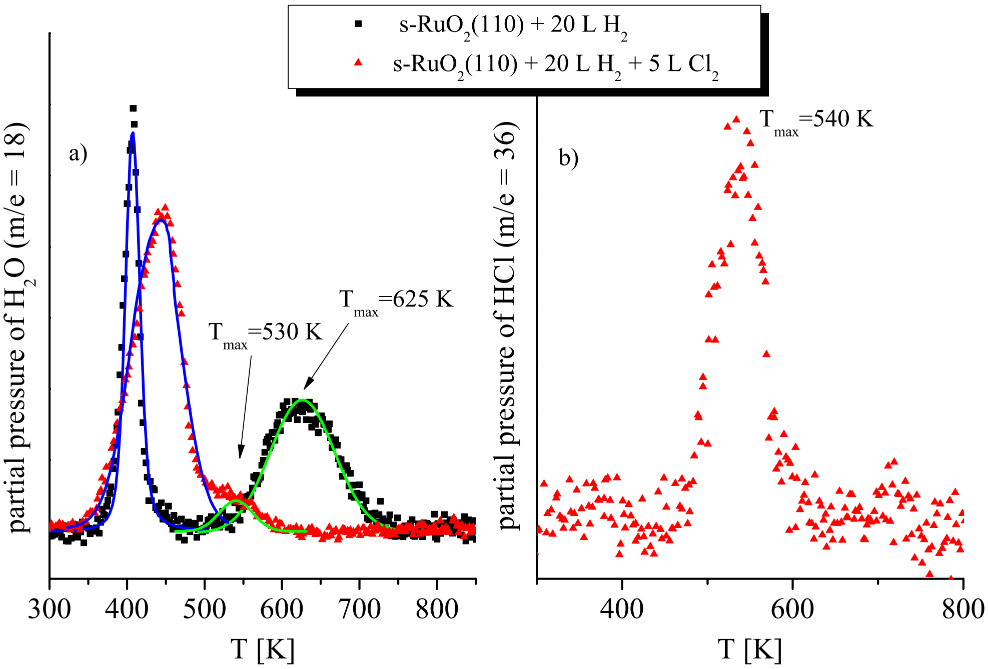

Figure 12.6: Temperature programmed H_2O and HCl desorption spectra from a hydrogen pre-exposed $RuO_2(110)$ surface (20 L H_2 at $T = 300$ K) without (black data points) and with (red data points) the presence of Cl_{ot} (5 L Cl_2 at $T = 300$ K). The recombination of two O_{br}-H groups on the chlorine-free oxide happens at $T_{max} = 625$ K (green curve). This H_2O desorption feature shifts to $T_{max} = 530$ K upon exposure of the surface to Cl_2, indicating that Cl_{ot} promotes the water formation. The desorption maxima centered at $T = 410$ and 440 K are assigned to the desorption of O_{ot}-H_2 (blue line shapes).

12.5 Chlorination of CO Pre-reduced RuO_2(110) by Cl_2

The importance of hydrogen in the actual chlorination mechanism, i.e. the transformation of bridging oxygen atoms into water as a leaving group, is further corroborated by the successful CO mediated chlorination of s-RuO_2(110) by molecular chlorine. Carbon monoxide reacts with bridging O_{br} atoms to CO_2 as a further possible leaving group besides water. All experiments were carried out at beamline I311 at MAX-lab in Lund by S. Zweidinger and M. Knapp.

Starting from the stoichiometric RuO_2(110) surface, which exhibited no chlorine peaks in the Cl 2p HRCLS spectra, this surface was exposed to 10 L of Cl_2 at a temperature of $T = 500$ K. The corresponding spectra are displayed in figure 12.7. After dosing Cl_2 one can distinguish two sets of Cl 2p peaks. One doublet is assigned to Cl_{ot} (196.0/197.6 eV) and the other doublet at 197.5/199.1 eV is due to small amounts of Cl_{br}, whereas the Cl $2p_{1/2}$ of Cl_{ot} and the Cl $2p_{3/2}$ of Cl_{br} overlap. A flash to $T = 600$ K led to desorption of Cl_{ot} indicated by the intensity loss of the doublet assigned to Cl_{ot} by 55%, the Cl_{br} signals doubled in intensity. Flashing to $T = 700$ K caused the complete desorption of Cl_{ot} and only the Cl_{br} features remained visible in the Cl 2p HRCL spectrum at 197.8/199.4 eV, unchanged in intensity as compared to the flash before. This small amount of bridge chlorination after dosing molecular chlorine should be only due to residual gas effects (CO and H_2) and therefore, should be negligible. Hence, no significant chlorination occurred by applying Cl_2 alone.

The relevance of the transformation of O_{br} into a good leaving group on stoichiometric RuO_2(110) for the chlorination was substantiated by the possibility to chlorinate s-RuO_2(110) by molecular chlorine *after* a preceding reduction by carbon monoxide.

Treating stoichiometric RuO_2(110) with CO at $T = 420$ K leads to the formation CO_2(gas) and bridging CO_{br} molecules on the surface [14]. These bridging CO_{br} molecules can be substituted by Cl atoms to form Cl_{br} under the present conditions:

$$CO_{br} + Cl_{ot} \rightarrow CO_{gas} + Cl_{br}. \tag{12.3}$$

Again, high resolution core level shift spectroscopy was used to confirm this hypothesis. Figure 12.7 reveals chlorination of the bridging sites upon treatment of

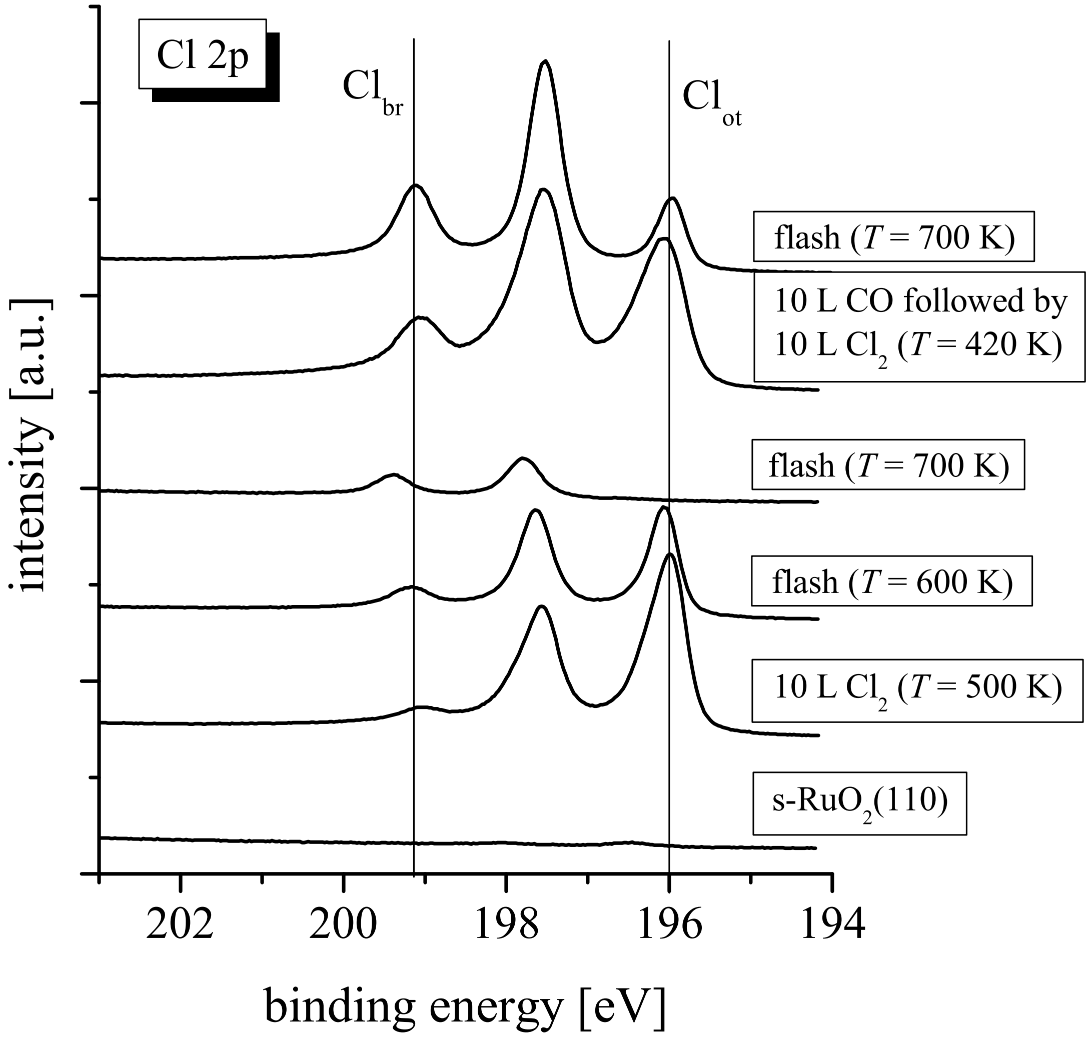

Figure 12.7: Comparison of the Cl 2p HRCLS spectra of $RuO_2(110)$ after exposure to 10 L Cl_2 alone and to 10 L CO followed by 10 L Cl_2, respectively.

s-RuO_2(110) by carbon monoxide followed by Cl_2 at $T = 420$ K.

After the Cl_2 exposure/annealing steps described above, the surface was subsequently exposed to 10 L CO and 10 L Cl_2 at a temperature of $T = 420$ K. The HRCLS spectrum taken after this step revealed three times larger Cl_{br} signals, indicating that the chlorination of the bridging positions is facilitated by treatment of the surface with CO in advance. Heating the sample to $T = 700$ K led again to partial desorption of Cl_{ot} (albeit not completely), and a further increase of the Cl_{br} signature. The observed HRCLS shifts were assigned by use of the DFT calculated values shown in table 12.1 and are in good agreement with them.

Although a chlorination of s-RuO_2 by applying CO followed by Cl_2 is possible, the chlorination efficiency of the H_2/HCl method, described in section 9.3 is significantly higher and was therefore adopted as the standard (re-)chlorination procedure.

Chapter 13

Determination of the Degree of Chlorination

13.1 The $(\sqrt{3} \times \sqrt{3})$R30°-Cl-Ru(0001) Phase

In order to calibrate the Auger spectra for chlorine, the spectrum of a well defined, chlorine containing structure - namely the $(\sqrt{3}\times\sqrt{3})$R30°-Cl-Ru(0001) phase with a chlorine coverage $\theta_{Cl} = \frac{1}{3}$ - has been measured [129].

The phase was prepared in the LEED chamber after a recipe of Zweidinger et al. [130]:

The thoroughly cleaned Ru(0001) crystal (Ar$^+$-sputtering: $p(\mathrm{Ar}) = 2 \times 10^{-6}$ mbar, $I_{em} = 20$ mA, $E = 1$ keV, $t = 20$ min, $T = 640$ K, flash to $T = 1050$ K) was cooled to $T = 200$ K. Subsequently, 1×10^{-8} mbar Cl_2 were introduced to the chamber. The chlorine uptake was monitored by the intensity of the LEED reflexes ($E = 75$ eV) of the $(\sqrt{3} \times \sqrt{3})$R30°-Cl-Ru(0001) overlayer. The LEED pattern of the clean Ru(0001) surface and the $(\sqrt{3} \times \sqrt{3})$R30°-Cl-Ru(0001) overlayer after saturation of the corresponding $I(t)$-curve are shown in figure 13.1. The dosage of Cl_2 was stopped when the intensity of the LEED reflexes, labelled in figure 13.1, reached the maximum.

The Auger spectrum of the $(\sqrt{3} \times \sqrt{3})$R30°-Cl-Ru(0001) phase was measured directly after the preparation of the phase at $T < 200$ K without heating to avoid a deflection of the Auger electrons by the magnetic field caused by the direct heating current, which is in the range of 10-30 A.

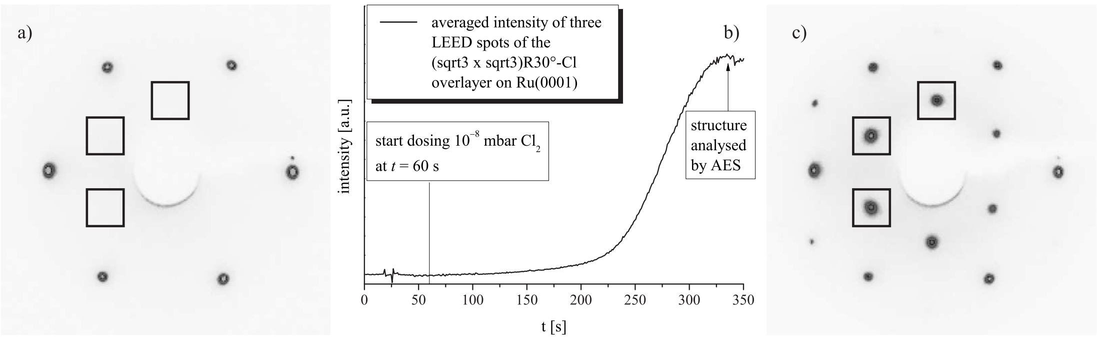

Figure 13.1: LEED pattern of *a)* pristine Ru(0001) before dosing Cl_2 and *c)* after dosing Cl_2 at $T = 200$ K, taken at $E = 75$ eV. The corresponding LEED-$I(t)$-curve *b)* connects the two LEED pattern. The structure shown in *c)* was then analysed by means of Auger electron spectroscopy in order to determine the chlorine signal from the saturated $(\sqrt{3} \times \sqrt{3})$R30 °-Cl-Ru(0001) phase.

Figure 13.2 presents the Auger electron spectra of two independently prepared $(\sqrt{3} \times \sqrt{3})$R30°-Cl-Ru(0001) phases. The comparison of both spectra, i.e. of the intensities of the Ru_{MNN} signals at 273 eV and the Cl_{LMM} signals at 181 eV shows a reproducibility of approximately 10%.

The $(\sqrt{3} \times \sqrt{3})$R30°-Cl-Ru(0001) ($\theta_{Cl} = \frac{1}{3}$) contains $\frac{1}{3}$ Cl atom per Ru(0001) surface unit cell ($A = 6.36$ Å^2) (cf. figure 13.3, left) as determined by a quantitative LEED analysis [130]. Thus, the surface concentration of chlorine amounts to σ_{Cl}(Ru)= 0.052 Cl atoms/Å^2.

RuO_2(110) bears two possible adsorption sites for Cl atoms: on top and bridging positions. Thus, RuO_2(110) is able to accommodate a maximum of two Cl atoms per surface unit cell ($A = 19.91$ Å^2). For $\theta_{Cl} = 1$, the surface concentration is $\sigma_{Cl}(RuO_2) = 0.050$ Cl atoms/Å^2 and for $\theta_{Cl} = 2$, $\sigma_{Cl}(RuO_2) = 0.10$ Cl atoms/Å^2.

Since the surface concentrations of the $(\sqrt{3} \times \sqrt{3})$R30°-Cl-Ru(0001) ($\theta_{Cl} = \frac{1}{3}$) phase and RuO_2(110), bearing one Cl atom per surface unit cell are very similar, the Cl_{LMM} Auger signals can be related vice versa assuming a calibration factor of $\frac{\sigma_{Cl}(Ru)}{\sigma_{Cl}(RuO_2)} = 1.04$.

The chlorine content on RuO_2(110) can now be determined, based on the calibration of the Auger Cl_{LMM} signal using the $(\sqrt{3} \times \sqrt{3})$R30°-Cl-Ru(0001) ($\theta_{Cl} = \frac{1}{3}$) phase.

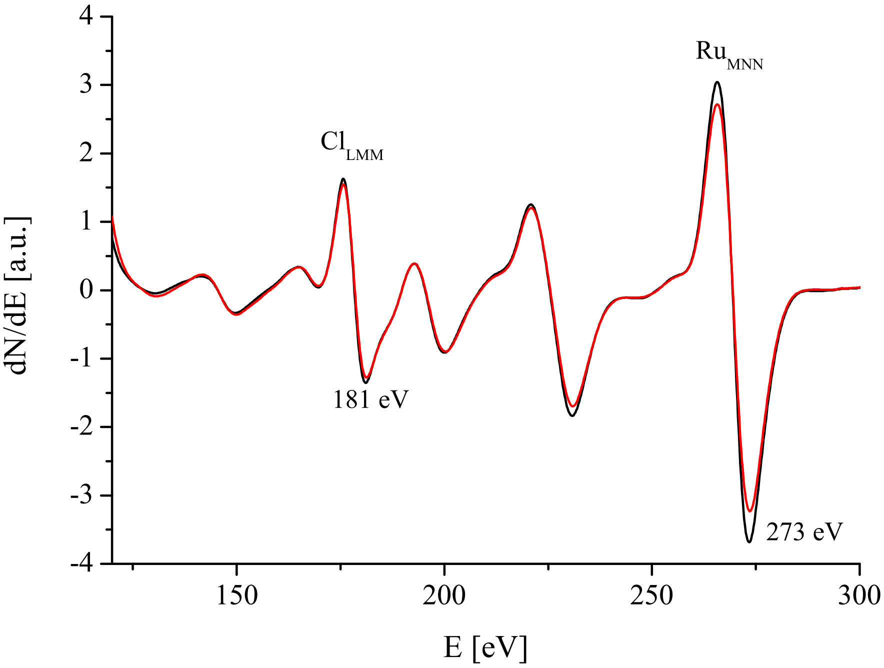

Figure 13.2: Auger electron spectra ($E = 3$ keV) of two independently prepared $(\sqrt{3} \times \sqrt{3})$-R 30°-Cl-Ru(0001) phases. The comparison of the intensity of the Ru$_{MNN}$ signals at 273 eV and the Cl$_{LMM}$ signals at 181 eV shows the reproducibility of the preparation of the Cl phase on Ru(0001) within 10%.

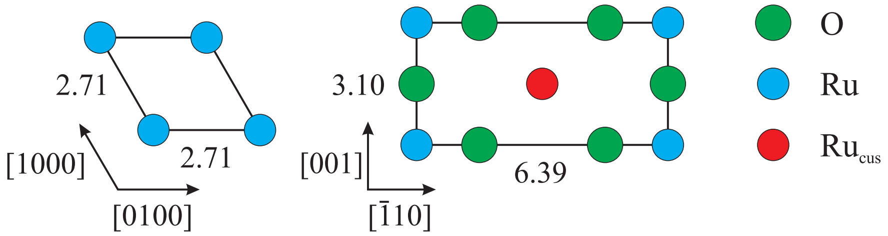

Figure 13.3: Surface unit cells of Ru(0001) and RuO_2(110) [36]. Unit vectors are given in Å

13.2 Chlorine Content on $RuO_{2-x}Cl_x(110)$

How much chlorine does a 'fully' chlorinated RuO_2 contain?

In order to determine the highest possible chlorine uptake of a stoichiometric oxide, Auger spectra of freshly chlorinated and rechlorinated ruthenium dioxides have been recorded. Chlorinated $RuO_2(110)$ was prepared and rechlorinated following the standard procedure, (cf. chapter 9.3). Auger spectra have been taken at room temperature *a)* directly after the chlorination step (flash to $T = 700$ K in $p(\mathrm{HCl}) = 5 \times 10^{-8}$ mbar), *b)* after a flash to $T = 550$ K, and *c)* after a further flash to $T = 700$ K (figure 13.4).

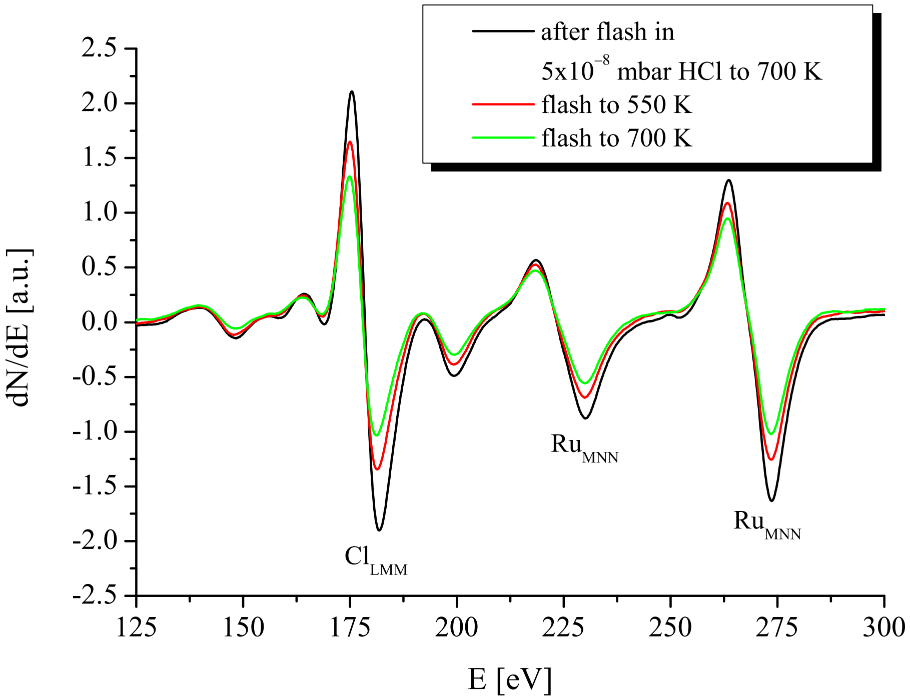

Figure 13.4: Auger electron spectra ($E = 3$ keV) of rechlorinated $RuO_2(110)$ directly after the flash in $p(\mathrm{HCl}) = 5 \times 10^{-8}$ mbar (black), after a flash to $T = 550$ K (red) and to $T = 700$ K (green).

The Auger spectra measured directly after the chlorination step contain HCl_{ot}, Cl_{ot}, and chlorinated bridges Cl_{br}. Hence, they reveal the largest Cl_{LMM} Auger signal as a composition of the three above-mentioned chlorine species.

Since the desorption temperature of HCl_{ot} is as high as $T = 520$ K [9], HCl_{ot}

should desorb during a flash of the sample to $T = 550$ K. The Cl_{LMM} intensity dropped by the amount of HCl_{ot} molecules, which desorbed thermally. The difference of the Cl_{LMM} signals in the Auger spectrum taken directly after the chlorination/rechlorination and the spectrum after a flash to $T = 550$ K can therefore serve as an estimation for the amount of HCl_{ot} adsorbed on the surface after the chlorination.

Flashing the specimen to $T = 700$ K leads to recombinative desorption of Cl_{ot} species [10]. Thus, the 1f-cus Ru sites should be unoccupied and remaining Cl atoms should be found only in bridging positions. The amount of Cl_{ot} atoms on the surface is accessible via the difference of the Cl_{LMM} intensities of the Auger spectra, after flashing the sample to $T = 550$ K and $T = 700$ K.

Table 13.1 shows the evaluated surface concentrations σ' [number of atoms/molecules per surface unit cell of $RuO_2(110)$] of HCl_{ot}, Cl_{ot}, and Cl_{br} on $RuO_2(110)$ after chlorination and two rechlorination procedures of the same stoichiometric $RuO_2(110)$ surface. The evaluation of the surface concentrations was enabled by the calibration described in chapter 13.1.

stage	$I_{Cl,300K}$ / σ'_{Cl}	$I_{Cl,550K}$ / σ'_{Cl}	$I_{Cl,700K}$ / σ'_{Cl}	σ'_{HCl}	$\sigma'_{Cl_{ot}}$
chlorination	2.71 / 0.94	1.91 / 0.66	1.74 / 0.61	0.28	0.05
1^{st} rechlor.	4.01 / 1.39	3.00 / 1.04	2.36 / 0.82	0.35	0.22
2^{nd} rechlor.	3.62 / 1.26	3.41 / 1.19	2.23 / 0.76	0.07	0.43

Table 13.1: Chlorine contents on $RuO_{2-x}Cl_x(110)$ after the initial chlorination (20 L H_2 at $T = 300$ K followed by an annealing step to $T = 700$ K in $p(HCl) = 5\times10^{-8}$ mbar) and two subsequent rechlorination steps under the same conditions. I_{Cl} in arbitrary units corresponds to the peak to peak difference of the Cl_{LMM} peak in the Auger spectra at $E = 181$ eV. The unit of σ' is # of atoms/molecules per surface unit cell of $RuO_2(110)$. σ'_{HCl} was obtained as the difference in σ'_{Cl} between the Auger spectra taken at $T = 300$ K and after a flash to $T = 550$ K. The surface concentration of Cl_{ot} atoms $\sigma'_{Cl_{ot}}$ was given by the difference of $\sigma'_{Cl}(550\text{ K})$ and $\sigma'_{Cl}(700\text{ K})$. The relative error of the determination of the surface concentrations of Cl σ'_{Cl} was estimated to be ±10%.

The first chlorination of the pristine, stoichiometric RuO_2 did not lead to the maximum achievable chlorination. Flashing to $T = 700$ K led to a bridging chlorination of only 60 % ($\sigma'_{Cl} = 0.6$). This value could be increased to 80 % ($\sigma'_{Cl} = 0.8$) by two further chlorination steps, i.e. the maximally chlorinated $RuO_2(110)$ contains 80 % Cl_{br} and 20 % O_{br} in the bridging rows. DFT calculations suggest, that full chlorination (100 % bridge chlorination) is thermodynamically unfavourable by 0.37 eV with respect to 50 % bridge chlorination. Therefore, the maximally chlorinated $RuO_2(110)$ (80 % bridge chlorination) does not bear the most stable bridging configuration.

During the first chlorination step, the biggest amount of adsorbed Cl atoms moved into bridging positions, which is reflected by the small number of desorbing Cl atoms during the flash of the sample to $T = 700$ K, since the bridging rows were occupied by only O_{br} atoms before. With increasing number of chlorine bridges, the amount of residual Cl_{ot} increased, because a further chlorination of the bridging positions was blocked due to a higher chlorine content and thereby repulsion (cf. table 13.1).

13.2.1 Determination of the Sum Formula of Chlorinated RuO_2

Merely as an estimation, the value of 'x' in the formula of chlorinated ruthenium dioxide $RuO_{2-x}Cl_x(110)$ will be determined in the following paragraph. He et al. described the thickness of $RuO_2(110)$ to be approximately 1.6 nm, corresponding to five layers of $RuO_2(110)$ epitaxially grown on Ru(0001) [36]. The thickness is mostly related to the preparation temperature. Furthermore, the oxide growth was found to be self-limiting, i.e. no progression of the oxidation through the whole bulk crystal has been observed by means of SXRD. Assuming a thickness of RuO_2 of five layers and 100 % chlorinated bridging rows while the 1f-cus Ru sites stay unoccupied, the absolute upper maximum value of 'x' equals 0.1, i.e. the sum formula of fully chlorinated ruthenium dioxide is $\mathbf{RuO_{1.9}Cl_{0.1}}$. However, the idealised value of $x = 0.1$ can not be reached, as shown in the preceding section, since the maximum achievable amount of bridging chlorination has been observed to be approximately 80 %. Thus, the experimental values for 'x' should be within the range of $0.04 \leq x \leq 0.08$ for stable and 'over'-chlorinated RuO_2 surfaces.

13.3 Summary: Chlorination of $RuO_2(110)$

During the last two chapters, a profound knowledge about the chlorination mechanism of RuO_2, i.e. the introduction of a stable bridging chlorine species, has been gained, mainly by means of high resolution core level shift spectroscopy, Auger electron spectroscopy and DFT calculations. The combination of theory and experiment has been a very useful tool in the elucidation of the chlorination mechanism. The chlorination process involves the formation of bridging water as a good leaving group and subsequently formation of bridging vacancies, which were in turn filled by diffusion of Cl_{ot} atoms. Although the existence of the bridging vacancies as intermediates could not be proven experimentally, they are essential for the chlorination process, since a concerted bridging chlorination reaction could not be confirmed by nudged elastic band calculations.

The chlorination mechanism under hydrogen deficient conditions (mechanism B) is a possible candidate to explain the observed chlorination of the RuO_2 catalyst in the Sumitomo process - the oxidation of HCl by oxygen [9]. Presumably, the stability of the catalyst during the oxidation reaction is due to an endothermic adsorption of HCl adjacent to a bridging Cl_{br} atom.

The maximum degree of chlorination was determined to be 80% by means of Auger electron spectroscopy. The Cl_{LMM} signal was calibrated against a reference measurement of a well-defined Cl phase on Ru(0001), which has been structurally determined by LEED - namely the $(\sqrt{3}\times\sqrt{3})$-R 30°-Cl-Ru(0001) ($\theta_{Cl} = \frac{1}{3}$) phase.

DFT caculations suggest that a fully bridge chlorinated surface is thermodynamically not stable in comparison to a half-chlorinated RuO_2 surface by 0.37 eV.

The understanding of the mechanisms which account for the selective substitution of bridging O_{br} atoms by Cl is the first, very important step for a correct interpretation of the dynamical beahviour of the chlorine atoms accommodated on $RuO_{2-x}Cl_x(110)$ in the next part of the present thesis.

Part IV

Structural Dynamics of Chlorinated RuO_2

Chapter 14

Interaction of CO with $RuO_{2-x}Cl_x(110)$

The second main part of the present work is intended to gain more insight into the dynamic processes taking place on the surface of a chlorinated $RuO_2(110)$ model catalyst.

Recently, Farkas et al. have nicely demonstrated the application of CO as a probe molecule to investigate the properties of a stoichiometric $RuO_2(110)$ model catalyst towards CO oxidation by means of reflection absorption infrared spectroscopy (RAIRS) [13, 14]. The goal of this chapter is to establish CO as a probe molecule to study the influence of Cl atoms on the stability and reactivity of the $RuO_2(110)$ surface with respect to CO oxidation.

14.1 CO Adsorption on $RuO_{2-x}Cl_x(110)$

Reflection absorption infrared spectroscopy (RAIRS) and high resolution core level shift spectroscopy (HRCLS) have been applied to study the adsorption behaviour of carbon monoxide molecules on chlorinated ruthenium dioxide at low temperatures under UHV conditions. The aim of these experiments was the characterisation of the vibrational properties of CO adsorbed on $RuO_{2-x}Cl_x(110)$, the characterisation of the influence of Cl atoms on the 1f-cus Ru adsorption sites and the comparison of these results with those of stoichiometric, not chlorinated $RuO_2(110)$. After this study, it should be possible to utilise CO as a probe molecule to characterise the chlorinated ruthenium dioxide surface just as well as s-RuO_2(110) [13].

The chlorinated $RuO_{2-x}Cl_x$(110) surface is terminated by O_{br} and Cl_{br} species in the bridging positions, while the 1f-cus Ru sites are accessible for CO adsorption from the gas phase. Depending on the thermal pretreatment of the sample one can find Cl_{ot} atoms as well, which are also able to influence the CO adsorption on the 1f-cus Ru sites.

14.1.1 HRCLS Study: CO Adsorption on $RuO_{2-x}Cl_x$(110)

The influence of CO adsorption on $RuO_{2-x}Cl_x$(110) and its thermal desorption from this surface have been investigated by means of high resolution core level shift spectroscopy. $RuO_{2-x}Cl_x$(110) was prepared after the standard procedure (cf. chapter 9.3) and was subsequently flashed to $T = 700$ K to desorb the excess of Cl_{ot} atoms. The sample was cooled and a XP spectrum was taken. Afterwards, 10 L CO were dosed at $T = 200$ K and another XP spectrum was taken. Finally, CO was desorbed by a annealing to $T = 450$ K and the resulting surface was again cooled and a XP spectrum was recorded. Figure 14.1 shows the corresponding Cl 2p and O 1s HRCL spectra.

The doublets at 199.3/197.7 eV in the Cl 2p spectra belong to bridging Cl atoms (cf. table 12.1). No Cl_{ot} has been observed. Furthermore, the Cl 2p spectra did not change significantly upon the adsorption/desorption of one monolayer of CO, indicating the stability of the chlorine substitution against CO adsorption, at least under UHV conditions. Upon CO adsorption, the characteristic signal of CO showed up in the O 1s spectrum of the CO adsorbate on $RuO_{2-x}Cl_x$(110) at 532.5 eV ($E_{calc}(C\mathbf{O}_{ot}) = 532.4$ eV for RuO_2(110)-1x1-1Cl_{br}-1CO_{ot}). Annealing to $T = 450$ K led to the recovery of the O 1s spectrum of the pristine surface, which additionally exhibited CO_{br} molecules in the bridging rows as indicated by a shoulder in the O 1s spectrum at 531.4 eV ($E_{calc}(C\mathbf{O}_{br}) = 531.4$ eV for RuO_2(110)-1x2-2Cl_{br}-1CO_{br}).

Annealing of the CO_{ot} saturated, chlorinated oxide led to the formation of a CO_{br} species. A further reduction of the oxide did not take place, as evidenced by the fully recovered O_{bulk} emission in the O 1s spectrum after desorption of CO.

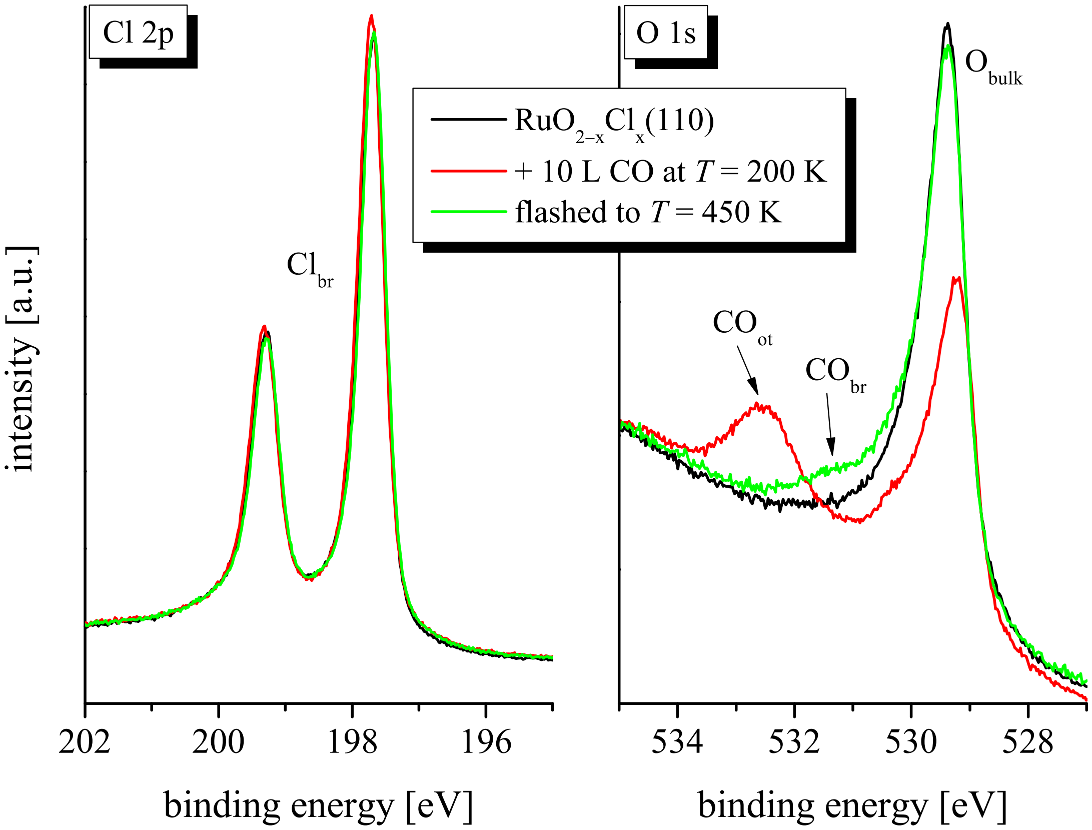

Figure 14.1: Cl 2p and O 1s high resolution core level shift spectra of pristine $RuO_{2-x}Cl_x(110)$, CO_{ot}-saturated $RuO_{2-x}Cl_x(110)$ and the surface after a flash to $T = 450$ K.

14.1.2 Adsorption of CO on $RuO_{2-x}Cl_x(110)$ under UHV

In the following experiment, $RuO_{2-x}Cl_x(110)$ was exposed to CO at low pressure, in order to build up gradually a CO_{ot} monolayer. This enabled a detailed, time-resolved RAIRS study of the growth of the CO_{ot} phase. Thus, different stages of formation of a saturated CO monolayer could be identified, starting from very small CO coverages, i.e. isolated CO_{ot} molecules.

The chlorinated $RuO_2(110)$ surface was prepared following the standard preparation procedures, described in chapter 9.3.

The surface was exposed to carbon monoxide ($p(\mathrm{CO}) = 5 \times 10^{-9}$ mbar) during the measurement of the RAIR spectra at temperatures below $T < 120$ K. Each spectrum was recorded by averaging of ten interferograms, the time difference between two spectra was 13 s. During the acquisition of each spectrum the CO dosage increased by 0.07 L. RAIR spectra were taken continuously up to a cumulated CO dosage of 2.8 L, where the position and intensity of the RAIRS absorption band have saturated. The series of measured RAIR spectra is shown in figure 14.2.

The assignment of the spectral features in the RAIR spectra is based on the interpretation proposed in chapter 10. At the initial stage of the adsorption experiment very few CO_{ot} molecules reside on the 1f-cus Ru sites and are randomly distributed, no interaction between the molecules is assumed. The absorption line at $\tilde{\nu}(\mathrm{CO}) = 2094\ \mathrm{cm}^{-1}$ observed in the first RAIR spectra can therefore be assigned to isolated CO_{ot} molecules (singletons). The vibration frequency of these singletons will be denoted by Ω_1. At $\tilde{\nu}(\mathrm{CO}) = 2103\ \mathrm{cm}^{-1}$, the next spectral feature appears as a shoulder of the absorption band at $\tilde{\nu}(\mathrm{CO}) = 2094\ \mathrm{cm}^{-1}$. With increasing CO exposure the band center shifts to $\tilde{\nu}(\mathrm{CO}) = 2106\ \mathrm{cm}^{-1}$. At a CO dosage of 1.2 L, the CO absorption peak narrows and shifts continuously to $\tilde{\nu}(\mathrm{CO}) = 2112\ \mathrm{cm}^{-1}$, where its saturation is observed. The same RAIRS peak has been obtained after exposing the pristine, freshly chlorinated oxide to 6 L CO at $T < 230$ K which was flashed to $T = 700$ K before CO dosing. Annealing to $T = 700$ K was necessary in order to free the 1f-cus Ru sites from remaining Cl_{ot}. This recipe for dosing CO was used to produce a saturated CO_{ot} coverage in the case of stoichiometric RuO_2 as well.

In the following, the experimental results of the CO gradual adsorption exper-

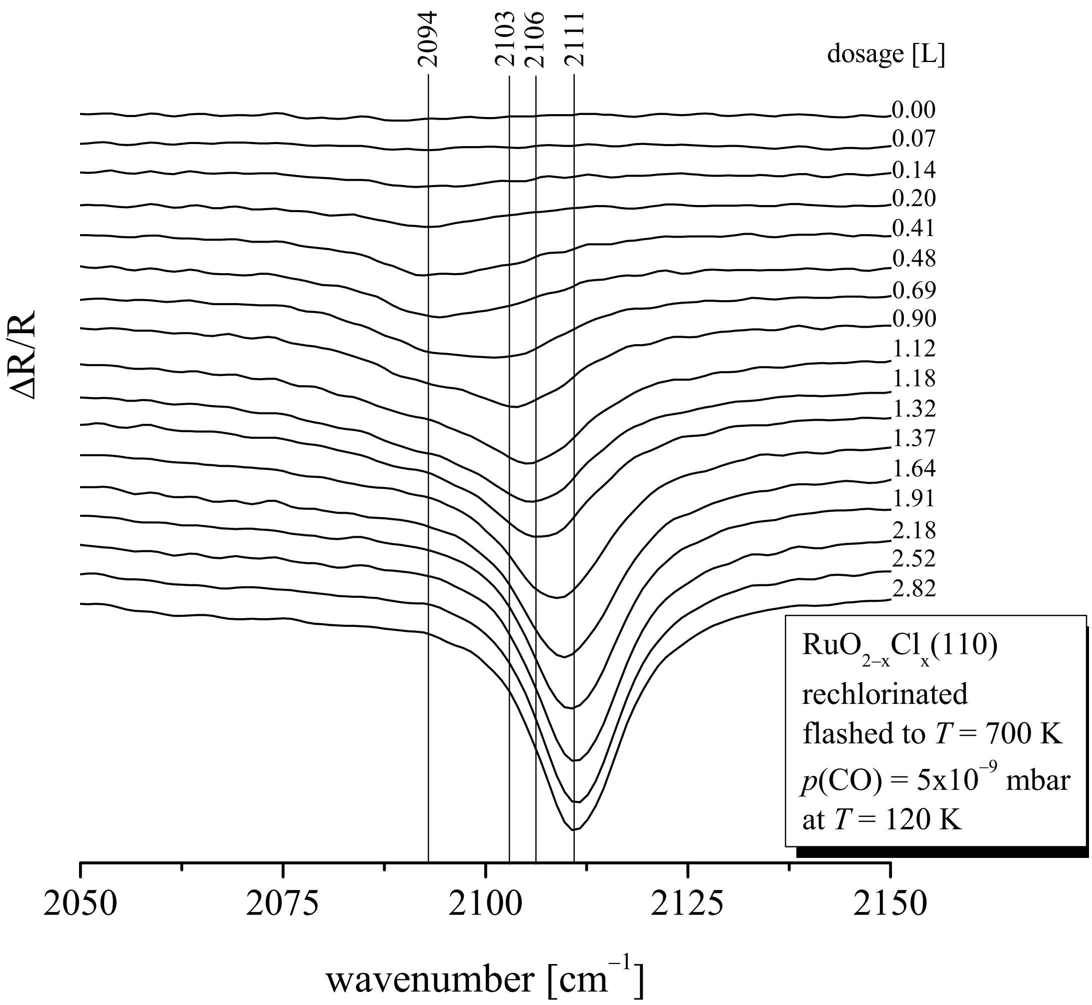

Figure 14.2: RAIR spectra recorded during the adsorption of CO on chlorinated RuO_2 at $p(CO) = 5 \times 10^{-9}$ mbar and T =120 K. With increasing CO coverage of the 1f-cus Ru sites, distinct vibrational bands develop in the range of $\tilde{\nu}(CO) = 2094$ to 2112 cm^{-1}.

Chain length k	$\Omega(k)_{calc}$ **[cm^{-1}]**	$\Omega(k)_{meas}$ **[cm^{-1}]**
1	2094.0	2094
2	2102.8	2103
3	2106.5	2106
4	2108.2	-
5	2109.2	-
⋮	⋮	⋮
20	2111.4	2111.2

Table 14.1: Comparison of the experimental frequencies of the CO_{ot} bands in figure 14.2 with the eigenfrequencies of coupled oscillators as given by equation 14.1, with $\Omega_1 = 2094$ cm^{-1} and $\Gamma = 272$ cm^{-1}.

iment on $RuO_{2-x}Cl_x(110)$ will be compared with the theoretical evaluation of the dipole-dipole coupling between the CO_{ot} molecules upon the formation of pairs, triples, and finally longer chains of CO_{ot} on the cus-rows. For the evaluation of the eigenfrequencies of a chain of k neighbouring CO_{ot} molecules, the chain has been treated as a chain of k identical harmonic oscillators. Provided that only nearest neighbour interactions are considered between the oscillators in the chain, the eigenfrequency $\Omega(k)$ of the mode in which all k oscillators are vibrating in phase is given by

$$\Omega(k) = \sqrt{\Omega_1^2 + \Gamma^2 \cos\left(\frac{\pi}{k+1}\right)} \tag{14.1}$$

where Ω_1 is the singleton frequency of an isolated CO_{ot} and Γ is the coupling constant between neighbouring oscillators in the chain [13]. Assuming that the coupling constant $\Gamma = 272$ cm^{-1} evaluated by Farkas for CO_{ot} adsorbed on stoichiometric ruthenium dioxide [13] remains unchanged for the chlorinated surface, $\Omega(k)$ was calculated for the CO adsorption on $RuO_{2-x}Cl_x(110)$ as well. With $\Omega_1 = 2094$ cm^{-1} as determined from the RAIR spectra (cf. figure 14.2), the frequency of the principal CO band at high coverage (long CO_{ot} chains) was reproduced very well and is in good agreement with the experimental data. The computed eigenfrequencies and the corresponding spectral features are compiled in table 14.1. The calculated values of $\Omega(k)$ could be assigned to experimentally observed features in the spectra of CO during the gradual adsorption experiment, shown in figure 14.2.

Given that the absorption in the RAIR spectra measured at the very begin-

System	Ω_1 **[cm^{-1}]**	$\langle n_{2\pi^*} \rangle$
s-$RuO_2(110)$	2101	0.415 ± 0.034
$RuO_{2-x}Cl_x(110)$	2094	0.423 ± 0.035
Variation upon chlorination	7	1.9%

Table 14.2: Comparison of the population of the $CO_{2\pi^*}$ orbital $\langle n_{2\pi^*} \rangle$ for stoichiometric and chlorinated ruthenium dioxide. Ω_1 represents the singleton C-O stretching vibration wavenumber of isolated CO molecules. The changes of the orbital populations are small compared to the changes observed for varying the metal atom in carbonyl complexes [131].

ning of the CO adsorption experiment at $\tilde{\nu}(CO) = 2094$ cm^{-1} corresponds to CO_{ot} singletons, the absorption feature at $\tilde{\nu}(CO) = 2103$ cm^{-1} originates from pairs of CO_{ot} molecules occupying neighbouring on top sites while the feature developing at $\tilde{\nu}(CO) = 2106$ cm^{-1} is due to isolated groups of three CO_{ot} molecules. The present assignment closely parallels the results presented for stoichiometric ruthenium dioxide [13].

In order to estimate the influence of the bridging chlorine atoms on the electronic structure of the CO_{ot} molecules, the population of the $2\pi^*$ orbital of CO $\langle n_{2\pi^*} \rangle$ has been evaluated based upon the theory for the electronic structure of transition metal carbonyl complexes given by Baerends et al. [131]

$$\langle n_{2\pi^*} \rangle = \frac{2456 \text{ cm}^{-1} - \Omega_1(\text{CO})}{856 \text{ cm}^{-1}} \tag{14.2}$$

The evaluation of the populations of the $CO_{2\pi^*}$ orbital for adsorption on both stoichiometric ($\Omega_1(CO) = 2101$ cm^{-1}) and chlorinated ($\Omega_1(CO) = 2094$ cm^{-1}) RuO_2 indicates that there is no significant change in the population of the $CO_{2\pi^*}$ orbitals (see table 14.2). One may conclude that the electronical properties of the 1f-cus adsorption site remain almost identical upon the substitution of O_{br} by Cl_{br}.

DFT calculations support the above-mentioned conclusion showing a negligible change in the binding energy of CO_{ot} neighbouring Cl_{br} or O_{br}, respectively. CO_{ot} is adsorbed on $RuO_2(110)$ ($\theta_{CO} = 0.5$) by -1.48 eV irrespective if a Cl_{br} or O_{br} is neighbouring the CO molecule (see figure 14.3) as determined by DFT calculations.

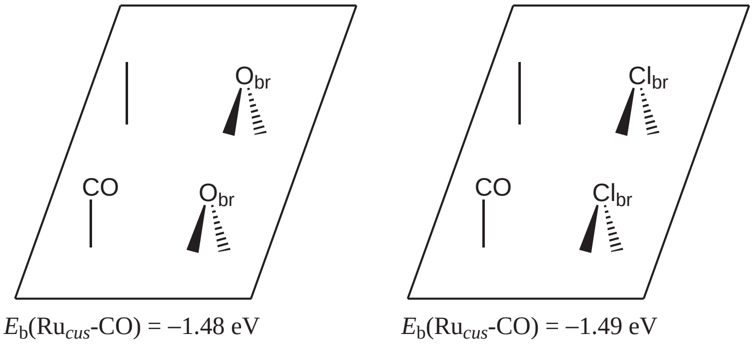
O_{br}
CO
O_{br}
Cl_{br}
CO
Cl_{br}
$E_b(Ru_{cus}\text{-}CO) = -1.48$ eV
$E_b(Ru_{cus}\text{-}CO) = -1.49$ eV

Figure 14.3: Comparison of the calculated binding energies E_b of CO_{ot} adsorbed on s-RuO_2(110) (left) and $RuO_{2-x}Cl_x$(110) (right). The coverage of CO_{ot} was 0.5 in both cases.

14.1.3 Influence of Cl_{ot} on the Vibrational Properties of CO_{ot}

Flashing a chlorinated RuO_2(110) to only 550 K after chlorination or rechlorination led to the desorption of HCl_{ot} but not to the recombinative desorption of Cl_{ot}, which needs temperatures above 650 K. Thus, the adsorption behaviour of CO dosed at low temperatures to saturate the surface, as well as its vibrational properties were altered by the presence of the remaining Cl_{ot} atoms. After saturation of the chlorinated surface with CO and a flash to only T = 550 K, the absorption line of the saturated CO_{ot} layer occurred at 2106 cm^{-1}. The spectra belonging to this experiment are compiled in figure 14.4 and table 14.3.

Sample	**$\tilde{\nu}$(CO) [cm^{-1}]**	**Peak Area [a.u.]**	**FWHM [cm^{-1}]**
with Cl_{ot}	2106	0.10	11.8
without Cl_{ot}	2112	0.12	12.0

Table 14.3: Compiled data of the CO absorption bands for $RuO_{2-x}Cl_x$(110), with and without Cl_{ot}, respectively (figure 14.4).

The surface was then flashed to T = 700 K, which led to the desorption of Cl_{ot}. Subsequent saturation of the surface with CO at T = 120 K resulted in a CO band at $\tilde{\nu}$(CO) = 2112 cm^{-1}, which corresponds to a Cl_{ot}-free CO_{ot} adsorbate on chlorinated RuO_2(110).

Furthermore, the amount of adsorbed CO increased by 20 % upon flashing the sample to T = 700 K, which indicates that these 1f-cus Ru sites were occupied by

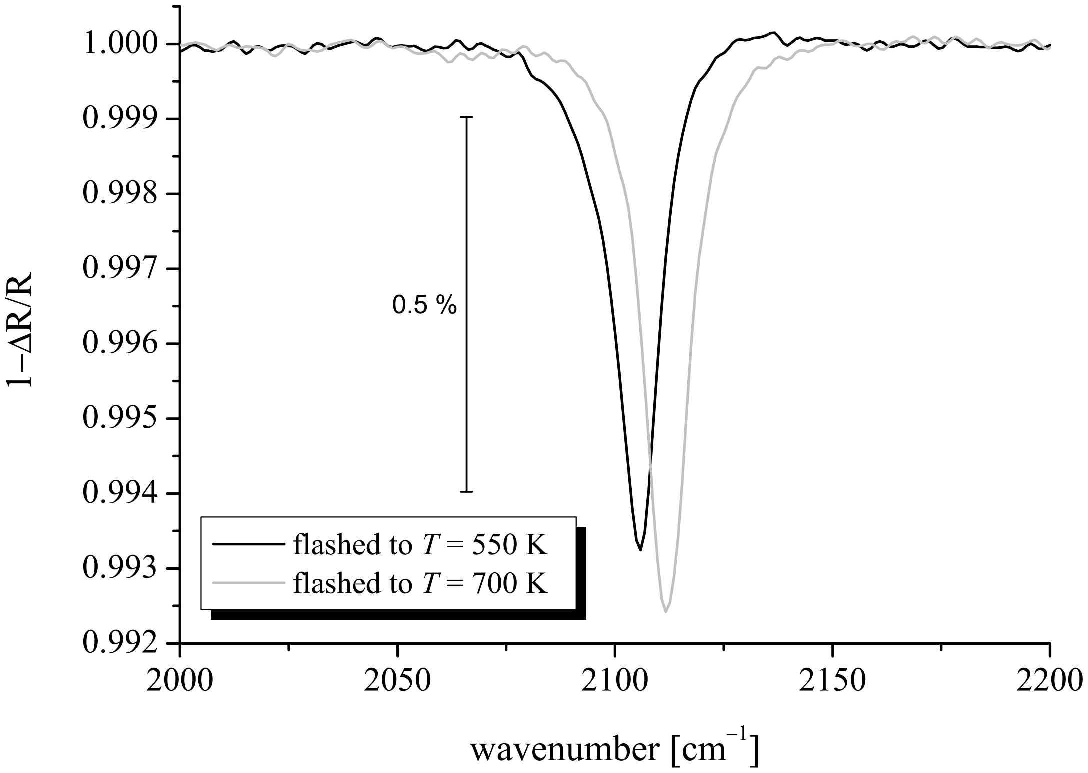

Figure 14.4: RAIR spectra of CO adsorbed on chlorinated $RuO_2(110)$ and its dependence to the annealing temperature. The peak centred at $\tilde{\nu}(CO) = 2106$ cm^{-1} (black) corresponds to a $(CO_{ot}+Cl_{ot})/(Cl_{br}+O_{br})$ coadsorbate obtained after flashing the rechlorinated surface to $T = 550$ K. Further annealing to $T = 700$ K led to the desorption of Cl_{ot}. Subsequent saturation with CO at $T = 120$ K results in a blue shift of the CO adsorption to $\tilde{\nu}(CO) = 2112$ cm^{-1} (grey) and in an increase in intensity.

Cl_{ot} before flashing to $T = 700$ K. An increase of 20 % in the CO RAIRS signal indicates that on average every fifth 1f-cus Ru site was occupied by Cl_{ot}. This finding is consistent with Auger electron spectroscopy results, which yielded Cl_{ot} contents of 0.05 to 0.4 monolayers (cf. table 13.1).

The observed red shift induced by the presence of Cl_{ot} can be explained - while neglecting electronic effects of Cl_{ot} on the CO_{ot} adsorbate - by a segmentation of extended chains of CO_{ot} molecules on the cus-rows. A wavenumber of $\tilde{\nu}(CO) = 2106\ cm^{-1}$ then corresponds to triplets and quads of adsorbed CO_{ot} molecules (cf. table 14.1), which also is in line with a Cl_{ot} coverage of about 0.2 ML. The FWHM width of the CO adsorption features remained essentially unchanged after flashing to $T = 550$ K and $T = 700$ K, respectively, indicating that the CO_{ot} adsorbate is composed of chain fragments of similar length (3-4 CO molecules).

14.1.4 CO_{ot} + O_{ot} Coadsorbates

The influence of O_{ot} on the vibrational characteristics of coadsorbed CO_{ot} has been studied by RAIRS on s-$RuO_2(110)$ in reference [13] for the system $O_{br}/(CO_{ot}^{sg} + O_{ot})$, i.e. for a saturated O_{ot} coverage with a small amount of isolated CO_{ot} molecules. The IR absorption wavenumber of this phase has been reported to be $\tilde{\nu}(CO) = 2150\ cm^{-1}$. This value is even larger than the vibration frequency of gas-phase CO ($\tilde{\nu}(CO_{gas}) = 2143\ cm^{-1}$). Similar blue-shifted CO stretching frequencies have been found on other oxide surfaces and explained by a strong electrostatic interaction of the surface O species with the adsorbed CO molecules [132].

A more detailed study with varying O_{ot} coverages has been carried out within this thesis in order to elucidate the influence of O_{ot} on the vibrational characteristics of (CO_{ot}+O_{ot}) coadsorbates on s-$RuO_2(110)$ as well as on $RuO_{2-x}Cl_x(110)$.

CO_{ot} + O_{ot} coadsorption on s-RuO_2

Stoichiometric $RuO_2(110)$ was exposed to varying dosages of O_2 at low temperatures ($T < 200$ K) to produce well-defined coverages of O_{ot}, starting from small values. Thereafter, the surface, i.e. the remaining unoccupied 1f-cus Ru sites, was saturated by dosing 6 L CO at ($T < 200$ K) and a RAIR spectrum was recorded. After taking a RAIRS spectrum, the stoichiometric $RuO_2(110)$ was restorated in

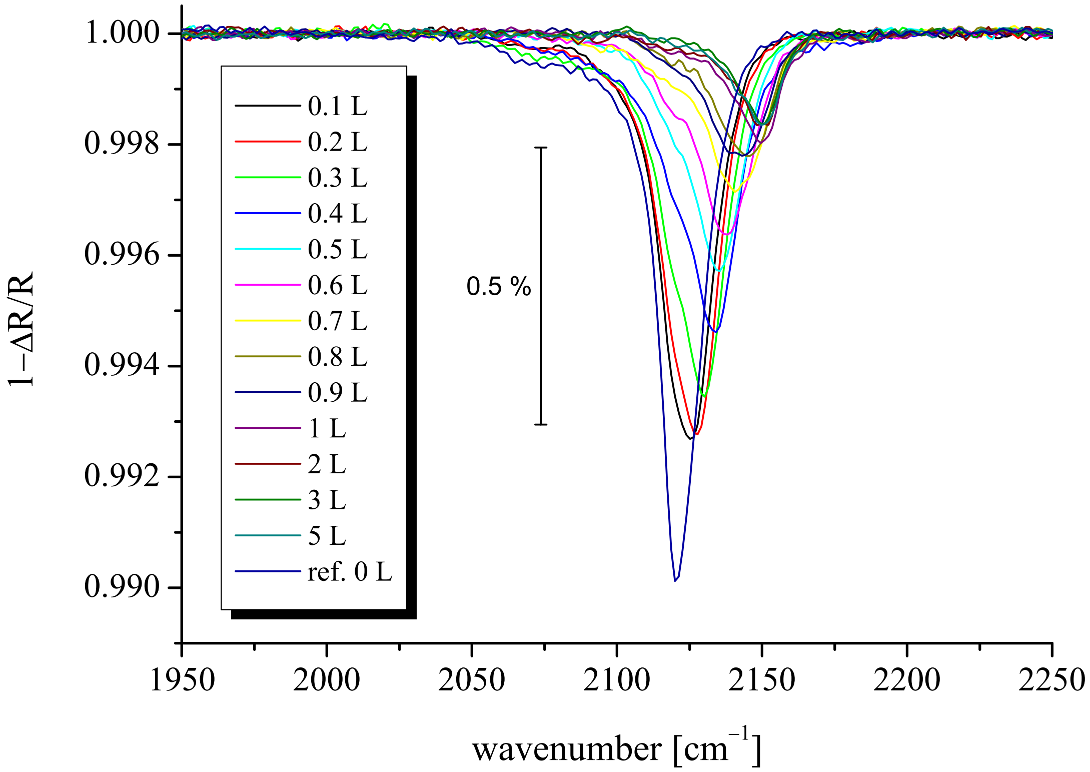

Figure 14.5: RAIR spectra of CO adsorbed on s-$RuO_2(110)$ with varying coverages of O_{ot}. The O_{ot} phase was prepared by dosing different amounts of O_2 at temperatures below $T < 200$ K as indicated in the plot. All spectra were obtained after saturating the surface by dosing 6 L CO at $T < 200$ K.

oxygen. The corresponding RAIR spectra for O_2 dosages ranging from 0 to 5 L are shown in figure 14.5.

The RAIR spectrum of the CO_{ot} saturated s-$RuO_2(110)$ exhibits an absorption peak at $\tilde{\nu}(CO) = 2121$ cm^{-1} with maximum intensity which corresponds to long, unperturbed chains of CO_{ot} molecules (cf. [13]). With increasing O_{ot} coverage, the CO IR band shifts to higher wavenumbers, whereas the $\tilde{\nu}(CO) = 2121$ cm^{-1} component remains visible up to a O_2 dosage of circa 0.8 L. The wavenumber shift with increasing O_2 exposure is displayed in figure 14.6.

A saturation of the wavenumber shift leading to a CO absorption line centred at $\tilde{\nu}(CO) = 2150$ cm^{-1} has been achieved after an oxygen dose of 1 L. At this coverage, the O_{ot} adsorption seemed to be saturated since the integrated intensity of the CO absorption line did not decrease significantly upon further dosing of O_2 at low temperatures, as can be seen from figure 14.7 which gives the integrals of the CO RAIR spectra displayed in figure 14.5.

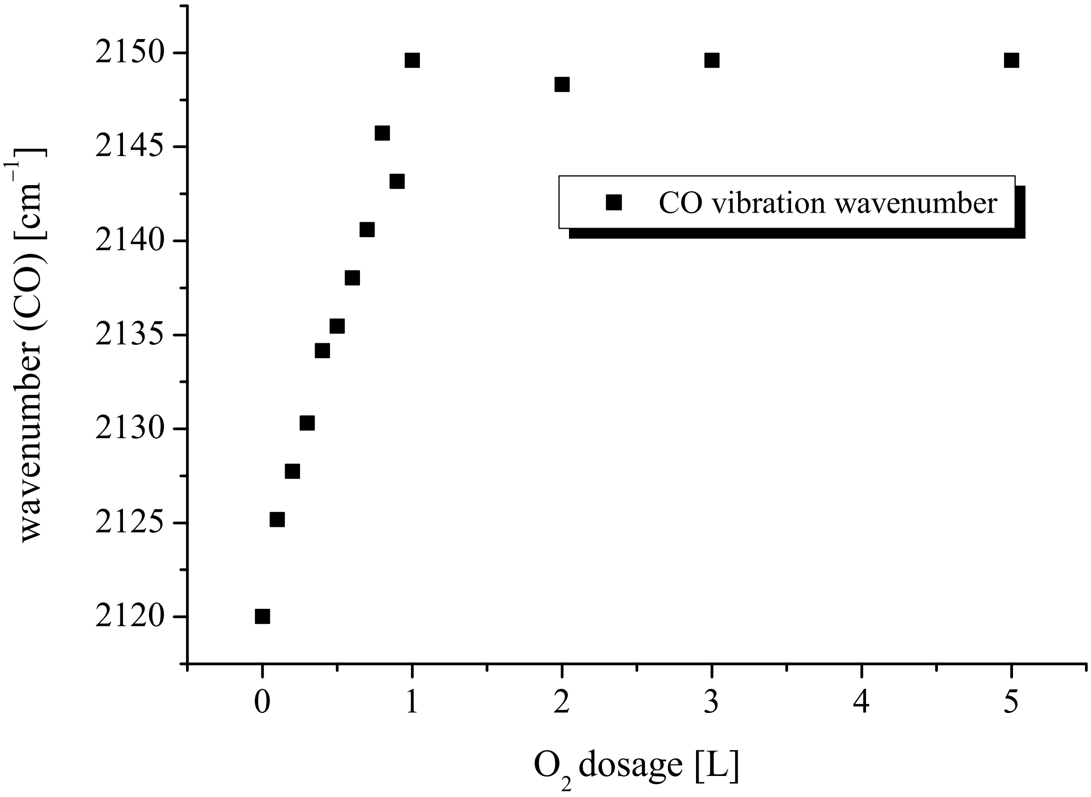

Figure 14.6: Peak positions of the RAIR spectra of CO_{ot} coadsorbed with O_{ot} on stoichiometric $RuO_2(110)$ as a function of the O_2 dosage. A saturation of the wavenumber shift occurred at O_2 dosages above 1 L.

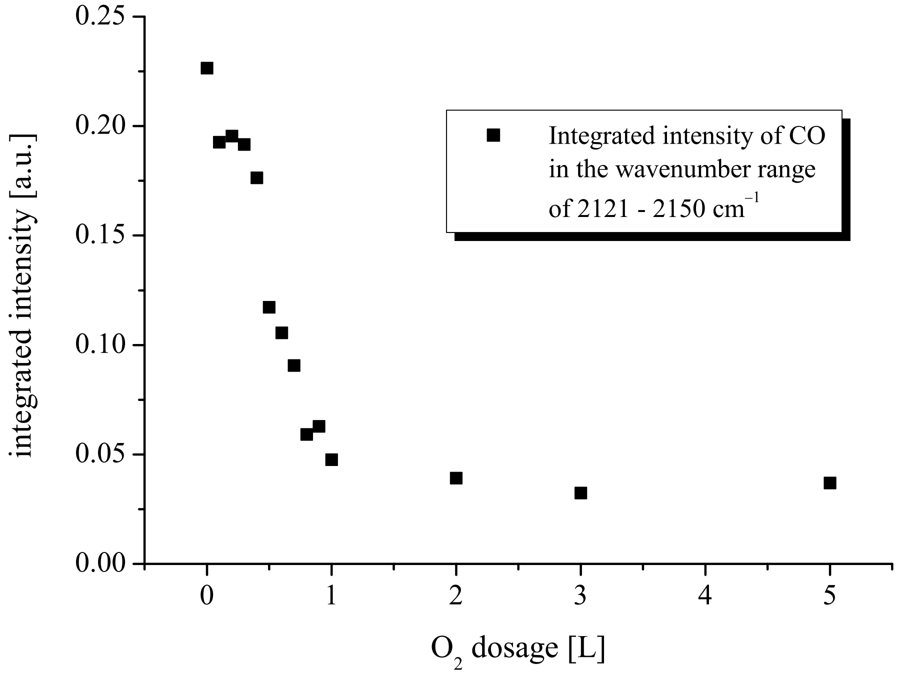

Figure 14.7: Integrated intensities of the RAIRS features of CO of CO_{ot} coadsorbed with O_{ot} on stoichiometric $RuO_2(110)$ as a function of O_2 exposure. The minimum CO_{ot} absorption intensity was reached after predosing 1 L of O_2 and amounts to 14 % of the initial value (CO_{ot} on s-RuO_2, no O_{ot}). Hence, the maximum O_{ot} coverage can be estimated to be 0.86 ML, assuming no change in the polarisability of CO_{ot} upon coadsorption with O_{ot}.

The maximum coverage of O_{ot} adsorbed on s-$RuO_2(110)$ has been determined to be 0.86 ML (assuming that the polarisability of CO did not change), which matches the value described by Kim et al. [133]. Furthermore, Monte Carlo simulations yielded a maximum O_{ot} coverage on s-$RuO_2(110)$ of $\Theta(O_{ot} = 0.864 \pm 0.003$ [134], which are in line with recent results of Schneider et al. [107]. Thereby, the assumption of a constant polarisability is further substantiated and thus, the intensity of the RAIRS absorption of CO may be used as a measure of the CO coverage.

CO_{ot} + O_{ot} coadsorption on $RuO_{2-x}Cl_x(110)$

A similar blue shift of the CO stretching frequency upon coadsorption with O_{ot} has also been observed on $RuO_{2-x}Cl_x(110)$. The surface was flashed to $T = 700$ K to remove Cl_{ot} and subsequently exposed to 5 L O_2 at $T = 300$ K. Figure 14.8 displays the RAIR spectra of a O_{ot} saturated CO_{ot}+O_{ot} coadsorbate ($\tilde{\nu}(CO) = 2141\ cm^{-1}$) and a pure CO_{ot} adsorbate on $RuO_{2-x}Cl_x(110)$ ($\tilde{\nu}(CO) = 2112\ cm^{-1}$). Compared to CO singletons on $RuO_{2-x}Cl_x(110)$, the CO singletons adsorbed in a O_{ot} matrix experience a blue shift of $\Delta\nu(CO) = +\ 47\ cm^{-1}$ from $\Omega_1 = 2094\ cm^{-1}$ to $\tilde{\nu}(CO) = 2141\ cm^{-1}$ which compares well to the blue shift observed for CO_{ot}^{sg}+O_{ot} on stoichiometric $RuO_2(110)$ ($\Delta\nu(CO) = +\ 50\ cm^{-1}$). Thus, the behaviour of the CO+O coadsorbate on both s-$RuO_2(110)$ and $RuO_{2-x}Cl_x(110)$ are equivalent. Bridging chlorine substitution on $RuO_2(110)$ simply led to a red shift ($\Delta\nu(CO) = -10\ cm^{-1}$) of both singleton frequencies of CO_{ot}^{sg} and CO_{ot}^{sg}+O_{ot} by lowering the electron withdrawing effect of oxygen in the bridging rows (EN(Cl) = 3.0, EN(O) = 3.5) and thus increasing backdonation into the $2\pi^*$ orbital of the CO_{ot} molecules.

14.2 Mild Reduction of $RuO_{2-x}Cl_x(110)$

A careful determination of the maximum achievable bridging chlorination showed a maximum amount of about 80% Cl_{br} (cf. chapter 13.2). The remaining bridging positions are filled by O_{br}. Therefore, the question arises if these bridging oxygen atoms are reducible by CO and if they can be replaced by CO_{br}.

Furthermore, the influence of Cl_{br} on the vibrational characteristics of CO_{br} and CO_{ot} adsorbed on $RuO_{2-x}Cl_x(110)$ will be investigated by means of reflection

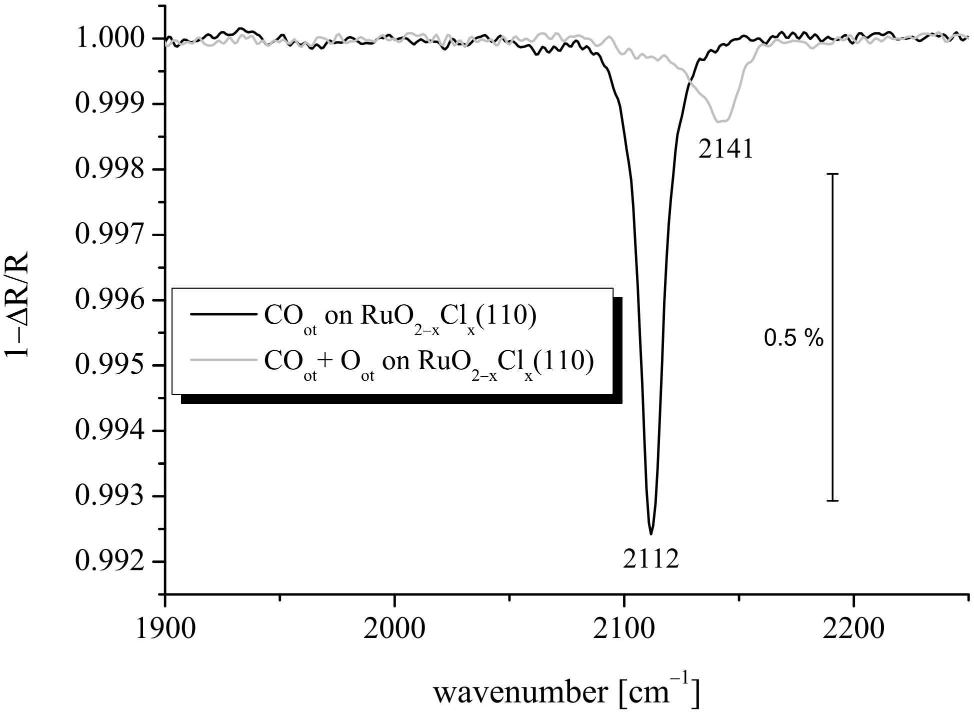

Figure 14.8: RAIR spectra of CO adsorbed on $RuO_{2-x}Cl_x(110)$ (black) and CO coadsorbed with O_{ot} (grey) on $RuO_{2-x}Cl_x(110)$.

absorption IR spectroscopy, especially in comparison to s-$RuO_2(110)$.

14.2.1 Reduction of $RuO_{2-x}Cl_x(110)$ by CO in a *One-Step* Procedure

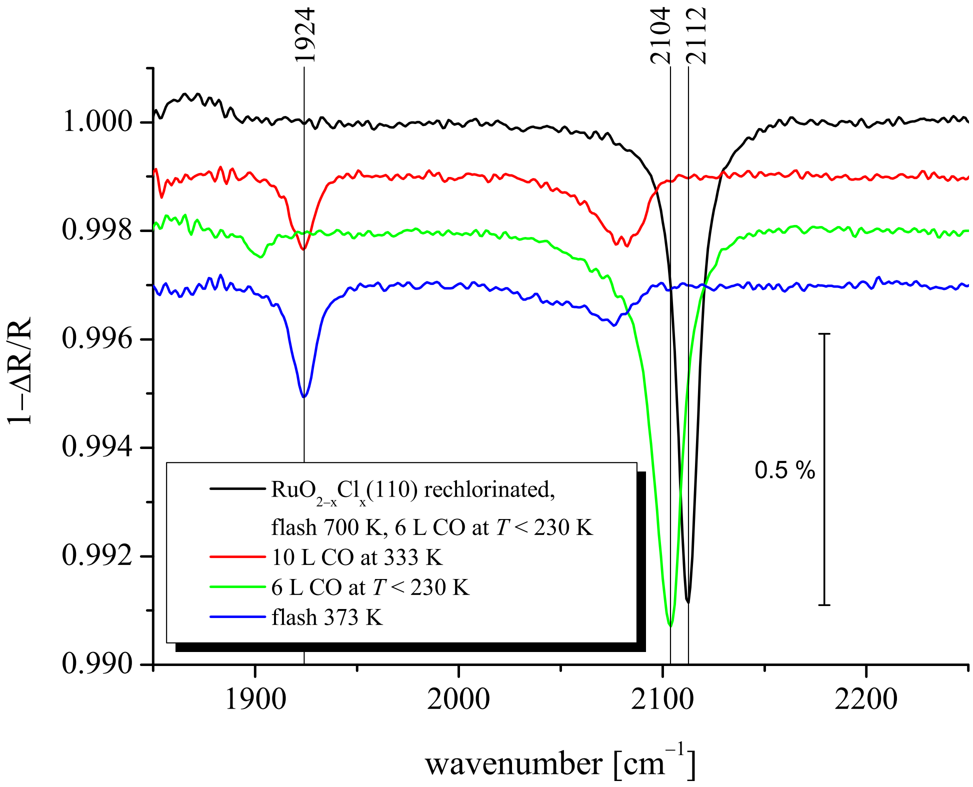

Figure 14.9: RAIR spectra of CO adsorbed on $RuO_{2-x}Cl_x(110)$ recorded during the preparation of the mildly reduced, chlorinated ruthenium dioxide.

The freshly rechlorinated $RuO_2(110)$ was flashed to $T = 700$ K to ensure the absence of Cl_{ot} atoms, which was confirmed by measuring the RAIR spectrum of CO_{ot} after saturation of the 1f-cus Ru rows by exposure of 6 L CO at T <230 K ($\tilde{\nu}(CO) = 2113$ cm^{-1}, cf. figure 14.9). This absorption feature corresponds to long chains of CO_{ot} molecules neighbouring Cl_{br} or O_{br}, respectively as described in section 14.1. Afterwards, the sample was exposed to 10 L CO at a temperature of $T = 333$ K in order to reduce the bridging oxygen atoms. The RAIR spectrum

(CO turned off, $T < 310$ K) taken at this point exhibited two RAIRS absorptions. The band at $\tilde{\nu}$(CO) = 1924 cm^{-1} is assigned to CO_{br} molecules in a Cl_{br} matrix ($(CO_{br}+Cl_{br})/(-)_{ot}$) in analogy to s-$RuO_2$ [13, 135]. The absorption at $\tilde{\nu}$(CO) = 2080 cm^{-1} belongs to a mixed phase of CO_{br} in a Cl_{br} matrix with a small number of CO_{ot} adsorbed on the 1f-cus Ru sites. The CO_{ot} molecules are dipole-coupled to the bridging CO molecules. This phase will be addressed in more detail in the following (thermal desorption experiment, see section 14.2.2).

In order to study the $(Cl_{br}+CO_{br})/CO_{ot}$ phase, the surface was saturated with 6 L CO at $T < 230$ K. The spectrum showed the absorption at $\tilde{\nu}$(CO) = 2104 cm^{-1}, which was assigned to $(Cl_{br}+CO_{br})/CO_{ot}$. The blue shift by $\Delta\tilde{\nu}$(CO) = +20 cm^{-1}, which has been observed in comparison to CO_{br}/CO_{ot} on mildly reduced r-RuO_2(110) ($\tilde{\nu}$(CO) = 2085 cm^{-1}, [13]), is caused by the presence of bridging chlorine atoms as electronegative substituents. This effect could not be observed on mildly reduced r-RuO_2(110), since this surface is fully capped by CO molecules both in on top and bridging positions. The peak at $\tilde{\nu}$(CO) = 2104 cm^{-1} has contributions of both CO_{ot}, adsorbed in long chains on the cus-rows and CO_{br} in a Cl_{br} matrix. Both species are coupled by dipole-dipole interactions, leading to one single absorption peak in the RAIR spectrum. Removal of the CO_{ot} atoms by flashing the sample to $T = 373$ K yielded the pure $(CO_{br}+Cl_{br})/(-)_{ot}$ phase with a characteristic absorption band at $\tilde{\nu}$(CO) = 1928 cm^{-1}.

14.2.2 Thermal Desorption of CO_{ot} from $(Cl_{br}+CO_{br})/CO_{ot}$ on $RuO_{2-x}Cl_x(110)$

The development of the $(Cl_{br}+CO_{br})/CO_{ot}$ phase on $RuO_{2-x}Cl_x(110)$ has been investigated by thermal desorption starting from a fully CO_{ot} covered $(Cl_{br}+CO_{br})/CO_{ot}$ phase. This experiment can be used to confirm the assignment of the CO vibration features observed in the RAIR spectra depending on the CO coverage on mildly reduced $RuO_{2-x}Cl_x(110)$.

The fully CO_{ot} covered $(Cl_{br}+CO_{br})/CO_{ot}$ phase was prepared by mild reduction of the chlorinated oxide in analogy to the previously described experiment: The oxide was rechlorinated, flashed to $T = 700$ K, and exposed to 10 L of CO at $T = 333$ K. After saturation of this surface at $T < 200$ K by dosing 6 L CO, stepwise heating to higher annealing temperatures ($\Delta T = 25$ K, starting from $T = 175$ K) led to the gradual desorption of the CO_{ot} molecules. The corre-

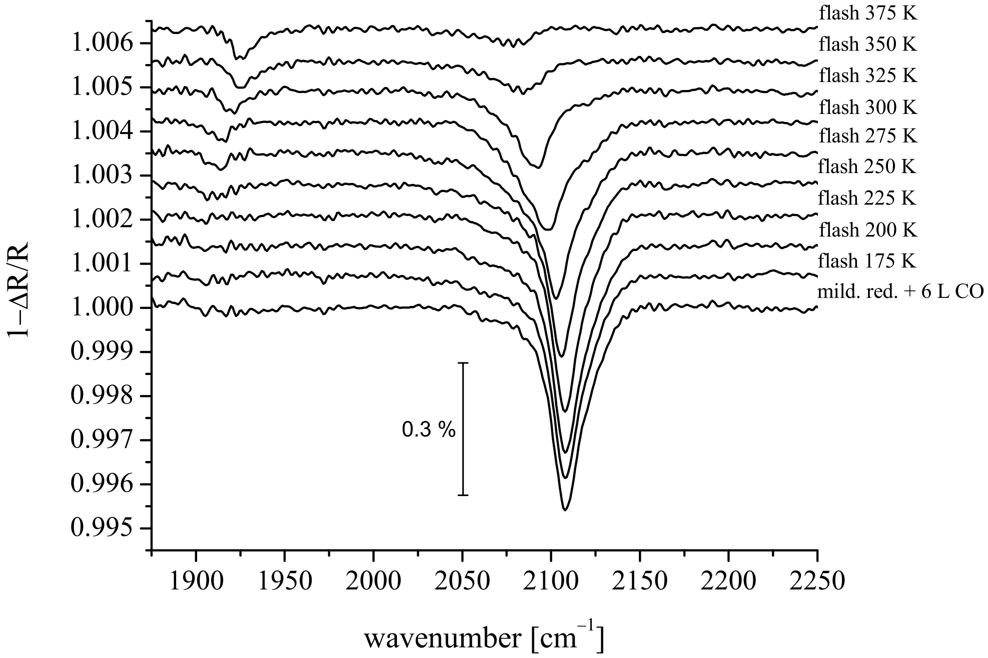

Figure 14.10: RAIR spectra of CO adsorbed on mildly reduced $RuO_{2-x}Cl_x(110)$. The set of spectra was obtained by stepwise annealing of the adsorbate to higher temperatures.

sponding RAIR spectra after each annealing step are displayed in figure 14.10. The reference spectrum was taken after the reduction of the rechlorinated and restored $RuO_{2-x}Cl_x(110)$ (10 L CO at $T = 333$ K) and saturation of the cus-rows by dosing 6 L CO at $T < 230$ K. The peak at $\tilde{\nu}(CO) = 2108$ cm^{-1} is due to the $(Cl_{br}+CO_{br})/CO_{ot}$ phase, where the cus-rows are occupied by extended chains of CO_{ot} molecules. As already mentioned above, CO_{br} is present at this stage and couples with CO_{ot} by dipole-dipole interactions, resulting in a band at $\tilde{\nu}(CO) = 2108$ cm^{-1}.

At temperatures above $T = 250$ K, this RAIRS peak started to lose intensity, accompanied by a red shift of the peak. In figure 14.11, the integrated intensities of the absorption features are plotted versus the temperature of the preceding flash. The more CO_{ot} molecules are desorbed from the formerly saturated phase, the more pronounced is the red shift. Concomitant with the decrease in intensity of the RAIRS peak belonging to the $(Cl_{br}+CO_{br})/CO_{ot}$ phase an absorption band of (Cl_{br}+CO_{br})/(–) evolves, starting from $\tilde{\nu}$(CO) = 1910 cm^{-1} and converging towards $\tilde{\nu}$(CO) = 1923 cm^{-1}. The growth of this peak around 1900 cm^{-1} is due to the progressing dipole-dipole decoupling induced by the desorption of CO_{ot}, leaving the CO_{br} species isolated.

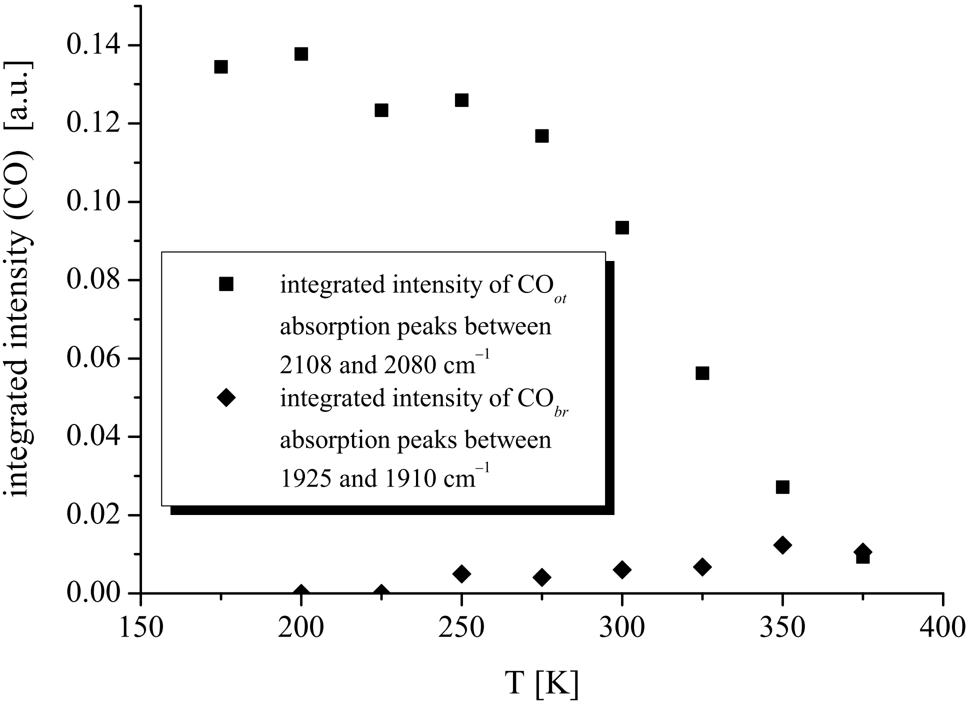

Figure 14.11: Integrated intensities of the CO RAIRS peaks on r-$RuO_{2-x}Cl_x(110)$. The dependence on the annealing temperature is a consequence of the desorption of CO_{ot}. Peaks between 2080-2108 cm^{-1} correspond to (Cl_{br}+CO_{br})/CO_{ot} and peaks in the region from 1910 cm^{-1} to 1925 cm^{-1} belong to (Cl_{br}+CO_{br})/$(-)_{ot}$.

At $T > 350$ K most of the CO_{ot} molecules have left the surface. Therefore, the observed remaining small absorption band at $\tilde{\nu}$(CO) = 2080-2084 cm^{-1} in the RAIR spectra recorded above $T = 350$ K can be assigned to CO_{ot} molecules vibrating on a chlorinated $RuO_2(110)$ with CO_{br} substituted in the bridging chlorine rows (Cl_{br}+CO_{br})/CO_{ot}^{sg}). The temperature programmed desorption experiment gave insight into the gradual desorption of the CO_{ot} adsorbate and interconnected the fully CO_{ot} covered (Cl_{br}+CO_{br})/CO_{ot} phase with the (Cl_{br}+CO_{br})/$(-)_{ot}$ phase, confirming thereby the spectral assignment carried out in the previous experiment.

Eventually, the term ‘mildly reduced’ does not describe the surface correctly in the case of chlorinated $RuO_2(110)$. It seems to be more precise to specify the surface as bridge chlorinated with single bridging position substituted by CO_{br}.

14.3 Chapter Summary

All experiments presented in this chapter aim to describe the complete vibrational characteristics of CO adsorbed on the on top and bridging positions on chlorinated $RuO_2(110)$, denoted as $RuO_{2-x}Cl_x(110)$. The vibrational spectra of CO also reflect the interaction with the relevant surface species $O_{br/ot}$ and $Cl_{br/ot}$ through electron donation/backdonation. CO was successfully introduced as a probe molecule to investigate the nature of the 1f-cus Ru adsorption site and the influence of chlorine substitution. As a probe molecule, CO offers in addition the possibility to study the dynamic behaviour of the Cl atoms on the oxide surface, which will be in the focus of the following chapters. Table 14.4 summarises the vibrational assignments of CO adsorbed on both stoichiometric $RuO_2(110)$ (from reference [13]) and chlorinated $RuO_{2-x}Cl_x(110)$ (this work).

Substrate	**Adsorbate**	$\tilde{\nu}$**(CO) [cm^{-1}]**
$RuO_2(110)$	$CO_{br}^{II}/(-)_{ot}$	1867-1893
data taken from [13]	$(CO_{br}^{sg}+O_{br})/(-)_{ot}$	1953
	$CO_{br}/(-)_{ot}$	1992-2002
	CO_{br}/CO_{ot}^{sg}	2000, 2016
	CO_{br}/O_{ot}	2033-2046
	CO_{br}/CO_{ot}	2016-2086
	O_{br}/CO_{ot}^{sg}	2101
	O_{br}/CO_{ot}	2101-2123
	$O_{br}/(O_{ot}+CO_{ot}^{sg})$	2146-2152
$RuO_{2-x}Cl_x(110)$	$(CO_{br}+Cl_{br})/(-)_{ot}$	1920-1928
	$(CO_{br}+Cl_{br})/CO_{ot}$	2080-2108
	$(Cl_{br}+O_{br})/CO_{ot}^{sg}$	2094
	$(Cl_{br}+O_{br})/CO_{ot}$	2112
	$(Cl_{br}+O_{br})/(CO_{ot}+Cl_{ot})$	2105
	$(Cl_{br}+O_{br})/(CO_{ot}^{sg}+O_{ot})$	2140-2145

Table 14.4: Compilation of characteristic vibrational frequencies of CO species on $RuO_{2-x}Cl_x(110)$ compared to $RuO_2(110)$.

In addition to the characterisation of CO as a probe molecule, it has been shown by means of HRCLS and RAIRS that $RuO_{2-x}Cl_x(110)$ contains a certain amount of reducible bridging oxygen atoms, which is in accordance with the results of the Auger electron spectroscopy study in chapter 13. This corroborates in turn the result, that a maximally chlorinated $RuO_2(110)$ only contains up to 80% bridging Cl atoms, the residual places being occupied by O_{br}, which can be reduced by CO exposure. The HRCLS and RAIRS results were then substantiated by a more detailed analysis of the mild reduction reaction of the chlorinated oxide, i.e. the reduction of the O_{br} atoms by CO forming CO_{br} molecules. The influence of both Cl_{ot} and O_{ot} atoms on the vibrations of CO has been investigated. Based upon the results of the present chapter, one may formulate a rule of thumb which describes the influence of substituting surface O by Cl:

The introduction of bridging Cl atoms on s-RuO_2(110) leads to a red shift of $\Delta\tilde{\nu} \cong -10$ *cm^{-1} of the RAIR features of CO_{ot} in comparison to stoichiometric RuO_2(110).*

This statement seems to be quite general as can be seen from the vibrational shifts induced by Cl:

- O_{br}/CO_{ot}^{sg} vs. $(Cl_{br}+O_{br})/CO_{ot}^{sg} \Rightarrow$ 2101 vs. 2094 cm^{-1}
- O_{br}/CO_{ot}(full) vs. $(Cl_{br}+O_{br})/CO_{ot}$(full) $\Rightarrow$ 2123 vs. 2112 cm^{-1}
- $O_{br}/(O_{ot}+CO_{ot}^{sg})$ vs. $(Cl_{br}+O_{br})/(CO_{ot}^{sg}+O_{ot}) \Rightarrow$ 2150 vs. 2140 cm^{-1}

The electronic influence of Cl_{br} on the adsorbed CO_{ot} molecules is small, taking into account that the change in electronegativity going from O to Cl is only Δ(EN) = 0.5 and this difference effects the C-O bond over a distance of five bonds. Only a very small difference in the electronic structure of CO has been evaluated by inspecting the change of the population of the $2\pi^*$ orbital upon exchanging O_{br} by Cl_{br} (statistically to an amount of 80%). However, this small effect could be observed by means of RAIR spectroscopy, underlining nicely the very high sensitivity of the RAIR spectra upon changes in the chemical environment of the probe molecule CO.

The vibrational characterisation of the CO species adsorbed on chlorinated $RuO_{2-x}Cl_x(110)$ together with the coadsorption experiments with oxygen atoms and the mild reduction experiments of $RuO_{2-x}Cl_x(110)$ allow for a deeper understanding of the dynamical behaviour of the chlorine atoms accommodated on the surface, both upon O_2 exposure and under CO oxidation conditions in the following chapters.

Chapter 15

Influence of Oxygen on $RuO_{2-x}Cl_x(110)$

The scope of the present chapter is the investigation of the possible reactions of adsorbed oxygen with the $RuO_{2-x}Cl_x(110)$ surface. The interaction of surface oxygen atoms with both Cl_{br} and Cl_{ot} atoms will be studied experimentally by means of TDS, AES, HRCLS, RAIRS and theoretically by DFT calculations.

15.1 Thermal Stability of $RuO_{2-x}Cl_x(110)$

In the following section, the thermal degradation of chlorinated $RuO_{2-x}Cl_x(110)$ will be investigated by means of TDS, AES, HRCLS and DFT calculations. The thermal degradation is related to the interaction of O_{bulk} with the bridging chlorine atoms as will be shown in the present section. The experiments will conclude with a mechanistic discussion of the dechlorination process as well as the protecting properties of a bridging chlorine 'capping layer' - which is actually not a complete monolayer of Cl_{br} as evidenced in chapter 13.

Figure 15.1 shows the thermal desorption spectrum of chlorinated RuO_2 and overlayed the TP-Auger signal, monitoring the temperature dependent evolution of the Cl_{LMM} signal at $E = 181$ eV in the Auger spectrum. At $T = 400$ K O_{ot} desorbs as can be seen from the small O_2 desorption signal in the mass spectrum. Chlorine atoms, adsorbed on top of 1f-cus Ru sites desorb via recombination of two Cl_{ot} forming Cl_2. This led to the Cl_2 peak centred at $T = 690$ K, which is in accordance with the findings reported by Crihan et al. [9]. At this temperature, the first linear decrease in Auger intensity could be seen. Upon further heating, the bridging chlorine atoms (Cl_{br}) left the surface with a desorption maximum of HCl centred at $T = 890$ K. Here, the inflection point of the Cl_{LMM} Auger signal is shifted by approximately 20 K to lower temperatures, which is caused by a lower heating rate β in the case of the TP-Auger experiment ($\beta_{TDS} = 5$ K/s vs. $\beta_{TP-Auger} = 3$ K/s). After desorption of Cl_{br} bulk oxygen left the surface at $T_{max} = 1000$ K.

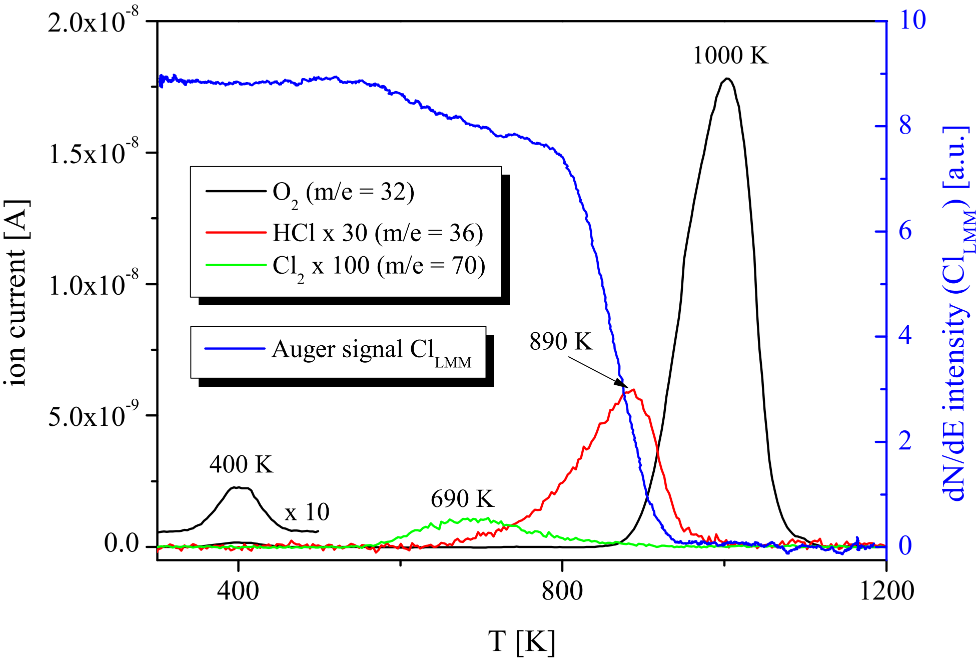

Figure 15.1: Combined plot of both a thermal desorption spectrum and a TP-Auger spectrum of chlorinated ruthenium dioxide (110).

At temperatures around $T = 700$ K, the prevailing process which accounts for chlorine loss from the surface should be the recombinative desorption of two Cl_{ot} atoms to form Cl_2. However, the tail of the HCl peak ($T_{max} = 890$ K) reaches down to $T = 680$ K, i.e. a desorption of Cl_{br} atoms should be possible already at temperatures as low as $T = 700$ K, albeit with a small rate. A recombination of Cl_{br} with either Cl_{br} or Cl_{ot} to form Cl_2 should not be feasible at these temperatures in analogy to the DFT calculations for the recombination of O_{br} atoms on s-$RuO_2(110)$ by Reuter et al. [136].

The knowledge about the desorption of Cl_2 gained by TD spectroscopy was further enhanced by means of a thermal stability HRCLS experiment carried out at beamline I311 at MAX-lab in Lund.

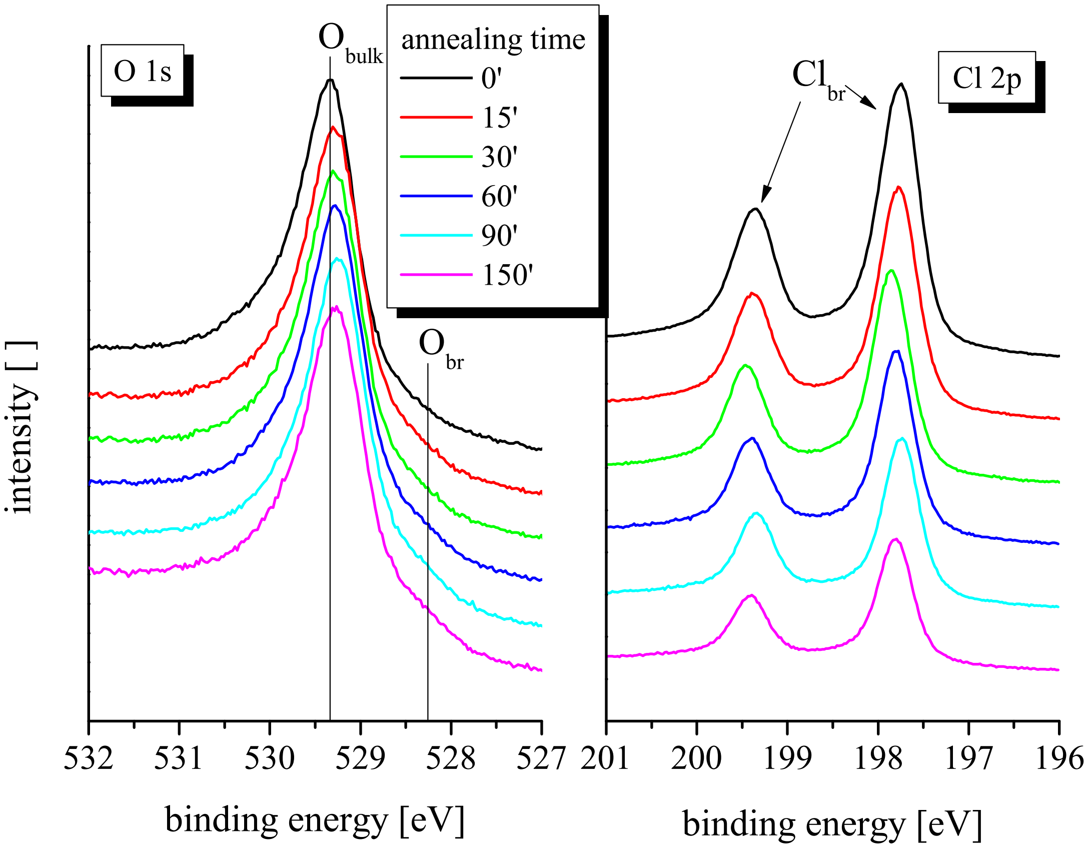

Figure 15.2: Thermal stability of $RuO_{2-x}Cl_x(110)$ at T = 700 K as followed by O 1s and Cl 2p HRCLS spectra.

Starting from chlorinated $RuO_{2-x}Cl_x(110)$, the sample was annealed at T = 700 K for a cumulated time span of 150 min (increments: 15', 15', 30' 30', 60'). After each annealing step, Cl 2p and O 1s HRCLS spectra were recorded in order to follow the changes in surface chemical composition upon annealing. The spectra are compiled in figure 15.2. Spectral assignments are based on table 12.1. Upon heating, the chlorine content decreases steadily with time as can be seen from figure 15.3. At a temperature of T = 700 K only bridging chlorine species Cl_{br} should be present on the surface, since Cl_{ot} readily recombines at this temperature and leaves the surface as Cl_2.

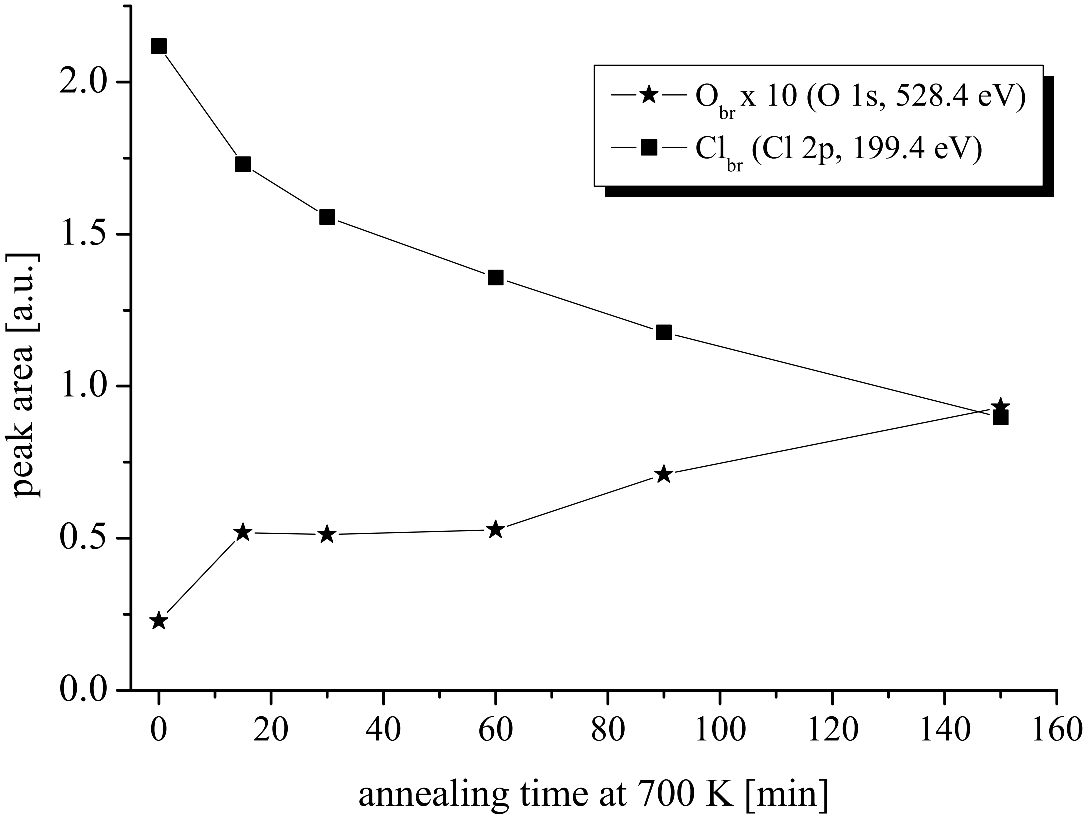

Figure 15.3: Thermal stability of $RuO_{2-x}Cl_x(110)$ at T = 700 K: Plot of the HRCLS peak areas corresponding to Cl_{br} (squares) and O_{br} (stars) versus annealing time. The oxygen peak areas are multiplied by a factor of 10 for better visibility reasons.

With gradual chlorine loss (factor of 2.2 ± 0.5 after 150 min), the HRCLS signal in the O 1s spectra assigned to bridging oxygen O_{br} at 528.4 eV increased in intensity (cf. figure 15.3) by a factor of 4 ± 1 after 150 min. Obviously, the bridging Cl_{br} atoms are replaced by O_{br} during the annealing step; a process which is relatively slow, since otherwise the high temperature Cl_{br} desorption signal in the TD spectrum would be shifted to lower temperatures (cf. figure 15.1). The only source of oxygen atoms under the present experimental conditions (UHV, no oxygen supply from the gas phase besides residual gas, $p_{BG} < 1 \times 10^{-10}$ mbar) to substitute the Cl_{br} atoms is from the bulk of RuO_2.

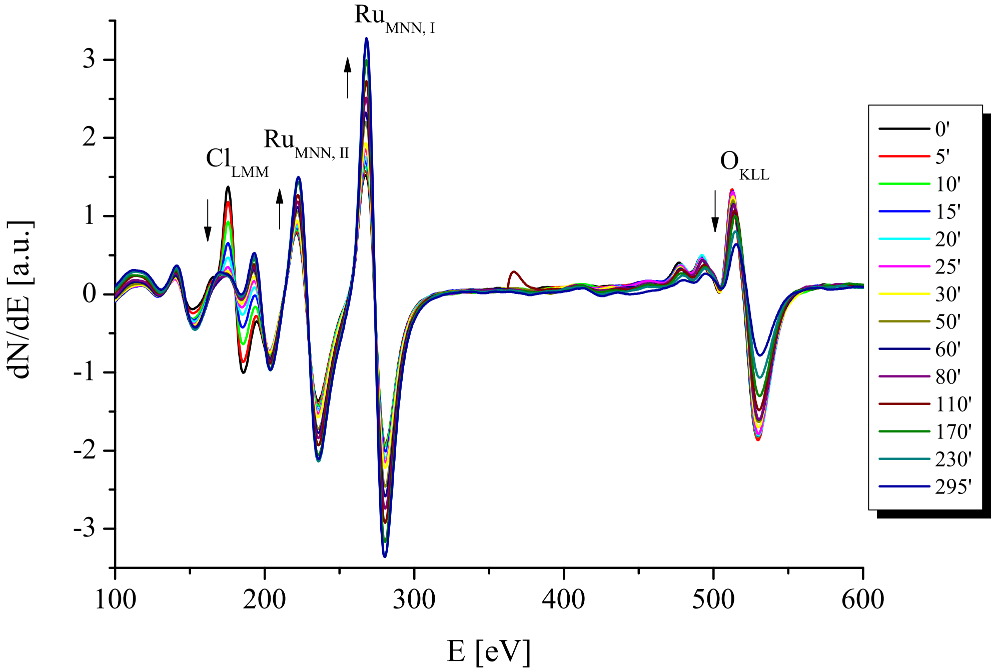

Figure 15.4: Auger electron spectra of chlorinated $RuO_2(110)$ ($U_b = 3$ kV, $T = 700$ K). Upon thermal treatment of the sample at $T = 700$ K, chlorine leaves the surface, indicated by the continuous loss of intensity of the Cl_{LMM} peak. With increasing annealing time, a loss in the O_{KLL} signal could be observed, starting after most of the Cl atoms have left the surface. The Ru_{MNN} peaks rise in intensity because the Ru atoms are gradually uncovered upon Cl/O loss. The background pressure during heating the sample in the UHV chamber was $p_{BG} = 3 \times 10^{-9}$ mbar.

The thermal stability of $RuO_{2-x}Cl_x(110)$ at T = 700 K was studied experimentally by HRCLS under UHV conditions. However, the influence of a higher background pressure ($p_{BG} = 3 \times 10^{-9}$ mbar instead of $p_{BG} < 1 \times 10^{-10}$ mbar), was checked by means of Auger electron spectroscopy. To unravel the behaviour of $RuO_{2-x}Cl_x(110)$ upon thermal treatment, the chlorinated oxide $RuO_{2-x}Cl_x(110)$ was hold at T = 700 K in UHV ($p_{BG} = 3 \times 10^{-9}$ mbar) and Auger spectra were recorded after certain time intervals of annealing. The spectra are displayed in figure 15.4.

Figure 15.5 shows the peak-to-peak height of the Auger peaks of Cl_{LMM}, Ru_{MNN}, and O_{KLL} plotted versus the annealing time at T = 700 K.

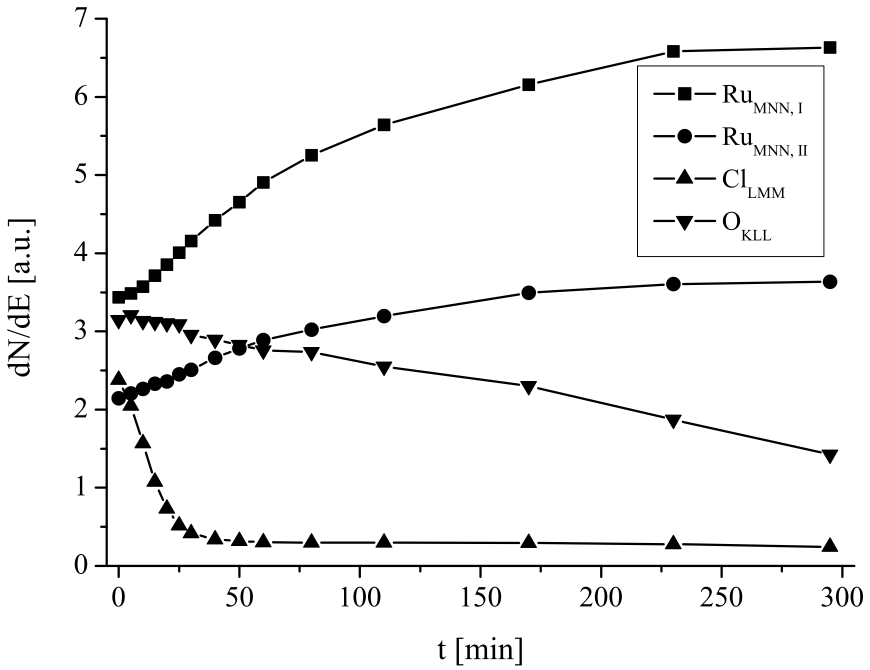

Figure 15.5: Time development of the Auger intensities of Cl_{LMM}, O_{KLL}, and Ru_{MNN} peaks with increasing annealing time at T = 700 K.

In contrast to the HRCLS experiment, the chlorine content dropped to a constant value already after 30 min. After the biggest amount of Cl atoms has left the surface, the oxygen O_{KLL} signal began to decrease steadily. Concomitant with the thermal degradation of the oxide, the Ru_{MNN} signals started to rise, indicating that the surface was being reduced. A qualitative LEED analysis of this phase showed a clear Ru(0001)-2x2-O pattern, which is known to be the stable phase after removing the oxide by thermal treatment. Obviously, the higher background pressure led to a continuous removal of the bridging oxygen atoms either by CO oxidation or water formation. Once the bridging chlorine coverage is diminished by Cl_2 desorption, the reduction of the bulk oxide can proceed via CO and H_2 from the residual gas.

Later, it will be shown that under sufficient supply of oxygen from the gas phase, the RuO_2 film remains stable.

15.2 The $Cl_{br} \leftrightarrow Cl_{ot}$ Shift Reaction

As implied by the results of the thermal dechlorination, oxygen atoms are able to substitute Cl_{br} by O_{br} after shifting of the Cl_{br} atoms to on top positions. The interaction of O_2 supplied from the gas phase with the chlorine atoms on $RuO_{2-x}Cl_x(110)$ and the interconnected complex behaviour of the surface chlorination will be investigated in the following section by means of HRCLS, RAIRS, AES, and theoretically by DFT calculations.

15.2.1 HRCLS Study: O_2 Treatment of $RuO_{2-x}Cl_x(110)$

High resolution core level shift spectroscopy was applied to study the behaviour of $RuO_{2-x}Cl_x(110)$ upon exposing the chlorinated oxide to 10 L of O_2 at various temperatures up to $T = 700$ K. The measurements were conducted by M. Knapp and S. Zweidinger at beamline I311, MAX-lab in Lund (November 2007).

The chlorinated $RuO_2(110)$ surface was exposed to 1 L of HCl at $T = 500$ K. Afterwards the sample was flashed to $T = 650$ K to desorb HCl_{ot} and a XP spectrum was recorded. The corresponding Cl 2p spectra are summarised in figure 15.6. The typical doublet signature of Cl_{br} on a clean, chlorinated $RuO_{2-x}Cl_x(110)$ showed up at 199.2/197.6 eV. Subsequently, the surface was exposed to 10 L of O_2 at $T = 420$ K. Again, a XP spectrum was recorded. At 196.1 eV a peak emerged, which is assigned to Cl_{ot}, whereby the Cl $2p_{1/2}$ emission of this species overlaps with the Cl $2p_{3/2}$ feature of the more abundant Cl_{br}. The sample was subsequently exposed to 10 L O_2 at $T = 500$ K, which led to a further increase of the Cl_{ot} emissions and a decrease of Cl_{br}. Upon exposing the surface to 10 L O_2 at $T = 600$ K and $T = 700$ K, both the Cl_{ot} and Cl_{br} intensities decreased due to desorption of Cl_2. The integrated intensities of the Cl 2p emissions for both Cl_{ot} and Cl_{br} are plotted versus the annealing temperature in figure 15.7.

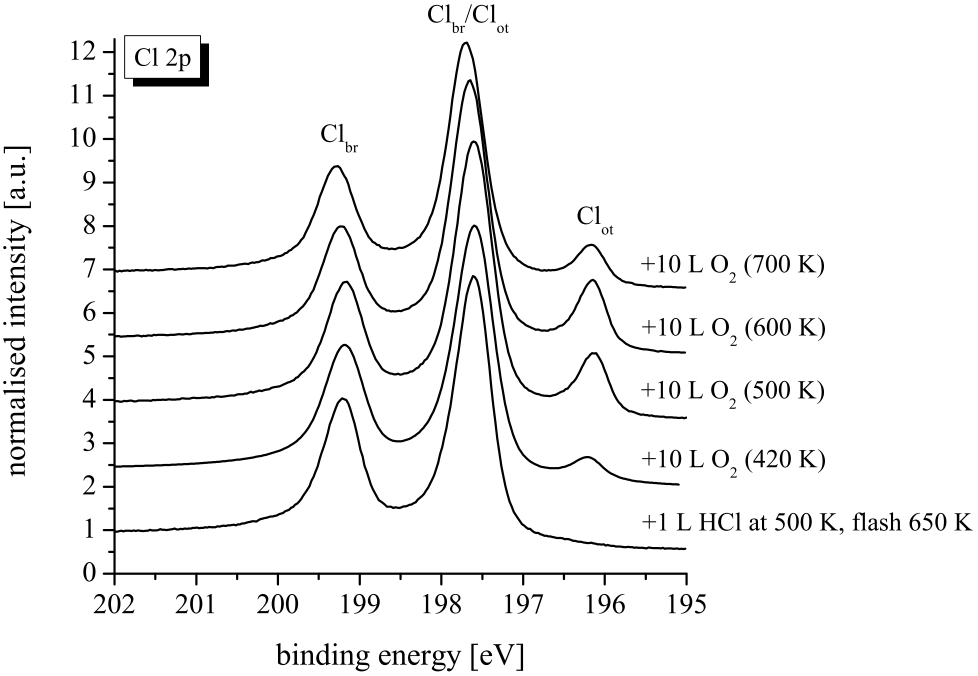

Figure 15.6: Cl 2p HRCL spectra of $RuO_{2-x}Cl_x(110)$ which was exposed to 10 L O_2 at various temperatures, as indicated in the plot.

The temperature evolution of the intensities (figure 15.7) of the Cl 2p emissions upon exposing the sample to 10 L of O_2 indicates that with increasing temperature, more and more Cl_{br} is transferred to on top positions, as evidenced both by an increase in the Cl_{ot} emissions and a decrease of the Cl_{br} signals. The steady increase of the Cl_{ot} integral up to $T = 500$ K shows accumulation of Cl_{ot} on the 1f-cus rows. At temperatures of $T > 600$ K, the recombinative desorption of Cl_{ot} sets in, leading to a decrease in the Cl_{ot} emission integral. The loss of bridging chlorine atoms proceeds via a shift of Cl_{br} from a bridging to a 1f-cus Ru site. The total surface concentration of Cl decreases by this process.

A similar experiment will be presented in the next section, where the decrease of the chlorine surface concentration at $T = 700$ K in oxygen atmosphere was monitored by means of RAIRS spectroscopy, applying CO as a probe molecule.

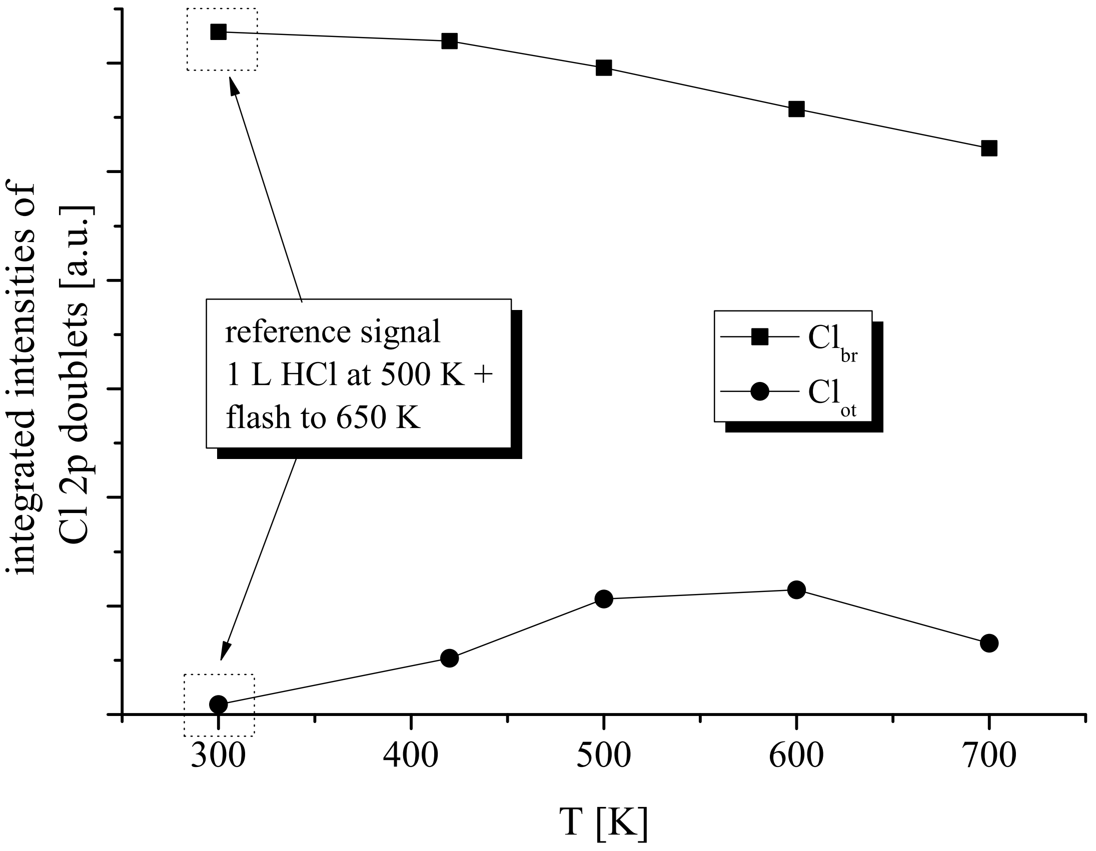

Figure 15.7: Integrated intensities of the Cl 2p emission doublets of Cl_{br} (199.2/197.6 eV) and Cl_{ot} (197.7/196.1 eV). The HRCLS spectra were recorded after the surface was exposed to 10 L of O_2 at the temperatures indicated on the abscissa.

15.2.2 RAIRS Study: O_2 Treatment of $RuO_{2-x}Cl_x$(110) at T = 700 K

The influence of an O_2 atmosphere on $RuO_{2-x}Cl_x$(110) upon heating the surface to $T = 700$ K, was investigated by means of RAIRS complementing the HRCLS results of the previous section. $RuO_{2-x}Cl_x$(110) will be exposed to oxygen at $T = 700$ K to study the chlorine loss. At $T = 700$ K, the bridging Cl_{br} atoms shift gradually to on top positions from where they desorb as Cl_2. The bridging vacancies are in turn filled by oxygen as shown in chapter 15.1.

Stoichiometric RuO_2(110) was chlorinated following the standard procedure (cf. chapter 9.3) and flashed to $T = 700$ K to desorb Cl_{ot} atoms and thus, to get a pristine $RuO_{2-x}Cl_x$(110) surface. This surface was flashed in oxygen (5×10^{-8} mbar) to $T = 673$ K, and afterwards flashed to $T = 700$ K without oxygen exposure to desorb O_{ot} and Cl_{ot}. After flashing, the chlorinated ruthenium dioxide was saturated by 6 L CO at $T < 230$ K and a RAIR spectrum was recorded. The corresponding RAIR spectra are shown in figure 15.8, the spectral details are compiled in table 15.1.

Taking the RAIR spectrum of a CO saturated s-RuO_2(110) as a reference ($\tilde{\nu}$(CO) = 2121 cm^{-1}), the CO absorption band experiences a redshift to $\tilde{\nu}$(CO) = 2112 cm^{-1} upon chlorination and restoration. The number of 1f-cus Ru adsorption sites accessible for CO adsorption has decreased, as indicated by the 30% smaller peak area of the CO absorption line (cf. table 15.1).

After four more restoration procedures, each followed by a RAIRS experiment with CO saturation of the on top sites, the CO absorption shifts by $\Delta\tilde{\nu}$(CO) = +2 cm^{-1} to $\tilde{\nu}$(CO) = 2114 cm^{-1} and the integral of the CO RAIRS line increased further.

Subsequently, the surface was exposed to 5×10^{-8} mbar of oxygen at $T = 700$ K for 30 min. After this thermal treatment in oxygen, the chlorine has left the surface almost completely. This is in accordance with the findings of the previous section, where annealing to $T = 700$ K in UHV led to the almost complete desorption of chlorine from the surface. After saturation of the surface by 6 L CO at $T < 230$ K, a RAIR spectrum was recorded to analyse the modification of the adsorbate structure during the roasting step. The corresponding spec-

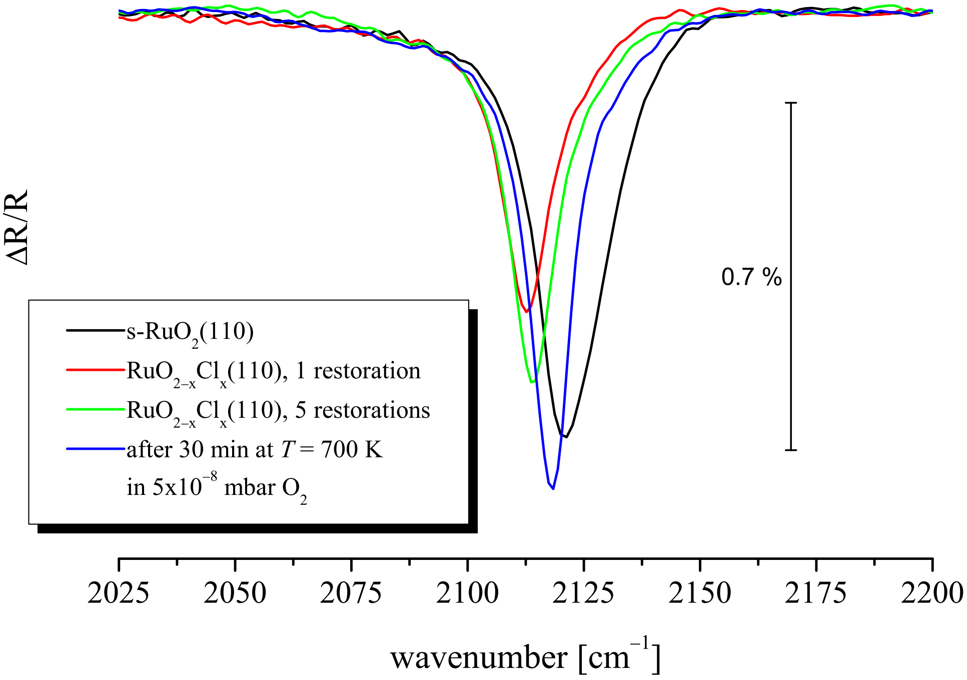

Figure 15.8: Influence of oxygen exposure at $T = 700$ K on the chlorine content of chlorinated $RuO_2(110)$ after 1 and 5 restoration procedures and after annealing in oxygen for 30 min at $T = 700$ K. The RAIR spectra show the CO absorption at saturation coverage (6 L CO at $T < 230$ K) on $RuO_{2-x}Cl_x(110)$.

trum in figure 15.8 shows a higher wavenumber absorption of CO adsorbed on $RuO_{2-x}Cl_x(110)$ at $\tilde{\nu}(CO) = 2118$ cm^{-1}. According to this blue shift, the surface now resembles more a s-$RuO_2(110)$ than a chlorinated one. In addition, the amount of adsorbed CO (as determined from the integrated RAIRS absorption) is equal to that of stoichiometric $RuO_2(110)$. This corroborates the transformation of the chlorinated oxide back into an almost stoichiometric one by roasting for prolonged periods in molecular oxygen.

The data of the peak fit of the RAIR spectra shown in figure 15.8 are compiled in table 15.1.

system	$\tilde{\nu}$(CO)[cm^{-1}]	area [a.u.]	FWHM [cm^{-1}]
s-$RuO_2(110)$	2121	0.17	17.5
$RuO_{2-x}Cl_x(110)$, 1 restoration	2112	0.12	13.4
$RuO_{2-x}Cl_x(110)$, 5 restorations	2114	0.14	12.7
$RuO_{2-x}Cl_x(110)$, 30 min at 700 K in 5×10^{-8} mbar O_2	2118	0.17	11.5

Table 15.1: Peak positions, peak areas and FWHM of the CO RAIRS absorptions.

The corresponding Auger spectra of the initial state of the chlorinated surface and after the five restorations and 30 min of roasting are displayed in figure 15.9. Auger spectroscopy revealed that the chlorine content of the oxide decreased by 57 %.

The initial amount of chlorine was 0.63 Cl atoms per $RuO_2(110)$ surface unit cell. If one assumes that all Cl atoms are residing in bridging positions, the degree of bridge chlorination would be 63% Cl_{br}. During reaction of $RuO_{2-x}Cl_x(110)$ with O_2 at $T = 700$ K most of the chlorine has left the surface. One can thus assume a minimum chlorine coverage of $RuO_{2-x}Cl_x(110)$ of 0.27 Cl atoms per surface unit cell after the oxygen treatment. Furthermore, the Auger electron spectra show that the oxygen content of the bulk oxide remained nearly constant. This implies that the underlying $RuO_2(110)$ substrate has not changed its composition or has not been reduced.

15.2.3 The $Cl_{br} \leftrightarrow Cl_{ot}$ Shift Reaction

The shift reaction which transfers $Cl_{br} \rightarrow Cl_{ot}$ is dependent on the presence of O atoms, since a substitution of Cl_{br} by O_{br} leads to a thermodynamically more stable situation on the surface. In the following, the influence of CO supplied

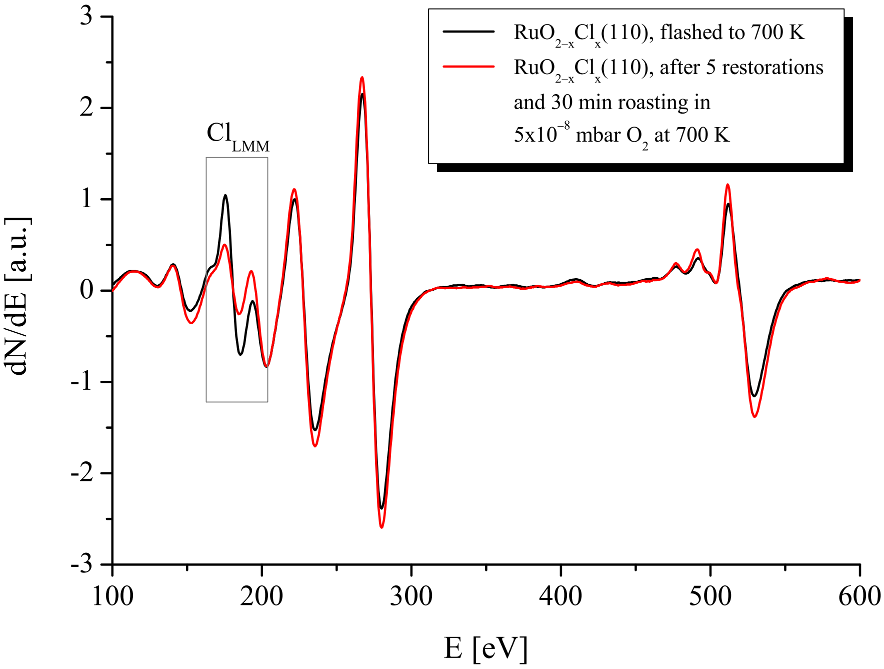

Figure 15.9: Auger electron spectra (E = 3 keV) of pristine $RuO_{2-x}Cl_x(110)$ (black curve) and of $RuO_{2-x}Cl_x(110)$ after multiple restorations in O_2 and roasting in oxygen ($T = 700$ K, 30 min, $p(O_2) = 5 \times 10^{-8}$ mbar, red curve).

from the gas phase on the $Cl_{br} \leftrightarrow Cl_{ot}$ shift reaction and thereby its effect on the dynamics of the surface chlorine atoms on $RuO_{2-x}Cl_x(110)$ will be studied by means of TDS and RAIRS as well as DFT calculations.

TDS Study: Multiple Restorations of $RuO_{2-x}Cl_x(110)$

To further investigate the impact of oxygen on the chlorination of $RuO_{2-x}Cl_x(110)$, thermal desorption spectroscopy has been utilised to determine the influence of repeated oxygen restorations on the chlorinated surface. The TDS experiments were conducted by S. Zweidinger [137].

Stoichiometric $RuO_2(110)$ has been prepared after the standard procedure (cf. chapter 9.2). The surface was restored in O_2 (flashed to $T = 600$ K and cooled to $T = 300$ K in $p(O_2) = 1 \times 10^{-8}$ mbar). The restored, and O_{ot} covered surface was then flashed to $T = 600$ K and a TD spectrum was taken following the signals of water ($\frac{m}{e} = 18$) and oxygen ($\frac{m}{e} = 32$). The oxygen desorption signals of each of the eight consecutive restorations were taken as reference signal for the unoccupied, chlorine-free 1f-cus rows. The O_2 desorption signal during flashing the surface, following a restoration in oxygen, will serve as a measure for the coverage of the 1f-cus Ru sites by Cl_{ot} (the more Cl_{ot} is present, the smaller is the O_2 desorption signal and vice versa). The more on top sites are occupied by Cl_{ot}, the less O_{ot} can adsorb on the cus-rows, yielding a smaller O_2 desorption signal in the TD spectrum.

Figure 15.10 displays the integrated O_2 desorption signals of the TD experiments. The first five data points represent the oxygen desorption from the stoichiometric $RuO_2(110)$. The variation of these points gives an estimate of the reproducibility of the restoration procedure, which amounts to ±2% (the first restoration has been dismissed). In the next step, the stoichiometric $RuO_2(110)$ has been chlorinated by exposure to 15 L H_2 at room temperature followed by a flash to $T = 700$ K in $p(HCl) = 5 \times 10^{-8}$ mbar. The chlorinated oxide was then restored applying the same procedure like described above for s-$RuO_2(110)$. TD spectra (up to $T = 600$ K) have been recorded after each restoration.

One can clearly see the decline of the integrated O_2 desorption signal from initially 74 % of the maximum O_2 desorption after the first restoration to 44 % after the seventh restoration. This implies that with increasing number of restoration steps the amount of free 1f-cus Ru sites available for adsorption of

O_{ot} decreases. This result shows that with each restoration step, the amount of Cl_{ot} adsorbed on the 1f-cus Ru sites increases at the expense of the degree of chlorination of the bridging sites.

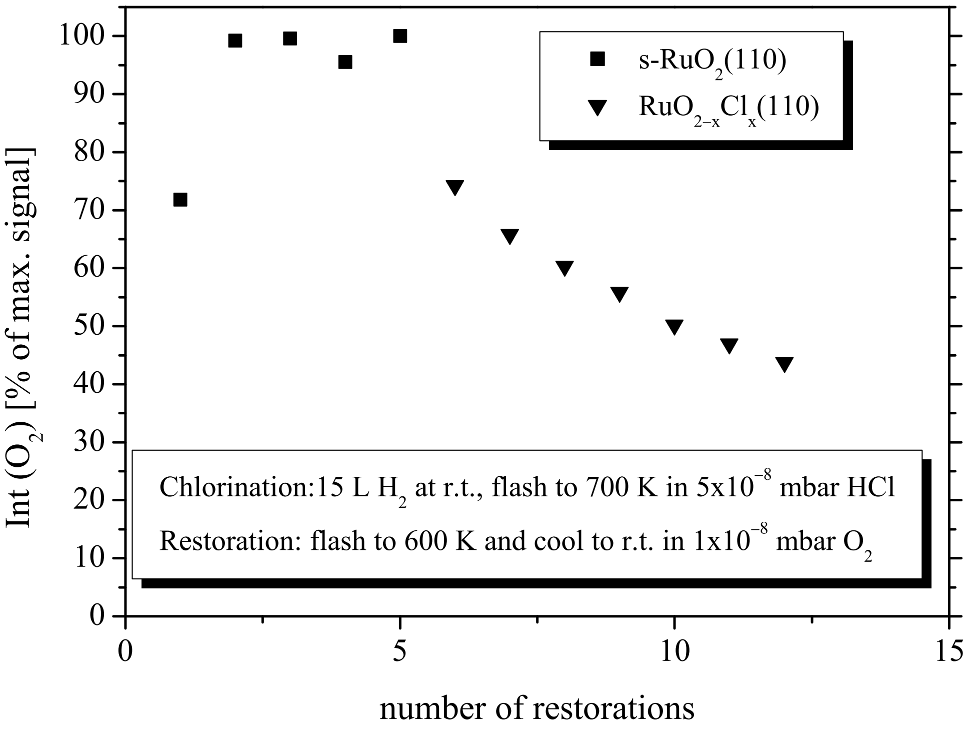

Figure 15.10: Integrated O_2 thermal desorption signals ($\frac{m}{e} = 32$) from O saturated s-$RuO_2(110)$ and $RuO_{2-x}Cl_x(110)$, respectively after multiple restoration procedures in oxygen.

TDS Study: Multiple Restorations of $RuO_{2-x}Cl_x(110)$ with intermediate CO treatment

A different situation emerges if the restoration steps are followed by CO saturation of the 1f-cus Ru rows, in order to probe the surface by means of RAIR spectroscopy. Under these circumstances, the surface experiences only minor changes in composition, as will be shown by RAIR spectroscopy. In order to assess the influence of the CO probe molecules on the restoration process and therewith on the chlorination, the reaction taking place under these experimental conditions was also studied by TDS, similar to the previous section.

The following experiments have been carried out starting from a freshly prepared stoichiometric $RuO_2(110)$ surface. As already described above, the stoichiometric surface was restored in oxygen atmosphere four times, in order to get a calibration reference for the maximum amount of adsorbed O_{ot} on stoichiometric $RuO_2(110)$. Figure 15.11 displays the integrated O_2 thermal desorption signals from s-$RuO_2(110)$ or $RuO_{2-x}Cl_x(110)$, respectively, taken after each restoration. For the stoichiometric oxide, a reproducibility of ±5 % has been obtained. Afterwards, s-$RuO_2(110)$ was chlorinated following the standard procedure (cf. chapter 9.3) and flashed to $T = 700$ K to desorb excess HCl_{ot} and Cl_{ot}. After chlorination, the surface was restored (flash to $T = 675$ K in 5×10^{-8} mbar O_2, followed by TDS), subsequently cooled down to $T = 200$ K and saturated by dosing 10 L CO. CO was desorbed during a flash to $T = 700$ K and the next restoration cycle started. All in all, eight of these cycles were carried out. The O_2 desorption signals displayed in figure 15.11 remain nearly constant at (51.6±2.3) % of the maximum achievable O_2 desorption signal measured on s-$RuO_2(110)$.

If chlorine atoms were shifted and accumulated from Cl_{br} to on top sites, the O_2 desorption signal would have dropped as observed in the previous TDS experiment (cf. figure 15.10). A chlorine loss by desorption upon flashing to $T = 700$ K via recombination of two neighbouring Cl_{ot} atoms would have led to a ‘more’ stoichiometric surface, i.e. a continuous decrease of the surface concentration of chlorine. This chlorine loss should have led to a stepwise higher O_2 desorption feature, approaching the value observed for stoichiometric $RuO_2(110)$. However, this increase has not been observed, leading to the conclusion that the chlorine content did not change during this experiment. An explanation of the constancy of the observed integrated O_2 TD signal will be proposed in the following.

RAIRS Study: Multiple Restorations of $RuO_{2-x}Cl_x(110)$ with intermediate CO treatment

The stability of the concentration of surface chlorine atoms upon CO saturation between the restoration procedures was also corroborated by the following RAIRS experiment, where only minor changes in the RAIRS absorption were detected.

Starting from freshly chlorinated and flashed $RuO_{2-x}Cl_x(110)$, the surface

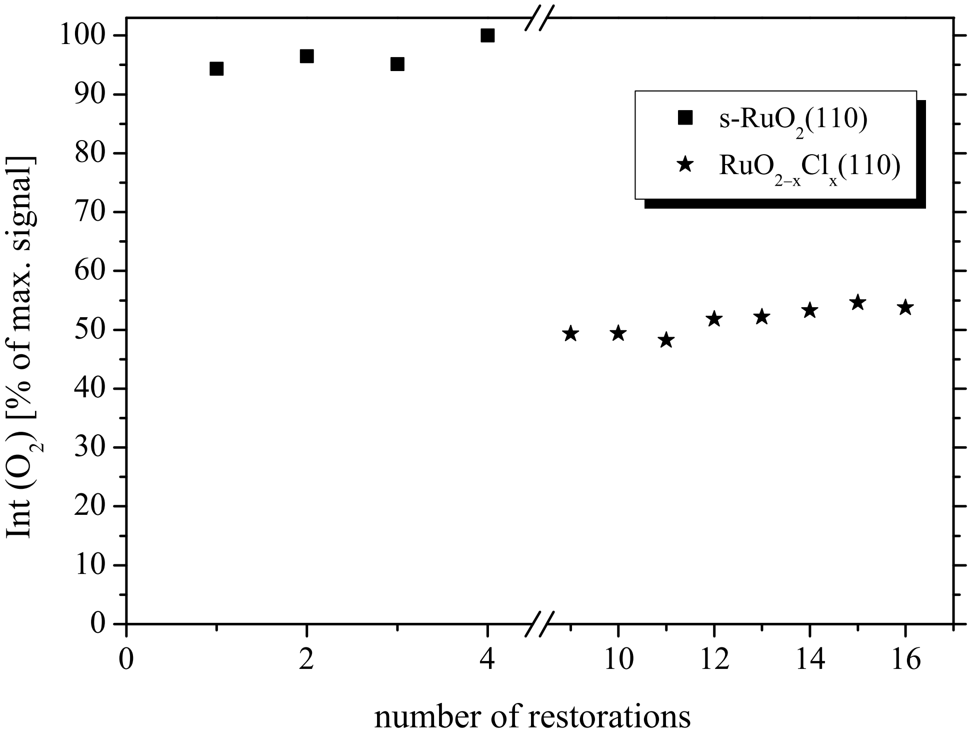

Figure 15.11: Integrated O_2 thermal desorption signals from O saturated $RuO_{2-x}Cl_x(110)$ after multiple restoration procedures in oxygen and CO treatment in between. This TDS experiment is necessary to assess the influence of the IR probe molecule CO on the restoration process of $RuO_{2-x}Cl_x(110)$ by oxygen.

was restorated in oxygen (flash to T = 673 K in $p(O_2) = 5 \times 10^{-8}$ mbar) and then probed in RAIRS with CO (6 L at $T < 230$ K). This cycle was repeated five times and the corresponding RAIR spectra are compiled in figure 15.12.

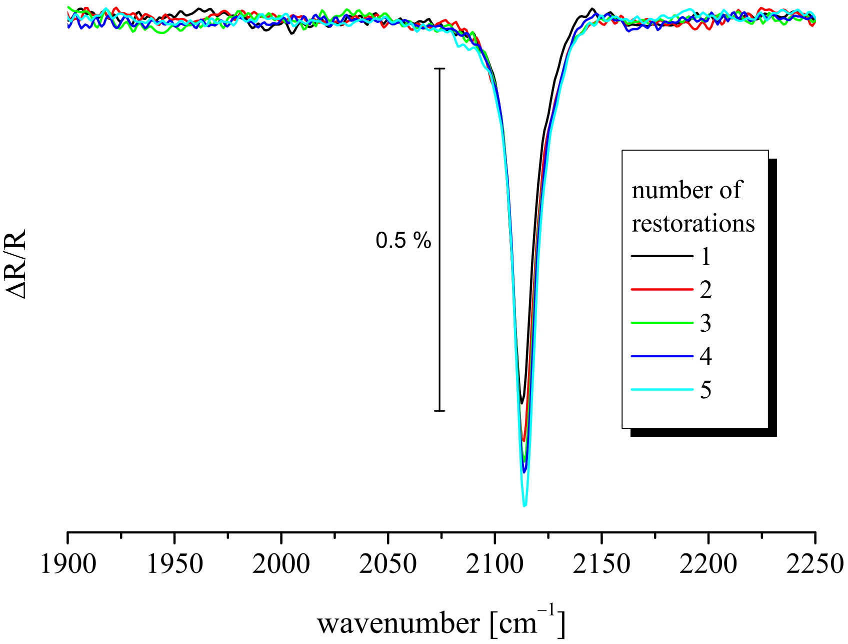

Figure 15.12: RAIR spectra of CO adsorbed at saturation coverage on repeatedly restored $RuO_{2-x}Cl_x(110)$. The number of restorations is given in the legend.

Upon multiple restoration, the RAIRS features of CO adsorbed on the restored, chlorinated oxide experienced only marginal changes. The shift in the wavenumber of the CO absorption peak after 5 restorations amounted to $\Delta\tilde{\nu}$(CO) = +2 cm^{-1} (from 2112 to 2114 cm^{-1}) indicating only a small percentage of chlorine loss, presumably by recombinative desorption of Cl_{ot}. Although the increase of the intensity of the CO RAIRS absorption showed that a small amount of surface Cl atoms left the surface, it was not transformed into a stoichiometric $RuO_2(110)$ surface. This has only been achieved to a significant extent by 30 min annealing to T = 700 K in $p(O_2) = 5 \times 10^{-8}$ mbar (cf. figure 15.8).

In conclusion, CO has hindered the loss of surface Cl atoms by reduction of O_{br} atoms, thus making vacancies available that could be refilled by Cl_{ot} atoms. This conclusion is further substantiated by the finding of the CO-induced chlorination of $RuO_2(110)$ by Cl_2 exposure, as reported in section 12.5. The CO induced rechlorination reaction takes place at temperatures below $T = 700$ K, when in the presence of CO the major part of the Cl_{ot} atoms is transferred back into the bridging rows before the recombinative desorption sets in. This explains why the surface chlorine content was observed to be relatively stable during both TDS and RAIRS experiments described above. The shift of $Cl_{ot} \rightarrow Cl_{br}$ in the presence of CO emerges as the salient feature of the TD and RAIRS experiments described in the present section. Together with the oxygen induced $Cl_{br} \rightarrow Cl_{ot}$ shift, the interplay of both reactions accounts for dynamics on the $RuO_{2-x}Cl_x(110)$ surface. In the following, the mechanism of the shift reaction will be treated by means of DFT calculations.

DFT Study: Mechanism of the $Cl_{br} \leftrightarrow Cl_{ot}$ Shift Reaction

DFT calculations were used at this point to study the energetics lying behind the observed oxygen induced $Cl_{br} \rightarrow Cl_{ot}$ shift reaction on $RuO_{2-x}Cl_x(110)$. The reaction mechanism was modelled for the case that oxygen is available as on top oxygen as supplied from the gas phase after dissociative adsorption of O_2 on the 1f-cus Ru sites.

Figure 15.13 shows the relevant structures involved in the oxygen induced $Cl_{br} \rightarrow Cl_{ot}$ shift reaction. The thermodynamically more stable configuration is present when Cl is accommodated on an on top site and an O atom occupies a bridging position. The energy difference of 0.25 eV accounts for the driving force towards shifting more and more $Cl_{br} \rightarrow Cl_{ot}$ upon O_2 exposure. The presence of CO on the surface leads in turn to a thermodynamically by 0.61 eV more stable situation, when Cl sits in a bridging position and CO occupies a 1f-cus Ru site. As already mentioned in chapter 12 in connection with the chlorination mechanism, the (re)-chlorination of the bridge site has to be promoted by either H_2 (water formation) or by CO (CO oxidation) exposure to form better leaving groups.

According to these results, one may summarise the reaction steps taking place during the $Cl_{br} \leftrightarrow Cl_{ot}$ shift reaction in the presence of CO and O on the surface:

- *dechlorination*
  - dechlorination in O_2 atmosphere: $Cl_{br} + O_{ot} \rightarrow Cl_{ot} + O_{br}$
  - thermal dechlorination in UHV: $Cl_{br} + O_{bulk} \rightarrow Cl_{ot} + V_{bulk} + O_{br}$

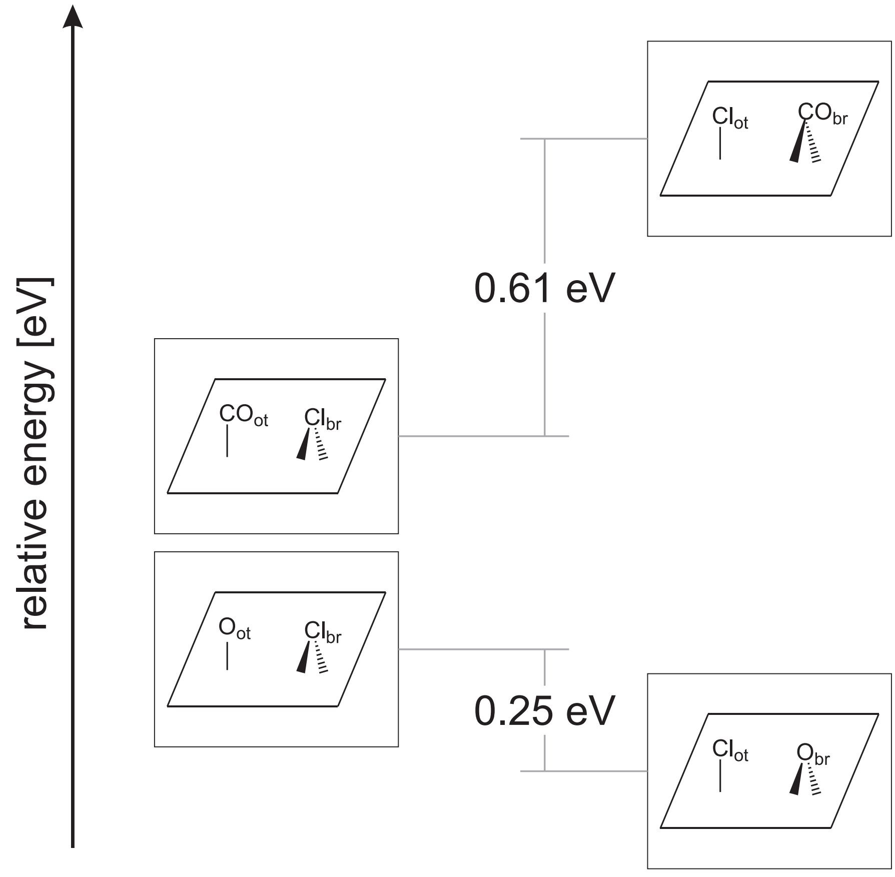
relative energy [eV]
Cl$_{ot}$
CO$_{br}$
0.61 eV
CO$_{ot}$
Cl$_{br}$
O$_{ot}$
Cl$_{br}$
0.25 eV
Cl$_{ot}$
O$_{br}$

Figure 15.13: Relative energies for the Cl_{br} ↔ Cl_{ot} shift reaction as determined by DFT calculations. All calculation were done on a 2x2 $RuO_2(110)$ surface unit cell.

  - chlorine loss from the surface at $T > 700$ K: 2 $Cl_{ot} \rightarrow Cl_2$(gas)

- *rechlorination in the presence of CO*
  - 2 $CO_{ot} + O_{br} \rightarrow CO_2(\text{gas}) + CO_{br}$
  - $Cl_{ot} + CO_{br} \rightarrow Cl_{br} + CO_{gas}$

15.2.4 CO RAIRS Double Feature after Restoration of $RuO_{2-x}Cl_x(110)$ in O_2

If chlorinated $RuO_{2-x}Cl_x(110)$ is treated by O_2 in terms of a standard restoration procedure as described for s-$RuO_2(110)$ (cf. chapter 9.2), where the sample was flashed not higher than to $T = 550$ K , one can observe a CO absorption feature in the RAIR spectrum after CO saturation at low temperatures, which exhibits two maxima. They are located at $\tilde{\nu}(CO) = 2112$-2114 cm^{-1} and $\tilde{\nu}(CO) = 2125$-2128 cm^{-1}, and the intensity ratio depends on the annealing temperature after the restoration step. Figure 15.14 illustrates the RAIR spectra for different restoration procedures, subsequently carried out on the same initial $RuO_{2-x}Cl_x(110)$. The most prominent high frequency feature has been obtained by flashing the surface after restoration to $T = 473$ K.

The RAIRS signal at higher wavenumbers is present up to an annealing temperature of about 600 K. Flashing the O_{ot} covered surface after restoration to $T = 700$ K led to the disappearance of the high frequency component of the double peak, yielding a single absorption band centered around $\tilde{\nu}(CO) = 2112$-2114 cm^{-1}. From former experiments, this band is known to belong to extended rows of CO adsorbed on the 1f-cus Ru sites, denoted as $(Cl_{br}+O_{br})/CO_{ot}$. The high frequency component should stem from a coadsorbate constituted of CO_{ot} and Cl_{ot} as well as O_{ot}. The more electronegative oxygen is responsible for the blue shift of the CO absorption band, as already shown in chapter 14.1.4. However, it was not possible to determine the amount of O_{ot} atoms remaining on the 1f-cus sites from the RAIR spectra, because the presence of both O_{ot} and Cl_{ot} lead to a shift of the CO adsorption band, each species to different extents.

To demonstrate the impact of O_{ot} on the observed spectra and to determine the reasons for the high threshold temperature for the disappearance of the double feature, the coadsorbate has been tempered to 350 K, a temperature where CO

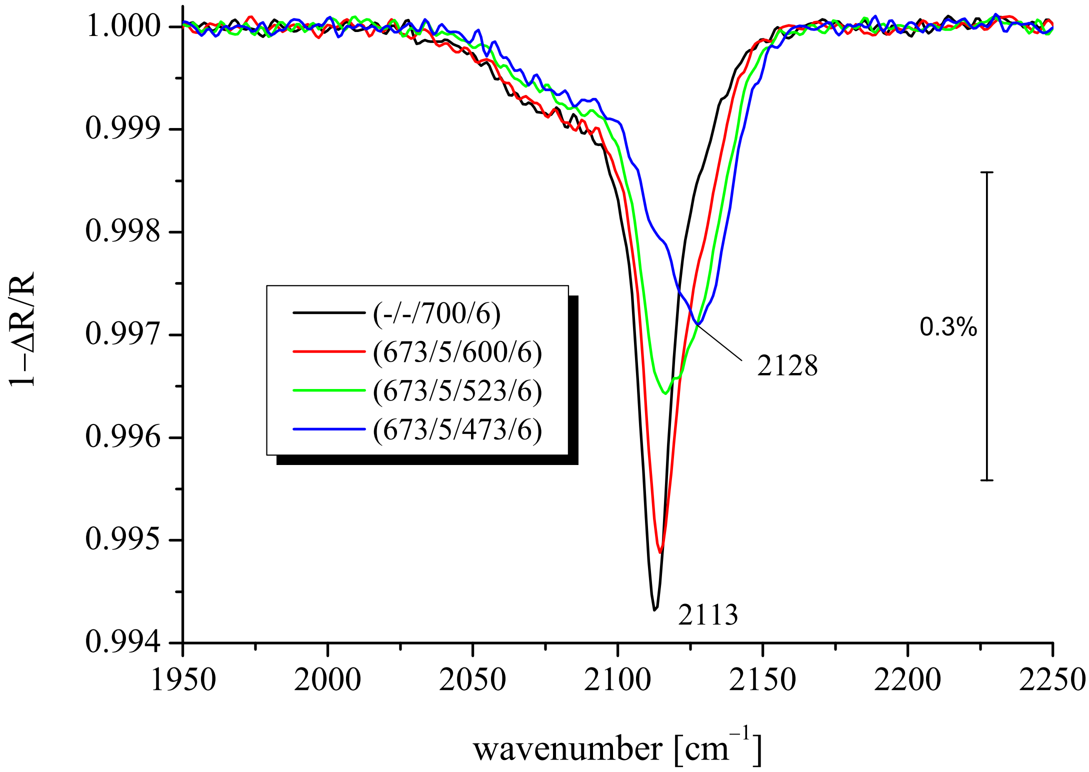

Figure 15.14: RAIR spectra of CO adsorbed on $RuO_{2-x}Cl_x(110)$, which was restored in oxygen and flashed to different temperatures. The spectra of the surface which was flashed to only $T < 600$ K exhibit a distinct double peak composed of a component centred at $\tilde{\nu}(CO) = 2112\text{-}2114\ cm^{-1}$ and another feature at $\tilde{\nu}(CO) = 2125\text{-}2128\ cm^{-1}$. The legend reads as follows: (T_{resto} [K] / in $p(O_2)$ [10^{-8} mbar]/ T_{flash} [K] / CO dosage at $T < 230$ K [L])

oxidation on $RuO_2(110)$ takes place, but no O_{ot} desorption is possible. This treatment led to a decrease of the component at $\tilde{\nu}(CO) = 2128$ cm^{-1} and an increase of intensity of the lower frequency component located at $\tilde{\nu}(CO) = 2112$ cm^{-1} (figure 15.15). This outcome can be explained by means of reaction of the O_{ot} species neighbouring CO_{ot} molecules to form CO_2 upon annealing to $T = 350$ K. This results in a smaller O_{ot} coverage, which led to a smaller intensity of the high wavenumber peak after saturation of the surface with CO at $T < 230$ K. In addition, annealing of a CO_{ot} phase on $RuO_{2-x}Cl_x(110)$ led to a depletion of Cl_{ot} species via the reversed $Cl_{br} \rightarrow Cl_{ot}$ shift reaction after the reaction of CO_{ot} with O_{br} to form bridging vacancies, as described in section 15.2.3. If this reaction would have not taken place, one would have expected an IR absorption at $\tilde{\nu}(CO) = 2105$ cm^{-1} (cf. section 14.1.3), which has not been observed in the spectra recorded within this experiment.

The reaction steps leading to the disappearance of the double feature under the presence of CO_{ot} will be summarised:

- $CO_{ot} + O_{ot} \rightarrow CO_2$
    - leads to a depletion of O_{ot}, i.e. a decrease of the high frequency RAIRS signal at $\tilde{\nu}(CO) = 2125$ cm^{-1} and an increase of the lower frequency component at $\tilde{\nu}(CO) = 2112$ cm^{-1} after saturation with 6 L CO at $T < 230$ K.
- $CO_{ot} + O_{br} \rightarrow CO_2$
    - leads to a depletion of Cl_{ot} via:
        * $2\ CO_{ot} + O_{br} \rightarrow CO_2 + V_{ot} + CO_{br}$
        * $CO_{br} + Cl_{ot} \rightarrow Cl_{br} + CO_{gas}$
    - resulting in the $\tilde{\nu}(CO) = 2112$ cm^{-1} absorption
    - no absorption at $\tilde{\nu}(CO) = 2105$ cm^{-1} has been observed, i.e. no Cl_{ot} is present (cf. chapter 14.1.3)

Thereby, the influence of O_{ot} on the CO absorption frequency in the presence of $Cl_{br/ot}$ has been experimentally confirmed. The argumentation is in line with all results stated above regarding CO_{ot} adsorption on $RuO_{2-x}Cl_x(110)$ on either

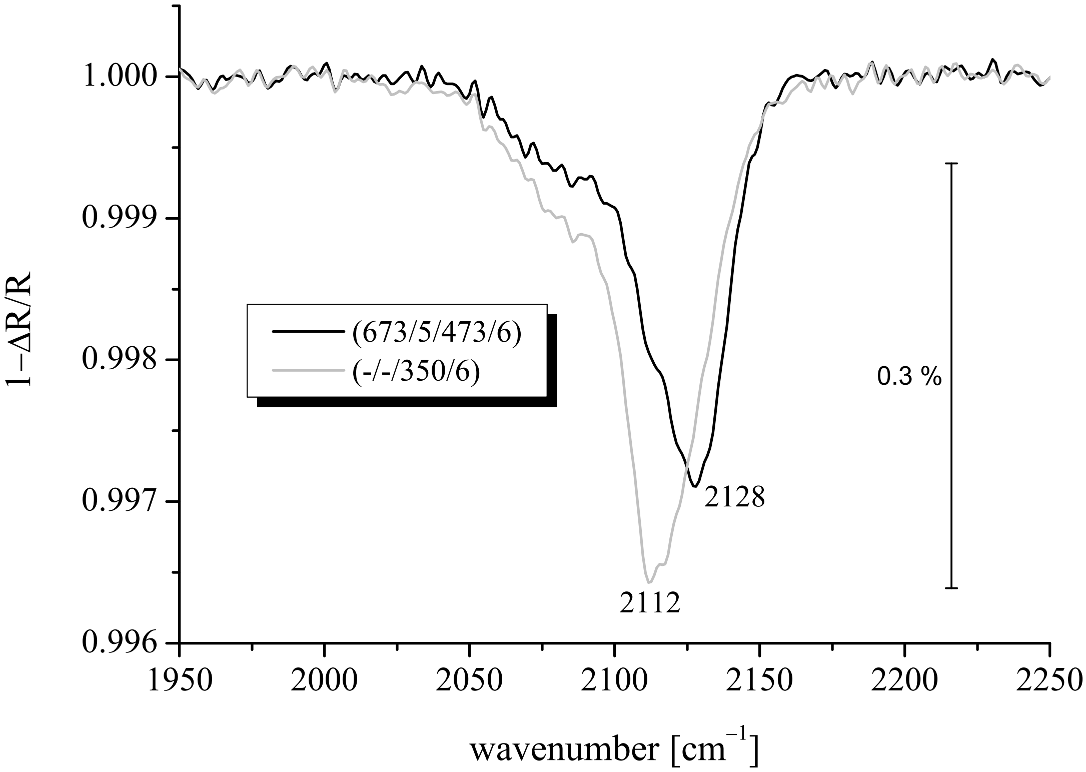

Figure 15.15: RAIR spectra of CO_{ot} adsorbed on restored $RuO_{2-x}Cl_x(110)$ (flash to $T = 673$ K in $p(O_2) = 5 \times 10^{-8}$ mbar). The surface was saturated by CO after a subsequent flash to $T = 473$ K. The corresponding RAIR spectrum (black) exhibits a stronger high frequency component at $\tilde{\nu}(CO) = 2128$ cm^{-1}. Annealing of this CO_{ot} saturated surface to $T = 350$ K resulted in a decrease of the $\tilde{\nu}(CO) = 2125$ cm^{-1} feature and an increase of the absorption at $\tilde{\nu}(CO) = 2112$ cm^{-1} (grey spectrum). The legend reads as follows: (T_{resto} [K] / in $p(O_2)$ [10^{-8} mbar] / T_{flash} [K] / CO dosage at $T < 230$ K [L]).

clean cus-rows (flash to $T = 700$ K after (re)-chlorination) or in the presence of Cl_{ot} (flash to $T = 550$ K after (re)-chlorination).

The experimental outcomes are further corroborated by DFT calculations concerning the relative energetics of both CO, O, and Cl adsorbates on $RuO_2(110)$, sitting either in on top or in bridging positions, respectively, as compiled in table 15.2 (cf. also figure 15.13).

ref#	**system**	**structure 1**	**structure 2**	$\boldsymbol{E_2 - E_1}$ **[eV]**
1	$RuO_2(110)$-2x2	$Cl_{ot} + O_{br}$	$Cl_{br} + O_{ot}$	0.25
2	$RuO_2(110)$-1x2	$CO_{ot} + O_{br}$	$CO_{br} + O_{ot}$	0.88
3	$RuO_2(110)$-1x2	$CO_{ot} + Cl_{br}$	$CO_{br} + Cl_{ot}$	0.61
4	$RuO_2(110)$-2x2	$V_{ot} + Cl_{br}$	$V_{br} + Cl_{ot}$	1.66
5	$RuO_2(110)$-1x1	$V_{ot} + O_{br}$	$V_{br} + O_{ot}$	1.15
6	$RuO_2(110)$-1x2	$1O_{br}+1Cl_{br}$	$2Cl_{br}$	0.37

Table 15.2: Compilation of relative DFT energies of adsorbate species on s-$RuO_2(110)$ and $RuO_{2-x}Cl_x(110)$

According to the relative energies listed in table 15.2, a structure where both chlorine and oxygen is present, is energetically by 0.25 eV more favourable, if chlorine sits on top of a 1f-cus Ru site and oxygen occupies the neighbouring bridging site ($Cl_{ot}+O_{br}$). If oxygen is substituted by carbon monoxide, the inverse situation, namely $CO_{ot} + Cl_{br}$, is energetically advantaged by 0.61 eV. These results, together with the previous experiments, allow for the following statements, which should be generally applicable for $RuO_{2-x}Cl_x(110)$:

1. *The presence of oxygen atoms on chlorinated* RuO_2*(110) forces a certain amount of chlorine atoms to shift from bridging positions to on top positions.*

2. *The presence of carbon monoxide molecules on chlorinated* RuO_2*(110) forces a certain amount of chlorine atoms to shift from on top positions to bridging positions.*

The phase yielding the double CO absorption feature will be denoted as $(Cl_{br}+O_{br})/(CO_{ot}+O^{sg}_{ot}+Cl_{ot})$. Finally, the very high desorption temperature of O_{ot} and therefore, the temperature dependence of the emerging CO double peak in the RAIRS spectra have to be interpreted.

For both s-$RuO_2(110)$ and $RuO_{2-x}Cl_x(110)$ the desorption temperature of O_{ot} has been reported to be approximately $T = 400$ K as already shown in figure

15.1. In the particular case, where the chlorinated oxide was exposed to O_2 during thermal treatment (restoration procedure), the above-mentioned $Cl_{br} \rightarrow Cl_{ot}$ shift reaction takes place, leading to a certain amount of Cl_{ot} on the 1f-cus Ru sites. Thus, one expects a coadsorbate of Cl_{ot} + O_{ot} on the cus-rows, which was then annealed to temperatures between T = 450-700 K in order to desorb the on top oxygen in terms of a standard restoration. During the flash, neighbouring O_{ot} atoms may recombine to desorb into the gas phase as O_2; the desorption should be centred at the typically observed O_{ot} desorption temperature at around $T = 400$ K. However, since Cl_{ot} is present, a situation may occur where a singular, isolated O_{ot} atom is surrounded by only Cl_{ot} species. Thus, a recombinative desorption of O_2 is frustrated and the isolated O_{ot} atoms are only able to desorb, when Cl_{ot} recombination sets in, which is typically observed at $T = 700$ K. This line of reasoning is able to explain the observed temperature dependence of the double-feature. Moreover, the results are in accordance with the findings of P. Krause et al. [138], who studied the coadsorption of HCl and oxygen on s-$RuO_2(110)$ by TD spectroscopy and observed a second, high temperature O_2 desorption from a HCl_{ot}+O_{ot} coadsorbate concomitant with the desorption of Cl_2 from the surface.

15.3 Discussion

The tendency of the maximally chlorinated surface to stabilise itself by partial dechlorination of the bridging positions, in order to reach a thermodynamically more stable bridging substitution pattern, leads to a $Cl_{br} \rightarrow Cl_{ot}$ shift reaction which is induced by oxygen atoms. The source of the substituting oxygen atoms can be either the underlying RuO_2 bulk substrate or O_{ot} atoms supplied by dissociative adsorption of O_2 from the gas phase. Since the only way how Cl_{ot} atoms can leave the surface at $T > 650$ K is the recombination to Cl_2, the chlorine loss from the surface (also from the bridging positions), will proceed via Cl_{ot} recombination. The recombination is promoted by the driving force of dechlorinating the bridging rows by means of substitution through O_{br}. In the case of thermal decomposition of $RuO_{2-x}Cl_x(110)$ under UHV conditions, O_{bulk} drives the $Cl_{br} \rightarrow Cl_{ot}$ shift reaction, whereas under O_2 atmosphere O_{ot} atoms lead to the shift reaction.

The oxygen mediated $Cl_{br} \rightarrow Cl_{ot}$ shift reaction turned out to be the key reaction for the observed dynamic behaviour of the Cl atoms on the $RuO_{2-x}Cl_x(110)$ surface. Experimental evidence was given by means of HRCLS, RAIRS, TDS and AES substantiating thereby the DFT calculated energetics of the reaction. A shift of the Cl_{br} atoms to 1f-cus Ru sites enables a mobility of the Cl_{ot} at temperatures as low as $T = 350$ K due to a diffusion barrier along the cus-rows of $E_{diff} < 0.9$ eV. The mobility studied in this chapter serves as a explanatory tool in the interpretation of the observed reactivity and stability of $RuO_{2-x}Cl_x(110)$ towards the CO oxidation in the following chapters of this work.

The CO RAIRS double feature was used as an example to demonstrate the importance of the $Cl_{br} \leftrightarrow Cl_{ot}$ shift reaction in the interpretation of the complex spectral behaviour of CO adsorbed on $RuO_{2-x}Cl_x(110)$. Furthermore, it has been shown that Cl_{ot} prevents the recombination of O_{ot} atoms leading to a higher temperature desorption of the O_{ot} atoms, by recombination only above temperatures where the Cl_{ot} recombination set in. This result is comparable with the findings of Krause et al., who studied this effect with HCl+O_2 coadsorption experiments on s-RuO_2 [138]. This configurational blockade of the 1f-cus Ru sites by Cl_{ot} will play a key role in the CO oxidation on $RuO_{2-x}Cl_x(110)$ as well.

In conclusion, it has been found that oxygen atoms lead to a certain mobility of the surface chlorine atoms. The effects observed upon introducing O_{ot} atoms as a further reactive component on the surface could be explained by means of the $Cl_{br} \rightarrow Cl_{ot}$ shift reaction. The highly dynamic manner of the surface chlorination is further increased by the presence of CO, which enables the backward reaction of the $Cl_{br} \rightarrow Cl_{ot}$ shift, i.e. the CO mediated rechlorination of the bridging positions - the mechanism of this process was described in chapter 12.5.

The principal result of this chapter has already been formulated in terms of the two following statements, explaining the dynamics of the surface chlorine atoms on $RuO_{2-x}Cl_x(110)$ under CO/O_2 exposure:

- *The presence of oxygen atoms on chlorinated RuO_2(110) forces a certain amount of chlorine atoms to shift from bridging positions to on top positions.*
- *The presence of carbon monoxide molecules on chlorinated RuO_2(110) forces a certain amount of chlorine atoms to shift from on top positions to bridging positions.*

This novel insight into the dynamics of Cl atoms on the $RuO_{2-x}Cl_x(110)$ surface opens the possibility of studying the CO oxidation reaction on that particular surface under in situ reaction conditions beyond UHV pressures. The experiments carried out in the following sections will always be discussed in terms of the processes observed on stoichiometric $RuO_2(110)$ [13, 14].

Chapter 16

The Influence of Chlorine on the Reactivity of $RuO_{2-x}Cl_x(110)$ in the CO Oxidation

Since chlorine forms a relatively stable bridging species on $RuO_{2-x}Cl_x(110)$, it is of special interest to study the question, to what extent it is able to influence the reactivity of $RuO_2(110)$ towards different reactions. In the present thesis, CO oxidation will be the model reaction to study the reactivity of $RuO_{2-x}Cl_x(110)$ and to estimate the influence of the chlorine atoms and their dynamic behaviour on the surface in this context. Since chlorine is not able to react directly with the components of the feed gas, i.e. CO and O_2, it acts merely as a spectator in the CO oxidation reaction on RuO_2. Furthermore, one has to note that the system increases considerably in complexity by introducing chlorine as a third atomic component on the surface.

16.1 O_{ot} Titration by CO - RAIRS Study

A first approach to appraise the impact of chlorine substitution in the bridging rows of $RuO_2(110)$ on the reactivity of that surface towards the CO oxidation was the analysis of the reaction of an O_{ot} adsorbate on $RuO_{2-x}Cl_x(110)$ with CO - step by step in terms of titration experiments. To be able to compare the results from the chlorinated surface with the reactivity of s-$RuO_2(110)$, preliminary experiments have been carried out on the stoichiometric surface.

16.1.1 O_{ot} Titration on s-$RuO_2(110)$

The first experiment was carried out on s-$RuO_2(110)$, covered by O_{ot} (86 %, cf. chapter 14.1.4 and references [133, 134]), whereby all annealing steps to $T = 350$ K in $p(CO) = 1 \times 10^{-8}$ mbar started from the initially prepared O_{ot} coverage.

The restored stoichiometric $RuO_2(110)$ (flash $T = 600$ K in $p(O_2) = 1 \times 10^{-8}$ mbar, flash $T = 600$ K (without the presence of O_2)) was exposed to 5 L of oxygen at $T = 298$ K and subsequently saturated with 6 L CO at $T < 230$ K, afterwards a RAIR spectrum was taken (see figure 16.1). This reference spectrum showed the characteristic $O_{br}/(CO_{ot}^{sg}+O_{ot})$ signature (isolated CO_{ot} molecules in a O_{ot} matrix) at $\tilde{\nu}(CO) = 2150$ cm^{-1}. Flashing this coadsorbate to $T = 350$ K without any CO exposure (spectrum 0') during the annealing led to an apparent reduction of the O_{ot} coverage as has been shown by saturation of the surface by dosing 6 L CO at $T < 230$ K again. The integral has increased and the position of the CO absorption peak has slightly shifted to lower wavenumbers indicating a lower O_{ot} content in the $CO_{ot}+O_{ot}$ coadsorbate (cf. section 14.1.4). In the next step, the surface was annealed to $T = 350$ K and exposed to CO ($p(CO) = 1 \times 10^{-8}$ mbar); the total annealing time is displayed in the legend of figure 16.1.

After each annealing step in CO, a RAIR spectrum was taken at $T = 350$ K (hot spectra are not shown in the plot) and the sample was cooled down to $T < 230$ K and saturated by 6 L CO. A RAIR spectrum was taken to monitor the CO saturated surface, displayed in figure 16.1. After this RAIR spectrum, the surface was heated to $T = 350$ K for the next CO exposure step. With increasing exposure time the CO RAIRS absorption gained intensity and shifted towards the absorption wavenumber reported for CO adsorbed on mildly reduced r-$RuO_2(110)$ ($\tilde{\nu}(CO) = 2085$ cm^{-1}) [13]. After approximately 10 minutes the surface has reached its stable state and was fully covered by CO_{br}/CO_{ot}. Beyond this annealing time the RAIR spectra did not change anymore.

In the O_{ot} titration experiment reported here, the effect of heating the CO saturated (at $T < 230$ K) O_{ot} adsorbate (necessary for RAIRS), cannot be distinguished from the actual CO oxidation reaction taking place at $T = 350$ K with CO supplied from the gas phase ($p(CO) = 1 \times 10^{-8}$ mbar). Heating a CO saturated O_{ot} phase to $T = 350$ K or exposing the O_{ot} phase at $T = 350$ K should lead to different CO oxidation reaction rates, since the surface concentrations of CO during both procedures should differ.

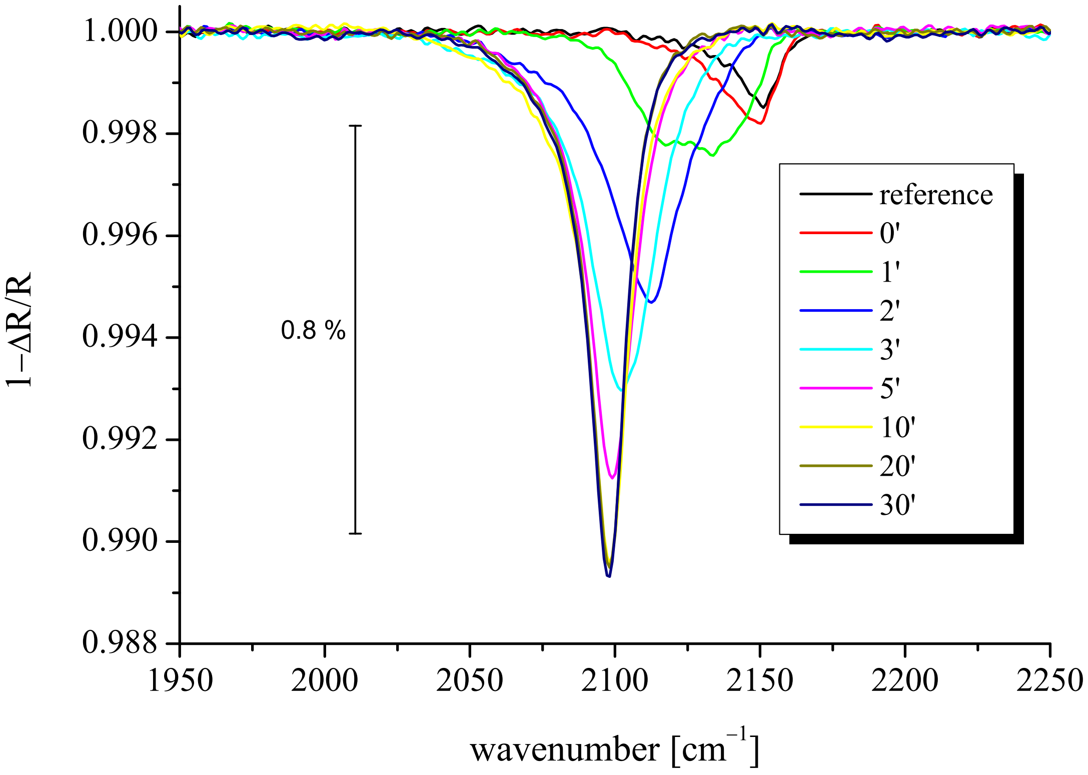

Figure 16.1: O_{ot} titration experiment by CO on restorated **s-RuO$_2$(110)** at $T = 350$ K. All annealing steps in CO ($p(\mathrm{CO}) = 1 \times 10^{-8}$ mbar) were done on the initially prepared O_{ot} coverage. RAIR spectra were taken after CO saturation (6 L at $T < 230$ K).

To check the influence of heating the saturated CO_{ot}+O_{ot} coadsorbate, another set of experiments was carried out on stoichiometric $RuO_2(110)$ where the O_{ot} coverage has been renewed after each RAIRS measurement. The restored stoichiometric $RuO_2(110)$ (flash $T = 673$ K in $p(O_2) = 5 \times 10^{-8}$ mbar, flash $T = 673$ K), which was exposed to 5 L of oxygen at $T = 298$ K, was saturated with 6 L CO at $T < 230$ K and a RAIR spectrum was taken (see figure 16.2). The spectrum (0') showed the characteristic $O_{br}/(CO_{ot}^{sg}+O_{ot})$ signature (isolated CO_{ot} molecules in a O_{ot} matrix) at $\tilde{\nu}(CO) = 2150$ cm^{-1}. According to the experiment described above, the surface was treated for different time periods with CO ($p(CO) = 1 \times 10^{-8}$ mbar) at $T = 350$ K as indicated in figure 16.2. The O_{ot} adsorbate was renewed after measuring the RAIR spectrum of the CO saturated surface after each annealing step. Figure 16.2 shows the RAIR spectra of the CO saturated surface after the corresponding reaction time. The time evolution of the peaks shows, that the progression of the reduction is slower than in the experiment with one single starting O_{ot} coverage. After 10 min the surface has not yet reached the mildly reduced state CO_{br}/CO_{ot}. This state is reached only after 20 min of reaction at $T = 350$ K in $p(CO) = 1 \times 10^{-8}$ mbar.

The difference between the spectra of both O_{ot} titration experiments on s-$RuO_2(110)$ was the time interval during which the complete mildly reduced $RuO_2(110)$ surface has been obtained from the restored, O_{ot} covered s-$RuO_2(110)$. As shown above, it makes a difference whether the cooled, CO saturated surface is annealed to the reaction temperature of $T = 350$ K or not. Exposing the surface to CO only at $T = 350$ K led not to the same time evolution like saturating with CO at $T < 230$ K, annealing to $T = 350$ K and dosing CO at $T = 350$ K, because the achievable CO surface concentration at $T = 350$ K is less than at $T = 230$ K. Thus, the number of available CO molecules for CO oxidation reaction on the surface was higher in the case of titrating one initially prepared O_{ot} coverage.

16.1.2 O_{ot} Titration on $RuO_{2-x}Cl_x(110)$

After the O_{ot} titration by the CO oxidation reaction has been studied on the stoichiometric s-$RuO_2(110)$ surface, the influence of a bridging chlorination will be treated in the following.

In the previous section, a difference has been found for s-$RuO_2(110)$ between

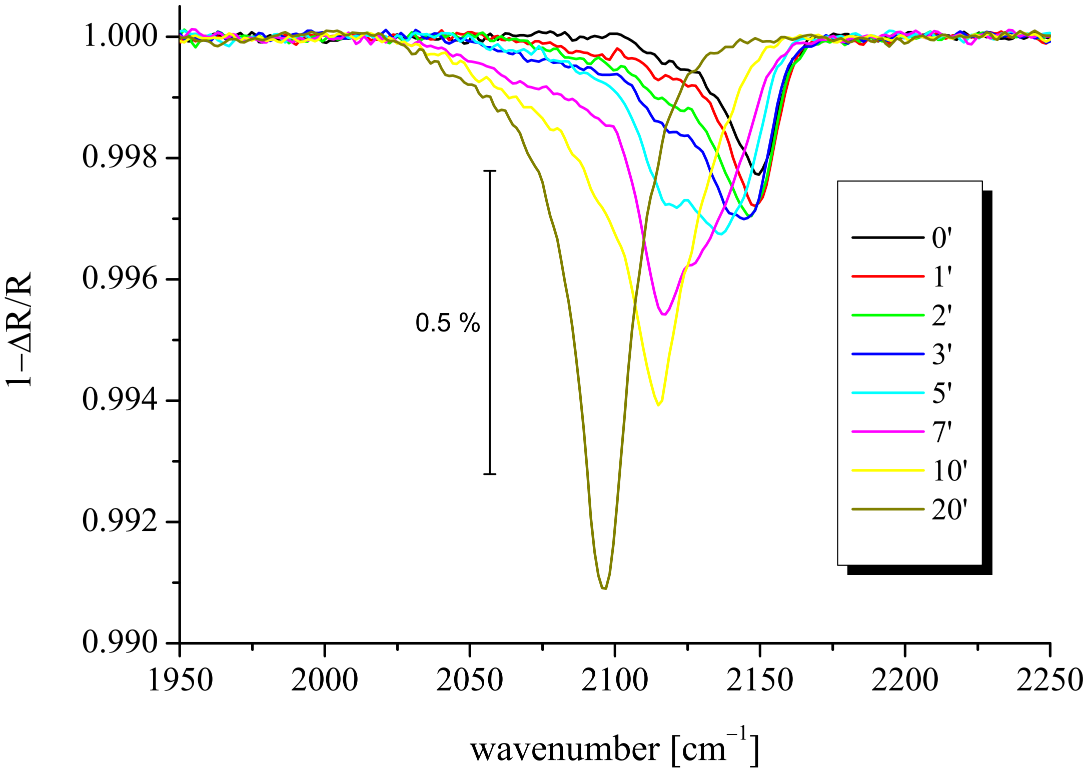

Figure 16.2: O_{ot} titration experiment by CO on restorated **s-RuO$_2$(110)** at $T = 350$ K. All annealing steps in CO ($p(\mathrm{CO}) = 1 \times 10^{-8}$ mbar) were done on freshly prepared O_{ot} adsorbates after restoration. RAIR spectra were taken after CO saturation (6 L at $T < 230$ K).

reducing the O_{ot} adsorbate from CO supplied only from the gas phase or heating from a CO saturated O_{ot}+CO_{ot} coadsorbate to the reaction temperature of T = 350 K + supplying CO from the gas phase at this temperature. The next experiments have been run identically, except that the stoichiometric oxide was chlorinated in advance.

RuO_2(110) has been prepared and chlorinated after the standard procedures stated above. The following set of experiments of O_{ot} titration is carried out on the initially prepared O_{ot} coverage, without renewal of the O_{ot} adsorbate after CO saturation at $T < 230$ K.

$RuO_{2-x}Cl_x$(110) was restored in oxygen (flash $T = 673$ K in $p(O_2) = 3 \times 10^{-8}$ mbar, flash $T = 700$ K) and afterwards exposed to 5 L O_2 at $T = 298$ K in order to get a maximally O_{ot} covered surface. The reference spectrum at the beginning of the experiment was obtained by saturating this O_{ot} covered $RuO_{2-x}Cl_x$(110) surface by 6 L CO at $T < 230$ K. The recorded RAIR spectra after CO saturation at $T < 230$ K are compiled in figure 16.3. The reference spectrum showed an absorption at $\tilde{\nu}$(CO) = 2143 cm^{-1}, which is the typical wavenumber for the (Cl_{br}+O_{br})/(CO_{ot}^{sg}+O_{ot}) phase, i.e. isolated CO_{ot} molecules vibrating in a matrix of O_{ot} atoms in the presence of both Cl_{br} and O_{br} bridging atoms (cf. chapter 14.1.4). Upon further annealing to $T = 350$ K in $p(CO) = 1 \times 10^{-8}$ mbar and RAIRS measurements of the CO saturated surface at $T = 230$ K, the CO absorption increased accompanied by a red shift, which both are due to a loss of O_{ot} atoms. The reported disappearance of O_{ot} atoms is caused by reduction of O_{ot} by CO coming either from the gas phase or adsorbed CO species, to form CO_2. Compared to s-RuO_2(110) the reduction of the O_{ot} adsorbate proceeded slower and the total amount of CO accommodated on the surface after the last reaction step was smaller as can be seen from a comparison of the time evolution of the integrals of the CO absorption in both experiments.

After 20 minutes of reaction a surface state was reached, where the O_{ot} species were reacted off and the surface was mainly covered by CO both in on top and bridging positions ($\tilde{\nu}$(CO) = 2102 cm^{-1}). A flash to $T = 550$ K followed by CO saturation at $T < 230$ K finally led to the recovery of the CO_{ot} and CO_{br} saturated, chlorinated $RuO_{2-x}Cl_x$(110) phase at $\tilde{\nu}$(CO) = 2105 cm^{-1} as described in chapter 14.2.1).

In contrast to the preceding experiment, the CO oxidation on $RuO_{2-x}Cl_x$(110)

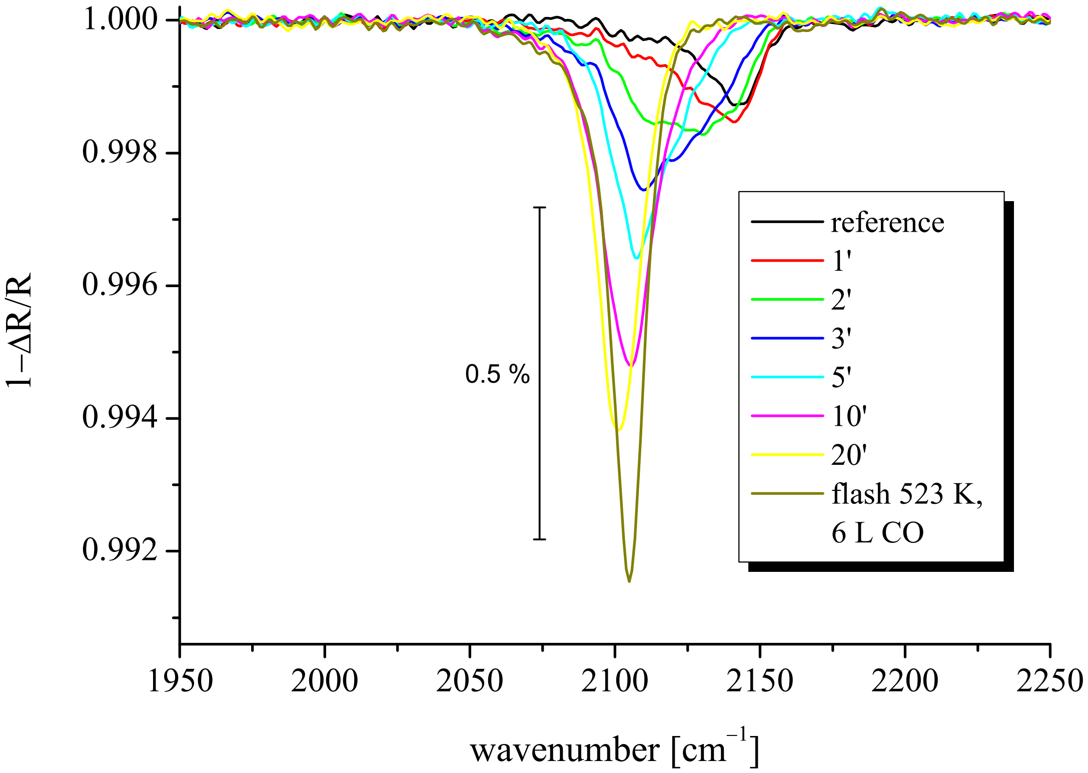

Figure 16.3: O_{ot} titration experiment by CO on **$RuO_{2-x}Cl_x$(110)** (initially flashed to T = 700 K) at T = 350 K. All annealing steps in CO (p(CO) = 1×10^{-8} mbar) were done on the initially prepared O_{ot} coverage. RAIR spectra were taken after CO saturation (6 L at T < 230 K).

is blocked, when starting the annealing steps from always freshly prepared O_{ot} coverages. In this case, CO was only supplied from the gas phase ($p(\mathrm{CO}) = 1 \times 10^{-8}$ mbar) at the reaction temperature of $T = 350$ K.

The RAIR spectra taken during this experiment after CO saturation of the surface at $T < 230$ K are displayed in figure 16.4. It can clearly be seen, that even after 20 min of reaction, no significant change in the spectra has happened, i.e. the O_{ot} coverage has not been changed neither by reaction nor by thermal desorption at $T = 350$ K, whereas the presence of O_{ot} was confirmed by the RAIRS absorption wavenumber located at $\tilde{\nu}(\mathrm{CO}) = 2137\ \mathrm{cm}^{-1}$.

This is unlike the reaction on s-$RuO_2(110)$, where under the same experimental conditions a reduction of the O_{ot} adsorbate by CO supplied only from the gas phase has been successful (cf. figure 16.2).

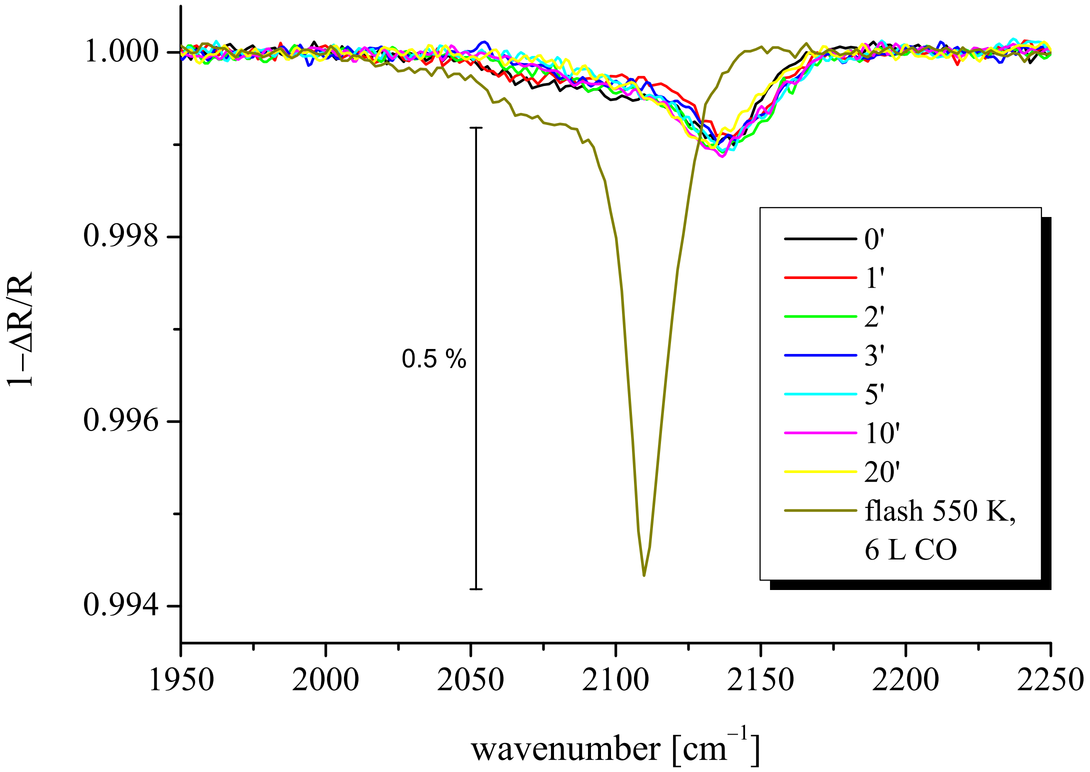

Figure 16.4: O_{ot} titration experiment by CO on $\mathbf{RuO_{2-x}Cl_x(110)}$ (initially flashed to $T = 700$ K) at $T = 350$ K. All annealing steps in CO ($p(\mathrm{CO}) = 1 \times 10^{-8}$ mbar) were done on freshly prepared O_{ot} adsorbates after restoration. RAIR spectra were taken after CO saturation (6 L at $T < 230$ K).

In the following, all four O_{ot} titration experiments on both s-$RuO_2(110)$ and $RuO_{2-x}Cl_x(110)$ will be compared based on the time development of the integrated intensities of the CO RAIRS absorption bands (see figure 16.5).

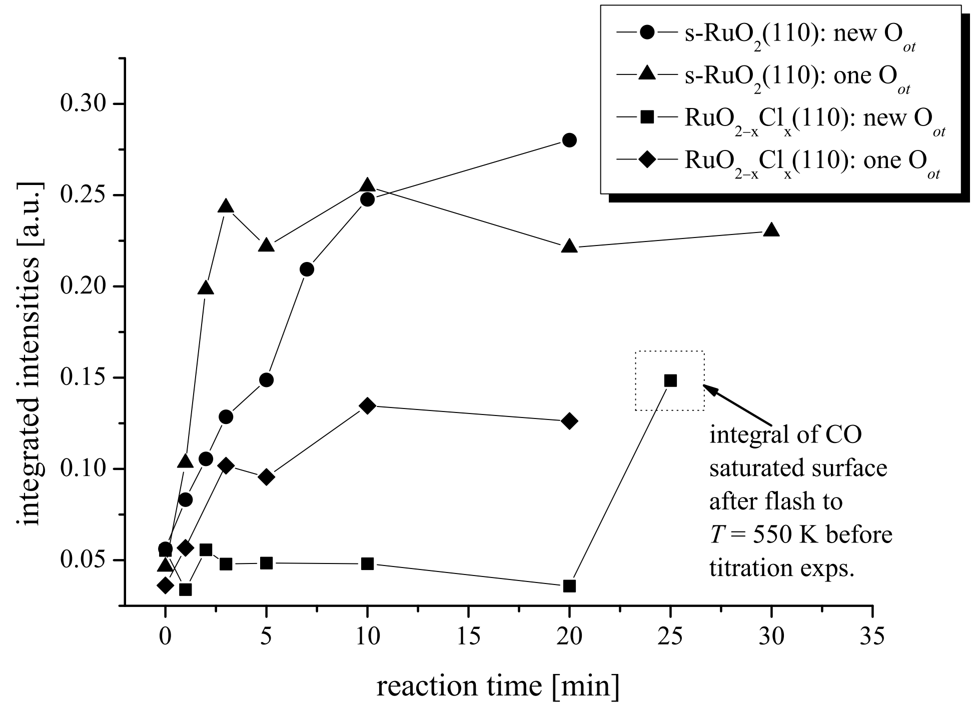

Figure 16.5: Comparison of the integrated intensities of the CO absorption bands from RAIR spectra taken during the four different O_{ot} titration experiments by CO, on s-$RuO_2(110)$ and $RuO_{2-x}Cl_x(110)$, respectively.

The comparison of the integrals of the CO RAIR spectra recorded during the O_{ot} titration experiments carried out on s-$RuO_2(110)$ and $RuO_{2-x}Cl_x(110)$ indicates on the one hand that $RuO_{2-x}Cl_x(110)$ is only able to accommodate $(50 \pm 10)\%$ of the CO molecules which s-$RuO_2(110)$ can accommodate due to the presence of surface chlorine atoms. On the other hand, the difference in the RAIR spectra caused by the differing CO exposure protocols (one initial O_{ot} coverage vs. new O_{ot} coverages after each RAIR spectrum; CO saturation at low temperatures vs. CO exposure at $T = 350$ K) is very much more pronounced on $RuO_{2-x}Cl_x(110)$ than on s-$RuO_2(110)$. The integrated intensities of the CO RAIRS absorption bands recorded during the set of O_{ot} titrations starting from newly prepared O_{ot} coverages on $RuO_{2-x}Cl_x(110)$ indicate nicely how the O_{ot}

phases remained ‘untouched’ during exposure to CO at $T = 350$ K. This finding can possibly be explained by a reactivity change induced by the presence of chlorine atoms on the surface.

But how do the surface chlorine atoms exert their influence on the CO oxidation reaction? To answer this question, the experimental protocols carried out on the chlorinated oxide are schematically summarised in figure 16.6

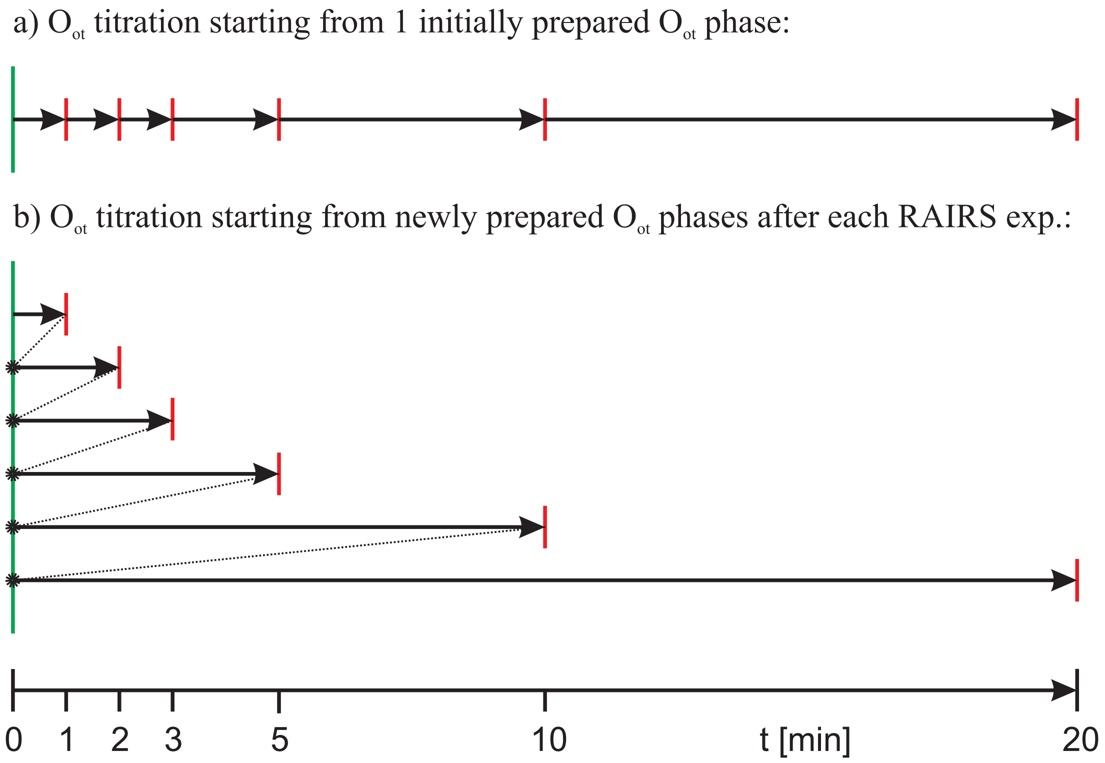
a) O_{ot} titration starting from 1 initially prepared O_{ot} phase:

b) O_{ot} titration starting from newly prepared O_{ot} phases after each RAIRS exp.:

Figure 16.6: Diagram of experimental procedures of the O_{ot} titration experiments carried out on $RuO_{2-x}Cl_x(110)$. a) O_{ot} titration starting from a single, initially prepared O_{ot} phase. b) O_{ot} titration on newly prepared O_{ot} phases. Green lines: preparation of the O_{ot} phase (5 L O_2 at $T = 298$ K), red lines: measurement of RAIR spectra (cool to $T < 230$ K, 6 L CO), arrows: anneal to and hold at $T = 350$ K in $p(\mathrm{CO}) = 1 \times 10^{-8}$ mbar for the indicated time, dotted lines: flash to $T = 523$ K to desorb CO_{ot}+O_{ot}.

Generally, heating of the O_{ot} covered $RuO_{2-x}Cl_x(110)$ to the reaction temperature of $T = 350$ K or desorbing the CO_{ot}+O_{ot} coadsorbate after RAIRS measurement by a flash to $T = 523$ K leads to the $Cl_{br} \rightarrow Cl_{ot}$ shift reaction, which is responsible for a transfer of bridging chlorine atoms to 1f-cus Ru sites. This transfer yields a mixed Cl_{ot}+O_{ot} phase, which reveals a different reactivity towards CO oxidation as the pure O_{ot} phase present on s-$RuO_2(110)$ (cf. chapter 15.2.4).

In the case of a single, initially prepared O_{ot} phase (figure 16.6 a) this mixed Cl_{ot}+O_{ot} phase is repeatedly saturated by CO at low temperatures for RAIRS measurement and annealed to the reaction temperature again without refreshing the O_{ot} coverage. The CO saturation of the surface at $T < 230$ K causes a high CO coverage, which can not evolve at $T = 350$ K. Annealing from the CO saturated Cl_{ot}+O_{ot} phase should in turn enable for reaction of CO_{ot} with both bridging O_{br} and O_{ot}, as far as they are accessible for CO and not geometrically shielded by Cl_{ot}.

The reaction of CO_{ot} with O_{br} now opens a way to remove the Cl_{ot} atoms from the 1f-cus Ru sites, via rechlorination of bridging vacancies - assuming a certain mobility of the on top species to reach the required configurations. For diffusion barriers along the cus-rows below 1 eV, the required mobility should be ensured even at $T = 350$ K. The filling of the bridging vacancy by an on top oxygen is thermodynamically favoured and leads to a depletion of preferentially O_{ot} atoms over Cl_{ot}. However, both processes lead to a depletion of O_{ot} as confirmed in the RAIR spectra by a gradual increase of the intensity of the RAIRS absorption accompanied by a red shift of this signal. The on top coverage contains less and less O_{ot} and Cl_{ot} each time due to the repeated annealing of the CO saturated surface. Thus, the RAIR signature of this surface converges to that of a mildly reduced, bridge chlorinated $RuO_2(110)$.

Coming now back to the newly prepared O_{ot} phases (figure 16.6 b)), the CO induced, stepwise depletion of both O_{ot} and Cl_{ot} is not possible, if CO is only supplied from the gas phase to the surface at $T = 350$ K. At this temperature, the surface concentration of CO is too small to run the above-mentioned processes. Furthermore, the repeated annealing of the CO saturated Cl_{ot}+O_{ot} coadsorbate was lacking in this experimental protocol, since the O_{ot} coverage was renewed after each CO saturation / RAIR spectrum by flashing the surface to $T = 523$ K and exposing to 5 L O_2 at room temperature.

The result is that the O_{ot} coverage on $RuO_{2-x}Cl_x(110)$ remains nearly constant under these conditions (CO supplied only from the gas phase at $T = 350$ K), whereas the O_{ot} phase on the stoichiometric oxide is reduced, because the reaction of CO_{ot}+O_{ot} on s-$RuO_2(110)$ is not perturbed by the presence of Cl_{ot}

atoms. The postulate of an activated adsorption of CO onto $RuO_2(110)$ was discarded because then an increase of the surface temperature to $T = 350$ K would have led to an increased adsorption rate of CO and thus, a higher CO oxidation rate, which was not observed for neither s-$RuO_2(110)$ nor $RuO_{2-x}Cl_x(110)$.

A DFT evaluation of the electronic influence of a bridging chlorine substitution on the activation barrier of the CO_{ot}+O_{ot} reaction showed that Cl_{br} led to an increase in the activation energy by 0.1 eV (0.83 eV for $RuO_{2-x}Cl_x(110)$ vs. 0.75 eV for s-RuO_2) [73]. This increase may lead to an approximately ten times lower turn-over-frequency of the catalyst but not to a complete loss of activity at temperatures of $T = 350$ K and beyond. Thus, Cl_{br} atoms seem not to be not responsible for the observed inhibition of the CO_{ot}+O_{ot} reaction path.

In conclusion, one may state, based on the results of the O_{ot} titration experiments on both s-$RuO_2(110)$ and $RuO_{2-x}Cl_x(110)$, that Cl_{ot} atoms account for the observed inhibition of the CO oxidation reaction at least under UHV conditions. The blocking is merely a configurational issue on the cus-rows, where the Cl_{ot} species prevent the recombination of the reactants CO_{ot} and O_{ot} adsorbed in a 1-dimensional manner along the cus-rows. The problem can be circumvented by CO mediated rechlorination of the bridging rows and thereby a depletion of Cl_{ot} atoms - a similar concept as already described in connection with the RAIRS CO double feature upon restoration in oxygen (cf. chapter 15.2.4).

16.2 *in situ* CO Oxidation Reaction Experiments on $RuO_{2-x}Cl_x$(110) - RAIRS Study

The O_{ot} titration experiments carried out in the previous section gave an idea how Cl_{ot} may change the reactivity of $RuO_{2-x}Cl_x(110)$ towards CO oxidation.

In the following, the reactivity of $RuO_{2-x}Cl_x(110)$ surfaces towards the CO oxidation reaction will be studied by *in situ* reflection absorption infrared spectroscopy (RAIRS) at elevated pressures under steady-state conditions. The data obtained for the chlorinated system will be compared with the results for the CO oxidation on the stoichiometric oxide at $T = 350$ K in the high vacuum regime as reported by Farkas et al. [13, 14]. The spectral assignment of the *in situ* CO RAIR spectra in this work are based on the vibrational characterisation carried out in chapter 14 and by Farkas [13]. The most interesting point was the configurational change of the $RuO_{2-x}Cl_x(110)$ surface upon variations of the composition of the feed gas. *In situ* RAIR spectroscopy allowed for the analysis of the surface CO species and with it, of the chemical environment of the CO molecules under reaction conditions.

16.2.1 CO Oxidation on $RuO_{2-x}Cl_x(110)$ under HV conditions (10^{-6} mbar)

$RuO_2(110)$ was prepared and restored following the standard protocols stated in chapters 9.2 and 9.3. After chlorination (10 L H_2 at $T = 298$ K, flash to $T = 700$ K in $p(HCl) = 5 \times 10^{-8}$ mbar) the surface was flashed to $T = 550$ K to desorb HCl_{ot} and a RAIR background spectrum was taken at $T = 350$ K, the temperature at which the steady-state CO oxidation reaction was run.

In the following, the chlorinated surface was exposed to $p(CO) = 2\times10^{-6}$ mbar at $T = 350$ K (constant flow of reactant gas). After a delay of 5 min, a RAIR spectrum was taken (figure 16.7a). The spectrum exhibited two characteristic bands: the one at $\tilde{\nu}(CO) = 1920$ cm^{-1} can be assigned to isolated CO_{br} molecules in a Cl_{br} matrix, according to table 14.4. The second absorption, centred at $\tilde{\nu}(CO) = 2089$ cm^{-1} is due to a mixed $(CO_{br}+Cl_{br})/CO_{ot}$ coadsorbate, whereby the cus-rows are to a large extent occupied by CO_{ot}.

The next RAIR spectrum (figure 16.7b) was taken after introduction of O_2 ($p(O_2) = 1 \times 10^{-6}$ mbar) leading to a stoichiometric feed gas composition. At this point, a very surprising effect happened: the peak formerly assigned to the $(CO_{br}+Cl_{br})/(-)_{ot}$ coadsorbate vanished and an absorption at $\tilde{\nu}(CO) = 1865$ cm^{-1} emerged. This absorption has not been observed on $RuO_{2-x}Cl_x(110)$ under UHV conditions in this work before. Farkas assigned this peak to a symmetric CO_{br} species on s-$RuO_2(110)$ under *in situ* conditions [13]. He ascribed the reactivity of s-$RuO_2(110)$ towards CO oxidation to this adsorbate, which coexists with regions on the surface, which are completely covered by CO_{br}/CO_{ot} under reaction conditions. These densely packed CO_{br}/CO_{ot} 'islands' form at $T = 350$ K at $p(CO) > 1 \times 10^{-6}$ mbar and were reported to be inactive in the CO oxidation, because they block the adsorption of oxygen from the gas phase.

The higher frequency peak at $\tilde{\nu}(CO) = 2082$ cm^{-1} contains contributions of CO_{ot} and CO_{br} in a Cl_{br} and Cl_{ot} surrounding according to the results of chapter

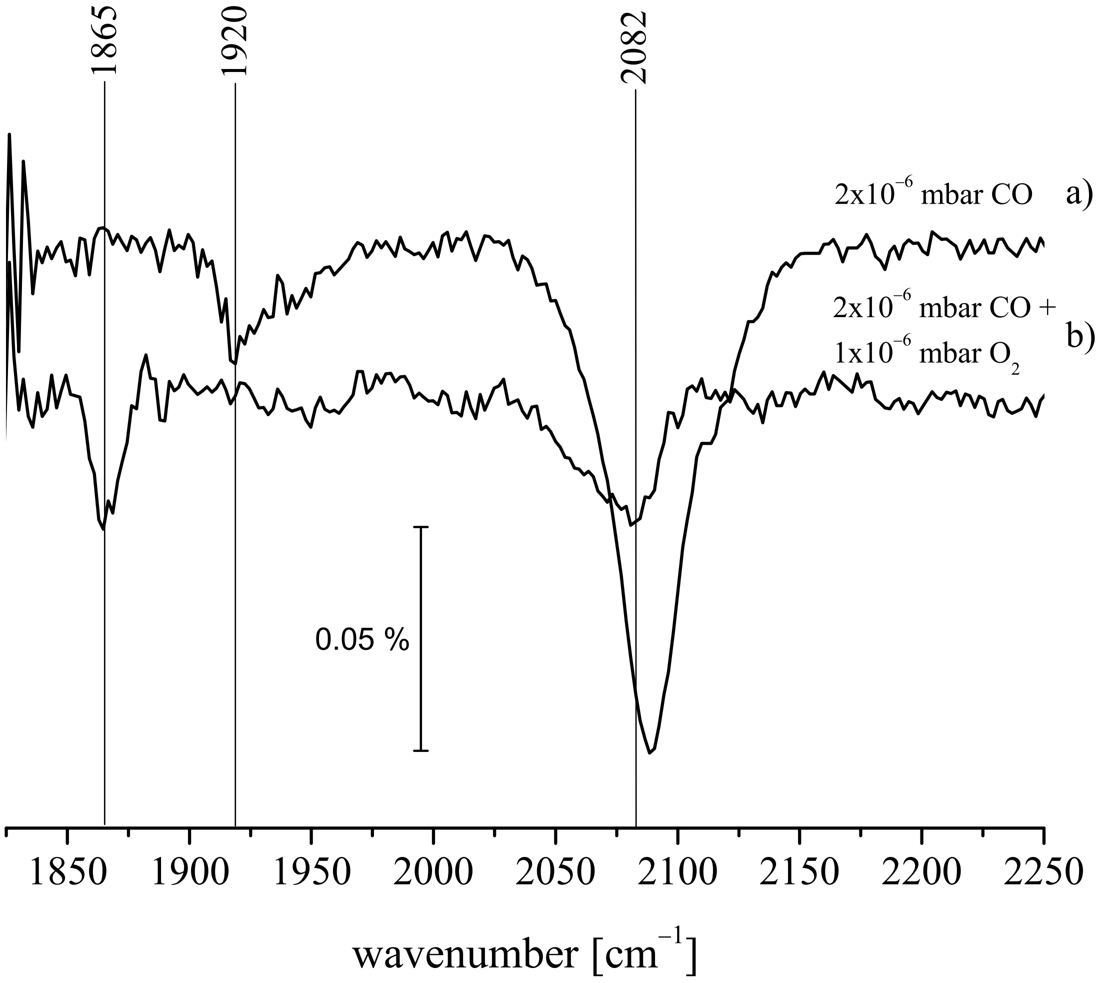

Figure 16.7: *In situ* RAIR spectra of $RuO_{2-x}Cl_x(110)$ as model catalyst during CO oxidation reaction under HV conditions at $T = 350$ K. Assignment led by [13] and the vibrational characterisation of CO on $RuO_{2-x}Cl_x(110)$ in chapter 14.

14 (cf. table 14.4).

Auger electron spectroscopy indicated that the amount of surface chlorine atoms did not change significantly during CO oxidation reaction, as can be seen from figure 16.8, neither did the underlying oxide. However, a loss of Cl atoms would only be expected at temperatures above $T > 600$ K, which were not reached during this experiment.

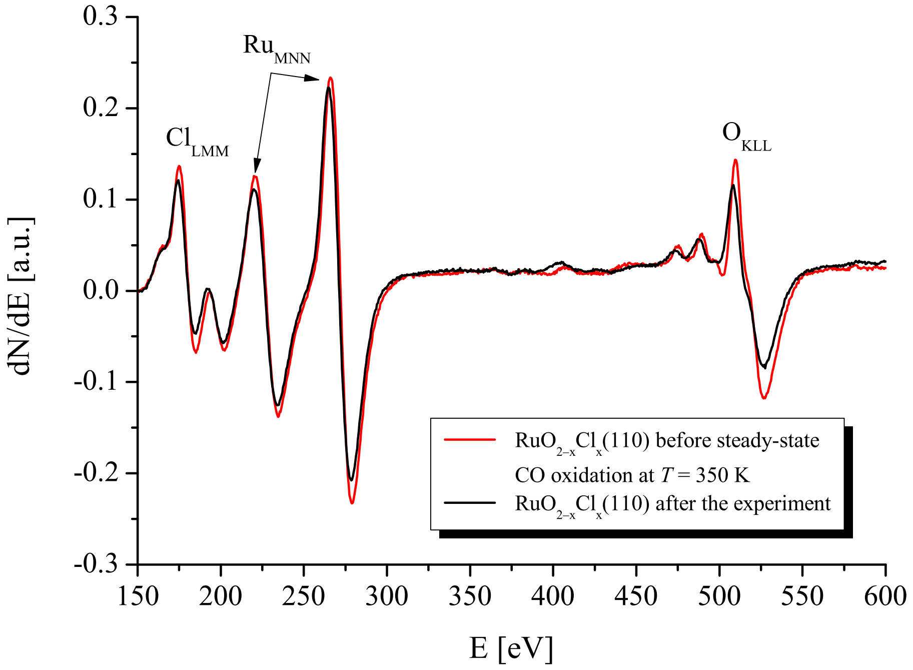

Figure 16.8: Auger electron spectra ($E = 3$ keV) of $RuO_{2-x}Cl_x(110)$ before and after the steady-state CO oxidation reaction experiments under HV conditions ($p_{max} = 3 \times 10^{-6}$ mbar) at $T = 350$ K indicating that no chlorine left the surface and the oxide was not reduced during the experiment.

To reproduce the observed behaviour of $RuO_{2-x}Cl_x(110)$ towards CO oxidation under HV conditions and to check the transferability of these results to higher temperatures, another set of identical *in situ* experiments has been carried out on $RuO_{2-x}Cl_x(110)$, but now at a temperature of $T = 400$ K. As can be inferred from figure 16.9, the spectra behave very similarly upon variations in the feed gas composition, i.e. the peak at $\tilde{\nu}(CO) = 1928$ cm^{-1} vanished upon introduction of O_2 resulting in a stable surface configuration, which did not respond significantly to feed gas composition changes in the 10^{-6} mbar regime. The surface was dominated mainly by a symmetrical CO_{br} species (1865 cm^{-1}). The peak at $\tilde{\nu}(CO) =$ 2070 cm^{-1}, emerging after the initial CO exposure, is less intense compared to the spectra recorded at $T = 350$ K in the previous experiment. Moreover, the peak shifted to $\tilde{\nu}(CO) = 2050$ cm^{-1} indicating a smaller CO_{ot} coverage (cf. chapter 14.2.2). Both effects can be traced back to a higher desorption probability of CO due to the higher temperature of $T = 400$ K.

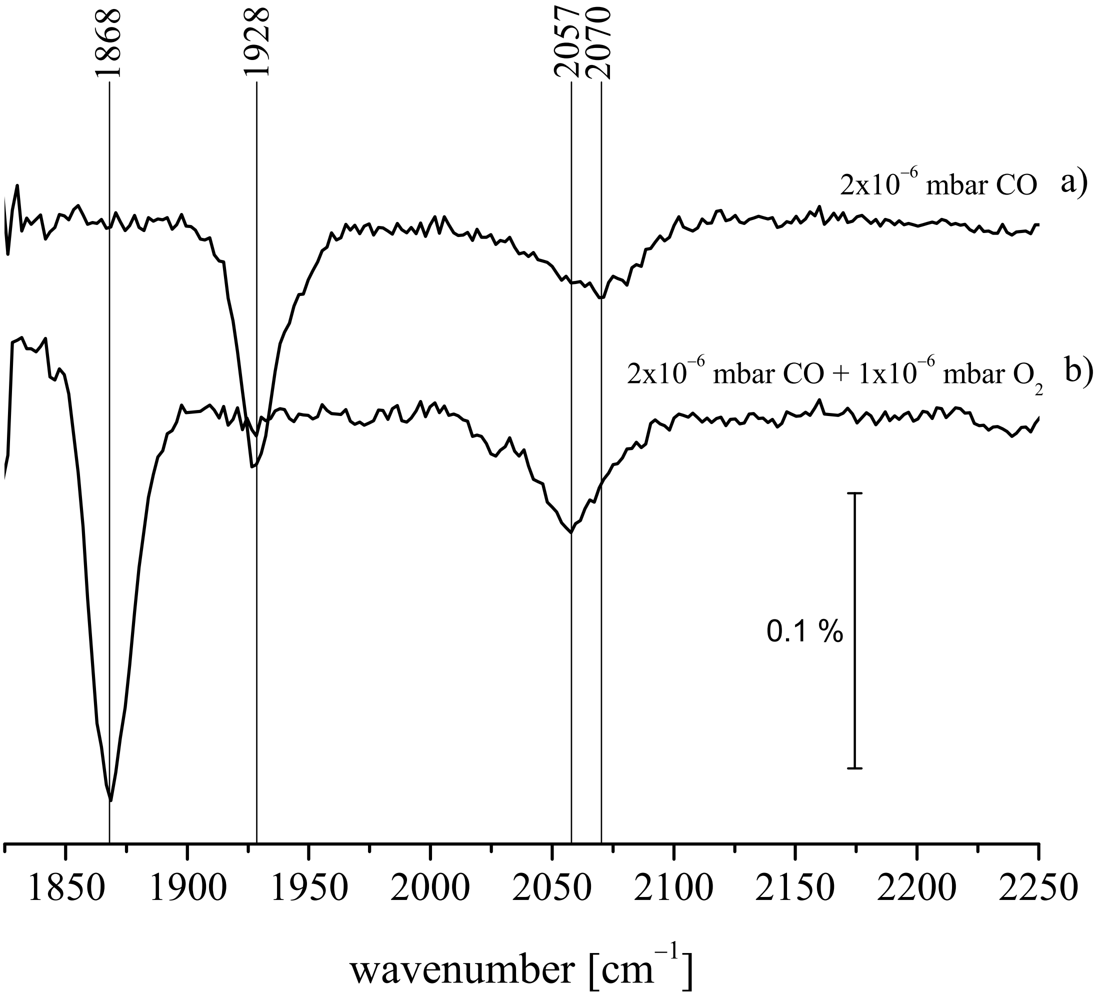

Figure 16.9: *In situ* RAIR spectra of $RuO_{2-x}Cl_x$(110) as model catalyst during the steady-state CO oxidation reaction under HV conditions at $T = 400$ K.

The loss of the absorption band at $\tilde{\nu}(CO) = 1920$-1930 cm^{-1} at the expense of another feature emerging at $\tilde{\nu}(CO) = 1865$ cm^{-1}, upon introducing oxygen into the reaction chamber is probably the most interesting result achieved during the *in situ* CO oxidation experiments on $RuO_{2-x}Cl_x$(110). As long as only CO is present in the feed gas, Cl_{br} atoms remain preferentially in the bridging positions due to thermodynamics. This is evidenced in the RAIR spectrum by the absorption at $\tilde{\nu}(CO) = 1920\text{-}1930\ cm^{-1}$, corresponding to a $(CO_{br}{+}Cl_{br})/(-)_{ot}$ coadsorbate.

Upon the introduction of O_2, the $Cl_{br} \rightarrow Cl_{ot}$ shift reaction is enabled by the presence of O_{ot} atoms. A driving force towards a replacement of Cl_{br} by O_{ot} is given and leads to the formation of a certain amount of Cl_{ot} under O_2 exposure. In contrast to bridging chlorine atoms, which are rather static, the Cl_{ot} atoms accommodated on 1f-cus Ru sites are mobile due to a low diffusion barrier of $E_{diff} < 0.9$ eV as determined from DFT calculations. Thus, a highly dynamic situation exists under stoichiometric feed gas ($p(CO) = 2p(O_2)$): The $Cl_{br} \rightarrow Cl_{ot}$ shift reaction provides mobile Cl_{ot} atoms and in addition, the CO molecules present on the surface facilitate the rechlorination of the bridging sites. Hence, the 1-dimensional behaviour of the bridging chlorination and thus, the 1-dimensionality of the cus-rows is abolished.

The emergence of the RAIRS feature at $\tilde{\nu}(CO) = 1865\ cm^{-1}$, ascribed to symmetric $CO_{br}/(-)_{ot}$, may consequently be due to a segregation of CO_{br} molecules in form of ‘islands’ which are mainly covered by that particular CO species and do not contain significant amounts of Cl or O atoms. The segregation behaviour of CO on s-$RuO_2(110)$ was extensively described by Farkas et al. [14]. There, a certain mobility of the surface species was also an important prerequisite for the observed segregation of CO resulting in island formation. However this hypothesis remains speculative, since there has been no direct experimental evidence for island formation.

The dynamics of the CO+O+Cl coadsorbate on $RuO_2(110)$ described above may cause a reactivation of the chlorinated ruthenium dioxide by the formation of quasi-stoichiometric, Cl-free regions on the surface, which shall consist of ’islands’ of symmetrically bridging CO_{br} molecules - the active reaction area, at least on s-$RuO_2(110)$ [13]. The remaining surface area in turn should accommodate a relatively higher number of Cl atoms.

These results, obtained by *in situ* RAIR spectroscopy for $RuO_{2-x}Cl_x(110)$ under HV conditions (10^{-6} mbar regime) may be helpful in the interpretation of the CO oxidation experiments run at even higher pressures (ESRF, *in situ* SXRD combined with mass spectrometry) in terms of the ‘bridging-the-pressure-gap’ approach.

16.3 Reactivity and Stability of $RuO_{2-x}Cl_x$(110) during CO Oxidation - SXRD Study

The knowledge about the dynamical processes taking place on chlorinated ruthenium dioxide in the presence of both O_2 and CO in the feed gas allowed for a more detailed analysis of the reactivity and stability of the oxide under even higher pressures of CO and O_2 (mbar region). Experiments in this direction were carried out at beamline ID03 at ESRF in Grenoble in cooperation with O. Balmes and E. Lundgren. The batch reactor for harsh conditions at ID03 (as described in chapter 4) enabled a combined surface X-ray diffraction and mass spectrometry analysis of the reaction system. The results obtained will give insight in both the reactivity and stability of $RuO_{2-x}Cl_x$(110) under CO oxidation conditions.

16.3.1 Combined Reactivity and Stability Measurements under Reducing Feed Gas Composition

The disadvantage of the *in situ* RAIRS measurements presented in the preceding section was the lack of a mass spectrometric analysis, to check whether the CO oxidation was running or not under stoichiometric CO/O_2 feed. However, the highly dynamical behaviour of the chlorinated surface could have been demonstrated successfully leading to a better understanding of the catalyst's behaviour under $CO+O_2$ exposure.

On-line mass spectrometric analysis of the CO oxidation reaction was possible at ESRF, in combination with SXRD-monitoring of the stability of the chlorinated oxide, under batch reaction conditions at pressures in the mbar regime. To assess the reactivity of stoichiometric RuO_2(110) under these conditions and to determine the characteristics of the batch reactor system, a reference reaction has been run on s-RuO_2(110), which was prepared by exposing the pristine Ru(0001) surface to $p(O_2) = 1 \times 10^{-3}$ mbar at $T = 690$ K. Afterwards, the batch reactor was filled with 0.5 mbar of a reducing feed gas mixture of CO/O_2 ($p(CO) > 3p(O_2)$), which has been prepared in advance in a separate cylinder. The SXRD reflex at (**H**, **K**, **L**) = 0.884, 0.884, 1.3, indicative of the presence of RuO_2(110) (cf. figure 4.4), was recorded simultaneously with the temperature and the QMS signals of CO (m/e = 28), O_2 (m/e = 32) and CO_2 (m/e = 44) versus time. The temperature was increased in three steps starting from $T = 360$ K to $T = 560$ K. The corresponding data are summarised in figure 16.10. The rise in the SXRD reflex intensity with increasing temperature was due to thermal variations in the z-axis alignment of the crystal relative to the beam.

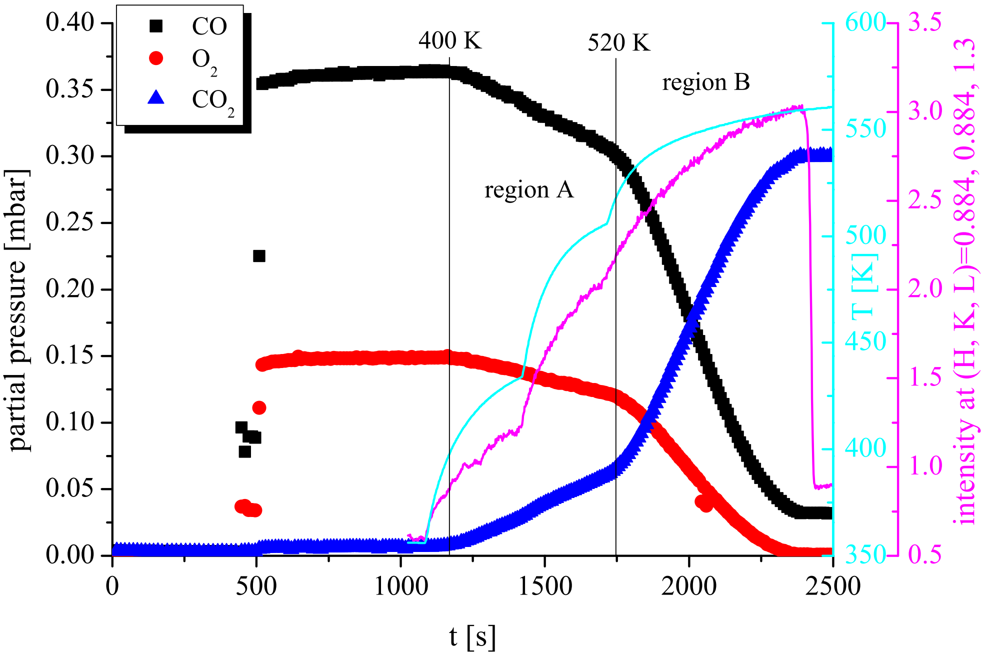

Figure 16.10: CO oxidation reaction in batch mode over **s-RuO$_2$(110)** under reducing feed gas composition at temperatures between $T = 360$ and 560 K. Displayed are the partial pressures of CO (black squares), O_2 (red dots) and CO_2 (blue triangles) versus time on the left ordinate and the temperature (right, cyan ordinate) as well as the intensity of a characteristic $RuO_2(110)$ SXRD reflex at (**H**, **K**, **L**) = 0.884, 0.884, 1.3 (right, magenta ordinate).

The CO oxidation started slowly at a temperature of $T = 400$ K (region A), the maximum conversion rate was reached at temperatures above $T = 520$ K (region B). After the oxygen was completely consumed, the intensity of the $RuO_2(110)$ SXRD reflex dropped, indicating the complete loss of the oxide. At this temperature, s-$RuO_2(110)$ was immediately reduced in a background pressure of pure CO ($p(CO) \cong 3 \times 10^{-2}$ mbar). This observation showed that the stoichiometric $RuO_2(110)$ is structurally stable at temperatures as high as $T = 550$ K under (net reducing) CO oxidation conditions as long as the feed gas contains enough oxygen. As soon as the oxygen is consumed by CO oxidation and the surface is exposed to pure CO, it is reduced to Ru metal.

A very similar experiment was then carried out on $RuO_{2-x}Cl_x(110)$. The stoichiometric $RuO_2(110)$ substrate was prepared as described above and the chlorination was achieved by exposing the surface to $p(HCl) = 2 \times 10^{-7}$ mbar at $T = 540$ K. After cooling the surface, the batch reactor was filled with 0.5 mbar of the same reducing feed gas mixture of CO/O_2 ($p(CO) > 3p(O_2)$) as used before. The same parameters were monitored over time and an identical temperature curve was run to assure the compatibility of the two reaction experiments. Figure 16.11 compiles the data of the CO oxidation in the batch reactor versus time.

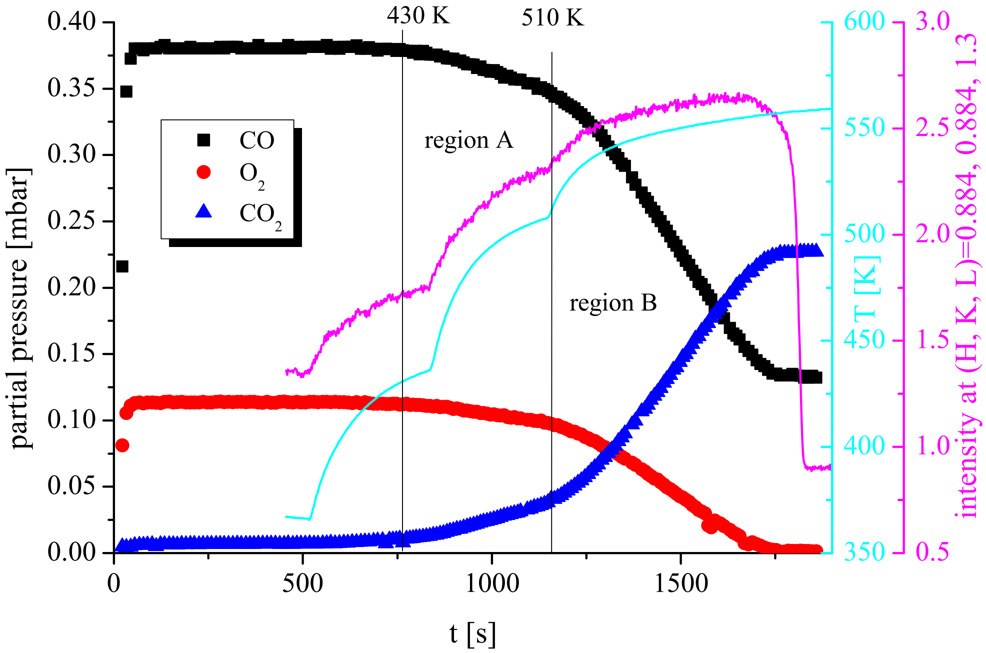

Figure 16.11: CO oxidation reaction in batch mode over $\mathbf{RuO_{2-x}Cl_x(110)}$ under reducing feed gas composition at temperatures between $T = 360$ and 560 K. Displayed are the partial pressures of CO (black squares), O_2 (red dots) and CO_2 (blue triangles) versus time on the left ordinate and the temperature (right, cyan ordinate) as well as the intensity of a characteristic $RuO_2(110)$ SXRD reflex at ($\mathbf{H}$, $\mathbf{K}$, $\mathbf{L}$) = 0.884, 0.884, 1.3 (right, magenta ordinate).

At a first glance, the time and temperature development of the mass signals during the CO oxidation experiment look similar to that of the stoichiometric oxide. However, the ignition temperature was slightly shifted to higher temperatures (T = 430 K). The lower conversion region A reached from T = 430 to T = 510 K. An acceleration of the CO oxidation reaction was observed for temperatures above T = 510 K (region B). The reactivity of s-RuO_2(110) was throughout higher in both regions, as easily can be seen from the steeper slope in the CO_2 production curve.

The chlorinated catalyst was also reduced to Ru metal at the point, where all oxygen was consumed in the batch reactor and the surface was exposed to CO alone, whereas the loss of the oxide reflex is not that steep as in the case of s-RuO_2(110), i.e. the reduction to the metal proceeded slower, especially at the beginning. In addition, the thickness of both oxides was similar, since the **L**-scans taken at $\mathbf{H} = 0.73$, $\mathbf{K} = 0$ in advance to the reaction of both s-RuO_2(110) and $RuO_{2-x}Cl_x$(110) revealed a similar FWHM of 0.29 and 0.30, respectively.

An evaluation of the turn over frequencies (TOF) of the CO oxidation reaction over both stoichiometric and chlorinated catalysts has been carried out based on the reactivity data obtained by means of mass spectrometry. The TOF is given by

$$TOF = \frac{dp(CO_2)}{dt} \cdot \frac{V \cdot L}{\#Cat \cdot RT} = -\frac{dp(CO)}{dt} \cdot \frac{V \cdot L}{\#Cat \cdot RT} = -2\frac{dp(O_2)}{dt} \cdot \frac{V \cdot L}{\#Cat \cdot RT}$$

where V is the reactor volume (0.002 m^3) [38], p the pressure (in Pa), L the Avogadro constant (6.022×10^{23} mol^{-1}), R the gas constant (8.3 $JK^{-1}mol^{-1}$), T the temperature of the gas (300 K) and $\#Cat$ the number of the catalytically active sites (set to 10^{15} assuming a surface of the single crystal of 1 cm^2).

The *TOFs* have been evaluated for two temperature regimes for each catalyst denoted by region A and B in the graphs (figure 16.10 and 16.11).

The comparison of the two temperature regimes for both s-RuO_2(110) and $RuO_{2-x}Cl_x$(110) indicates a factor of ≈4 in the TOF between the low temperature region A and the high temperature region B. Hence, the relative temperature response of both catalysts is similar. However, the chlorinated surface reveals throughout lower turn over frequencies by a factor of 1.2 ± 0.1. This finding may be interpreted in two ways: First, the number of active sites is equal in both cases. That implies that the reactivity of the chlorinated surface is smaller due

system	**region**	$\boldsymbol{TOF}$**(CO$_2$)**	$\boldsymbol{TOF}$**(CO)**	$\boldsymbol{TOF}$**(O$_2$)**	$\boldsymbol{TOF}_{av}$
s-RuO_2(110)	A	4.8	5.0	5.5	5.1
	B	18.2	20.0	17.8	18.7
$RuO_{2-x}Cl_x$(110)	A	4.0	4.4	4.3	4.2
	B	15.5	17.5	15.6	16.2

Table 16.1: Turn over frequencies (TOF) for the CO oxidation reactions over s-RuO_2(110) and $RuO_{2-x}Cl_x$(110) given in Hz. The *TOFs* have been evaluated based on the partial pressures of the involved species CO_2, CO and O_2 (differences about 0.3 mbar). TOF_{av} is the average value over the *TOFs* for the single species. The relative error of the turn over frequencies amounts to ±7%.

to the presence of Cl_{br}. Second: The active phase of both catalysts is of the same chemical and structural nature. Then, the observed difference in the *TOFs* can be explained by a smaller number of active sites, i.e. sites are blocked by Cl, where no reaction can take place. The first argument can possibly be ruled out by means of DFT calculations. Cl_{br} substitution of the bridging O atoms have led to an increase in the activation energy of the recombination of $CO_{ot}+O_{ot}$ by 0.08 eV. This difference induces a factor of roughly seven (at $T = 500$ K) in the reaction rates of the CO oxidation over s-RuO_2(110) compared to $RuO_{2-x}Cl_x$(110). However, this strong inhibition could not be observed in the CO oxidation reactions presented here. Thus, it is more feasible to treat the active phase of the chlorinated catalyst as being quasi-stoichiometric, but with a smaller number of active sites. Taking the evaluation of the *TOFs* into account, the number of active sites would be ca. 15-20 % smaller on the chlorinated surface due to the presence of surface chlorine atoms. Overall, the turn over frequencies evaluated for the present experiments are in good agreement with the data of Over et al. obtained for s-RuO_2(110) at higher pressures [123].

A more detailed picture of the stability of the chlorinated catalyst under reducing feed gas atmosphere in the batch reactor was given by another CO oxidation reaction carried out on $RuO_{2-x}Cl_x$(110) at a temperature of $T = 540$ K, where high conversion rates have been reported from the preceding operando SXRD experiments. Here, the stability of the oxide was not monitored continuously by the ($\mathbf{H}$, $\mathbf{K}$, $\mathbf{L}$) $=$ 0.884, 0.884, 1.3 reflex but by means of $\mathbf{H}+\mathbf{K}$ scans ($\mathbf{L} = 1.3$) recorded after various time intervals during the reaction. The conversion of CO was measured by QMS sniffing from the batch reactor as described above. The **H+K** scans at the beginning indicated the presence of the oxide layer.

The $RuO_2(110)$ surface was chlorinated by exposure to $p(HCl) = 2 \times 10^{-7}$ mbar at $T = 550$ K and cleaned by a further flash to $T = 660$ K. Subsequently, it was cooled to $T < 350$ K and subjected to a reducing CO/O_2 feed gas mixture ($p(CO) = 4 \times 10^{-1}$ mbar, $p(O_2) = 1 \times 10^{-1}$ mbar). Afterwards the sample was heated to $T = 540$ K, where the reaction started after a short time delay. Figure 16.12 shows the MS data, i.e. the progress of the CO oxidation reaction over time and on the right hand side of the diagram the corresponding **H+K** scans, which confirmed the presence of the oxide during the CO oxidation reaction.

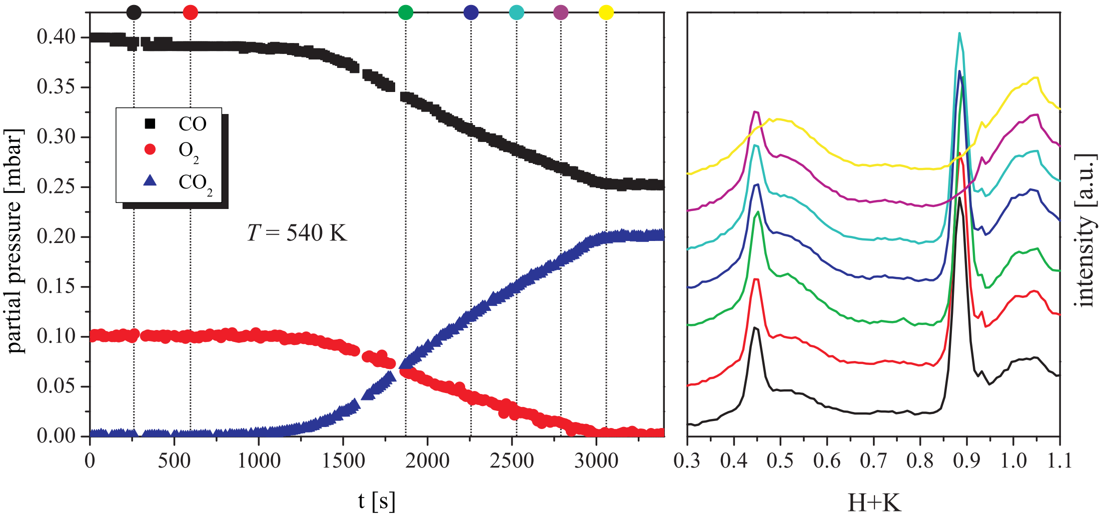

Figure 16.12: CO oxidation reaction in batch mode over $\mathbf{RuO_{2-x}Cl_x(110)}$ in $p(CO) = 4 \times 10^{-1}$ mbar and $p(O_2) = 1 \times 10^{-1}$ mbar at $T = 540$ K. Left: partial pressures of CO (black squares), O_2 (red dots) and CO_2 (44, blue triangles) in mbar versus time. Right: **H+K** scans of the catalyst sample recorded during the CO oxidation (*in operando*). The colour code of the **H+K** scans relates the scans to certain times in the MS signals (left) by identically coloured dots at the upper abscissa.

During this experiment, the chlorinated catalyst behaved similar in comparison to the CO oxidations run before. After all oxygen was consumed, the oxide was reduced within one **H+K** scan (≈230 s), as can be seen from the purple **H+K** scan in figure 16.12. Heating in pure CO led to the reduction of the oxidic catalyst to Ru metal. The fate of the surface Cl atoms upon complete reduction of the underlying oxide substrate could not be resolved by these experiments.

In conclusion, one may state, that the chlorinated catalyst revealed a comparable reactivity towards the CO oxidation as reported for s-$RuO_2(110)$[139]. The CO oxidation on $RuO_{2-x}Cl_x(110)$ is configurationally blocked by Cl_{ot} atoms, which prevent the encounter of the reactants on the cus-rows of the oxide, as shown in chapter 16.2. The dynamics of the surface chlorine atoms, induced by the presence of oxygen and CO on the surface supplied from the gas phase, may then lead to a reactivation of the surface by means of formation of chlorine free regions, which contain preferentially a symmetric bridging CO_{br} species at low coverages - the active phase in the CO oxidation on $RuO_2(110)$.

16.3.2 Stability against CO in Different Pressure Regimes

The stability of RuO_2 is an essential issue in connection with industrial, heterogeneously catalysed processes like the hydrogen chloride oxidation [140], where RuO_2 supported on TiO_2 (or SnO_2) are used as catalysts. Wolf et al. claim the stability of the SnO_2-supported RuO_2 catalysts during HCl oxidation containing CO in the feed gas. Carbon monoxide can be present in relatively large amounts as an impurity in the HCl waste gas in process steps for the preparation of isocyanates, such as phosgenation (up to 5 vol.% CO). It causes problems due to the exothermicity of the CO oxidation reaction, which takes place on the HCl oxidation (recycling) catalyst, resulting in unwanted overheating and hot spots in the catalyst bed. In the previous section, it has been shown that both s-$RuO_2(110)$ and $RuO_{2-x}Cl_x(110)$ are structurally stable under CO oxidation conditions, as long as oxygen is present in the feed gas.

The stability of $RuO_{2-x}Cl_x(110)$ against the reductant carbon monoxide is in the scope of the following experiments. Both HV and higher pressure SXRD experiments have been carried out to study the stability of $RuO_{2-x}Cl_x(110)$ against CO and later, its degradation via reduction by CO at elevated temperatures in comparison to the stoichiometric oxide.

Stability of $RuO_{2-x}Cl_x(110)$ against CO at 10^{-5} mbar

For stability tests by means of surface X-ray diffraction, s-$RuO_2(110)$ has been chlorinated by annealing the sample to $T = 560$ K in $p(\mathrm{HCl}) = 2 \times 10^{-7}$ mbar for a prolonged time, afterwards it was cleaned by a flash to $T = 660$ K. The stability of the chlorinated oxide was then studied first under CO pressures as low as $p(\mathrm{CO}) = 1 \times 10^{-5}$ mbar at $T = 440$ K. Figure 16.13 displays a time scan of a reflex at (**H**, **K**, **L**) = (0.884, 0.884, 1.3) of the chlorinated $RuO_2(110)$ sample which is indicative of the presence of the oxide. It can easily be seen from the time development of this reflex at $T = 440$ K in a background pressure of $p(\mathrm{CO}) = 1 \times 10^{-5}$ mbar that the surface is stable under these conditions. No significant reduction of the chlorinated oxide could be achieved by applying the above-mentioned protocol, quite in contrast to $RuO_2(110)$ which was significantly reduced within one hour under the present reducing conditions.

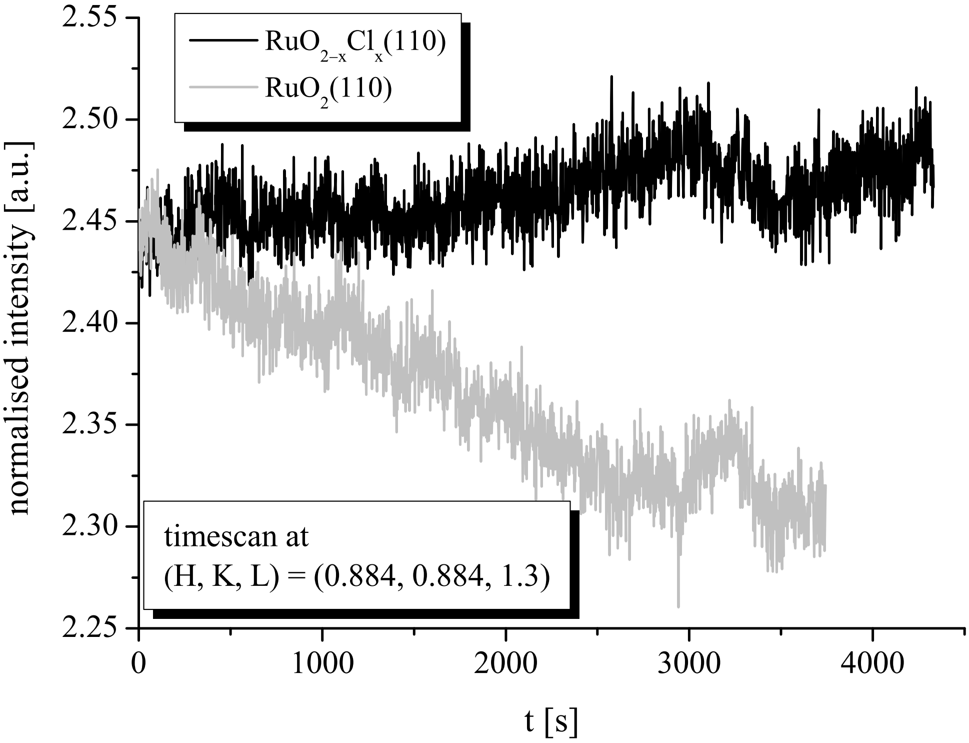

Figure 16.13: SXRD: time development of the (**H**, **K**, **L**) = (0.884, 0.884, 1.3) reflex of $RuO_{2-x}Cl_x(110)$ (black) and s-$RuO_2(110)$ (grey) at $T = 440$ K in $p(\mathrm{CO}) = 1 \times 10^{-5}$ mbar.

Stability of $RuO_{2-x}Cl_x(110)$ against CO at 1 mbar

Experiments under HV conditions have shown that the chlorinated oxide is stable at least over a time period of one hour. The reduction process at $p(\mathrm{CO}) = 1$ mbar of both s-$RuO_2(110)$ and $RuO_{2-x}Cl_x(110)$ will be studied in the next experiment. The stability of both oxides will be compared regarding the temperature where the reduction to the Ru metal takes place. Therefore, both stoichiometric $RuO_2(110)$ and $RuO_{2-x}Cl_x(110)$ (two samples) were exposed to $p(CO) = 1$ mbar and the temperature was gradually increased starting from $T = 350$ K. Figure 16.14 shows the temperature programmed reduction experiment. As an indicator for the presence and the structural integrity of the surface oxide phase, the SXRD reflex at (**H**, **K**, **L**) = (0.884, 0.884, 1.3) was used. Both the stoichiometric and the chlorinated oxides were immediately reduced as soon as the temperature increased above approximately $T = 500$ K.

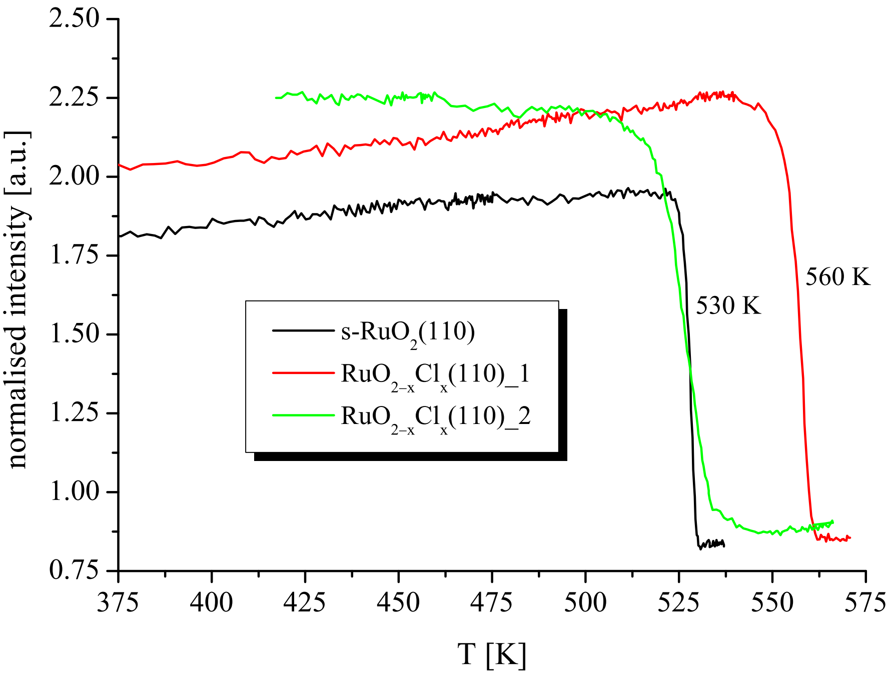

Figure 16.14: Temperature programmed reduction of both s-$RuO_2(110)$ and $RuO_{2-x}Cl_x(110)$ in a background pressure of $p(CO) = 1$ mbar. As an indicator for the presence of the oxidic phase the SXRD reflex at (**H**, **K**, **L**) = (0.884, 0.884, 1.3) was monitored over time/temperature.

Among the three samples, the stoichiometric one was reduced first with the steepest descent of the SXRD reflection. Both chlorinated ruthenium dioxide samples were reduced with a smaller initial slope, indicating a higher stability of the chlorinated oxide in comparison to s-RuO_2(110), which should be due to the presence of surface Cl atoms accounting for a passivating effect. However the protection is not sufficient under these reducing conditions during this experiment at temperatures as high as $T = 550$ K. The difference in the temperature of maximum reduction speed between the two chlorinated oxide is probably due to different degrees of chlorination of the oxide and/or different amounts of residual HCl in the reactor cell.

In the HV pressure regime (10^{-5} mbar) the chlorination of RuO_2 was stable at $T = 440$ K and was able to protect the oxide substrate from reduction. The first step in the microscopic reaction mechanism for the reduction of the oxide under CO atmosphere is the reduction of O_{br}. The O_{bulk} induced $Cl_{br} \rightarrow Cl_{ot}$ shift reaction leads to more O_{br} atoms, which can also be reduced by CO supplied from the gas phase. However, the bridging vacancies created by the reduction of O_{br} may be filled again by Cl_{ot}, which is thermodynamically favourable in the presence of CO_{ot}. Thereby, the chlorinated surface is self-protecting. Nevertheless, the reduction process overrules this protection process, when the surface is heated to higher temperatures, since then the O_{bulk} induced $Cl_{br} \rightarrow Cl_{ot}$ shift reaction is much faster and can not be compensated rechlorination.

16.4 Summary of the Results - CO Oxidation over $RuO_{2-x}Cl_x$(110)

Chlorine atoms, accommodated on 1f-cus Ru sites have been identified to inhibit the combination reaction of CO_{ot} and O_{ot} atoms along the cus-rows in a configurational manner. Nevertheless, this inhibition could be overcome by a dynamic exchange of the surface chlorine atoms between bridging and on top sites. The exchange process and therefore the dynamics of the chlorine atoms on $RuO_{2-x}Cl_x$(110) is induced by the interplay of both surface accommodated oxygen atoms and carbon monoxide molecules, whereas oxygen is accounting for the dechlorination of the bridging positions and CO provides the required reactivity to rechlorinate O_{br} by Cl_{ot} atoms. This results were mainly achieved by means of the RAIRS O_{ot} titration experiments as a first-order model approach for the CO oxidation described in chapter 16.1.

In situ RAIR spectroscopy during steady-state CO oxidation, on both s-$RuO_2(110)$ and $RuO_{2-x}Cl_x(110)$ at $T = 350$ and 400 K respectively, gave valuable insight into the restructuring of the catalyst surface under operating conditions. IR spectroscopy revealed that as long as only CO was present in the feed gas, the surface behaved rather statically concerning the bridging chlorination pattern. With the introduction of O_2 making the feed gas stoichiometric, the $Cl_{br} \rightarrow Cl_{ot}$ shift reaction set in and induced a dynamic process which may lead to the formation of Cl-free CO_{br} islands, which were ascribed to be the active phase during the CO oxidation (cf. [13, 14]). In this way, the chlorinated catalyst has a possibility to reactivate itself and to circumvent the configurational blockade by the Cl_{ot} atoms, which obstructs the recombination of CO_{ot} and O_{ot}.

The model of the reactivating catalyst bearing CO_{br} islands as the active phase was successfully transferred to higher pressure CO oxidation experiments together with stability measurements by *in operando* surface X-ray diffraction. Here, the catalyst was reported to be stable and active under harsh reducing feed gas conditions, at temperatures up to $T = 550$ K, as long as a residual amount of oxygen was present in the feed. A comparison of the turn over frequencies of both s-$RuO_2(110)$ and $RuO_{2-x}Cl_x(110)$ showed a similar reactivity of both catalysts, whereas the chlorinated catalyst has a smaller number of active sites, accounting for the smaller production rate of CO_2 observed during the combined *in operando* SXRD-MS experiments.

SXRD confirmed the stability of the chlorinated oxide at $T = 440$ K under pure CO atmosphere in the high vacuum region. Furthermore, the degradation process of the chlorinated oxide under 1 mbar CO at temperatures of $T > 530$ K was shown to proceed slower than on s-$RuO_2(110)$, indicating a higher stability of $RuO_{2-x}Cl_x(110)$ which is due the presence of surface chlorine atoms.

Chapter 17

Atmospheric Pressure Reaction Experiments: CO Oxidation on RuO_2 Powder Catalysts

The following chapter is dedicated to atmospheric pressure CO oxidation reaction experiments over RuO_2 powder catalysts in a fixed bed reactor system, which was described in chapter 8. All experimental data are by courtesy of C. H. Kanzler [78].

The main goal of the atmospheric pressure reaction experiments in the fixed bed reactor was to check whether the results obtained for the CO oxidation on $RuO_{2-x}Cl_x(110)$ under UHV/HV conditions can be transferred to more realistic conditions. Therefore, the influence of preceding HCl exposure, i.e. surface chlorination, on the reactivity of the RuO_2 powder catalyst samples towards CO oxidation has been studied.

17.1 CO Oxidation over Fully Oxidised RuO_2

Beginning with two standard experiments for the characterisation and validation of the fixed bed reactor system, the CO oxidation over i) fully oxidised RuO_2 and ii) reduced RuO_2 powders was studied. Similar experiments had been carried out already by Narkhede [141] and Aßmann et al. [76]. The data collected during the present measurement will be compared with the cited references.

9.0 mg of the RuO_2 powder catalyst (sintered, sieve fraction 255-350 μm) were introduced into the reactor system and flushed with argon at room temperature (15 min, $f(\mathrm{Ar}) = 50$ sccm). Afterwards, the catalyst was reduced by annealing in hydrogen (60 min, $T = 773$ K, f(5.2% v/v H_2 in Ar) = 50 sccm) in order to obtain a defined starting material, then cooled down to $T = 693$ K in $f(\mathrm{Ar}) = 50$ sccm and oxidised in f(10% v/v O_2 in Ar) = 50 sccm for further 60 min according to [141]. The catalyst bed was then cooled down to room temperature again in $f(\mathrm{Ar}) = 50$ sccm.

The treatment mentioned above led to a fully oxidised RuO_2 powder catalyst which was subsequently used for the CO oxidation in the fixed bed reactor system. The catalyst was exposed to a constant flow of a stoichiometric reaction mixture consisting of CO and O_2 (f(0.9% v/v O_2 + 1.8% v/v CO in Ar) = 50 sccm) and the temperature was varied as indicated in table 17.1 and figure 17.1.

Δ *t* [h]	***T*(furnace) [K]**	***T*(catalyst bed) [K]**
1.6	395	395
1.9	415	416
16.3	444	445
1.4	416	417
2.2	396	396
1.6	395	396
2.0	415	417
14.3	443	445
1.8	416	417
7.8	395	396

Table 17.1: Temperature programme during CO oxidation in the fixed bed reactor. Δt corresponds to the time increment.

The conversion for both CO and O_2 are independent of the catalyst bed temperature. No significant production of CO_2 has been found, measured as a 'zero' conversion of both CO and O_2. For an active RuO_2 sample one expects a reactivity in the temperature regime during the present reaction experiments. As reported by Narkhede et al. the fully oxidised RuO_2 does not display any reactivity [141], which is in line with the results presented here. The variations in the conversion curves can thus be related to instabilities in either the flow of the reactant gases through the reactor, or instabilities of the QMS system (leak valve or ion source and secondary electron multiplier). The absolute error in the conversion has been estimated to be approximately ±5%.

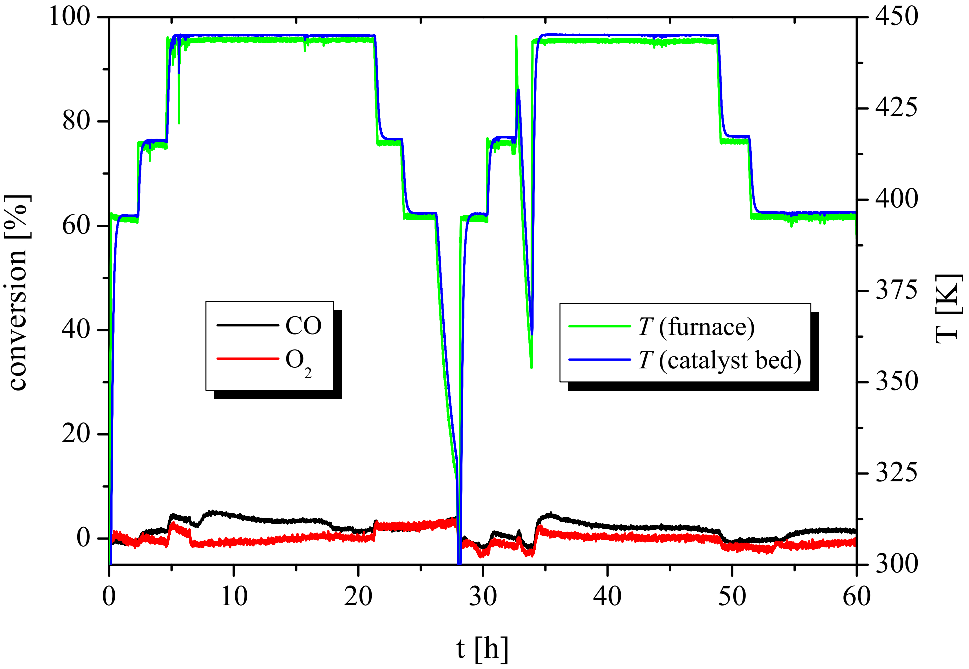

Figure 17.1: CO oxidation reaction in the fixed bed reactor over fully oxidised RuO_2 powder. Conversions are based on QMS analysis (m/e = 28 for CO, m/e = 32 for O_2, m/e = 44 for CO_2).

The temperature in the catalyst bed is roughly 2 K higher than the temperature measured in the oven, which is due to uncertainties in the temperature measurement. Since there was no CO oxidation reaction observable by mass spectrometry, this temperature difference can not be related to reaction exothermicity.

17.2 CO Oxidation over H_2-Reduced RuO_2

As reported by Narkhede et al., a treatment of the fully oxidised (and inactive) RuO_2 powder catalyst by hydrogen, i.e. a complete reduction of the catalyst particles to ruthenium metal, led to an activation with respect to CO oxidation [141].

Thus, the inactive catalyst stemming from the experiment described in the section before, was reoxidised again in oxygen at $T = 493$ K (60 min, f(10% v/v O_2 in Ar) = 50 sccm), flushed with Ar (15 min, f(Ar) = 50 sccm) and reduced at $T = 773$ K in the presence of hydrogen (60 min, f(5.2% v/v H_2 in Ar) = 50 sccm). The reduced catalyst was cooled down to room temperature in Ar (f(Ar) = 10 sccm) over night.

The CO oxidation reaction was run with an identical feed gas composition as described in the previous section (f(0.9% v/v O_2 + 1.8% v/v CO in Ar) = 50 sccm). The corresponding temperature programme is summarised in table 17.2.

$\Delta\ t$ [h]	**T(furnace) [K]**	**T(catalyst bed) [K]**	**conversion [%]**
2.8	394	399	<48
2.5	415	422	66
10.6	444	451	72
2.1	416	423	67
2.1	396	403	53
1.2	394	401	57
1.9	414	422	69
5.8	445	452	74
2.6	416	424	65
2.1	396	403	56

Table 17.2: Temperature programme during CO oxidation in the fixed bed reactor. Conversion is given as the mean value from the conversions of both CO and O_2, the absolute errors amount to ±2%.

Figure 17.2 shows the conversion of CO and O_2, respectively at the different temperature steps. Upon heating from room temperature to the first temperature step ($T = 395$ K), the catalyst experienced activation and afterwards was active towards the CO oxidation as can be seen from the high conversions. Throughout the measurement, the temperature of the catalyst bed is by 6-8 K higher than the furnace temperature, which can be ascribed to the CO oxidation taking place after initial activation of the catalyst.

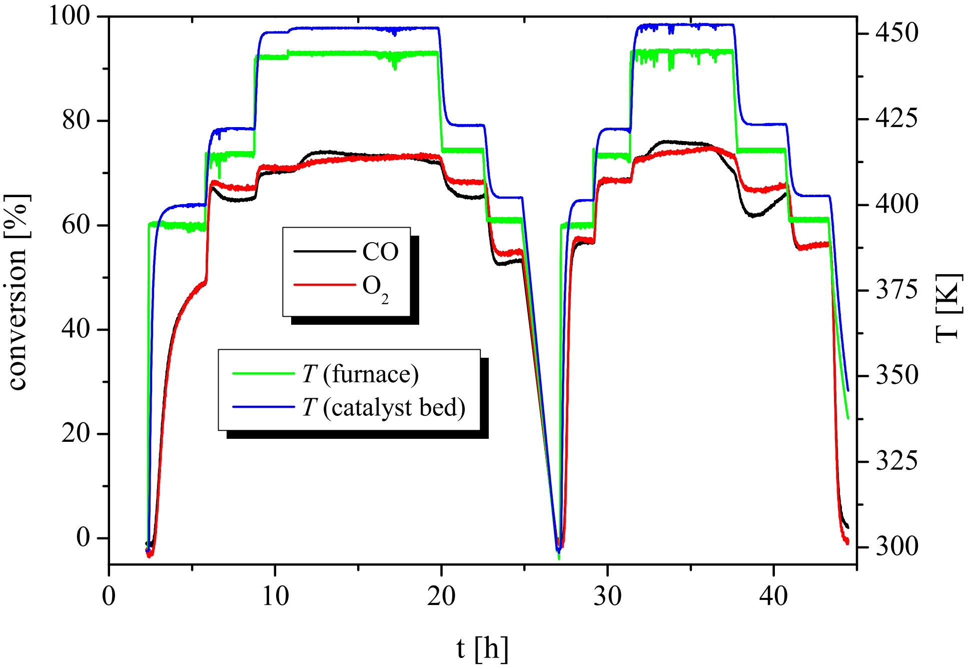

Figure 17.2: CO oxidation reaction in the fixed bed reactor over fully oxidised RuO_2 powder after a hydrogen treatment.

During the second temperature cycle, the conversions were reproduced in the range of ±5 %, which is an indicator for the longterm stability of the catalyst under the present reaction conditions.

In conclusion, the results obtained for the CO oxidation (stoichiometric feed) over hydrogen treated RuO_2 powder are in good agreement with the results reported in the literature [76, 141]. A further discussion of the results concerning the Ru catalyst is not in the scope of this thesis. The fixed bed atmospheric pressure reactor system set up by C. H. Kanzler can be regarded as being in a good working state, producing reliable data.

17.3 CO Oxidation over Chlorinated RuO_2

In this section, the influence of hydrogen chloride exposure on the activity of a RuO_2 powder catalyst in the CO oxidation reaction will be investigated. The active catalyst of the previous experiment, described in section 17.2, was treated with dry hydrogen chloride at room temperature for 30 min with a gas flow of 5 bubbles/sec (washing flask, filled with NaOH, c = 7 mol/l). After the HCl exposure, the reactor was heated to $T = 573$ K for 30 min in order to chlorinate the oxide. Excessive HCl and Cl_{ot} atoms, respectively were removed by flushing the reactor for 30 min by argon (f(Ar) = 50 sccm) at $T = 693$ K followed by cooling to room temperature in Ar (f(Ar) = 50 sccm).

The reactivity of the chlorinated catalyst with respect to the CO oxidation was then tested by reaction measurement. The reaction was carried out applying the same feed gas composition (f(0.9% v/v O_2 + 1.8% v/v CO in Ar) = 50 sccm), whereas the reactor was kept at $T = 445$ K for 14 hours. Figure 17.3 shows that the catalyst was not able to convert CO + O_2 to CO_2 after the HCl treatment. The conversion of both CO and O_2 were equal to zero, even at the temperature where the stoichiometric catalyst showed full conversion of CO to CO_2. Furthermore, no observable activation of the chlorinated RuO_2 occurred during heating in the feed gas flow. The variations in the conversion curves of CO and O_2 are due to instabilities and are within the error bars of ±5%.

17.4 CO Oxidation over Chlorinated RuO_2 after O_2 Treatment

After the experiment reported in section 17.3, the question arose if it would be possible to reactivate the catalyst by a roasting step in oxygen at $T = 693$ K, since it has been observed that heating to $T = 700$ K in oxygen leads to the desorption of chlorine from chlorinated RuO_2, at least under UHV conditions (cf. section 15.2.2). Oxygen induces a shift of bridging chlorine atoms to 1f-cus Ru sites from where they can desorb recombinatively at temperatures above $T > 650$

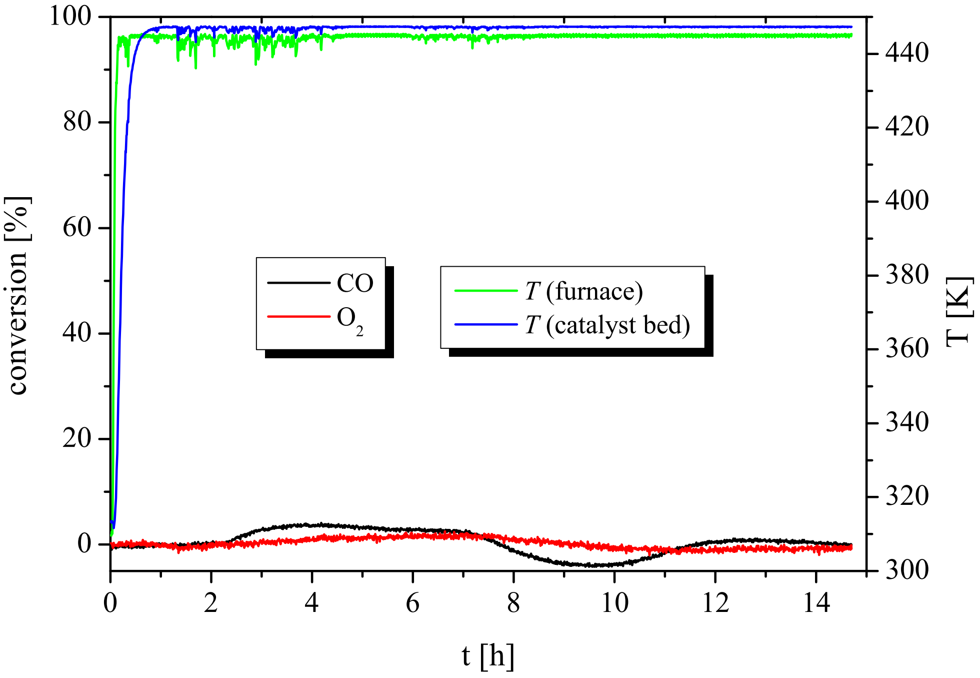

Figure 17.3: CO oxidation reaction in the fixed bed reactor over freshly chlorinated RuO_2 powder after a flash to $T = 700$ K.

K.

The inactive catalyst sample of the previous experiment (section 17.3), after chlorination and 14 hours of annealing in the feed gas at $T = 445$ K, was treated with oxygen (60 min, f(10% v/v O_2 in Ar) $=$ 50 sccm) at $T = 693$ K and cooled to room temperature in Ar (f(Ar) $=$ 50 sccm). After this dechlorination and reoxidation step, the catalyst was exposed to the feed gas again (f(0.9% v/v O_2 $+$ 1.8% v/v CO in Ar) $=$ 50 sccm) at $T = 445$ K. Once again, the RuO_2 catalyst did not show activity with respect to the CO oxidation, as can be inferred from figure 17.4. The conversion of both CO and O_2 were measured to be zero within the tolerance of the analysis setup.

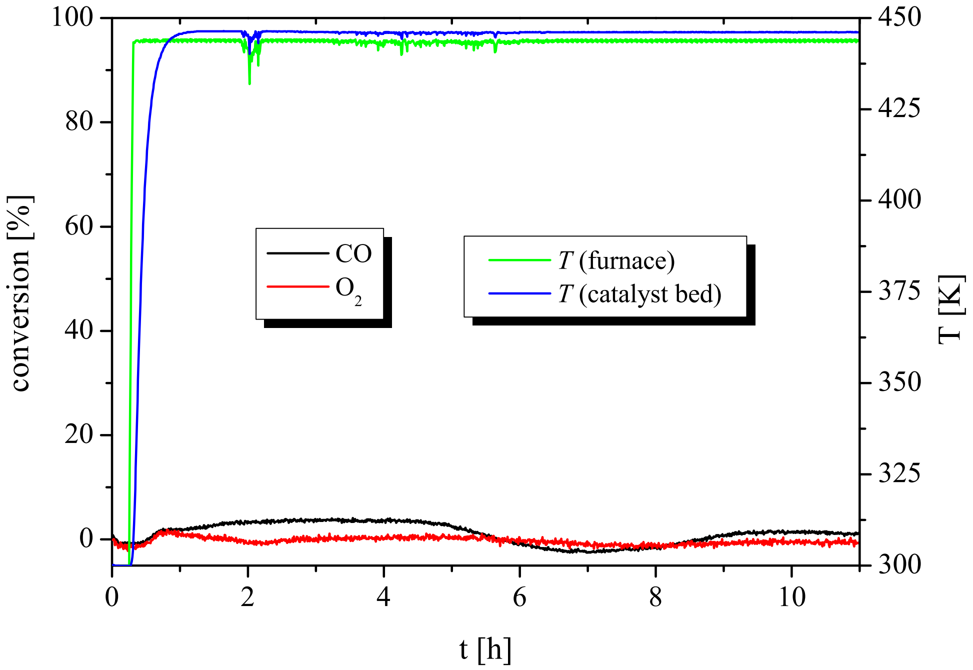

Figure 17.4: CO oxidation reaction in the fixed bed reactor over chlorinated RuO_2 powder after oxygen treatment.

After the oxygen treatment, the catalyst should be oxidised to a large extent and almost chlorine free and thus, should resemble the fully oxidised (and still inactive) catalyst presented in section 17.1. The reactivity data displayed in figure 17.4 confirm this consideration.

The question, if a fully oxidised and dechlorinated RuO_2 was present after these reaction and preparation steps could not be solved. However, it has been checked in the next chapter, whether reducing the catalyst by hydrogen exposure leads to a reactivation with respect to the CO oxidation as observed in chapter 17.2.

17.5 CO Oxidation over Chlorinated RuO_2 after Reduction by H_2

In order to determine the state of the RuO_2 powder catalyst after chlorination and roasting in oxygen, the sample was exposed to hydrogen at $T = 693$ K (60 min, f(5.2% v/v H_2 in Ar) = 50 sccm), cooled in Ar (f(Ar) = 50 sccm) to room temperature. The catalyst - now presumably metallic - was then subjected to a reaction measurement at $T = 445$ K to check its reactivity or its reactivation behaviour, respectively. The feed gas composition and the flow conditions were kept constant (f(0.9% v/v O_2 + 1.8% v/v CO in Ar) = 50 sccm) and the catalyst was exposed for 11 hours to the reactant gas. Figure 17.5 shows a reactivation of the catalyst, however the conversion levels of CO and O_2 reported in section 17.2 were not reached. The conversion of both reactant gases at $T = 445$ K reached 38 % at the beginning of the reaction and increased to approximately 49 % after 11 hours, corresponding to an ongoing (re)-activation and stabilisation of the catalyst under reaction conditions.

The reasons for the lower conversion levels observed in this experiment are manifold. Since the dechlorination of the sample by annealing in O_2 at 700 K liberates Cl_2, readsorption of Cl_2 in the catalyst bed may occur, which is not the case under UHV conditions. The total deactivation of the catalyst after HCl exposure may also be due to readsorption processes - leading to a persistent poisoning of the catalyst powder by HCl, which could not be removed by means of flushing with Ar at 693 K. Such a “HCl overkill” did not occur under UHV conditions probably due to the lower HCl dosages applied in the chlorination protocol.

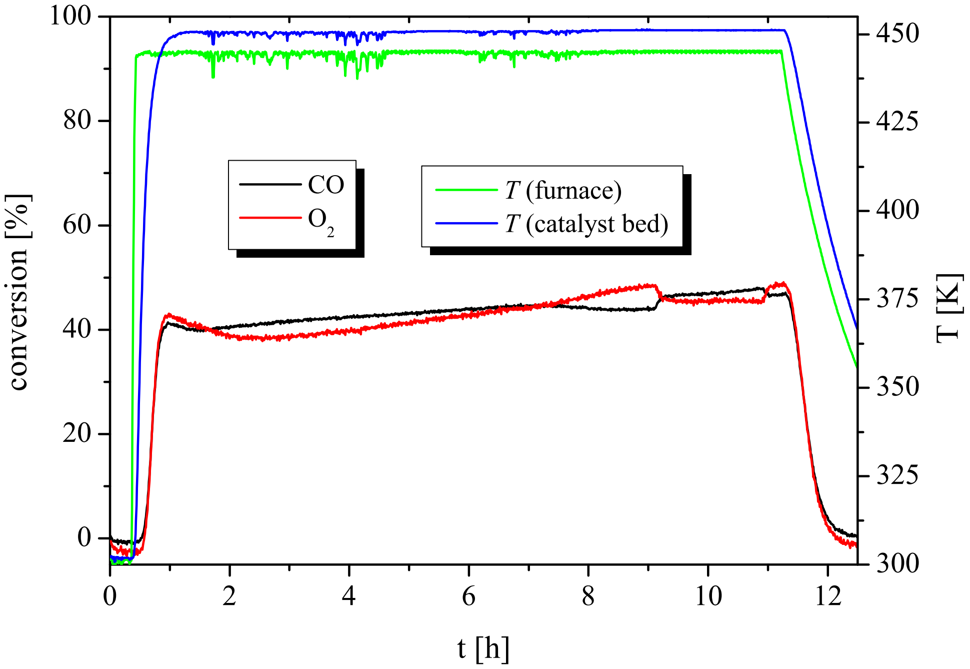

Figure 17.5: CO oxidation reaction in the fixed bed reactor over chlorinated RuO_2 powder after oxidation and H_2 treatment.

17.6 Discussion

The CO oxidation experiments carried out in the atmospheric pressure regime in the new fixed bed reactor setup on chlorinated RuO_2 powder catalysts demonstrated that HCl, applied to the catalyst, led to a severe deactivation towards CO oxidation. Although the analytic tools to determine the degree of the chlorination of the powder catalyst were not available, the deactivation of the catalyst by HCl exposure may be ascribed to a, at least partial, chlorination based on the total loss of reactivity. However, in comparison to the experiments of the previous chapters, where the chlorinated $RuO_2(110)$ model catalyst was reported to be able to reactivate by means of dynamic surface processes and restructuring of the surface chlorine coverage, the HCl exposure led to a total deactivation. Possibly, the HCl dosage applied under atmospheric pressure conditions led to a more stable chlorination, that may not be restricted to the surface alone quite in contrast to the surface selective chlorination observed for $RuO_2(110)$. Though, a chlorination of the RuO_2 bulk could not be evidenced by means of SXRD. As already mentioned, readsorption of HCl/Cl_2 in the catalyst bed may be a further issue accounting for the different behaviour of the RuO_2 catalysts under UHV and atmospheric pressure conditions. The mechanism of the deactivation by atmospheric pressure HCl exposure could not be elucidated by these preliminary experiments. At this point, in situ and operando techniques are required in order to analyse the chemical state and the composition of the catalyst sample under working conditions.

Part V

Conclusions

Chapter 18

Summary and Outlook

The main goal of the present thesis was to obtain a possibly accurate, molecular level insight to the modified stability and reactivity of chlorinated RuO_2 model catalysts. A detailed review of the results is given in the following, with special emphasis on the remarkable influence of coadsorbed species (CO and O) on the mobility of the surface accommodated chlorine atoms.

Mechanism of Chlorination of RuO_2(110) The hydrogen promoted chlorination of stoichiometric RuO_2(110) was in the scope of the first part of this thesis (chapter 12). By means of DFT calculations, a detailed reaction mechanism of the chlorination of the bridging rows on RuO_2(110) was proposed. The substitution of a bridging oxygen atom O_{br} by Cl stemming from adsorbed HCl_{ot} is crucially dependent on the formation of bridging water as a leaving group, by either dissociative adsorption of HCl adjacent to a bridging hydroxyl group (O_{br}-H) or by the recombination of two neighbouring O_{br}-H groups. The latter process necessitates a H-diffusion step along the O_{br} rows, for the case that no neighbouring O_{br}-H groups are present. As shown by TDS, the H-diffusion step is promoted by Cl_{ot} and accounts for the water formation at temperatures above $T = 520$ K for hydrogen deficient situations like present in the Sumitomo process ($HCl{:}O_2 > 1{:}4$). The desorption of the bridging water and thereby the formation of a bridging vacancy proceeds via a shift of O_{br}-H_2 to a 1f-cus Ru site, from which the water molecule desorbs. This shift reaction is decisively facilitated when the hydrogen bond stabilisation by the adjacent Cl_{ot} is weakened. The bridging vacancy, even if of a rather short lifetime, is subsequently chlorinated by diffusion of a Cl_{ot} into the vacancy.

The results of the DFT proposed chlorination mechanism could be confirmed by means of HRCLS measurements. Here, the important role of water formation during the chlorination process was demonstrated by a comparison of chlorination experiments starting from either s-RuO_2(110) or a hydrogen pre-treated s-RuO_2(110) surface, where hydrogen pre-exposure led to a more efficient chlorination even at lower temperatures.

Furthermore, the importance of the transformation of the bridging oxygen atoms into good leaving groups in the chlorination process has been shown by a CO-mediated chlorination of s-RuO_2(110) (CO_2 as leaving group) under Cl_2 exposure. This result was important in the later course of the thesis as well, since it is a prerequisite for the interpretation of the observed dynamics of the chlorinated surface under CO oxidation conditions.

By means of AES, the amount of Cl atoms accommodated on the surface was accurately determined (chapter 13). The necessary calibration of the spectrometer was achieved by preparation of a well defined $(\sqrt{3} \times \sqrt{3})$R30°-Cl-Ru(0001) phase, whose structure has been analysed by LEED. A maximum amount of 80 % Cl_{br} could be achieved on RuO_2(110) by repeated (re-)chlorination procedures, whereas DFT calculations suggest that a more stable bridging chlorination configuration contains about 50 % Cl_{br}.

CO as an IR probe molecule on $RuO_{2-x}Cl_x$(110) The detailed knowledge gained about the chlorination process and the amount of Cl atoms accommodated on the surface under different conditions constituted a solid fundament for a further investigation of the $RuO_{2-x}Cl_x$(110) model catalyst. CO was successfully established as a chemically sensitive IR probe molecule on $RuO_{2-x}Cl_x$(110), allowing for RAIRS studies under both UHV and higher pressure conditions (chapter 14). Similar to references [13, 14], well-defined phases of CO coadsorbed with O and Cl have been prepared under UHV conditions, their characteristic IR bands being used in the interpretation of RAIR spectra under higher pressure reaction conditions as well.

The influence of the substitution of O_{br} by chlorine led to a red shift of the CO_{ot} stretching vibrations of about $\Delta\tilde{\nu} \cong -10$ cm^{-1}, whereby the change in the electronic structure of the CO_{ot} molecule was determined to be very small. However, the high sensitivity of RAIRS allowed to detect even the presumably minor changes in the occupation of the $2\pi^*$ orbital of CO. The effect of Cl_{ot} atoms on the CO_{ot} vibrations was dominated by the property of Cl_{ot} to interrupt the formation of longer chains of CO_{ot}, thereby strongly influencing the strength of the dipole-dipole coupling between the CO molecules.

The determination of the amount of chlorination of the bridging sites indicated the presence of about 20 % residual O_{br} atoms. CO exposure at $T = 330$ K (mild reduction) followed by RAIRS analysis of the adsorbate confirmed their presence and the reducibility of the O_{br} atoms. This result was further corroborated by means of HRCLS measurements.

Based upon the mild reduction of $RuO_{2-x}Cl_x(110)$ and further coadsorption experiments of CO with O, the determination of the vibrational characteristics of the CO_{br} species was completed (cf. table 14.4). CO could now be used as an IR probe molecule in RAIR spectroscopy for the further investigation of $RuO_{2-x}Cl_x(110)$ under different experimental conditions.

Interaction of $RuO_{2-x}Cl_x(110)$ with oxygen: The $Cl_{br} \leftrightarrow Cl_{ot}$ shift reaction The interplay of oxygen atoms with the surface chlorine atoms was experimentally studied by means of TDS, AES, RAIRS and HRCLS. The experimental results were again substantiated and interpreted theoretically by DFT calculations.

Since the configuration O_{br}/Cl_{ot} is by 0.25 eV more stable than Cl_{br}/O_{ot}, a driving force towards shifting the Cl_{br} to on top positions exists when oxygen atoms are present. This concept was developed in chapter 15, starting with the investigation of the thermal decomposition of the chlorinated oxide by TDS, AES and temperature programmed AES. The thermal loss of the bridging Cl_{br} atoms at $T = 700$ K could be explained by an O_{bulk} induced shift of the Cl_{br} atoms to on top positions, from which they can desorb by recombination to yield Cl_2.

The oxygen induced $Cl_{br} \rightarrow Cl_{ot}$ shift reaction has been shown to be a key concept in the correct interpretation of the observed dynamics of the surface chlorination state of $RuO_{2-x}Cl_x(110)$: The diffusion of Cl_{ot} along the cus-rows is activated by $E_{diff} < 0.9$ eV and therefore feasible at temperatures just above room temperature.

The introduction of CO into the O/Cl adsorbate system on $RuO_2(110)$ as a third component enhances the dynamics of the surface chlorination by enabling the backward $Cl_{br} \rightarrow Cl_{ot}$ shift reaction, i.e. the CO induced rechlorination the bridging sites. As shown by DFT calculations and evidenced by experiments in chapter 15.2, a general rule could be formulated: the presence of O atoms forces Cl_{br} to move to on top positions and the presence of CO favours the occupation of bridging positions by the Cl_{ot} atoms. The complex interplay of the three surface species Cl, CO, and O thus leads to a highly dynamic situation on the surface.

The observed CO RAIRS double feature was used as an example to demonstrate the importance of the $Cl_{br} \leftrightarrow Cl_{ot}$ shift reaction in the interpretation of the complex behaviour of the IR spectra of CO adsorbed on $RuO_{2-x}Cl_x(110)$. It has been shown that Cl_{ot} prevents the recombination of O_{ot} atoms, leading to a late desorption of the O_{ot} atoms by recombination only above the temperature where Cl_{ot} recombination sets in (according to [138]). This configurational blockade of the 1f-cus Ru sites, will also be encountered in the context of CO oxidation on $RuO_{2-x}Cl_x(110)$.

CO oxidation over $RuO_{2-x}Cl_x(110)$ Equipped with the knowledge about the mutual interaction of CO molecules with O and Cl atoms and the insight provided by the detailed RAIRS study on s-$RuO_2(110)$ by Farkas et al. [13, 14], the reactivity of $RuO_{2-x}Cl_x(110)$ towards the CO oxidation has been studied and the influence of the Cl atoms has been elucidated.

By means of the O_{ot} titration experiments, the inhibiting role of Cl_{ot} on the CO oxidation has been ascribed to a configurational blockade by the Cl_{ot} atoms along the cus-rows preventing the encounter of CO_{ot} and O_{ot}. *In situ* RAIR spectroscopy of the CO oxidation over $RuO_{2-x}Cl_x(110)$ under steady-state conditions in the 10^{-6} mbar range has surprisingly revealed that the inhibiting effect of the Cl_{ot} atoms could be overcome by a restructuring of the surface, yielding Cl-free regions characterised by a low coverage of CO_{br}. This low coverage CO_{br} phase was assigned to be the active phase in the CO oxidation, providing a sufficient number of unoccupied, neighbouring 1f-cus Ru sites necessary for the dissociative adsorption of O_2 [14].

Applying this model, the reactivity of the chlorinated $RuO_{2-x}Cl_x(110)$ surface in the mbar regime was successfully explained. The combined SXRD-MS study carried out at ESRF showed an approximately 15-20 % lower turn over frequency of the chlorinated catalyst in the CO oxidation. This decrease in activity was assigned to a lower number of active sites, due to the presence of chlorine on the surface, the active phase being identical to that of the stoichiometric catalyst, as shown by the *in situ* RAIRS experiments. Moreover, the surface chlorination is responsible for a passivation of the chlorinated RuO_2 surface against exposure to reductants.

The inactivity of the chlorinated RuO_2 powder catalysts under atmospheric pressure reaction conditions could not be explained properly by the models developed for the single crystal experiments. Thus, a material gap is still existent with respect to the influence of HCl/Cl atoms on the powder catalyst. This point can only be elucidated only by further operando measurements of the working catalyst.

Conclusions and Outlook The observed dynamic behaviour of the surface chlorine atoms on $RuO_{2-x}Cl_x(110)$ should not be restricted to CO oxidation conditions alone, but should be relevant under HCl oxidation conditions as well. Since oxygen is present in the feed gas, the $Cl_{br} \rightarrow Cl_{ot}$ shift reaction is enabled. The corresponding backward reaction, i.e. the rechlorination of the bridging positions, is possible due to the presence of HCl providing H atoms as a prerequisite for the water formation and hence for the rechlorination of the bridging sites. One may thus expect a similar dynamic response of the surface under HCl oxidation conditions as well. This implies, that the 1-dimensionality of the catalyst along the cus-rows may be overcome by the proposed dynamics, leading to a more complex situation on the surface as formerly assumed.

During the present work, a reasonable amount of new knowledge about the atomic processes taking place on the chlorinated RuO_2 model catalysts has been achieved. This could provide a foundation for future investigations and may lead to further improvements of the RuO_2 catalysts for HCl oxidation. The author would gladly learn that the results presented here have contributed to a more efficient and sustainable resource management in the chlorine chemistry of the future.

Part VI

Appendices

Appendix A

Graphical Representations of the $RuO_2(110)$ Surface

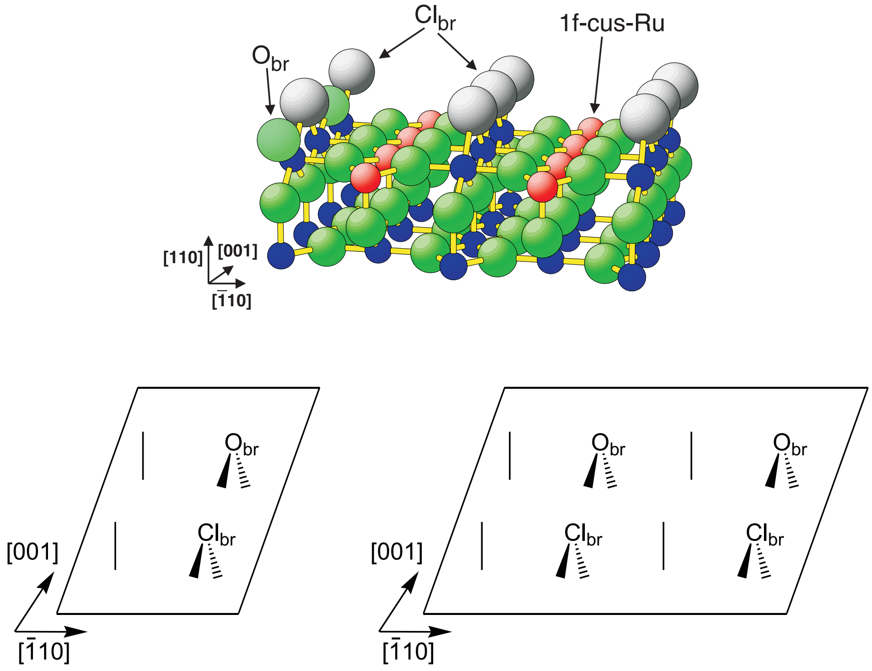
Cl$_{br}$
1f-cus-Ru
O$_{br}$
[110]
[001]
[$\bar{1}$10]
O$_{br}$
Cl$_{br}$
[001]
[$\bar{1}$10]
O$_{br}$
O$_{br}$
Cl$_{br}$
Cl$_{br}$
[001]
[$\bar{1}$10]

1x2 surface unit cell

2x2 surface unit cell

Figure A.1: i) Ball-and-stick model of bulk truncated $RuO_2(110)$ revealing undercoordinated surface atoms: bridging O atoms (O_{br}, green balls), bridging Cl atoms (Cl_{br}, grey balls) and one fold coordinatively unsaturated Ru-sites (Ru 1f-cus, red balls), which are called on-top sites. ii) Simplified representation of $RuO_2(110)$: Solid upright lines refer to 1f-cus Ru sites and double wedges indicate bridging positions.

Appendix B

Lebenslauf

Kontaktinformation

Jan Philipp Hofmann
Auf der Schanz 35
35606 Solms-Oberndorf

jan.p.hofmann@phys.chemie.uni-giessen.de

Staatsangehörigkeit: deutsch

geboren am 01.05.1982 in Weilburg

Schulbesuch

1988–1992	Grundschule in 35606 Solms-Oberndorf
1992–1998	Gesamtschule in 35606 Solms-Burgsolms
1998–2001	Oberstufengymnasium Goetheschule Wetzlar in 35578 Wetzlar

Studium

10/2001–12/2005	Chemie-Diplomstudium, Justus-Liebig-Universität 35392 Gießen
06.10.2003	Diplom-Vorprüfung
02/2005–07/2005	Auslandsstudium am Roskilde Universitetscenter, 4000 Roskilde, Dänemark (02.-07.2005) im Rahmen des ERASMUS-Programms, Anfertigung eines MSc projects (Diplomarbeit) zum Thema

	"Synthesis and Structural Characterisation of 3-Acyltetronic Acids"
19.12.2005	Verleihung des Akademischen Grads "Diplom-Chemiker", JLU Gießen
01/2006–03/2006	Wissenschaftlicher Mitarbeiter, Physikalisch-Chemisches Institut der JLU Gießen, AG Prof. Dr. H. Over
04/2006-12/2009	Doktorand, Physikalisch-Chemisches Institut der JLU Gießen, AG Prof. Dr. H. Over
16.12.2009	Disputation

Appendix C

Danksagung

Im Folgenden möchte ich mich bei allen Menschen bedanken, die die Entstehung dieser Dissertation ermöglicht haben und die mich auf meinem Weg dorthin begleitet und unterstützt haben.

An erster Stelle danke ich meinem Betreuer Prof. Dr. Herbert Over, der mich schon sehr früh in seine Arbeitsgruppe integriert hat und mir dieses Thema zur Verfügung gestellt hat. Seine freundschaftliche und erfrischend lockere Art, kombiniert mit dem ausgezeichneten Gefühl für die richtige wissenschaftliche Fragestellung, bereiteten mir stets viel Freude.

Dr. Georg Mellau bin ich für die frühe und in allen Facetten tief gehende Einführung in die Geheimnisse der Fourier-Transform-Infrarot-Spektroskopie sowohl hochauflösend in der Gasphase als auch auf Oberflächen zu Dank verpflichtet.

Dr. Attila Farkas war der Retter in letzter Minute. Ohne ihn und seine exzellenten Vorarbeiten wäre zumindest der RAIRS-Part dieser Arbeit wesentlich weniger umfangreich ausgefallen. Außerdem erinnere ich mich mit Freude an die Abende im Realkatalyse-Labor als dort noch keine Schutzbrillenpflicht bestand. Zudem bin ich ihm sehr für die gründliche Durchsicht meiner Dissertation sowie die vielen hilfreichen Tipps dankbar.

Eine weitere Bereicherung hat mein Dissertationsprojekt durch die Einbindung von DFT-Rechnungen erfahren. Diese Erweiterung wäre nicht ohne die Hilfe von Dr. Ari Paavo Seitsonen (damals Institut de Minéralogie et de Physique des Milieux Condensés, Université Pierre et Marie Curie, Paris) möglich gewesen. Im Rahmen von zwei Besuchen in Paris und vielen Skype-Unterhaltungen hat er mich zu einem Halbtheoretiker ausgebildet - das ist ein experimentell arbeitender

Physikochemiker mit Fähigkeiten und etwas Verständnis in der Theorie.

Prof. Dr. Jürgen Janek danke ich für die Übernahme des Zweitgutachtens. Er und die Mitglieder seiner Arbeitsgruppe sind zu einem großen Teil für die gute kollegiale Atmosphäre innerhalb des Physikalisch-Chemischen Instituts verantwortlich.

Dr. Olivier Balmes, Dr. Karina Schulte und Prof. Dr. Edvin Lundgren danke ich für die gute Betreuung und Zusammenarbeit während der Messzeiten am ESRF in Grenoble bzw. MAX-lab in Lund.

Schließlich möchte ich mich bei meinen Kollegen der AG Over bedanken. Stefan Zweidinger, der mich auf dem gesamten Weg durch mein 'neues' Dissertationsprojekt sowohl im Büro als auch im Labor und auf Messreisen begleitet hat, möchte ich für die vielen intensiven Diskussionen, das ausgezeichnete kollegiale Verhältnis sowie das gründliche Korrekturlesen dieser Arbeit danken. Dr. Marcus Knapp danke ich für die gute Zusammenarbeit auf Messzeiten und danach. Christian Kanzler hat im Rahmen seiner Diplomarbeit professionell und zielorientiert innerhalb kurzer Zeit das Realkatalyse-Labor zu dem gemacht, was es heute ist. Den Mitarbeitern der institutseigenen feinmechanischen Werkstatt (insbesondere Harry Heidt, Gerd Pfeiffer und Sascha Lember) und der Elektronikwerkstatt (Harald Weigand und Kurt Bürger) möchte ich für die technische Unterstützung bei An-, Um- und Abbauten im Rahmen meiner apparativen Arbeiten und Messungen danken.

Meinem langjährigen Freund Thomas Armbruster bin ich für die frühe Förderung meiner naturwissenschaftlichen Neigungen sehr dankbar. Ohne ihn und sein Interesse an meinen Interessen wäre ich vielleicht nicht Chemiker geworden.

Stellvertretend für meine Kommilitonen danke ich Markus Langsdorf und Mareike Machuy für die schöne Zeit während des Chemiestudiums und danach.

Dem Fonds der Chemischen Industrie danke ich für die finanzielle Unterstützung durch ein "Chemiefonds-Stipendium für Doktoranden". Der Studienstiftung des deutschen Volkes sowie meinem langjährigen Vertrauensdozenten Prof. Dr. Wolfram Martini danke ich für die ausgezeichnete ideelle und finanzielle Förderung während meines Diplom-Studiums und der Promotionsphase.

Zu guter Letzt möchte ich meiner Familie, allen voran meinen Eltern, danken, die mich von Anfang an mit all ihren Möglichkeiten gut unterstützt hat und meiner Freundin Saskia, die mir die Schlussphase meiner Promotionszeit sehr versüßt hat.

Appendix D

Eidesstattliche Erklärung

Hiermit versichere ich, dass ich die vorliegende Dissertation selbstständig verfasst und keine anderen als die angegebenen Quellen und Hilfsmittel benutzt habe.

Jan Philipp Hofmann

D-35392 Gießen, den 09. November 2009.

Appendix E

Zusammenfassung in deutscher Sprache

Strukturelle Dynamik von chlorierten Rutheniumdioxid-Modellkatalysatoren unter Reaktionsbedingungen

Die Rückgewinnung von Chlor (Cl_2) aus Chlorwasserstoff (HCl) als Abfallprodukt von diversen industriellen Prozessen, wie beispielsweise der Herstellung von Polyurethan-Kunststoffen, ist einer der energieaufwändigsten Prozesse der chemischen Industrie. Das heute hauptsächlich eingesetzte Elektrolyseverfahren nach Bayer&UhdeNora ist mit einem Energieverbrauch von 1.1 MWh/t (Cl_2) trotz einer kürzlich vorgestellten Prozessoptimierung immer noch sehr energieverzehrend.

Die Einführung des Deacon-ähnlichen Sumitomo-Prozesses - der heterogen katalysierten Oxidation von HCl mit Sauerstoff über TiO_2-stabilisiertem Rutheniumdioxid - kann somit als Durchbruch in der modernen Katalyseforschung angesehen werden. Das Verfahren benötigt lediglich 15 % der in der Elektrolyse eingesetzten Energie und ist durch die Verwendung von geträgerten Ru-Katalysatoren rohstoffschonend. Einer flächendeckenden Einführung dieses Verfahrens steht jedoch die geringe Verfügbarkeit von Ruthenium (Weltproduktion 8 t/a) entgegen.

Daher ist die wissensbasierte Weiterentwicklung von katalytischen Prozessen insbesondere im Hinblick auf die effiziente Nutzung von Ressourcen (Energie und Rohstoffe) von Bedeutung. Der in der industriellen Forschung immer noch häufig verwendete Trial-and-Error Ansatz ist diesbezüglich nicht zielführend. Aus diesem Grund widmet sich die vorliegende Arbeit der mikroskopischen Aufklärung der molekularen Prozesse auf den im Sumitomo-Prozess eingesetzten RuO_2 Katalysatoren.

In Vorarbeiten von Crihan et al. [8, 9] wurde gezeigt, dass der in der Sumitomo-Reaktion eingesetzte Ruthenium-basierte Katalysator unter Reaktionsbedingungen chloriert und dadurch stabilisiert wird. Im Rahmen dieser Dissertation wurde der Chlorierungsmechanismus von $RuO_2(110)$ als Modelloberfläche unter HCl-Begasung mit Hilfe von Photoelektronenspektroskopie (HRCLS), Auger-Elektronen-Spektroskopie (AES) sowie Dichtefunktionalrechnungen (DFT) aufgeklärt. Hierbei stellte sich heraus, dass die Chlorierung der Oberfläche die Bildung guter Abgangsgruppen wie Wasser oder Kohlendioxid voraussetzt. Der Chloreinbau erfolgt oberflächenselektiv und ist selbstlimitierend. Die Bildung von Ruthenium(oxi)chloriden konnte nicht nachgewiesen werden.

Mit dem Wissen über das Chlorierungsverhalten der $RuO_2(110)$ Oberfläche konnten nun weitere Untersuchungen bezüglich der Wechselwirkungen der Chloratome mit koadsorbierten Sauerstoffatomen und Kohlenmonoxid-Molekülen durchgeführt werden. Hierzu wurde zuerst das Schwingungsverhalten von CO in unterschiedlichen chemischen Umgebungen von O und Cl auf der RuO_2 Oberfläche en detail mit Reflektions-Absorptions-Infrarot-Spektroskopie (RAIRS) studiert. Erst dadurch war es möglich, mit diesem analytischen Werkzeug, die Eigenschaften und das Verhalten der Oberfläche unter verschiedenen Atmosphären und somit den Einfluss von O_2 und CO, zu untersuchen.

Die Wechselwirkung der chlorierten RuO_2 Oberfläche mit Sauerstoff ist relevant für das Verständnis der Stabilität des Sumitomo Katalysators unter den äußerst harschen Reaktionsbedingungen der HCl-Oxidation. So zeigte sich, dass Sauerstoff eine Verschiebung von Brückenchloratomen auf on-top-Plätze induziert. Diese Verschiebungsreaktion stellt den ersten Schritt in der beobachteten Dynamik der Oberfläche dar. Das Zusammenspiel von sauerstoffinduzierter Dechlorierung der Brückenpositionen auf $RuO_2(110)$ und CO-vermittelter Rechlorierung ermöglicht ein dynamisches Antwortverhalten der Oberfläche gegenüber Veränderungen des sie umgebenden Reaktionsgasgemisches. Die hier vorgestellten Ergebnisse wurden durch eine Kombination verschiedener Methoden aus der Oberflächenchemie (HRCLS, RAIRS, TDS, SXRD, AES) mit DFT-Rechnungen erhalten.

Des Weiteren wurde der Einfluss von Chlor auf die Reaktivität und Stabilität des $RuO_2(110)$ Katalysators bezüglich einer Modellreaktion (hier CO-Oxidation) untersucht. Chloratome, beeinflussen die Reaktivität des RuO_2 Katalysators bezüglich der CO-Oxidation durch eine vornehmlich konfigurationelle Blockade der Rekombination von CO und O auf den cus-Reihen der $RuO_2(110)$-Fläche. Durch die oben vorgestellte Dynamik der Oberflächenchlorierung ist es dem Katalysator jedoch möglich, sich durch Segregation von CO und Cl auf der Oberfläche selbst zu reaktivieren und so die durch Chlor verursachte Blockade der CO Oxidation zu umgehen. Durch den Einsatz von *in situ* Methoden (wie RAIRS und *in operando* SXRD) konnte das Reaktionsverhalten und die Dynamik der chlorierten Oberfläche auch unter höheren Drücken bis in den mbar-Bereich hinein untersucht werden. Die mit UHV-Methoden sowie DFT-Rechnungen entwickelten Modelle konnten so erfolgreich auch auf diese Druckbereiche übertragen werden.

Zusammenfassend lässt sich feststellen, dass die im Rahmen der vorliegenden Dissertation erhaltenen Ergebnisse und somit das molekulare Verständnis der dynamischen Prozesse auf chloriertem RuO_2 in Zukunft dazu beitragen können, sowohl Reaktivität als auch Stabilität der industriell eingesetzten Ruthenium-basierten Katalysatoren bezüglich einer effizienteren Ressourcennutzung zu optimieren.

Bibliography

[1] Eurochlor.org. Chlorine Industry Review 2008-2009. **2009**.

[2] Moussallem, I., Järissen, J., Kunz, U., Pinnow, S., and Turek, T. Chlor-alkali electrolysis with oxygen depolarized cathodes: history, present status and future prospects. *J. Appl. Electrochem.*, *38*, 1177–1194, **2008**.

[3] Deacon, H. Improvement in manufacture of chlorine. U.S. Patent, 165802, **1875**.

[4] Iwanaga, K., Seki, K., Hibi, T., Issoh, K., Suzuta, T., Nakada, M., Mori, Y., and Abe, T. The Development of Improved Hydrogen Chloride Oxidation Process. *Sumitomo Kagaku*, *1*, 1–11, **2004**.

[5] Gestermann, F. and Ottavini, A. *Modern Chlor-Alkali Technology*, chapter 'Chlorine Production with Oxygen-depolarised Cathodes on an Industrial Scale', 49–56. Wiley VCH, **2001**.

[6] Seitsonen, A.P. and Over, H. Intimate interplay of theory and experiments in model catalysis. *Surf. Sci.*, *603*, 1717–1723, **2009**.

[7] Norskov, J.K., Bligaard, T., Rossmeisl, J., and Christensen, C.H. Towards the computational design of solid catalysts. *Nature Chemistry*, *1*, 37–46, **2009**.

[8] Crihan, D. HCl-Oxidation auf RuO_2(110): Neuartiger Deacon-Prozess. Ph.D. thesis, Justus-Liebig-Universität Gießen, **2008**.

[9] Crihan, D., Knapp, M., Zweidinger, S., Lundgren, E., Weststrate, C., Andersen, J., Seitsonen, A., and Over, H. Stable Deacon Process for HCl Oxidation over RuO_2. *Angew. Chem. Int. Ed.*, *47*, 2131–2134, **2008**.

[10] Zweidinger, S., Crihan, D., Knapp, M., Hofmann, J.P., Seitsonen, A.P., Weststrate, C.J., Lundgren, E., Andersen, J.N., and Over, H. Reaction Mechanism of the Oxidation of HCl over $RuO_2(110)$. *J. Phys. Chem. C*, *112*, 9966–9969, **2008**.

[11] Seitsonen, A.P., Hofmann, J.P., and Over, H. Deacon Process over RuO_2 and TiO_2-Supported RuO_2. *LRZ Report*, *submitted*, **2009**.

[12] López, N., Gómez-Segura, J., Marín, R.P., and Pérez-Ramírez, J. Mechanism of HCl oxidation (Deacon process) over RuO_2. *J. Catal.*, *255*, 29–39, **2008**.

[13] Farkas, A. In situ IR spectroscopic studies of the CO oxidation reaction over a ruthenium model catalyst. Ph.D. thesis, Justus-Liebig-Universität Gießen, **2008**.

[14] Farkas, A., Mellau, G.C., and Over, H. Novel Insight in the CO Oxidation on $RuO_2(110)$ by in Situ Reflection-Absorption Infrared Spectroscopy. *J. Phys. Chem. C*, *113*, 14341–14355, **2009**.

[15] Campbell, C.T. and Paffett, M.T. The role of chlorine promoters in catalytic ethylene epoxidation over the Ag(110) surface. *Appl. Surf. Sci.*, *19*, 28–42, **1984**.

[16] Jankowiak, J.T. and Barteau, M.A. Ethylene epoxidation over silver and copper-silver bimetallic catalysts: II. Cs and Cl promotion. *J. Catal.*, *236*, 379–386, **2005**.

[17] Christmann, K. *Introduction to Surface Physical Chemistry*. Topics in Physical Chemistry. Springer, **1991**.

[18] Redhead, P.A. Thermal desorption of gases. *Vacuum*, *12*, 203–244, **1962**.

[19] Bludau, H. Strukturuntersuchungen an den Systemen Cs/Ru(0001) und Cs+O/Ru(0001). Ph.D. thesis, FU Berlin, **1992**.

[20] Siegbahn, K. Electron Spectroscopy for Atoms, Molecules and Condensed Matter. Nobel lecture, **1981**.

[21] Woodruff, D. and Delchar, T. *Modern techniques of surface science.* Cambridge University Press, 2^{nd} edition, **1994**.

[22] Hüfner, S. *Photoelectron Spectroscopy - Principles and Applications.* Springer, 3^{rd} edition, **2003**.

[23] Salmeron, M. and Schlögl, R. Ambient pressure photoelectron spectroscopy: A new tool for surface science and nanotechnology. *Surf. Sci. Rep.*, *63*, 169–199, **2008**.

[24] Koopmans, T. Über die Zuordnung von Wellenfunktionen und Eigenwerten zu den Einzelnen Elektronen Eines Atoms. *Physica*, *1*, 104 – 113, **1934**.

[25] Seah, M.P. and Dench, W.A. Quantitative electron spectroscopy of surfaces: A standard data base for electron inelastic mean free paths in solids. *Surf. Interf. Anal.*, *1*, 2–11, **1979**.

[26] Adams, D.L. and Andersen, J.N. *FitXPS.* Aarhus University, **2001**.

[27] Doniach, S. and Šunjić, M. Many-electron singularity in x-ray photoemission and x-ray line spectra from metals. *J. Phys. C*, *3*, 285–291, **1970**.

[28] Nyholm, R., Andersen, J.N., Johansson, U., Jensen, B.N., and Lindau, I. Beamline I311 at MAX-LAB: a VUV/soft X-ray undulator beamline for high resolution electron spectroscopy. *Nucl. Instrum. Meth. Phys. Res. A*, *467-468*, 520–524, **2001**.

[29] Resta, A. Interaction of Some Molecules with Complex Surfaces. Ph.D. thesis, Lund University, **2008**.

[30] Bragg, W.L. The Diffraction of Short Electromagnetic Waves by a Crystal. *Proc. Cambridge Phil. Soc.*, *17*, 43–57, **1913**.

[31] Bragg, W.L. The Structure of Some Crystals as Indicated by their Diffraction of X-rays. *Proc. Roy. Soc. (London)*, *A89*, 248–277, **1914**.

[32] Vickermann, J. and Gilmore, I., editors. *Surface Analysis: The Principal Techniques.* John Wiley & Sons Ltd, 2^{nd} edition, **2009**.

[33] Robinson, I.K. and Tweet, D.J. Surface X-ray Diffraction. *Rep. Prog. Phys.*, *55*, 599–651, **1992**.

[34] Robinson, I.K. Crystal truncation rods and surface roughness. *Phys. Rev. B*, *33*, 3830–3836, **1986**.

[35] Stierle, A., Delheusy, M., and Zweidinger, S. ANKA Karlsruhe, **2009**. Unpublished results.

[36] He, Y.B., Knapp, M., Lundgren, E., and Over, H. Ru(0001) model catalyst under oxidizing and reducing reaction conditions: in-situ high pressure surface X-ray diffraction study. *J. Phys. Chem. B*, *109*, 21825–21830, **2005**.

[37] Ackermann, M.D. Operando SXRD : a new view on catalysis. Ph.d. thesis, Leiden Institute of Physics, Faculty of Science, Leiden University, **2007**.

[38] Balmes, O., van Rijn, R., Wermeille, D., Resta, A., Petit, L., Isern, H., Dufrane, T., and Felici, R. The ID03 surface diffraction beamline for in-situ and real-time X-ray investigations of catalytic reactions at surfaces. *Catal. Today*, *145*, 220–226, **2009**.

[39] Lee, M.T., Wang, Z.Q., and Chang, J.R. Activated-Carbon-Supported NaOH for Removal of HCl from Reformer Process Streams. *Ind. Eng. Chem. Res.*, *42*, 6166–6170, **2003**.

[40] American Society for Testing and Materials. Standard Guide for Background Subtraction Techniques in Auger Electron Spectroscopy (E995-84). *Surf. Interf. Anal.*, *11*, 114–115, **1988**.

[41] Powell, C.J. and Seah, M.P. Precision, Accuracy, and Uncertainty in Quantitative Surface Analyses by Auger-Electron Spectroscopy and X-ray Photoelectron Spectroscopy. *J. Vac. Sci. & Technol. A: Vacuum, Surfaces, and Films*, *8*, 735–763, **1990**.

[42] Pantano, C. and Madey, T.E. Electron Beam Damage in Auger Electron Spectroscopy. *Appl. Surf. Sci.*, *7*, 115–141, **1981**.

[43] Godowski, P. and Przybylski, K. Effect of Peak Overlap on Auger Peak Amplitude Measurement Error in dN/dE Mode. *Vacuum*, *39*, 439–442, **1989**.

[44] Carlson, T.A. *Photoelectron and Auger Spectroscopy.* Plenum Press, 1^{st} edition, **1975**.

[45] Weber, R.E. and Johnson, A.L. Determination of Surface Structures using LEED and Energy Analysis of Scattered Electrons. *J. Appl. Phys.*, *40*, 314–318, **1969**.

[46] Labohm, F. A Simple Background Correction for AES Peak Height Measurements. *Surf. Interf. Anal.*, *4*, 194–196, **1982**.

[47] Davis, L.E., MacDonald, N.C., Palmberg, P.W., Riach, G.E., and Weber, R.E. *Handbook of Auger Electron Spectroscopy.* Physical Electronics Division Perkin-Elmer Corporation, **1976**.

[48] Bowker, M. and Waugh, K. The adsorption of chlorine and chloridation of Ag(111). *Surf. Sci.*, *134*, 639–664, **1983**.

[49] Bowker, M. and Waugh, K. Chlorine adsorption and chloridation of Ag(110). *Surf. Sci.*, *155*, 1–14, **1985**.

[50] Buffeteau, T., Desbat, B., and Turlet, J.M. Polarization Modulation FT-IR Spectroscopy of Surfaces and Ultra-thin Films: Experimental Procedure and Quantitative Analysis. *Appl. Spectrosc.*, *45*, 380–389, **1991**.

[51] Greenler, R.G. Infrared Study of Adsorbed Molecules on Metal Surfaces by Reflection Techniques. *J. Chem. Phys.*, *44*, 310–315, **1966**.

[52] Greenler, R.G. Design of a reflection–absorption experiment for studying the IR spectrum of molecules adsorbed on a metal surface. *J. Vac. Sci. Technol.*, *12*, 1410–1417, **1975**.

[53] Pfnür, H., Menzel, D., Hoffmann, F.M., Ortega, A., and Bradshaw, A.M. High resolution vibrational spectroscopy of CO on Ru(001): The importance of lateral interactions. *Surf. Sci.*, *93*, 431–452, **1980**.

[54] Hoffmann, F.M. Infrared reflection-absorption spectroscopy of adsorbed molecules. *Surf. Sci. Rep.*, *3*, 107–192, **1983**.

[55] Bradshaw, A.M. and Schweizer, E. *Spectroscopy of Surfaces.* John Wiley & Sons, Chichester, **1988**.

[56] Blyholder, G. Molecular orbital view of chemisorbed carbon monoxide. *J. Phys. Chem.*, *68*, 2772–2778, **1964**.

[57] Gerloch, M. and Constable, E.C. *Transition Metal Chemistry.* Wiley VCH, **1994**.

[58] Ibach, H. and Somorjai, G.A. Evidence for the weakening of the C-O bond upon coadsorption with hydrocarbons. *Appl. Surf. Sci.*, *3*, 293–296, **1979**.

[59] Moskovits, M. and Hulse, J.E. Frequency shifts in the spectra of molecules adsorbed on metals, with emphasis on the infrared spectrum of adsorbed CO. *Surf. Sci.*, *78*, 397–418, **1978**.

[60] Hollins, P. and Pritchard, J. Infrared studies of chemisorbed layers on single crystals. *Progr. Surf. Sci.*, *19*, 275–349, **1985**.

[61] Kohn, W. and Sham, L. Self-Consistent Equations Including Exchange and Correlation Effects. *Phys. Rev. A*, *140*, 1133–1138, **1965**.

[62] Martin, R.M. *Electronic Structure: Basic Theory and Practical Methods.* Cambridge University Press, **2004**.

[63] Perdew, J.P., Burke, K., and Ernzerhof, M. Generalized Gradient Approximation Made Simple. *Phys. Rev. Lett.*, *77*, 3865–3868, **1996**.

[64] Kohanoff, J. *Electronic Structure Calculations for Solids and Molecules.* Cambridge University Press, **2006**.

[65] Blöchl, P.E. Projector augmented-wave method. *Phys. Rev. B*, *50*, 17953–17979, **1994**.

[66] Kresse, G. and Furthmüller, J. Efficiency of ab-initio total energy calculations for metals and semiconductors using a plane-wave basis set. *Comp. Mat. Sci.*, *6*, 15–50, **1996**.

[67] Kresse, G. and Joubert, D. From ultrasoft pseudopotentials to the projector augmented-wave method. *Phys. Rev. B*, *59*, 1758–1775, **1999**.

[68] Kresse, G. and Furthmüller, J. *VASP the GUIDE.* Institut für Materialphysik, Universität Wien, Sensengasse 8, A-1130 Wien, Austria, **2005**.

[69] W.H. Press, B.P. Flannery, S.T. and Vetterling, W., editors. *Numerical Recipes.* Cambridge University Press, New York, **1986**.

[70] Seitsonen, A.P. Theoretical Investigations into Adsorption and Co-adsorption on Transition-Metal Surfaces as Models to Heterogeneous Catalysis. Ph.d. thesis, Technische Universität Berlin, **2002**.

[71] Pehlke, E. and Scheffler, M. Evidence for site-sensitive screening of core holes at the Si and Ge (001) surface. *Phys. Rev. Lett.*, *71*, 2338–2341, **1993**.

[72] Lizzit, S., Baraldi, A., Groso, A., Reuter, K., Ganduglia-Pirovano, M.V., Stampfl, C., Scheffler, M., Stichler, M., Keller, C., Wurth, W., and Menzel, D. Surface core-level shifts of clean and oxygen-covered Ru(0001). *Phys. Rev. B*, *63*, 205419, **2001**.

[73] Seitsonen, A.P. private communication, **2009**.

[74] Henkelman, G., Jóhannesson, G., and Jónsson, H. *Progress on Theoretical Chemistry and Physics*, chapter 'Methods for Finding Saddle Points and Minimum Energy Paths', 269–300. Kluwer Academic Publishers, **2000**.

[75] Jónsson, H., Mills, G., and Jacobsen, K.W. *Classical and Quantum Dynamics in Condensed Phase Simulations*, chapter 'Nudged Elastic Band Method for Finding Minimum Energy Paths of Transitions', 385–404. World Scientific, **1998**.

[76] Aßmann, J., Narkhede, V., Breuer, N.A., Muhler, M., Seitsonen, A.P., Knapp, M., Crihan, D., Farkas, A., Mellau, G., and Over, H. Heterogeneous oxidation catalysis on ruthenium: bridging the pressure and materials gaps and beyond. *J. Phys.: Condens. Matter*, *20*, 184017, **2008**.

[77] Aßmann, J. and Muhler, M. Der isotherme Labor-Festbettreaktor mit quantitativer Online-Analytik als vielseitiges Instrument in der Redoxkatalyse. *Chem. Ing. Tech.*, *78*, 862–868, **2006**.

[78] Kanzler, C.H. Katalytische Oxidation von CO an chlorierten RuO_2-Pulvern - Aufbau einer Festbett-Reaktionsapparatur und Experimente im kontinuierlichen Fluss bei Atmosphärendruck. Diploma thesis, Justus-Liebig-Universität Gießen, **2009**.

[79] Narkhede, V. Kinetic and Spectroscopic Investigations to Elucidate the Mechanisms of CO Oxidation over Ru and Au Catalysts. Ph.D. thesis, Ruhr-Universität Bochum, **2006**.

[80] Wendt, S. Komplexe Redox-Chemie auf der $RuO_2(110)$-Oberfläche. Phd thesis, FU Berlin, **2002**.

[81] Over, H., Seitsonen, A.P., Lundgren, E., Schmid, M., and Varga, P. Experimental and simulated STM images of stoichiometric and partially reduced $RuO_2(110)$ surfaces including adsorbates. *Surf. Sci.*, *515*, 143–156, **2002**.

[82] Kim, Y.D. Atomic-Scale Structure and Catalytic Reactivity of RuO_2. Ph.D. thesis, Freie Universität Berlin, **2000**.

[83] Knapp, M. Die Schlüsselrolle des Wasserstoffs im Reaktionsverhalten einer oxidischen Katalysatoroberfläche am Beispiel von $RuO_2(110)$. Ph.D. thesis, Justus-Liebig-Universität Gießen, **2006**.

[84] Wendt, S., Seitsonen, A., Kim, Y., Knapp, M., Idris, H., and Over, H. Complex redox chemistry on the $RuO_2(110)$ surface: experiment and theory. *Surf. Sci.*, *505*, 137–152, **2002**.

[85] Knapp, M., Crihan, D., Seitsonen, A., Lundgren, E., Resta, A., Andersen, J., and Over, H. Complex Interaction of Hydrogen with $RuO_2(110)$ Surface. *J. Phys. Chem. C*, *111*, 5363–5373, **2007**.

[86] Aßmann, J. Ruthenium als Oxidationskatalysator IR-spektroskopische und kinetische Untersuchung der Oxidation von CO. Ph.D. thesis, Ruhr-Universität Bochum, **2004**.

[87] Over, H., Kim, Y., Seitsonen, A., Wendt, S., Lundgren, E., Schmid, M., Varga, P., Morgante, A., and Ertl, G. Atomic-Scale Structure and Catalytic reactivity of the $RuO_2(110)$ surface. *Science*, *287*, 1474–1476, **2000**.

[88] Blume, R., Hävecker, M., Zafeiratos, S., Teschner, D., Kleimenov, E., Knop-Gericke, A., Schlögl, R., Barinov, A., Dudin, P., and Kiskinova, M. Catalytically active states of Ru(0001) catalyst in CO oxidation reaction. *J. Catal.*, *239*, 354–361, **2006**.

[89] Lindroos, M., Pfnür, H., Held, G., and Menzel, D. Adsorbate induced reconstruction by strong chemisorption: Ru(001)-$p(2 \times 2)$-O. *Surf. Sci.*, *222*, 451–463, **1989**.

[90] Pfnür, H., Held, G., Lindroos, M., and Menzel, D. Oxygen induced reconstruction of a close-packed surface: A LEED IV study on Ru(001)-$p(2\times1)$O. *Surf. Sci.*, *220*, 43–58, **1989**.

[91] Kim, Y.D., Wendt, S., Schwegmann, S., Over, H., and Ertl, G. Structural analyses of the pure and cesiated Ru(0001)-(2×2)-3O phase. *Surf. Sci.*, *418*, 267–272, **1998**.

[92] Stampfl, C., Schwegmann, S., Over, H., Scheffler, M., and Ertl, G. Structure and Stability of a High-Coverage (1×1) Oxygen Phase on Ru(0001). *Phys. Rev. Lett.*, *77*, 3371–3374, **1996**.

[93] Boettcher, A. and Niehus, H. Oxygen adsorbed on oxidized Ru(0001). *Phys. Rev. B*, *60*, 14396–14404, **1999**.

[94] Over, H. and Seitsonen, A.P. Oxidation of Metal Surfaces. *Science*, *297*, 2003–2004, **2002**.

[95] Kim, S.H. and Wintterlin, J. Morphology of $RuO_2(110)$ oxide films on Ru(0001) studied by scanning tunneling microscopy. *J. Chem. Phys.*, *131*, 064705, **2009**.

[96] Peden, C.H.F. Surface science of catalysis. Number 483 in ACS Symp. Ser., 143. **1992**.

[97] Over, H., Knapp, M., Lundgren, E., Seitsonen, A., Schmid, M., and Varga, P. Visualization of Atomic Processes on Rutheniumdioxide using Scanning Tunneling Microscopy. *Chem. Phys. Chem.*, *5*, 167–174, **2004**.

[98] Aßmann, J., Crihan, D., Knapp, M., Lundgren, E., Löffler, E., Muhler, M., Narkhede, V., Over, H., Schmid, M., Seitsonen, A.P., and Varga, P. Understanding the Structural Deactivation of Ruthenium Catalysts on an Atomic Scale under both Oxidizing and Reducing Conditions. *Angew. Chem. Int. Ed.*, *44*, 917–920, **2005**.

[99] Kiss, J.T. and Gonzalez, R.D. Catalytic oxidation of carbon monoxide over ruthenium/silicon dioxide. An *in situ* infrared and kinetic study. *J. Phys. Chem.*, *88*, 892–897, **1984**.

[100] Cant, N.W., Hicks, P.C., and Lennon, B.S. Steady-state oxidation of carbon monoxide over supported noble metals with particular reference to platinum. *J. Catal.*, *54*, 372–383, **1978**.

[101] Diebold, U. The surface science of titanium dioxide. *Surf. Sci. Rep.*, *48*, 53–229, **2003**.

[102] Kim, Y., Over, H., Krabbes, G., and Ertl, G. Identification of RuO_2 as the active phase in CO oxidation on oxygen-rich ruthenium surfaces. *Topics in Catal.*, *14*, 95–100, **2001**.

[103] LaFemina, J.P. Total energy computations of oxide surface reconstructions. *Crit. Rev. Surf. Chem.*, *3*, 297–386, **1994**.

[104] Seitsonen, A.P., Kim, Y.D., Knapp, M., Wendt, S., and Over, H. CO adsorption on the reduced RuO_2(110) surface: Energetics and structure. *Phys. Rev. B*, *65*, 035413, **2001**.

[105] Over, H., Seitsonen, A.P., Lundgren, E., Schmid, M., and Varga, P. Direct imaging of catalytically important processes in the oxidation of CO over RuO_2(110). *J. Am. Chem. Soc.*, *123*, 11807–11808, **2001**.

[106] Fan, C.Y., Wang, J., Jacobi, K., and Ertl, G. The oxidation of CO on RuO_2(110) at room temperature. *J. Chem. Phys.*, *114*, 10058–10062, **2001**.

[107] Wang, H., Schneider, W.F., and Schmidt, D. Intermediates and Spectators in O_2 Dissociation at the RuO_2(110) Surface. *J. Phys. Chem. C*, *113*, 15266–15273, **2009**.

[108] Lee, H.I. and White, J.M. Carbon monoxide oxidation over Ru (001). *J. Catal.*, *63*, 261–264, **1980**.

[109] Kim, Y.K., Morgan, G.A., and Yates, J.T. Role of atomic step defect sites on the catalytic oxidation of carbon monoxide: Comparison between Ru(001) and Ru(109) single-crystal surfaces. *J. Phys. Chem. C*, *111*, 3366–3368, **2007**.

[110] Peden, C.H.F. and Goodman, D.W. Kinetics of CO Oxidation over Ru(0001). *J. Phys. Chem.*, *90*, 1360–1365, **1986**.

[111] Over, H., Balmes, O., and Lundgren, E. Direct comparison of the reactivity of the non-oxidic phase of Ru(0001) and the RuO_2 phase in the CO oxidation reaction. *Surf. Sci.*, *603*, 298–303, **2009**.

[112] Goodman, D., Peden, C., and Chen, M. CO oxidation on ruthenium: The nature of the active catalytic surface. *Surf. Sci.*, *601*, L124–L126, **2007**.

[113] Over, H., Muhler, M., and Seitsonen, A. Comment on CO oxidation on ruthenium: The nature of the active catalytic surface by D.W. Goodman, C.H.F. Peden, M.S. Chen. *Surf. Sci.*, *601*, 5659–5662, **2007**.

[114] Goodman, D., Peden, C., and Chen, M. Reply to comment on CO oxidation on ruthenium: The nature of the active catalytic surface by H. Over, M. Muhler, A.P. Seitsonen. *Surf. Sci.*, *601*, 5663–5665, **2007**.

[115] Flege, J.I., Hrbek, J., and Sutter, P. Structural imaging of surface oxidation and oxidation catalysis on Ru(0001). *Phys. Rev. B*, *78*, 165407, **2008**.

[116] Lundgren, E., Kresse, G., Klein, C., Borg, M., Andersen, J.N., De Santis, M., Gauthier, Y., Konvicka, C., Schmid, M., and Varga, P. Two-Dimensional Oxide on Pd(111). *Phys. Rev. Lett.*, *88*, 246103, **2002**.

[117] Gustafson, J., Mikkelsen, A., Borg, M., Lundgren, E., Köhler, L., Kresse, G., Schmid, M., Varga, P., Yuhara, J., Torrelles, X., Quirós, C., and Andersen, J.N. Self-Limited Growth of a Thin Oxide Layer on Rh(111). *Phys. Rev. Lett.*, *92*, 126102, **2004**.

[118] Ackermann, M.D., Pedersen, T.M., Hendriksen, B.L.M., Robach, O., Bobaru, S.C., Popa, I., Quiros, C., Kim, H., Hammer, B., Ferrer, S., and Frenken, J.W.M. Structure and Reactivity of Surface Oxides on Pt(110) during Catalytic CO Oxidation. *Phys. Rev. Lett.*, *95*, 255505, **2005**.

[119] Dudin, P., Barinov, A., Gregoratti, L., Kiskinova, M., Esch, F., Dri, C., Africh, C., and Comelli, G. Initial Oxidation of a Rh(110) Surface Using Atomic or Molecular Oxygen and Reduction of the Surface Oxide by Hydrogen. *J. Phys. Chem. B*, *109*, 13649–13655, **2005**.

[120] Gustafson, J., Westerstrom, R., Mikkelsen, A., Torrelles, X., Balmes, O., Bovet, N., Andersen, J.N., Baddeley, C.J., and Lundgren, E. Sensitivity of catalysis to surface structure: The example of CO oxidation on Rh under realistic conditions. *Phys. Rev. B (Condensed Matter and Materials Physics)*, *78*, 045423, **2008**.

[121] Gao, F., McClure, S., Cai, Y., Gath, K., Wang, Y., Chen, M., Guo, Q., and Goodman, D. CO oxidation trends on Pt-group metals from ultrahigh vacuum to near atmospheric pressures: A combined in situ PM-IRAS and reaction kinetics study. *Surf. Sci.*, *603*, 65–70, **2009**.

[122] Gao, F., Wang, Y., Cai, Y., and Goodman, D.W. CO Oxidation on Pt-Group Metals from Ultrahigh Vacuum to Near Atmospheric Pressures. 2. Palladium and Platinum. *J. Phys. Chem. C*, *113*, 174–181, **2009**.

[123] Over, H., Balmes, O., and Lundgren, E. In situ structure-activity correlation experiments of the ruthenium catalyzed CO oxidation reaction. *Catal. Today*, *145*, 236–242, **2009**.

[124] Wang, J., Fan, C., Jacobi, K., and Ertl, G. The kinetics of CO oxidation on RuO_2(110): bridging the pressure gap. *J. Phys. Chem. B*, *106*, 3422–3427, **2002**.

[125] Ziff, R.M., Gulari, E., and Barshad, Y. Kinetic Phase Transitions in an Irreversible Surface-Reaction Model. *Phys. Rev. Lett.*, *56*, 2553–2556, **1986**.

[126] Over, H., Seitsonen, A., Lundgren, E., Schmid, M., and Varga, P. Direct imaging of catalytically important processes in the oxidation of CO over RuO_2(110). *J. Am. Chem. Soc.*, *123*, 11807–11808, **2001**.

[127] Knapp, M., Crihan, D., Seitsonen, A., and Over, H. Hydrogen Transfer Reaction on the Surface of on Oxide Catalyst. *J. Am. Chem. Soc.*, *127*, 3236–3237, **2005**.

[128] Zweidinger, S. HCl Oxidation over RuO_2 catalysts - Working title. Ph.D. thesis, Justus-Liebig-Universität Gießen, **to be published**.

[129] Preyss, W., Ebinger, H., Fick, D., Polenz, C., Polivka, B., Saier, V., Veith, R., C.Weindel, and Jänsch, H. Adsorption of chlorine on Ru(0001) and codesorption with lithium. *Surf. Sci.*, *373*, 33–42, **1997**.

[130] Zweidinger, S., Hofmann, J.P., and Over, H. LEED laboratory, Justus-Liebig-Universität Gießen, **2009**. Unpublished results.

[131] Baerends, E.J. and Ros, P. The electronic structure of transition metal carbonyl complexes. *Mol. Phys.*, *30*, 1735–1747, **1975**.

[132] Rohmann, C., Wang, Y., Muhler, M., Metson, J., Idriss, H., and Wöll, C. Direct monitoring of photo-induced reactions on well-defined metal oxide surfaces using vibrational spectroscopy. *Chem. Phys. Lett.*, *460*, 10 – 12, **2008**.

[133] Kim, Y.D., Seitsonen, A.P., Wendt, S., Wang, J., Fan, C., Jacobi, K., Over, H., and Ertl, G. Characterization of Various Oxygen Species on an Oxide Surface: RuO_2(110). *J. Phys. Chem. B*, *105*, 3752–3758, **2001**.

[134] Farkas, A. MonteCarlo simulations on RuO_2(110), **2009**. Unpublished results.

[135] Paulus, U.A., Wang, Y., Jacobi, K., and Ertl, G. CO Adsorption on the Reduced RuO_2(110) Surface. *Surf. Sci.*, *547*, 349–354, **2003**.

[136] Reuter, K. and Scheffler, M. First-principles kinetic Monte Carlo simulations for heterogeneous catalysis: Application to the CO oxidation at RuO2(110). *Phys. Rev. B*, *73*, 045433, **2006**.

[137] Zweidinger, S. LEED laboratory, Justus-Liebig-Universität Gießen, **2009**. Unpublished results.

[138] Krause, P.P.T. and Zweidinger, S. LEED laboratory, Justus-Liebig-Universität Gießen, **2009**. Unpublished results.

[139] The determination of the surface chlorine concentration on RuO_2(110) was not possible by means of SXRD. The preparation protocol was adapted from UHV experiments.

[140] Wolf, A., Schluter, O.F.K., Haas, M., and Gerhartz, F. Processes for the Oxidation of Carbon Monoxide in a Gas Stream Containing HCl. U.S. patent, 20080267849, **2008**.

[141] Narkhede, V., Aßmann, J., and Muhler, M. Structure-Activity Correlations for the Oxidation of CO over Polycrystalline RuO_2 Powder Derived from Steady-State and Transient Kinetic Experiments. *Z. Phys. Chem.*, *219*, 979–995, **2005**.